Synthesis, Characterization, and In-situ Monitoring of Promoted ZnO Adsorbents for Desulfurization in Fuel Cell Applications

by

Achintya Sujan

A dissertation submitted to the Graduate Faculty of
Auburn University
in partial fulfillment of the
requirements for the Degree of
Doctor of Philosophy

Auburn, Alabama
May 6, 2017

Keywords: Fuel cells, Desulfurization, Cu-ZnO, ZnO, Fiber optics, In-situ spectroscopy

Copyright 2017 by Achintya Sujan

Approved by

Bruce J. Tatarchuk, Chair, Professor of Chemical Engineering
W. Robert Ashurst, Associate Professor of Chemical Engineering
Allan David, Associate Professor of Chemical Engineering
Minseo Park, Associate Professor, Department of Physics

Abstract

Energy from conventional power plants and transportation vehicles usually end up as low grade waste heat and this accounts for more than 70% of the fuel energy input. Fuel cell power systems for logistic or stationary applications are far more energy efficient and environmentally benign employing primarily hydrogen gas compared to conventional energy generating systems. Natural gas, Liquefied Petroleum Gas, and recently biogas and landfill gas are being considered as hydrogen rich sources as raw materials for fuel cells. However, the major presence of sulfur compounds in these sources can cause severe corrosion of processing equipment and irreversible poisoning of fuel processor catalysts and membrane electrode assemblies in fuel cells. Compact, light and small volume unit processes addressing the fuel conversion and purification are essential, especially for on-board logistic applications. Adsorptive desulfurization employing metal oxide sorbents is a low cost and less energy intensive choice compared to hydro-desulfurization which demands high hydrogen partial pressures and elevated temperatures. More over amine based sulfur absorptions processes involve the use of amines and solvents which are typically efficient when operating at the industrial scale. Reformation is the major step for hydrocarbon conversion to hydrogen for fuel cells. Pre-reformer desulfurization typically removes high molecular weight liquid phase sulfur compounds including thiophenes and mercaptans. To protect high value membrane catalysts in fuel cells, post-reformer desulfurization is necessary to remove low molecular residual sulfur compounds including H_2S and COS. This is achieved using ZnO, CuO, TiO_2, and Al_2O_3 that serve as polishing metal oxide sorbents with capacities higher than 50mgS/g.

This dissertation discusses the aspects of efficient gas phase desulfurization for fuel cell

applications and is focussed on the synthesis, characterization, and in-situ monitoring of promoted ZnO adsorbents for H_2S and COS removal. Highly dispersed ZnO doped (crystallites < 4nm) with transition metals on SiO_2 support was found to be effective sorbents for H_2S removal at ambient conditions with stable capacity over multiple adsorption regeneration cycles. $Cu_XZn_{100-X}O/SiO_2$ sorbents with a Cu concentration of 20 atomic % (X) was found to be optimized sorbent formulation for H_2S removal over wide operating conditions. Enhanced reactivity at ambient temperature is due to reduced mass transfer resistance in supported ZnO during interaction with H_2S. Crystal defects with oxygen vacancies in the ZnO lattice play an important role during the electronic effects in the H_2S adsorption process. The oxidation environment, electronic effects and degree of dispersion of CuO and ZnO in $Cu_XZn_{100-X}O/SiO_2$ sorbents were investigated via ex-situ and in-situ characterization techniques including UV-Vis Diffuse Reflectance Spectroscopy (UV-Vis DRS), X-ray Photoelectron Spectroscopy (XPS), X-ray Diffraction (XRD), and Electron Paramagnetic Resonance (EPR) Spectroscopy. It was found that Cu^{2+} in calcined specimen exists in a octahedral coordination environment with tetragonal distortions. In addition, Cu^{2+} ions created acceptor levels in the ZnO band structure causing persistent reduction in the ZnO band gap. Lower band gap means more stable valence band and enhanced ability to interact with the molecular orbitals of H_2S. The absence of quantum confinement effect was confirmed since the ZnO nano-particle radius was greater than the ZnO bohr excition radius (3.2 nm). However, XPS results indicate an increase in dispersion of surface Zn atoms when promoted with Cu concentrations up to 20 atomic%. In-situ EPR spectroscopy suggests that Cu^{2+} ions were in isolated form and interacted with H_2S that caused a reduction in oxidation state from +2 in calcined sorbents to +1 in sulfided sorbents. Further reducibility from +1 to 0 (metallic copper) was influenced by neighbouring iso-electronic Zn^{2+} ions.

A fiber optic based UV-Vis diffuse reflectance spectroscopic system was implemented as an embedded sensor in the desulfurizer assembly to measure the utilization of adsorbent beds during H_2S removal at 22 °C for logistic fuel cell applications. The efficacy of the embedded fiber optic sensor is evaluated as a function of (i) H_2S concentration (ii) H_2S contact time (iii) Presence of CO, CO_2 and moisture in feed stream and (iv) H_2S adsorption on 3/16 inch extrudates using a 6mm optical probe. It was shown that H_2S adsorption proceeds via change in color and optical properties of adsorbents. When the fiber optic probe embedded horizontally at bottom of packed bed of ZnO adsorbents, the time at derivative maxima of area under UV-Vis spectrum was close to H_2S breakthrough time. Adsorbent bed utilization determined from in-situ optical measurements over wide range of operating parameters is expected to provide significant savings in cost of adsorbent materials and avoid the need for over design of adsorption units during compact and small volume desulfurization operation.

Promotional effect of Cu^{2+} ion in $CU_XZn_{100-X}O/SiO_2$ adsorbents was assessed in terms of COS formation as a function of Cu:Zn molar ratio, moisture and temperature at constant H_2S partial pressure in a model reformate containing 30%CO + 30%CO_2 + 0.6% H_2S and balance H_2. COS concentration formed at saturation was lower in case of $Cu_{20}Zn_{80}O/SiO_2$ sorbent as compared to ZnO/SiO_2. Considering significant H_2 concentration in the feed stream, the lower COS concentration in the case of Cu-ZnO/SiO_2 was attributed to the catalytic hydrogenation of COS (at 200°C and higher) on Cu_2S, formed by reduction with H_2S. When experiments were carried out with 5000 ppmv moisture in feed, much lower concentration of COS at saturation was evident in case of both sorbents. Moisture had a COS inhibition effect most likely due to hydrolysis of COS, in which case ZnS is known to be a catalyst.

Pure ZnO and rare earth metal oxides (La^{3+}, Y^{3+} and Ce^{3+}) promoted ZnO were synthesized using a co-precipitation method and examined for the simultaneous removal of H_2S and COS from syngas at 400°C. The dual functional La_2O_3-ZnO bed showed a four-fold increase in sulfur saturation capacity per unit sorbent weight (176 mg/g) and three-fold increase in sulfur saturation capacity in terms of unit bed volume (56 mg/cm^3) compared to a mixed bed or layered bed consisting of a COS hydrolysis catalyst and H_2S adsorbent.

Acknowledgments

I would like to acknowledge the guidance and encouragement of my adviser Dr. Bruce Tatarchuk throughout my PhD degree. I would like to express my sincere gratitude to Dr. Allan David, Dr. Robert Ashurst, and Dr. Minseo Park for serving on my PhD committee. I am grateful to Dr. Dong-joo (Daniel) Kim for willing to serve as the university reader for this dissertation. I would also like to thank Dr. Evert Duin for EPR measurements in the department of Chemistry and Biochemistry at Auburn University. Special thanks to Steve Moore from Material Engineering department for his assistance with the Scanning Electron Microscopy and XRD measurements. I would also like to thank Matt Montgomery from Glass Shop at Auburn University. This work would not be possible without the unwavering support of Dr. Hongyun Yang and Dr. Paul Dimick from Intramicron Inc. The financial support from the U.S. Army (TARDEC) for this research is gratefully acknowledged.

I would like to thank all current and past colleagues at the Center for Microfibrous Materials Manufacturing (CM3), especially, Dr. Donald Cahela, Dr. Wenhua Zhu, Dwight Cahela, Kimberly Dennis, Dr. Abhijeet Phalle, Dr. A.H.M Shahadat Hussain, Dr. Sabrina Wahid, Dr. Amogh Karwa, Dr. Min Sheng, Dr. Guomin Xu, Dr. Pengfei Zhao, Mingyang Chi, William R. Yantz Jr., Dr. Zenda Davis, Xinquan Cheng, and Peng Cheng, without whom this work would not have been possible.

I am grateful to Dr. Christopher Roberts and Dr. Mario Eden for believing in me and giving me an opportunity to pursue a Ph.D. degree at Auburn University. Karen Cochran and Elaine Manning have been extremely helpful and I would like to thank them for their administrative support throughout my time at Auburn.

A special thanks to Dr. Shantanu Pradhan, Dr. Petra Kerscher, Dr. Pranav Vengsarkar,

Dr. Ramesh Pallapolu, Dr. Xiu Wang, Vikrant Dev, and Rohit Kanungo for their constant support throughout my PhD degree. They have made my life at Auburn enjoyable and memorable.

Most importantly, I would like to thank my wife, Mithuna Valsan for standing by side and sharing the joy and pain during my PhD degree. I remain indebted to my mother, grand-parents, and family for their unwavering support and encouragement. Finally, I would like to dedicate this work to my late father, Mr. Ratnam Sujan and my late grandfather Mr. C.K.Subraminian.

Table of Contents

List of Tables

List of Figures

List of Abbreviations

NG	Natural Gas
LPG	Liquefied Petroleum Gas
NGL	Natural Gas Liquids
FT	Fischer Tropsch
SMR	Steam Methane Reformer
OMR	Oxidative Methane Reformer
WGS	Water Gas Shift
T	Thiophene
BT	Benzothiophene
THT	Tetrahydrothiophene
EM	Ethyl Mercaptan
TBM	Terbutyl Mercaptan
DMS	Dimethyl Sulfide
PEM	Proton Exchange Membrane
SOFC	Solid Oxide Fuel Cell
HDS	Hydrodesulfurization
LDH	Layered Double Hydroxides
HTLC	Hydro-Talcite-Like-Compounds
PPMV	Part Per Million by Volume
GHSV	Gas Hourly Space Velocity
GC	Gas Chromatograph
UHP	Ultra High Purity

MFC	Mass Flow Controller
TCD	Thermal Conductivity Detector
PFPD	Pulsed Flame Photometric Detector
RH	Relative Humidity
BET	Brunauer Emmett Teller
BJH	Barrett Joyner Halenda
SMA	Sub Miniature Version A
CCD	Charged Coupled Device
PVC	Poly Vinyl Chloride
PTFE	Poly Tetra Fluoro Ethylene
Xe	Xenon
TMI	Transition Metal Intermediate
LUB	Length of Unused Bed
DC	Direct Voltage
XRD	X-Ray Diffraction
SEM	Scanning Electron Microscope
UV-Vis	Ultra Violet – Visible
DRS	Diffuse Reflectance Spectroscopy
KM	Kubelka Munk
IR	Infrared
FTIR	Fourier Transform Infrared
DFT	Density Functional Theory
XPS	X-ray Photoelectron Spectroscopy

DLD	Delay Lines Detector
BE	Binding Energy
KE	Kinetic Energy
CB	Conduction Band
VB	Valence Band
FWHM	Full Width Half Maximum
IMFP	Inelastic Mean Free Path
EPR	Electron Paramagnetic Resonance
EDS	Electron Diffraction Spectroscopy
TEM	Transmission Electron Microscopy
NMR	Nuclear Magnetic Resonance
LMCT	Ligand to Metal Charge Transfer
BT	Breakthrough time
MAX	Maximum

Nomenclature

h	Planck's constant, 6.626×10^{-34} m^2kg/s
G	Specific Gibbs free energy, kJ/mol
H	Reaction enthalpy, kJ/mol
L	Metal loading, % by weight
C_0	Initial concentration, ppmv
C	Final concentration, ppmv
X	Atomic concentration, mol %
y	Mole fraction in gas phase
x	Conversion, %
R	Universal gas constant, $8.314\frac{J}{mol-K}$
W	Weight, g
I	XPS Intensity, Arbitrary units
N_A	Avogadro's number, $6.02214\times10^{23}\frac{atoms}{mol}$
ML	Monolayer
T	Temperature, in °C or K
C_p	Heat capacity at constant pressure, kJ/mol K
k	Reaction rate constant
A_t	Area under diffuse reflectance spectrum at time t, nm
A_t	Area under 1st derivative of diffuse reflectance spectrum at time t, nm
UL	Un-utilized bed length, %
$t_{1/2}$	Time for 50% contaminant breakthrough, min

L_p	Axial length of fiber optic probe from top of packed bed, cm
L_b	Length of packed bed, cm
n	direct allowed transition for ZnO
$F(R_\infty)$	Kubelka-Munk absorbance for solids
R_{sample}	Diffuse reflectance of sample, %
m_e	Effective mass of an electron, 9.1×10^{-31}kg
e	Charge of an electron, 1.602×10^{-19}C
E_g	Energy band gap, eV

Greek symbols

σ	Photoelectron cross section of an element, nm
λ	Inelastic mean free path of an electron in an element, nm
γ	Gamma phase
ρ	Density, g/cm^3
∞	Infinity
β	Rate of change of energy band gap with temperature, eV/K
Δ	Difference in property
υ	Frequency of light
θ	XRD angle, in °
ε	Dielectric constant
ε_0	Vacuum relative permittivity, F m^{-1}

I. Introduction and Review of Literature

I.1. Existing and dominant desulfurization technologies [1]

I.1.1 Catalytic Hydro-desulfurization:

Hydro-desulfurization (HDS) is the removal of sulfur by a reduction treatment. Sulfur present as thiols, sulfides, disulfides and thiophenes in crude oil feed stocks undergoes hydrogenolysis to produce H_2S and a hydrocarbon. For example, in case of methyl mercaptan (CH_3SH) and thiophene (C_4H_4S),

$$CH_3SH + H_2 \rightarrow H_2S + CH_4$$

$$C_4H_4S + 3H_2 \rightarrow H_2S + C_4H_8$$

The reactivity decreases in the following sequence for R and R' groups:

RSH > RSSR' > RSR' > thiophenes

Where, R is an aliphatic or aromatic group.

HDS process is carried out in presence of a Co-Mo/Al_2O_3 catalyst (1-4wt% Co & 8-16% Mo).

I.1.2 Absorption into a Liquid

In this type of technology, liquid solutions are used to absorb the gaseous H_2S. During absorption, H_2S may either dissolve or react with the components in the solution to form corresponding sulfided solutions. Solutions used for this purpose typically comprise of alkanol-amines, aqueous ammonia, alkali (Na or K) salt solutions. Monoethanolamine, ($HOCH_2CH_2NH_2$) is one of the most widely used alkanolamines for H_2S absorptive removal. The reaction proceeds as follows:

$$2HOCH_2CH_2NH_2 + H_2S \rightarrow (HOCH_2CH_2NH_3)_2S$$

$$(HOCH_2CH_2NH_3)_2S + H_2S \rightarrow 2HOCH_2CH_2NH_3HS$$

The function of the hydroxyl group is to decrease the vapour pressure and increase the water solubility of the alkanolamine, and the amine group makes an aqueous solution of the compound basic so that it can neutralize acidic gases such as H_2S.

I.1.3 Removal of H_2S by Oxidation

The Claus process is a well-known process for removal of H_2S via oxidation. This process is used to recover sulfur from feed stocks containing high H_2S concentrations (ca. 1-4 wt%). In the first reaction, H_2S is oxidised in air to SO_2 at 550°C

$$H_2S + \frac{3}{2}O_2 \rightarrow H_2O + SO_2$$

The remaining H_2S then reacts with SO_2 at ca. 400°C on an Al_2O_3 based catalyst forming elemental sulfur.

$$2H_2S + SO_2 \rightarrow 3S \downarrow + 2H_2O$$

However, the above reaction is equilibrium limited and thus this method is unable to reduce the sulfur content of gas feed stocks to ppm levels. Furthermore, presence of CO_2 in the feedstock can react with H_2S to form COS and CS_2 in the high temperature oxidation stage of the process.

I.1.4 Adsorptive Removal of H_2S using Solid Sorbents

I.1.4a High Temperature Sorbents:

H_2S removal at temperatures in excess of 300°C has been carried out on oxides of Fe, Mo, Zn, Mn, Ca, Ba, Sr, Cu, W, Co and V [2]. Zinc titanate has also been identified at effective candidate for high temperature H_2S removal. The rate of formation of sulfide and saturation coverage of sulfide on ZnO and Zinc titanate [3] were similar at 720°C but sulfide coverage on TiO_2 was

much lower. Iron (III) oxide, calcium oxide and zinc oxide have also been investigated over the temperature range of 600-800°C [4].

I.2.4b Low Temperature Sorbents:

The main advantage of removing H_2S at low temperatures is that processing costs are substantially reduced. For compact fuel processors as shown in Figure I.1 in a fuel cell based power generation system, sorbent-based desulfurization at ambient temperatures temperature is relatively cost feasible compared to conventional HDS that requires high H_2 partial pressure and high temperature. In HDS, desulfurization of organic compounds in the presence of hydrogen takes place at 370°C, 40 bar over $CoO/MoO_3/Al_2O_3$ catalyst to generate H_2S. In spite of their availability, sulfur tolerant catalysts are not economically feasible due to the high costs arising out of Pt or Pd.

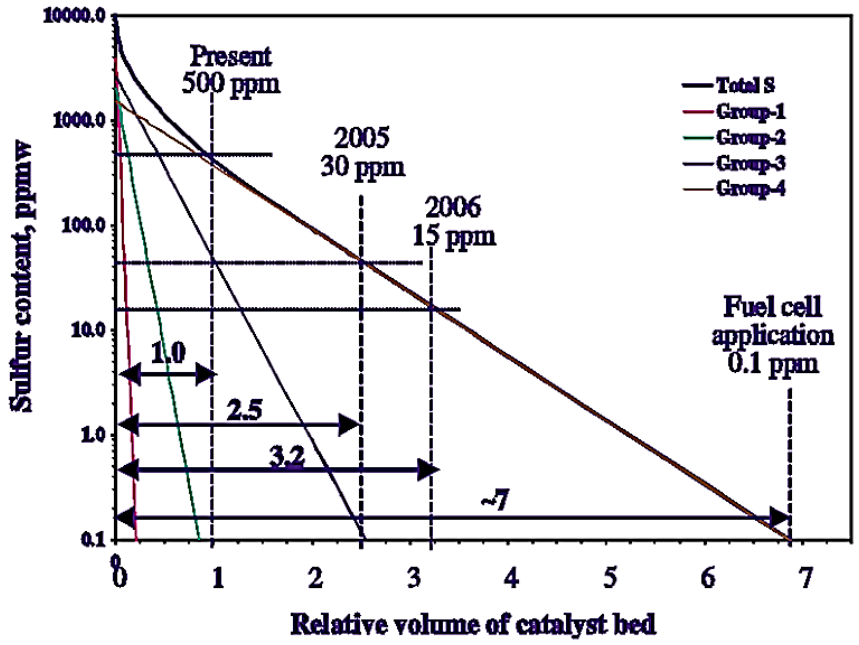

Figure I.1. Simulated HDS of Diesel to meet 15 and 0.1 ppm level on the basis of a conventional single-stage reactor, assuming 1 weight % sulfur in feed [5].

The low sulfur, methane rich stream is then fed to one of the following units: Steam Methane Reformer (SMR), Catalytic Partial Oxidizer (CPO) or an Auto Thermal Reformer (ATR), depending on the type of feedstock used for hydrogen production. The outlet of these reforming units is a H_2 rich stream containing CO (syngas), CO_2, water vapor (in case of SMR) and low molecular weight hydrocarbons. The sulfur compounds in reformate streams, if any, are usually converted to Hydrogen Sulfide (H_2S) and Carbonyl Sulfide (COS). The H_2S concentration can range from less than 10 ppmv for regulated diesel or gasoline to >10,000 ppmv for a coal containing > 3wt% sulfur that is gasified using an O_2 blown gasifier [6].

I.2. Introduction to desulfurization for fuel cell applications

Over 60% of precious fuel energy input to conventional power plants and transportation vehicles ends up as low-grade waste heat. Fuel cell systems are significantly more energy efficient and cleaner than conventional energy systems. The wide distribution network of natural gas and petroleum derivatives make them attractive H_2 rich fuels for fuel cells. R&D efforts are directed towards design of compact, efficient, light weight and small volume fuel processors for anode and cathode fuel enrichment. NG primarily consists of methane, but also small quantities of C_2-C_4 alkanes and impurities like H_2S, methyl mercaptan, mercury and inerts (CO_2, N_2 and water vapor)[6]. For safety reasons, sulfur odorants are added to NG as an indicator for leak detection before it is sold over the wide distributed network. THT (or Tetrahydrothiophene) is a common sulfur odorant used in Europe while a variety of sulfur compounds such as TBM (Tert-butyl mercaptan) or DMS (Di-methyl sulfide) may be used as odorants in the US. In the case of NG, the total sulfur concentration (including the odorant) is between 2-20 ppmv, while LPG could have up to 120 ppmv S [6]. However, when NG is used as the feedstock during H_2 production for

fuel cells the sulfur species contained in it act as severe poisons for the downstream fuel processor catalysts. The sulfur content in 'ppmw' in the various types of fuel is illustrated in Table I.1. A reduction in the cell voltage of a fuel cell 0.675V to 0.625V occurred in presence of only 1 ppmv H_2S in the feed stream [7] during a study to understand the effect of sulfur on the fuel cell performance. For high sulfur content present in mixtures of higher hydrocarbons such as heavy diesel or aviation fuel, desulfurization is usually performed upstream of the reformer to prevent sulfur poisoning of the reforming catalysts [8].

Table I.2. Sulfur content in the various hydrocarbon fuels and reformate streams after oxidative or steam reforming

Type of fuel	Sulfur (ppmw) Fuel	Sulfur (ppmw) Reformate
NG	2 – 12	0.4-2.4
LPG	20-100	2-13
Gasoline	30-80	3-10
Diesel	15	1.5-2.0
Jet Fuel	500-1500	50-190

Sulfur appears primarily as H_2S and COS in the reformate gas (syngas) when a sulfur containing fuel is reformed or gasified as shown in Figure I.2. The COS concentration depends on the operating conditions of the desulfurizer and an equilibrium between H_2S in presence of CO and CO_2. H_2S concentration can range from less than 10 ppmv for regulated diesel or gasoline to > 10,000 ppmv for a coal containing > 3 wt % sulfur that is gasified using an oxygen-blown gasifier. Complete desulfurization of this gas down to <0.1-1 ppmv (H_2S + COS) is necessary before it is used in a fuel cell. While efforts to develop adsorbents for high temperature sulfur

removal continue, only recently has there been an increasing interest in the development of sorbents for ambient temperature sulfur removal.

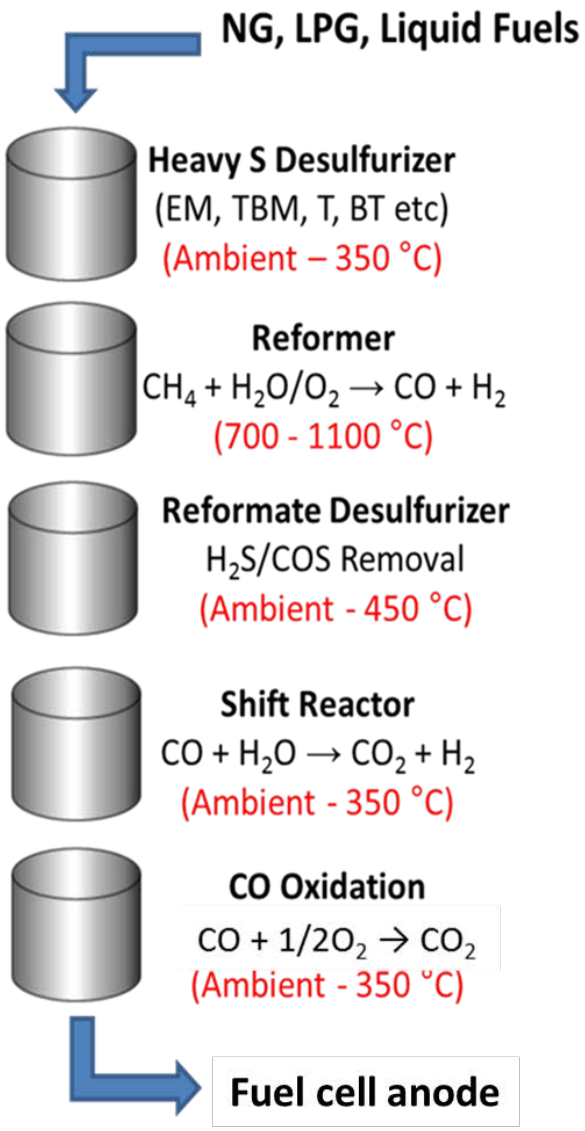

Figure I.2. Logistic fuel to H_2 conversion for fuel cells

This is essential during the cold startup or transition operations in a fuel cell system when the reactor experiences temperature variations ranging from ambient temperature to several hundred degree Celsius [9]. The low temperature operation is particularly attractive in vehicular applications wherein low pressure drop can be obtained due to lower viscosities of gases

operated at low temperatures [10]. As a result, the sorbent needs to maintain a stable performance over a wide temperature range without compromising on sulfur removal capacity. Table I.2 shows relative composition of sulfur impurities in the hydrocarbon fraction [11].

Table I.3. Composition of Total Percent of Sulfur in HC Fractions during Processing of NG

Hydrocarbon Fraction	H_2S (%)	COS (%)	Mercaptans (%)
Ethane	50	10	-
Propane	50	90	90
Butane	-	-	10

A few characteristics of adsorbents desirable for removal of sulfur from NG or LPG for fuel cell applications are as follows [6]:

1. High activity – removal of all sulfur compounds down to 0.1 ppmv before breakthrough above 0.1 ppmv of the first compound(s) that breakthrough.
2. High sulfur capacity – at least 1 g S/100 g sorbent, preferably 2.5 – 3 g S per 100 g sorbent prior to breakthrough.
3. No external heating of sorbent or fuel required for operation.
4. Low exothermicity
5. Color change due to sulfur compound adsorption to provide a visual indication of the impending breakthrough.
6. Non-pyrophoric or not liable to ignite spontaneously on exposure to air.
7. Scalable operation and sorbent preparation.
8. Regenerable if designed for reuse, in an environmentally acceptable manner.
9. Low cost in case of non-reusable (disposable).

10. Disposable as non-hazardous waste upon being spent.

I.3. Adsorbents for H_2S removal

I.3.1 Bulk ZnO sorbents

The easy availability and low production cost [12] of the micrometer-size ZnO particles compared to molecular sieves or zinc-titanium oxide make them successful adsorbent materials in the chemical industry [13] for removal of hydrogen sulfide (H_2S) in the temperature range of 350-450°C especially during steam reforming of hydrocarbon feed stocks for H_2 production[14]. Theoretical capacity of bulk ZnO is 400mgS/gZnO [15]. For fuel cell applications [6], the capacity expected to be 500mgS/g. The sorbent capacity needs to be maintained for fuel cell operating under mild conditions. However, commercial ZnO sorbents, usually consisting of large particles or extrudates suffer from sever mass transfer limitations at low temperatures (<100°C). For example, the performance of commercial ZnO sorbent operating in the range of 25-100°C was compared to high surface area metal oxides including nano-crystalline ZnO [16], it was shown that the yield of sulfidation is a factor of approx.13 higher for nano-crystalline ZnO due to both higher surface area and the higher “intrinsic reactivity” of the surface vs “bulk” form of ZnO.

I.3.2 Supported ZnO sorbents

The severe mass transfer resistance at low temperature may be overcome by the supported ZnO adsorbents that offer a very high degree of nano-dispersion of the active ZnO phase and therefore high yields of surface sulfidation reaction [17]. The concept of utilizing H_2S inert and stable oxide materials in the formulation of a supported ZnO sorbent was realized when a fine

dispersion of ZnO phase on ordered meso-porous silica (SBA-15) support offered an enhanced H_2S removal efficiency at low temperature [18]. Enhanced reactivity at ambient to low temperature due to nano-dispersed ZnO may be associated with one or more of the following (1) quantum size effects exhibited by nano-crystalline ZnO [19] with a probable indication of a change in the thermodynamics and/or kinetics of the sulfidation reaction (2) high surface/volume ratio with increased Zn atoms present on the surface and directly available for reaction with H_2S [17] (3) surface defects with the sulfidation-promoting behavior are known to be present in the ZnO nano-particles (NPs) of size ranges from 14.3 to 35.3 nm and characterized by TEM, TPR, XRD and XPS [20].

I.3.3 Transition metal promoted ZnO sorbents

The reactivity of nano-structured ZnO based sorbents at low temperature can be further improved by doping ZnO with transition metals like Mn, Fe, Co, Ni or Cu oxides since the thermodynamics of sulfidation of many TM oxides is more favorable than that of ZnO itself. It was previously observed that the doping of ZnO with 3d transition metals allowed an increase in the H_2S breakthrough capacity at room to moderate temperature [21-23]. The ZnO sulfidation yield can be increased by promoter effect of TM metal dopants in variety of ways such as (i) presence of sulfur and oxygen vacancies in the ZnO lattice [23] (ii) increase in active surface area of ZnO [24] or (iii) Promotion due to diffusion of H_2S i.e. HS^- and S^{2-} into ZnO [24]. Cu promoted ZnO based adsorbents employed for low temperature H_2S removal have been the object of interest for several years, owing to the synergistic effect of the CuO-ZnO binary oxide system compared to the performance of the pure metal oxides CuO and ZnO. Several theories have been proposed to explain the promotional effect of Cu^{2+} ion in Cu-ZnO adsorbents such as

(i) Well-proportioned distribution of the active phase inside the porous support material and the size of the metal oxide nano-particle [25] (ii) Reduction in ZnO particle size and increase in the available surface area for reaction with H_2S [21, 23] (iii) Acceleration of sulfur transport through grain boundary of the Cu containing ZnS layer due to presence of sulfur vacancies [13, 21, 26] (iv) Favorable sulfidation thermodynamics at room temperature [23] and so on. In order to overcome the problem of sintering, loss in surface area and lattice diffusion resistance as a result of multiple sulfidation-regeneration operating cycles, metal oxides may be deposited on high surface area supports.

Table I.4. Saturation capacity (mgS/g ZnO) of sorbents at 22°C when tested with 2% H_2S/H_2

Adsorbents	mg S/g ZnO	% Theoretical
ZnO (BASF)	19	4.8
ZnO (Sud-Chemie)	32	8.1
21% ZnO/SiO_2	253	64
Me^{n+} doped ZnO/SiO_2 class of sorbents*		
Mn^{2+} doped ZnO/SiO_2	238	59
Ni^{2+} doped ZnO/SiO_2	253	63
Co^{2+} doped ZnO/SiO_2	305	76
Fe^{3+} doped ZnO/SiO_2	329	82
Cu^{2+} doped ZnO/SiO_2	367	92

*M^{3+}/M^{2+} to Zn atomic ratio in sorbents = 5:95

Table I.3 illustrates the saturation capacity of bulk ZnO and various transition metal-promoted ZnO/SiO_2 sorbents for H_2S removal at 22°C and percent of theoretical capacity based on the following gas solid reaction,

$$ZnO_{(s)} + H_2S_{(g)} \rightarrow ZnS_{(s)} + H_2O_{(g)}$$

$$\text{Theoretical capacity } (\%) = \ 395 \frac{\text{mgS}}{\text{g}_{\text{ZnO}}}$$

I.4. Characterization of sorbents for H_2S removal

I.4.1 X-ray Photoelectron Spectroscopy (XPS)

A major criterion in the selection of an appropriate spectroscopic technique for analysis of the ZnO based sorbents is the sensitivity of the technique towards the element(s) of interest. In un-promoted ZnO sorbents of major interest are sites of Zn and S. XPS is an excellent technique suited for obtaining information on the electronic states of Zn^{+2} via the determination of Auger Parameter (AP) in the reactant ZnO (AP is ~2010.2 eV for ZnO) [27] while in the product ZnS (AP is 2011.4 eV for ZnS) [28] and was implemented by us in our previous investigation [29]. In terms of the Cu doped ZnO sorbents characterization via XPS [29] results indicate (1) BE of Cu $2p_{3/2}$ peak in CuS (932.3 eV) [30] is almost identical to the BE of Cu $2p_{3/2}$ peak [31] in Cu_2S as a result of which the different forms of Cu could not be distinguished (2) the XPS induced Cu containing samples were subjected to X-rays, heat, and secondary electrons causing a possible reduction of Cu^{+2} to Cu^{+1} observed commonly in other studies. Considering the possible limitations in the inherent construction (internal walls of the vacuum chamber susceptible to corrosion due to H_2S), general operating principle (high vacuum environment) and scarce literature on operando studies using X-ray Photoelectron Spectroscopy (XPS) there is a need for a complementary technique to study these sorbents.

I.4.2 Electron Paramagnetic Resonance Spectroscopy (EPR)

Techniques operating at low photon energy for the measurement of the spin states of the ions (Zn and/or S) may be useful to study the sulfidation and regeneration reactions of H_2S sorbents. However, the Zn^{+2} Cation with an electronic configuration of $[Ar]4s^0 3d^{10}$ is diamagnetic thus limits analysis via paramagnetic resonance methods such as ESR and electron nuclear double resonance (ENDOR). Zinc in its natural metallic form is composed of five stable isotopes namely, ^{64}Zn, ^{66}Zn, ^{67}Zn, ^{68}Zn, ^{70}Zn. The ^{64}Zn is most abundant isotope (48.6%). However, only the less (4.1%) abundant ^{67}Zn isotope has a nuclear spin (5/2). This is below the typical sensitivity of the NMR technique indicated simply by broad NMR lines.

I.4.3 UV-Vis Diffuse Reflectance Spectroscopy (UV-Vis DRS)

While the application of UV-Vis spectroscopy, coupled with photometers in the measurement of color and chemical concentration, continues, recent developments in the study of heterogeneous catalysts with the advent of high quality fiber optics, sensitive and affordable array detectors coupled with chemo-metrics have enabled the characterization under real-time [32] operating conditions to obtain essential information like the identification of active species [33], determination of temporal distribution of TMI species in the catalyst bed, and particles [34], the changes in oxidation states and coordination geometries occurring during the activation [35], during the catalytic reaction. UV-Vis DRS measurements reveal a distorted octahedral geometry of Cu^{+2} ion in the Cu-ZnO/SiO_2 sorbent matrix [36]. This technique will be implemented to determine metal oxide band gap and understanding the interaction of transition metal promoter with H_2S in the reformate feed.

I.4.4 Density Functional Theory (DFT)

In this section, the promotional effect of the Cu^{+2} site in the Cu-ZnO/SiO_2 sorbent during interaction with H_2S via DFT calculations [36]. During DFT analysis, an iso-desmic reaction is assumed in which type of bonds broken in the reactant are same as those formed in the product. The Cu atom is computed to be more stable by a magnitude of 15.6 kcal/mol embedded in $Cu_1Zn_{36}O_{37}$. It was shown that SH_2 prefers to bind towards Cu^{+2} site vs Zn^{+2} ions & the opposite is true in the case of H_2O. Another possibility to consider is the displacement of H_2O with H_2S at the Cu^{+2} ions in a ZnO surface with Zn^{+2} ions substituted with Cu^{+2}.

I.5. Embedded sensor for process monitoring of the adsorption process

Adsorbents undergo a color change upon interaction with the contaminant molecule. This color change can provide a visual indication of the impending breakthrough and can be monitored spectroscopically. Table I.5 shows list of sorbents and inherent color change upon adsorption reported in the literature.

Table I.5. Materials with color change upon adsorption

Adsorbent	Application	Color change	Ref
Silica gel	Moisture adsorption	Orange to White	[37]
Ag (Na) – Y Zeolite	DMS & TBM adsorption	White to yellow, orange or brown	[7]
Sulfa-trap	DMS adsorption	Color darkens on adsorption	[6]

Currently, the sulfur concentration in the outlet stream of the desulfurizer unit is measured using inline chromatography, detector tubes or portable electrochemical sensors. However, the measured concentration at the outlet cannot directly represent the utilization of an entire adsorbent bed. Moreover, the costs of these methodologies are relatively high and it is not

economically practical to integrate such methods for continuous analyses of sulfur compounds for small-scale applications such as miniaturized fuel processors in logistic applications. Several methodologies and techniques are commercially available to directly monitor the utilization of adsorbent beds [38-41]. Such methods are based on probing one or more physical properties of the adsorbent material such as color, density, magnetism, temperature etc. However, a few challenges exist such as (i) a separate unit in the desulfurization process was required in case of on-line detection of sulfur concentration downstream of adsorbent beds (ii) detection based on temperature difference required a fuel pre-heater with accurate temperature measurements at multiple points in the process (iii) detection based on color change of adsorbents using cameras had limitations while monitoring adsorbents with little or no color change such as SiO_2 supported ZnO [40]. Thus, there is a need for a technique to determine the degree of utilization and capacity of adsorbent or catalyst beds that does not require two or more sensors and the accuracy of which does not rely on the measurement of concentration of one or more contaminants.

I.6. Un-desired Carbonyl Sulfide (COS) formation during reformate desulfurization

Carbonyl Sulfide (COS) formation during desulfurization process contradicts the aim of desulfurization operation and the formed COS is unfavourable to the downstream process catalysts, equipment and fluid pipelines. Another concern is that presence of COS is known to cause compliance-testing failures while using Liquefied Petroleum Gas (LPG) or Natural Gas Liquids (NGL) as a raw material for H_2 production. COS was reported as a poison for a methanol synthesis catalyst [42], a commercial Fe-Cu-K Fischer Tropsch catalyst [43] and activated carbon [44] based catalyst. Removal of these sulfur compounds is imperative to prevent corrosion of the copper and brass tubing used in propane fed appliances. COS formation takes

place as a side reaction based on the reactions shown below:

$CO + H_2S \leftrightarrow COS + H_2$ ($\Delta H_f^0 = -10.9 \frac{kJ}{mol}$) ..... (A)

$CO_2 + H_2S \leftrightarrow COS + H_2O$ ($\Delta H_f^0 = +30.3 \frac{kJ}{mol}$)..... (B)

$CO_2 + CO + 2H_2S \leftrightarrow 2COS + H_2 + H_2O$ ..... (A + B)

Some requirements for a desulfurizer used in logistic fuel cell systems consist of a (i) small reactor, (ii) wide temperature operation, (iii) high capacity H_2S sorption. However, there exist some inherent challenges to the desulfurizer unit such as (1) the total sulfur breakthrough is determined by homogeneous/heterogeneous COS formation (2) during COS hydrolysis, the kinetics at low temperature is severely affected by site blockage (due to adsorption of species of reaction namely, CO_2, H_2O or H_2S).

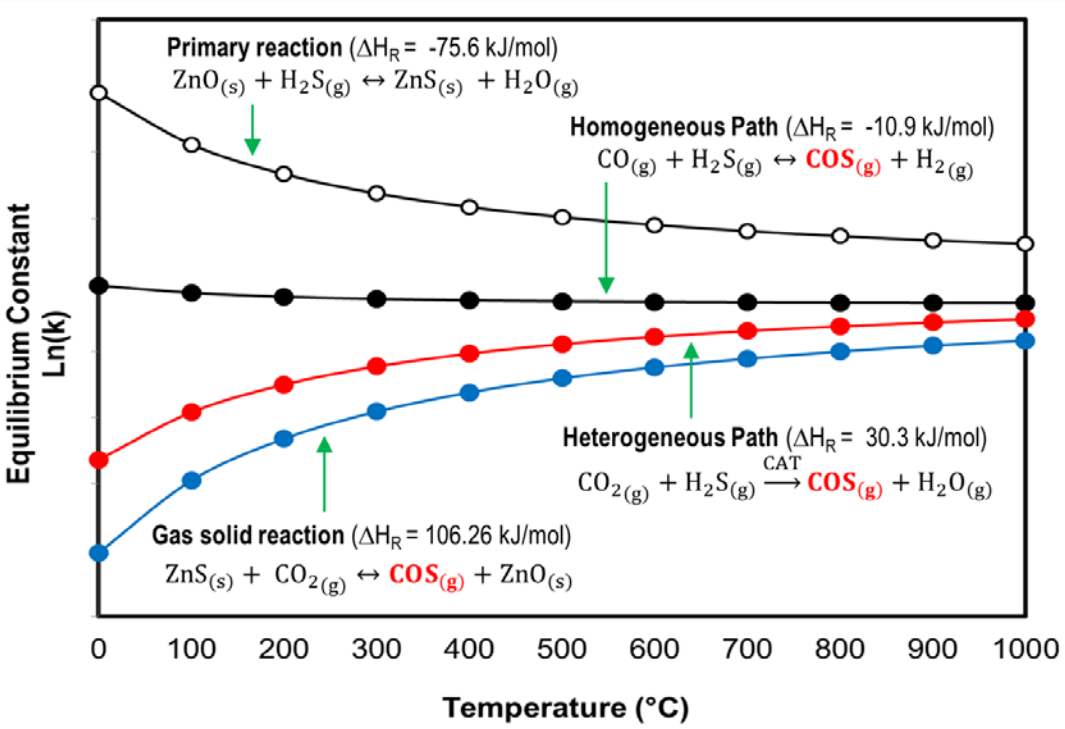

Figure II Equilibrium constant for reaction between CO/CO_2 with H_2S vs. temperature

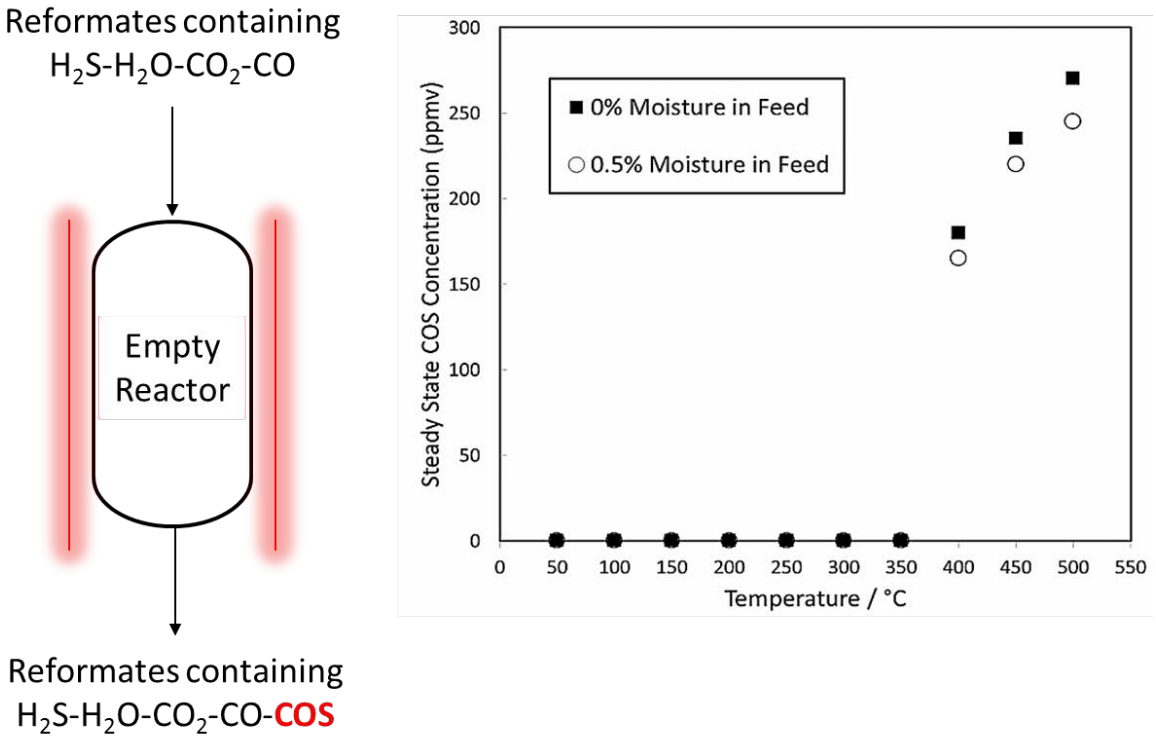

Figure III Non-catalytic pathway or homogeneous COS formation

Equilibrium calculations in Figure I.3 suggest that restricting the feed stream to low operating temperature means avoiding the reaction between CO_2 and H_2S. However, CO and H_2S still react homogeneously to form COS. To verify this experimentally, a feed stream consisting of 30% CO, 30% CO_2, 0.6% H_2S Balance H_2 was admitted to an empty reactor tube maintained at constant temperature as shown in Figure I.4. The components in the feed stream reacted homogeneously in absence of any material (sorbent or packing) to form COS. At 400°C, the steady state COS concentration observed was 180±10 ppm, whereas at 500°C, the steady state COS concentration observed was 260±10 ppm. This shows that the reactions (A) and (B) are equilibrium limited even in the presence of moisture (5000 ppmv) in the feed stream. In a similar fashion, the feed mixture consisting of 30% CO, 30% CO_2, 0.6% H_2S Balance H_2 and no moisture was passed through the empty quartz tube. In this test, steady state COS concentrations

at 400, 450 and 500 °C were 165, 220 and 245 ppm respectively. The presence of moisture prevents COS formation due to a shift in the equilibrium reaction between COS and H_2O to form H_2S and CO_2. Efficient H_2S removal can be achieved via highly dispersed ZnO supported on porous silica [9, 15, 45-47]. However, ZnO based adsorbents suffer from almost no capacity for COS at ambient conditions (discussed later in this section). Moreover, the adsorption kinetics of ZnO based sorbents is severely affected in presence of H_2S feed stream containing H_2O [47] due competitive adsorption between H_2O possessing higher polarity (Dipole = 1.85 Debye) as compared to H_2S (Dipole = 0.97 Debye). Molecular sieves pose another problem during H_2S removal as H_2S and CO_2 react within the framework of these zeolites to form COS. This is particularly evident in NG dehydration units containing 4A or 5A MS [48] that offer large surface area of crystals available for catalytic formation of COS, basicity of their crystal structure, concentration of H_2S and CO_2 with lack of H_2O within the sieve pores. COS is also formed as a secondary product on sulfided sorbents. For example, when ZnO was used as a sorbent for H_2S removal at 400°C, it was seen that interaction of sulfided specimen namely ZnS with CO_2 resulted in COS formation at the outlet of the desulfurizer even in absence of any H_2S at the inlet [47, 49]. Formation of COS in a desulfurizer operating in presence of CO/CO_2 in the feed ultimately reduces the efficiency of the desulfurization unit in terms of total sulfur removal [47, 50, 51].

I.7. Adsorptive Removal of Carbonyl Sulfide:

Adsorbents for COS removal have been summarized in Figure I.5 as a function of concentration and temperature. The low polarity of COS makes it difficult to adsorb on most adsorbent materials. Amongst the ones documented for COS removal at mild conditions are metal-exchanged zeolites [52], mixed oxides from layered double hydroxides (LDH) [52, 53] and activated carbon [54]. COS adsorption at elevated temperatures (>300 °C) was reported on rare-earth oxide promoted Fe-Mn mixed oxides [55] commercial activated carbon [56] and Zinc oxide [57]].

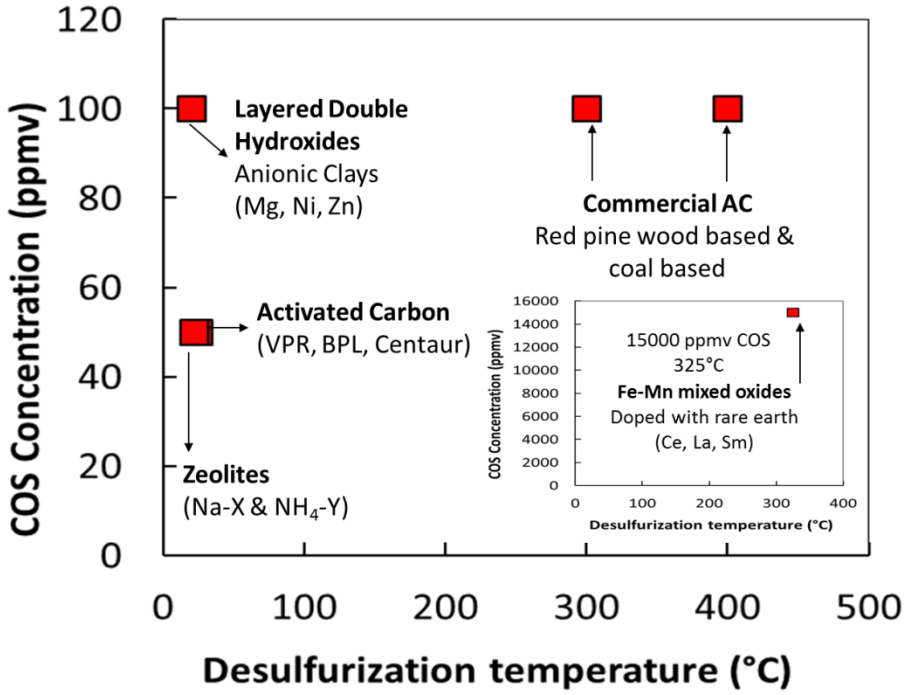

Figure I.5. COS adsorbents reported based on concentration and temperature

I.7.1 Adsorbents for COS Removal at Mild Temperatures (25-50 °C)

I.7.1a Layered Double Hydroxides

Layered Double Hydroxides (LDH) also known as Hydrotalcite-like compounds (HTLCs) are a

group of anionic clays. The general formula is $[M(II)_{1-x}M(III)_x(OH)_2]^{x+}(A^{n-})_{x/n}.mH_2O$, where M(II) and M(III) are divalent and trivalent cations in the octahedral positions within the hydroxide layers, x is the molar ratio $M(III)/M_{total}$ and its value ranges from 0.17-0.33, A^{n-} is an exchangeable interlayer anion[27, 58, 59]. LDH materials have been applied in low temperature catalysis & sorption, evidently due to their high surface areas, basic properties (in case of base catalysed reactions)[60], high metal dispersion[61] and high thermal stability[60-62]. Calcined LDHs were used as effective adsorbents for acidic molecules such as SO_2 [63], NO_X [64, 65] CO_2 [66], mercaptan, organo-sulfides, H_2S, CS_2 and thiophene from hydrocarbon streams [67]. LDH derived Ni/Mg/Al (atomic ratio 0.32/0.48/0.20) oxides showed promising adsorption properties at 20°C and atmospheric conditions for removal of COS from gas streams [53]. An Mg(0.75)Al(0.25) based LDH retained its ability to adsorb COS in presence of propene at 25°C [68]. Mg/Ni/Zn with Al based LDH were synthesized from corresponding nitrates and carbonates and tested for their COS adsorption capacities at 25°C [52]. However, LDH materials exhibited much lower COS adsorption capacities compared to Na-X type zeolites.

I.7.1b Activated Carbon

Carbon is an attractive material for gas purification applications due to its low cost and easy availability. The COS adsorption capacity of three different carbons (Vapour phase react, bituminous coal-based carbon and Centaur carbons from Calgon Cargon Corporation), the impact of relative humidity, extent of competitive adsorption between of COS in presence of H_2S and whether presence of NH_3 would impact the adsorption capacity was studied at ambient conditions of 25°C and a COS inlet concentration of 35-50 ppm[54]. The results from the study showed the following (1) Trend in adsorption capacity was Centaur > VPR > BPL (2) Trend in

capacity versus RH content of feed was 17% < 30% < 50% < 90% (3) COS adsorption capacity reduced in presence of H_2S depending upon the concentration of H_2S (4) Presence of NH_3 produced only slight increase in COS adsorption. The adsorption capacity of activated carbon is generally enhanced by the addition of transition metals [69], base metal oxides and hydroxides [70].

I.7.1c Zeolites

Zeolites are micro-porous, alumina-silicate materials commonly used as adsorbents and catalysts. Zeolites are solids possessing three-dimensional (3D) surfaces, replete with cages and channels, which may or may not intersect. Linking the pores and distributed in a more or less spatially uniform fashion throughout their bulk are the active sites which are bridging hydroxyl groups. The adsorption of CH_3SH (Methyl Mercaptan) and Carbonyl Sulfide (COS) on several metal exchanged zeolites [52] was investigated at 25°C and in presence of a feed stream containing 0.05 vol% CH_3SH or COS in CH_4.

I.7.2 Adsorbents for COS Removal at Elevated Temperature (>300 °C)

I.7.2a Iron-Manganese Oxides

Iron oxides have attracted recent attention over its reactivity towards sulfur compounds and high capacity [71, 72]. Simultaneous removal of H_2S and COS from fuel gases produced by a coal gasification process was achieved at elevated temperatures of 400°C – 800°C using FeO and MnO acceptors on γ-Al_2O_3 that allowed capacity recovery after regeneration.

I.7.2b Commercial Activated Carbon

Carbon-based adsorbent like activated carbons and carbon fibre have been extensively used for purification of water and gas streams [73, 74]. Two commercial activated carbons were studied for their capacity during simultaneous removal of H_2S and COS present in tarry compounds from biomass gasification in the temperature range of (300-400°C)[56].

I.8 Challenges during Adsorptive Removal of Carbonyl Sulfide

1. XPS data on a spent LDH-derived Ni/Mg/Al [53] mixed oxide sorbent for COS adsorption at 20 °C suggests that the limited capacity (only up to three adsorption-regeneration cycles) was due to sulfur chemisorption on the surface and/or sintering of the Ni and Mg phases.
2. For consumer systems, wherein the adsorbent cartridges need to be replaced at saturation levels, the limited regenerability of LDH materials necessitates the need for alternative materials.
3. While using carbon based adsorbents for COS removal, regeneration in an oxidizing environment (like steam, O_2 etc.) at elevated temperature of 200 °C and above results in production of ash, oxides of carbon including CO, CO_2 depending on the oxidation temperature.
4. In addition to COS, most gas streams also contain H_2S and mercaptans. Under such circumstances, the life of non-regenerable beds is reduced in presence of other sulfur species with greater affinity and acidity than COS for preferential adsorption.

I.9. Chemical conversion of COS

I.9.1 COS hydrolysis versus COS hydrogenation

Hydro-desulfurization does not remove or significantly affect the inhibition of carbonyl sulfide [75]. In the Claus process, H_2S-rich streams are processed to form elemental sulfur. However, some COS frequently is present in the feed stream entering the catalytic converters [76]. Hydrolysis of COS was recognized as the most promising process for reducing COS concentration in process hydrocarbon fuel streams due to mild reaction conditions and high conversion efficiency [77]. Moreover, the hydrolysis method offers advantages such as low reaction temperature, no consumption of hydrogen source, fewer side effects. First the thermodynamic requirement for the hydrolysis of COS in gas phase is examined. The COS hydrolysis is a moderately exothermic reaction given as,

COS Hydrolysis: $COS + H_2O \rightarrow H_2S + CO_2 \ldots \left(\Delta H_R = -33.7 \frac{kJ}{mol}\right)$

COS Hydrogenation: $COS + H_2 \rightarrow H_2S + CO \ldots \left(\Delta H_R = +11.7 \frac{kJ}{mol}\right)$

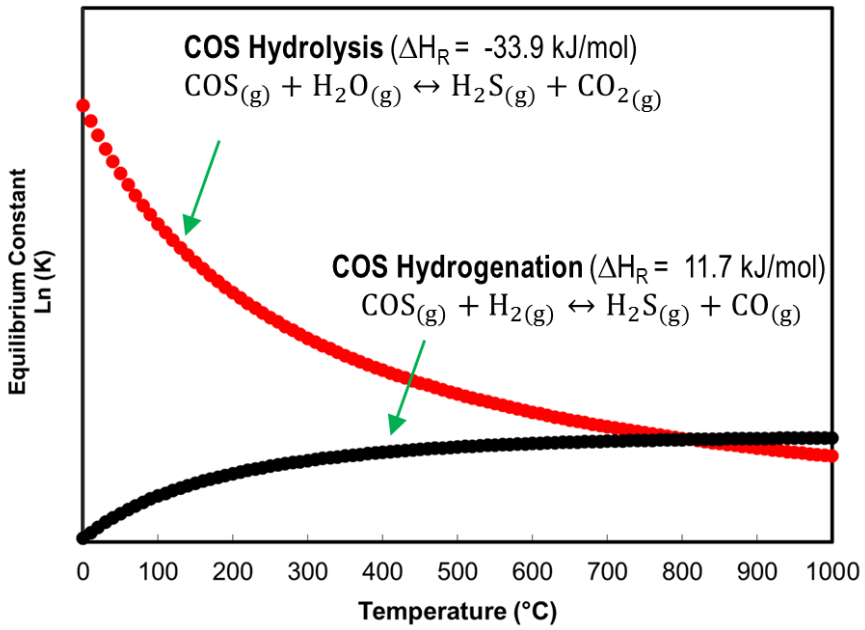

Figure I.6. Equilibrium constant for COS hydrolysis and COS hydrogenation

Thus, the equilibrium constant at 20°C is 6.22×10^5 whereas at 200°C is only 3612. Its equilibrium constant decreases with temperature. Reaching very low COS concentrations at the outlet requires low temperature operation and a high H_2O/COS ratio. The COS concentration levels in selected applications is compiled from various studies in the literature and shown below.

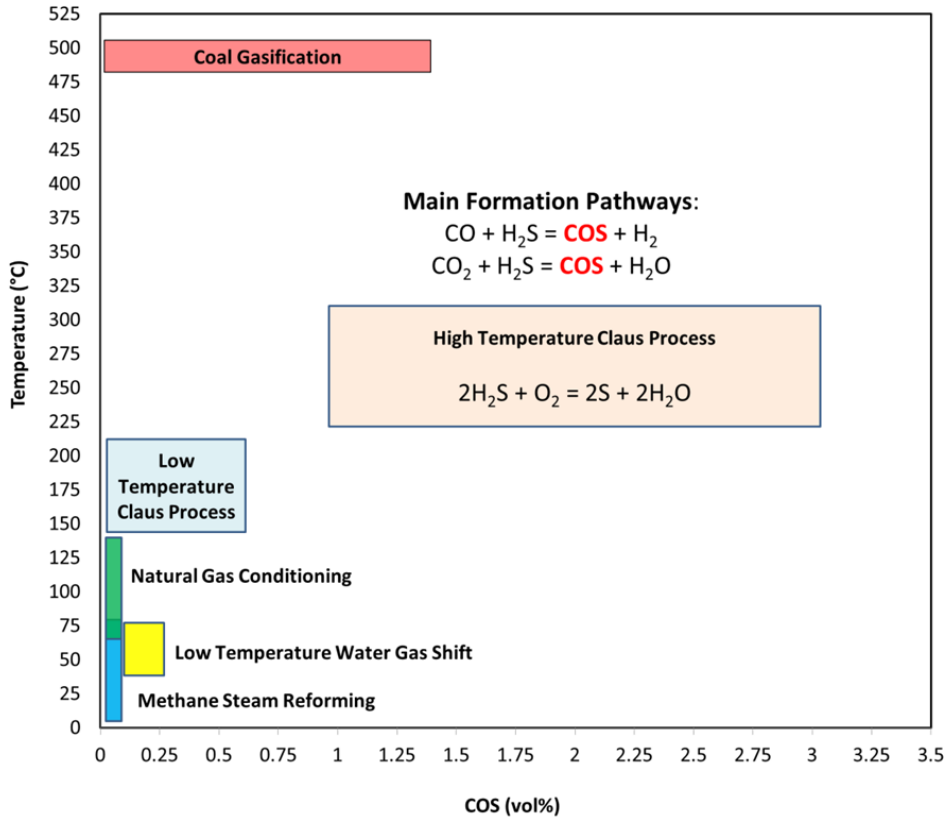

Figure IV.7. Commercial processes and conditions for COS hydrolysis

For instance, COS concentration levels can reach up to 30,000 ppm (by volume) in the Claus process operating between 250-325°C. The hydrolysis reaction mainly involves development of high activity catalysts and research on kinetics and mechanism. Hydrolysis catalysts consist of common metal oxides such as ZrO_2, TiO_2, γ-Al_2O_3 and Activated carbon. These basic oxides may be impregnated with a variety of metals including alkali metals, alkaline earth metals, rare-

earth metals and transition metals. The hydrolysis reaction is commonly used as a probe reaction to test the Bronsted basicity of catalysts since the first step of the base interaction involves the nucleophilic attack of the basic hydroxyl groups on the COS carbon atom [78-80]. Adiabatic temperature rise due to the hydrolysis reaction over wide temperature is calculated as follows and values are summarized in Table I.6 below for the temperature range of 25-150°C.

$$\Delta T_{ad} = \frac{|\Delta H_R| y_{COS} X}{C_{p_{mix}}}$$

Where,

y_{COS} = mole fraction of COS in the feed

ΔH_R = Reaction enthalpy for the hydrolysis reaction [J/mol]

X = COS conversion to H_2S/CO_2

C_{pmix} = heat capacity of gas mixture at constant pressure [J/mol K]

Table I.6. Adiabatic temperature rise in COS Hydrolysis as a function of COS concentration

COS concentration (ppmv)	Adiabatic temperature rise ΔT_{ad} (°C)
2500	2.2 ± 1
3000	2.8 ± 1
5000	4.5 ± 1
7500	6.4 ± 1

I.10. Catalysts for Hydrolysis at mild-low temperatures (40-200 °C)

I.10.1 Zirconia based Catalysts

The acidic and basic properties of mixed oxide ZrO_2-Al_2O_3 and ZrO_2-TiO_2 catalysts prepared from Propylate hydrolysis were characterized by FTIR spectroscopy and activity towards carbonyl sulfide hydrolysis [81]. ZrO_2 (23%) – TiO_2 (77%) revealed minimum basicity

compared to other ZrO_2-TiO_2 samples. On the other hand, the Lewis acidity of ZrO_2-Al_2O_3 samples increased with Al_2O_3 content and basicity decreased sharply when Al_2O_3 was introduced. The relative activities of various oxides including ZrO_2 for COS hydrolysis reaction was investigated [82] and then compared to the basicity of the hydroxyl group obtained from the number of hydrogen carbonate species resulting from CO_2 adsorption. The relative activity of the various oxides towards COS hydrolysis per unit area is: ZrO_2 >> Al_2O_3 > TiO_2.

I.10.2 Titania Catalysts

A Titania catalyst (50m^2/g, 85% Anatase and 15% Rutile) was tested for its activity in the COS hydrolysis reaction (1% COS and 18% H_2O) at 398 K [83]. FTIR spectroscopy showed that the mechanism of hydrolysis on TiO_2 was identical to that on Al_2O_3 at low temperatures suggesting surfaces acidic and basic hydroxyl groups are present on both supports. TiO_2 showed better resistance to sulphate formation as compared to Al_2O_3 when O_2 is present in the feed. At low temperature, the hydrolysis rate appears to be enhanced once the sulphate is removed by hydrogen sulfide as shown below without reducing Ti^{+4} to Ti^{+3}.

Sulfate ion removal due to H_2S: $SO_4^{2-} + H_2S \rightarrow S + SO_2 + H_2O$

TiO_2-Al_2O_3 mixed oxides [84] prepared by co-hydrolysis of Ti^{+4} ad Al^{+3} iso-propoxides were investigated for their acid-base properties using COS hydrolysis as a test reaction. FTIR spectroscopy on the test reaction showed that the hydroxyl basicity of the mixed oxides was lower than that of the two oxide components.

I.10.3 Alumina Catalysts

γ-Al_2O_3 is the most widely used catalyst for the COS hydrolysis reaction. IR spectroscopy and

quantum chemical calculations on samples revealed the mono-dentate hydroxyls of Al_2O_3 are involved in base catalysed COS hydrolysis reaction [79]. Particularly in the case of Al_2O_3, it was found that COS reacted with pre-adsorbed water even in the absence of H_2O in the feed. Upon restoration of H_2O flow, the catalytic activity was restored to near the level observed prior to cessation of H_2O. An Eley-Rideal mechanism was proposed to explain the observation but a different pathway could be possible where the rate determining step of reaction related to the competition between H_2O and COS for adsorption sites on the alumina that was proposed for the removal of COS from hydrocarbons [85]

Adsorption (*=adsorbed species) -

$$COS + Al_2O_3 \leftrightarrow Al_2O_3 \cdot COS^* \quad \text{..... (1)}$$

$$H_2O + Al_2O_3 \leftrightarrow Al_2O_3 \cdot H_2O^* \quad \text{..... (2)}$$

Reaction -

$$COS^* + H_2O^* \leftrightarrow CO_2^* + H_2S^* \quad \text{..... (3)}$$

Desorption -

$$Al_2O_3 \cdot CO_2^* \leftrightarrow Al_2O_3 + CO_2 \quad \text{..... (4)}$$

It was shown that above 30% H_2O, COS adsorption becomes inhibited on Al_2O_3 and equation (2) dominates over equation (1) at the cost of hydrolysis reaction. Alumina in its high purity form continues to be the catalyst of choice for the hydrolysis reaction. However, several researchers have investigated the potential of modifying Al_2O_3 with Transition metals (Cu, Ni, Zn, Fe), Alkaline metals (Na, K, Li), Alkali Earth (Mg, Ca, Ba), Rare Earth Metals (Y, Gd, Nd, La)

I.10.4 Layered Double Hydroxides and Metal Exchanged Zeolites

Co/Ni/Al based LDH were synthesized by hydrothermal method and tested for their COS

hydrolysis activity at 50°C and 1% COS/N_2 feed concentration [86]. Hydrolysis on metal-exchanged zeolites and LDHs was investigated in a study [52] to understand the affinity of sulfur on both types of species. The basicity of the catalysts was found to control the hydrolysis. LDH-based materials are more active catalysts than Me-zeolites. The CO_3^{2-} containing LDHs activated at 300 °C and the mixed oxides obtained after calcination at 450 °C exhibited good activity for COS hydrolysis performed at temperature lower than 100 °C.

I.11. Catalysts for Hydrolysis at Elevated Temperatures (>200 °C)

I.11.1 Commercial Alumina

The activity of commercial alumina catalysts[87] is affected by the O_2 content in the feed at elevated temperatures (>230°C). Poisoning effect of pentene isomers was also studied under reaction conditions. The hydrolysis activity was examined at 250°C on a commercial Cobalt-Molybdate–on Alumina catalyst[88]. However, in addition to COS hydrolysis, the following reactions were also examined on the same catalyst:

$$SO_2 + 2H_2S \leftrightarrow 2H_2O + \frac{3}{x}S_x$$

$$SO_2 + 2COS \leftrightarrow 2CO_2 + \frac{3}{x}S_x$$

No poisoning of CO_2 was observed for the COS hydrolysis reaction. The effect of catalyst basicity on the hydrolysis activity was investigated on the same catalyst by depositing 3.9% NaOH [89].

I.11.2 Commercial Titania

A commercial TiO_2 (anatase) with a BET surface area of 124 m^2/g supplied by Rhone Poulenc

was tested for hydrolysis activity at 230 °C and 1 atm [78]. The authors observed a less pronounced deactivation due to SO_2 on the commercial TiO_2 catalyst when compared to other metal oxides, ZrO_2 and Al_2O_3.

I.12. Sulfided adsorbents as catalysts for COS hydrolysis

Catalytic hydrolysis of COS over ZnS formed from desulfurization adsorbent ZnO [49] suggests that metal sulfides may be active catalysts for the reaction between COS and water. Rare earth oxy-sulfide catalysts of the nominal formula Re_2O_3 (Re = La, Nd, Sm, Eu, Gd, Dy, Ho, Er), Pr_6O_{11} and CeO_2 were prepared [90] and tested for their COS hydrolysis activity at 100-300°C in a COS inlet concentration of 150 ppm and 3.4 vol% H_2O [77]. At 200°C & SV 10,000h^{-1}, the activity of the rare earth oxides had the following order: La ≈ Pr ≈ Nd ≈ Sm > Eu > Ce > Gd ≈ Ho > Dy >Er. The rare earth oxy-sulfide catalysts were all resistant to poisoning of oxygen (at O_2 concentration below 1.5%).

Table I.6 shows a comprehensive list of operating conditions along with catalysts and their respective activation energies for the COS hydrolysis reaction.

Table I.7. List of COS hydrolysis reactor operating conditions, catalysts, and activation energy

Catalyst	Reactor T (°C)	%COS	%H_2O	%H_2	%CO	%CO_2	%SO_2	%CH_4	E_a kJ/mol	Ref.
Metal oxides	230	3								
Kaiser 201†	270-	0.5-2	9.7	-	-	-	-	-	-	[87]
KAS 201†	330	0.5	2-12	-	-	-	-	-	25.27	[85]
γ-Al_2O_3	220	0.004-	Unspecified	50	13	13	0.2	-	-	[91]
γ-Al_2O_3	50	0.02	0.01-0.12	-	-	-	-	-	45±10	[92]
γ-Al_2O_3	30	0.015	0.12	-	-	-	-	-	-	[75]
γ-Al_2O_3	230	1	2.2	-	-	-	-	-	-	[78]
γ-Al_2O_3	100	1	2.2	-	-	-	-	-	-	[82]
γ-Al_2O_3	230	0.05-	5-17	-	-	-	-	-	-	[76]
TiO_2 (Anatase)	230	0.3	2.2	-	-	-	-	-	-	[78]
CRS 31‡	270-	1	2.12	-	-	-	-	-	41.77	[85]
TiO_2	330	0.5-2	18	-	-	-	-	-	-	[83]
TiO_2	100	1	2.2	-	-	-	-	-	-	[82]
ZrO_2	100	1	2.2	-	-	-	-	-	-	[78]
ZrO_2	230	1	2.2	-	-	-	-	-	-	[82]
	100	1								
Mixed oxides										
TiO_2-Al_2O_3	100	1	2.2	-	-	-	-	-	-	[84]
ZrO_2-TiO_2	100	1	2.2	-	-	-	-	-	-	[81]
ZrO_2-Al_2O_3	100	1	2.2	-	-	-	-	-	-	[81]
Na^+, K^+, Cs^+	55-80	H_2O:COS > 100		-	-	-	-	-	-	[93]
Mg^{2+}, Ca^{2+}, Ba^{2+},	55-80	H_2O:COS > 100		-	-	-	-	-	-	[93]
Sr^{2+}	20	0.015	0.12	-	-	-	-	-	-	[94]
Activated carbon										
Fe/Cu/Ce/ACP	50	0.0650	3 (%RH)	-	-	-	-	-	-	[69]
Al-Na_2CO_3-ACP	40-70	0.02-0.1	21, 37, 46% RH	-	-	-	-	-	62.3	[44]
Zeolites										
Na^+,Ca^{2+},Ba^{2+},Mg^{2+}-Na^+,Cs^{2+}-Na^+	50	0.05	2.3	-	-	-	-	-	-	[52]
Hydrotalcites										
Zn-Ni-Al-Ce HTLC	50	0.065	3% RH	-	-	-	-	-	-	[95]
Co-Ni-Al HTLC¶	50	0.043	2.67	-	-	-	-	-	-	[96]
Co-Ni-Al HTLC¶	50	1	Unspecified	-	-	-	-	-	-	[86]
Zn-Ni-Fe HTLC	50	0.035	2	-	-	-	-	-	-	[95]

I.13. Challenges during catalytic hydrolysis of Carbonyl Sulfide

I.13.1 Pore blockage of catalysts due to condensation of elemental sulfur and/or water vapor

Porous catalysts operating at low temperatures are subjected to capillary condensation of sulfur in the pores, resulting in lower hydrolysis rate due to blocking access to reactive centres on the catalyst. In terms of the COS hydrolysis reaction, catalysts are mostly prone to deactivation due to sulfation or sulfidation [76]. For example, on a commercial γ-Al_2O_3 (Kaiser 201) [85] catalyst operating at 300°C, capillary condensation of sulfur vapour occurred in the pores below 2.2 nm in diameter and 55% reduction in surface area. The performance of bulk TiO_2 in cyclic temperature operations revealed a hysteresis in the conversion and selectivity due to deposition of elemental sulfur on the catalyst. The possibility of water vapour lowering the catalytic activity by blocking micro-pores via capillary condensation was investigated by Tong [97]. At a typical vapour concentration of 30 mole %, using the kelvin equation, the limiting radii of cylindrical pores to be influenced by capillary condensation of water was calculated to be 0.34 nm.

I.13.2 Sulfation of catalysts by SO_2 formed at high temperatures under O_2 rich environments

A mathematical model of COS removal at low temperature on a bi-functional catalyst was developed that accounts for important adsorption/catalytic characteristics such as external-film and pore-diffusion mass transfer mechanism and axial dispersion [44]. However, the use of gamma alumina as a catalyst for COS hydrolysis in presence of oxygen presents severe deactivation problems due to sulfation of the alumina surface [83]. The sulfate formation caused an increase in surface acidity that corresponds to the poisoning effect of oxygen [98]. On the other hand, Titania [99] when used as a catalyst (Claus temp: 250 – 350°C) offered much higher resistance against sulfation and no deactivation due to oxygen was observed. The activity of

ZrO_2, Al_2O_3 and TiO_2 was investigated [78] in presence of SO_2. The effect of sulfation was studied by impregnation of $(NH_4)_2SO_4$ or by exposure of catalysts to oxygen. It was found that with sulphate levels of 0.8 μmole/m^2, TiO_2 exhibited higher activity as compared to Al_2O_3. On the other hand, ZrO_2 showed highest activity.

I.13.3 Reduction in the hydrolysis activity due to presence of $H_2S/CO/CO_2$

Carbon monoxide is a common species at the outlet of a reforming unit. CO is usually converted to CO_2 via water gas shift reaction or partial oxidation. It is expected that presence of CO can interfere with the performance of desulfurization unit in terms of H_2S and COS removal activity. CO_2 properties are similar to properties of COS in the sense that CO_2 contains an extra oxygen atom instead of a sulfur atom. Poisoning of Al_2O_3 due to CO_2 has been reported [100]. It is possible that CO_2 poisons most of the active sites during initial stages of the reaction that usually takes place on the low energy sites requiring high activation energy for the reaction. COS hydrolysis reaction is a base catalysed reaction and presence of H_2S will cause preferential adsorption on the basic sites

I.14. H_2S and COS removal

Most of the hydrolysis catalysts used only target the COS issue. There is always a need to address the H_2S formed as a product of the hydrolysis reaction. A method proposed by Miura et al [72] claims to remove COS and H_2S simultaneously using a special form of iron oxide prepared by partial dehydration of α-FeOOH at around 200°C. The authors observed that the produced H_2S is stabilized as iron sulfides on the iron oxide, thus ensuring complete removal of COS from coke oven gas by use of iron oxide alone. Adsorption and catalytic decomposition of

H_2S and COS were investigated over active carbons in a fixed bed reactor system operating at 300-450°C [101]. It was observed that although H_2S was removed by active carbons at 400°C, the removal capacity of H_2S was much smaller than that of COS and H_2S did not decompose on the carbon sample. COS is less acidic and less polar than H_2S and ZnO is not efficient for removal. It was shown that in presence of H_2 at 500 °C and COS partial pressure of 30 Pa, COS is converted to H_2S (via hydrogenation) and water gas shift reaction accelerates the reaction between COS and ZnO while CO_2 did not affect the reaction [57]. In the same article, the following scheme was suggesting for the COS-ZnO gas solid reaction:

$$-\mathrm{ZnO} + \mathrm{COS} \rightarrow \mathrm{Zn} - \mathrm{S}^* + \mathrm{CO_2}$$

$$\mathrm{X}(-\mathrm{Zn} - \mathrm{S}^*) \rightarrow -\mathrm{Zn_y} - \mathrm{S}^*_{\mathrm{x}-1} + \frac{1}{\mathrm{y}}\mathrm{S_y}\ (\mathrm{gas})$$

$$-\mathrm{Zn} - \mathrm{S}^* \rightarrow \mathrm{ZnS}$$

$$-\mathrm{Zn_X} - \mathrm{S}^*_{\mathrm{X}-1} + \mathrm{COS} \rightarrow \mathrm{Zn} - \mathrm{S}^*_{\mathrm{X}} + \mathrm{CO}$$

Where, -Zn and $-S^*$ represent an active surface zinc species and active surface sulfur. Another study [50] was aimed at decreasing the formation of COS at 300°C in a simulated coal-derived gas (38-42% H_2, 30-33% CO, 19-21% CO_2, 1-2% H_2O, 100-1500 mgS/m^3 H_2S and balance N_2) via modification of the ZnO desulfurization sorbent by mixing active ZnO with additives including Al_2O_3, K_2CO_3 and graphite. It was shown that loading K_2CO_3 can increase the basicity of the ZnO sorbent and in turn promote COS hydrolysis rate within the same system since H_2S is more acidic than COS. Recently, rare earth metal doped SnO_2 sorbents were developed for removing H_2S and COS in single step at 300-400°C when COS and H_2O was fed to the desulfurizer.

I.15. Objectives of research

- Elucidate the structure of Cu^{2+} ions in $Cu_XZn_{100-X}O/SiO_2$ using XPS and understand the degree of dispersion of ZnO on SiO_2
- Determine the ZnO band gap in SiO_2 supported $Cu_XZn_{100-X}O$ adsorbents as a function of temperature and atomic Cu concentration.
- Study the electronic effects in Cu^{2+} and Zn^{2+} ions in $Cu_XZn_{100-X}O/SiO_2$ during H_2S adsorption using in-situ UV-Vis spectroscopy.
- Selectively probe the reduction behavior of Cu^{2+} ions with H_2S using EPR spectroscopy to complement observations from in-situ DRS experiments.
- To develop a rapid and accurate monitoring system for sorbent utilization and protect downstream processes from sulfur poisoning.
- Develop a novel catalyst sorbent system for simultaneous removal of H_2S and COS during high temperature desulfurization

I.16. Outline of this work

Chapter II describes the experimental section and analytical techniques used in this study.

Chapter III discusses the ex-situ and in-situ characterization of ZnO/SiO_2 and $Cu_XZn_{100-X}O/SiO_2$ sorbents using X-ray Photoelectron Spectroscopy, X-ray Diffraction, UV-Vis Diffuse Reflectance Spectroscopy, and Electron Paramagnetic Resonance Spectroscopy during H_2S adsorption at 22°C.

Chapter IV describes an in-situ fiber optic based technique for direct measurement of capacity utilization of ZnO adsorbent beds by monitoring bed color changes during desulfurization for fuel cell systems.

Chapter V assess the promotional effect of Cu dopant in $Cu_XZn_{100-X}O/SiO_2$ sorbents in terms of a COS formation characteristics as a function Cu:Zn molar ratio, moisture and temperature at constant H_2S partial pressure in a simulated reformate.

Chapter VI described the synthesis, performance and characterization of novel regenerable La_2O_3-ZnO sorbents for the simultaneous removal of H_2S and COS during high temperature syngas desulfurization as a function of (i) feed composition, (ii) choice of base precipitant, and (iii) desulfurization temperature.

II. Experimental

II.1. Adsorbent synthesis

II.1.1. Incipient wetness impregnation

Supported metal oxide sorbents are prepared via incipient wetness impregnation followed by drying and calcination in static air. In short, metal nitrate solutions of desired molarity are prepared by dissolving metal salt in de-ionized water. The metal nitrate solutions are then impregnated on 100 μm support, such as SiO_2, γ-Al_2O_3, ZrO_2, and TiO_2 depending on the supports pore volume. The impregnated samples are then dried overnight for 12h at 110 °C followed by calcination in air for 3h at 400-500 °C.

II.1.2. Co-precipitation

Metal oxides and bimetallic oxides were prepared using a co-precipitation method at room temperature. Depending on the desired metal oxide loading, metal nitrate solutions were prepared from metal nitrate salts dissolved in 200 mL of deionized water. For example, in case of bimetallic oxides, the nitrate solution of both metals was premixed in a flask in the desired molar ratio. This solution was then added to 400 mL of deionized water. 2 mol/L of one of the solutions such as KOH, K_2CO_3, NaOH, Na_2CO_3, NH_4OH, or $(NH_4)_2CO_3$ was added into the acidic solution with vigorously stirred to adjust the pH to 10. The slurry was maintained for 6 h 80°C followed by vacuum filtration and washing with deionized water until the pH reached 7. Finally, the precipitate was shaped in the form of 2 cm spheres and dried in air at 110°C overnight. The dried spheres were crushed and sieved to a final particle size of 100-250 microns and finally calcined at 400°C for 3 h in static air. This process is schematically shown in Figure I.8.

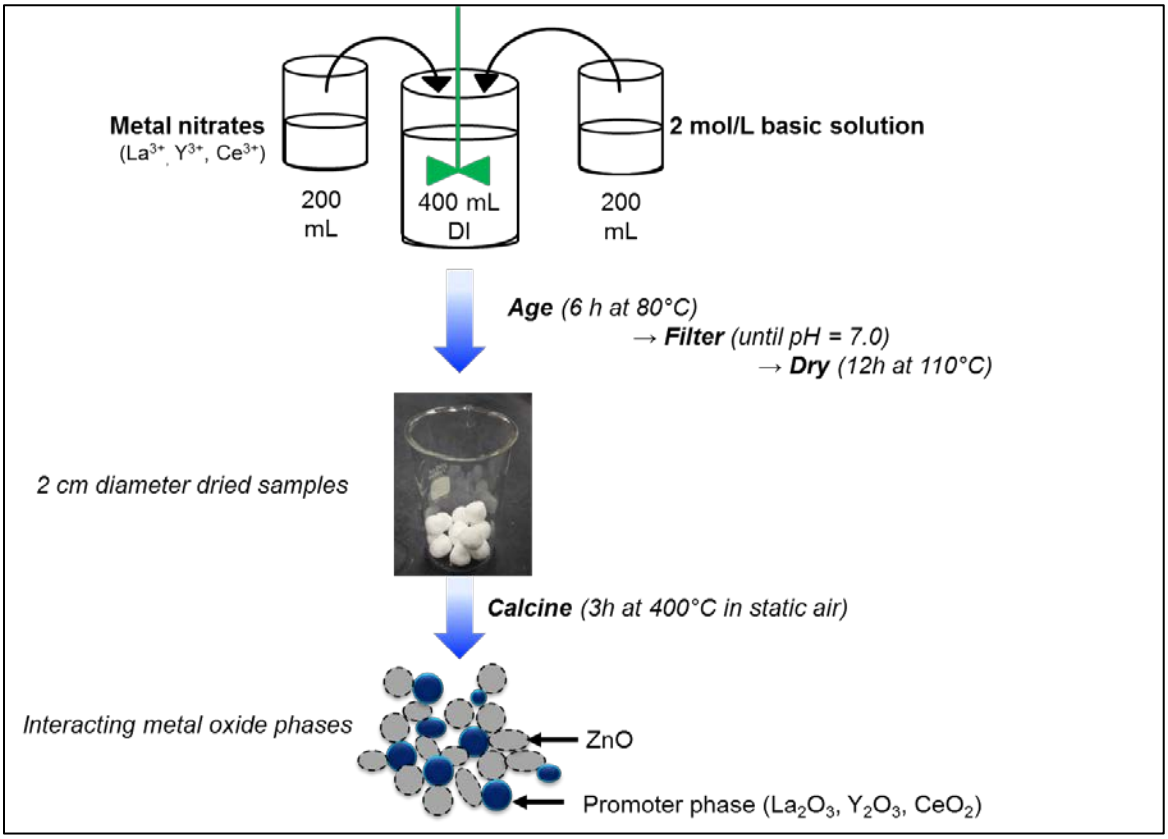

Figure II.1. Schematic of steps involved in the synthesis of adsorbents via co-precipitation

II.1.3. Deposition precipitation

A deposition–precipitation method was used to prepare La_2O_3-ZnO/SiO_2 sorbents which is similar to the co-precipitation in terms of the sequence of steps and materials used. The procedure, using 20%La_2O_3 - 60%ZnO/SiO_2 as an example, is as follows: SiO_2 (5 g, 100–200 microns) was added to deionized water (200 ml) at room temperature and the solution was stirred continuously. $La(NO_3)_3 \cdot 6H_2O$ (6.66 g) was dissolved in 200 mL deionized water. $Zn(NO_3)_2 \cdot 6H_2O$ (55.0 g) was dissolved in 200 mL deionized water. 400 mL of mixture (200 mL $La(NO_3)_3$ + 200 mL $Zn(NO_3)_2$) was added to the 200 mL SiO_2 solution at 22°C. 2 mol/L of KOH solution was added dropwise to the solution until a pH of 8.0 was attained. The suspension/solution was

stirred at 22°C for 30 min. The precipitate was then stored at 80°C for 6 h followed by vacuum filtration and repeated washing with deionized water until pH of 7.0 was reached. The precipitant cake was then shaped into 2 cm spheres and dried at 110°C overnight (12 h). The dried spheres were crushed an sieved to a particle size of 100-250 microns followed by calcination at 400°C for 3 h in static air to obtain the final 20%La_2O_3 - 60%ZnO/SiO_2 sorbent. This is schematically shown in Figure II.9.

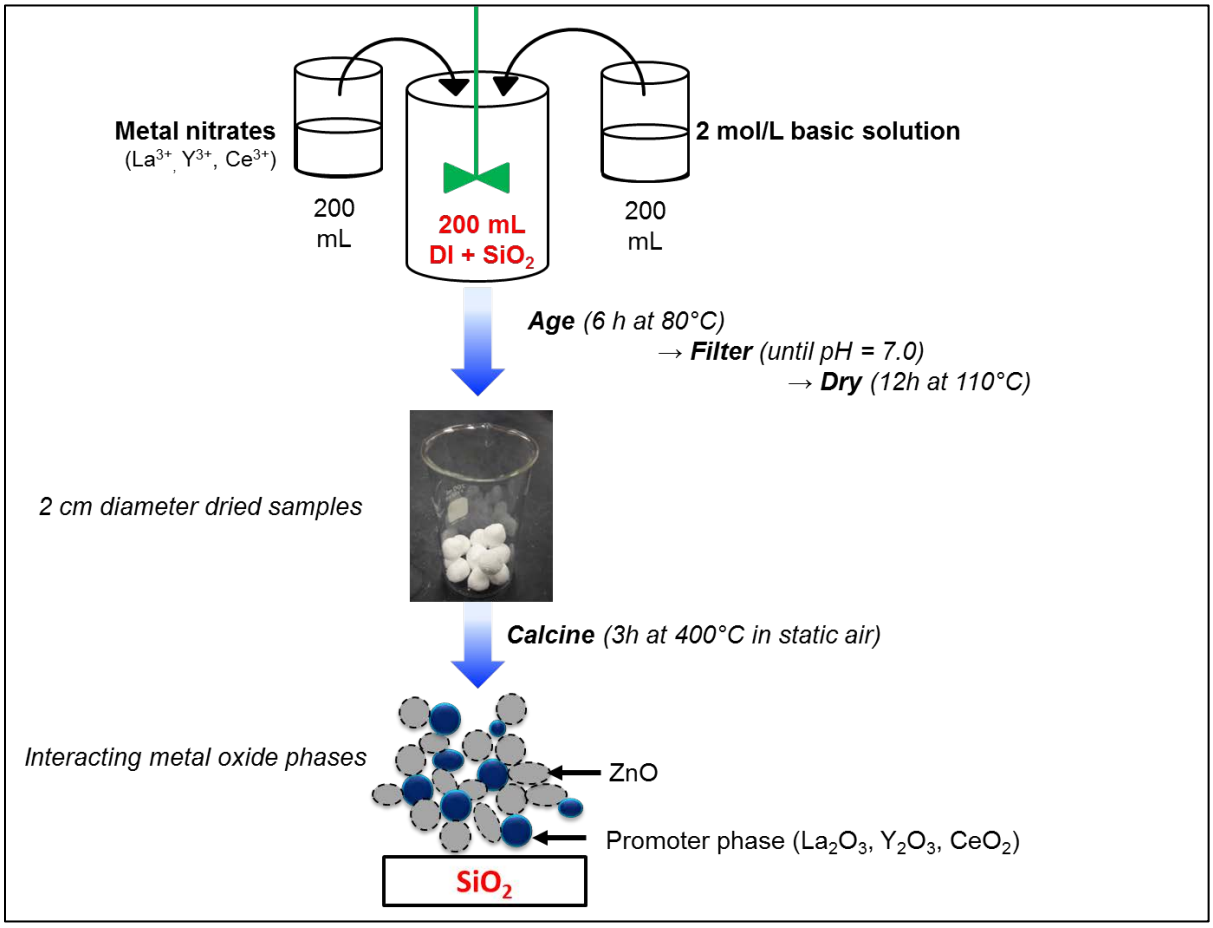

Figure V Schematic of steps in the synthesis of adsorbents via deposition precipitation

II.2. Challenge gas

This section presents calibration data for mass flow controllers (MFC) used to regulate gas from cylinders to generate desired concentration of various gaseous species in a reformate stream. Set

flow parameter is from control panel of the MFC and is calibrated against the actual flow measured with a universal gas flow meter (Agilent). The following gases were used from the cylinders purchased from Airgas Inc. (i) 1% COS in N_2, (ii) 2% H_2S in H_2, (iii) UHP CO, (iv) UHP CO_2, (v) UHP H_2, and (vi) UHP N_2. The calibration data is shown in Figure II.10 below.

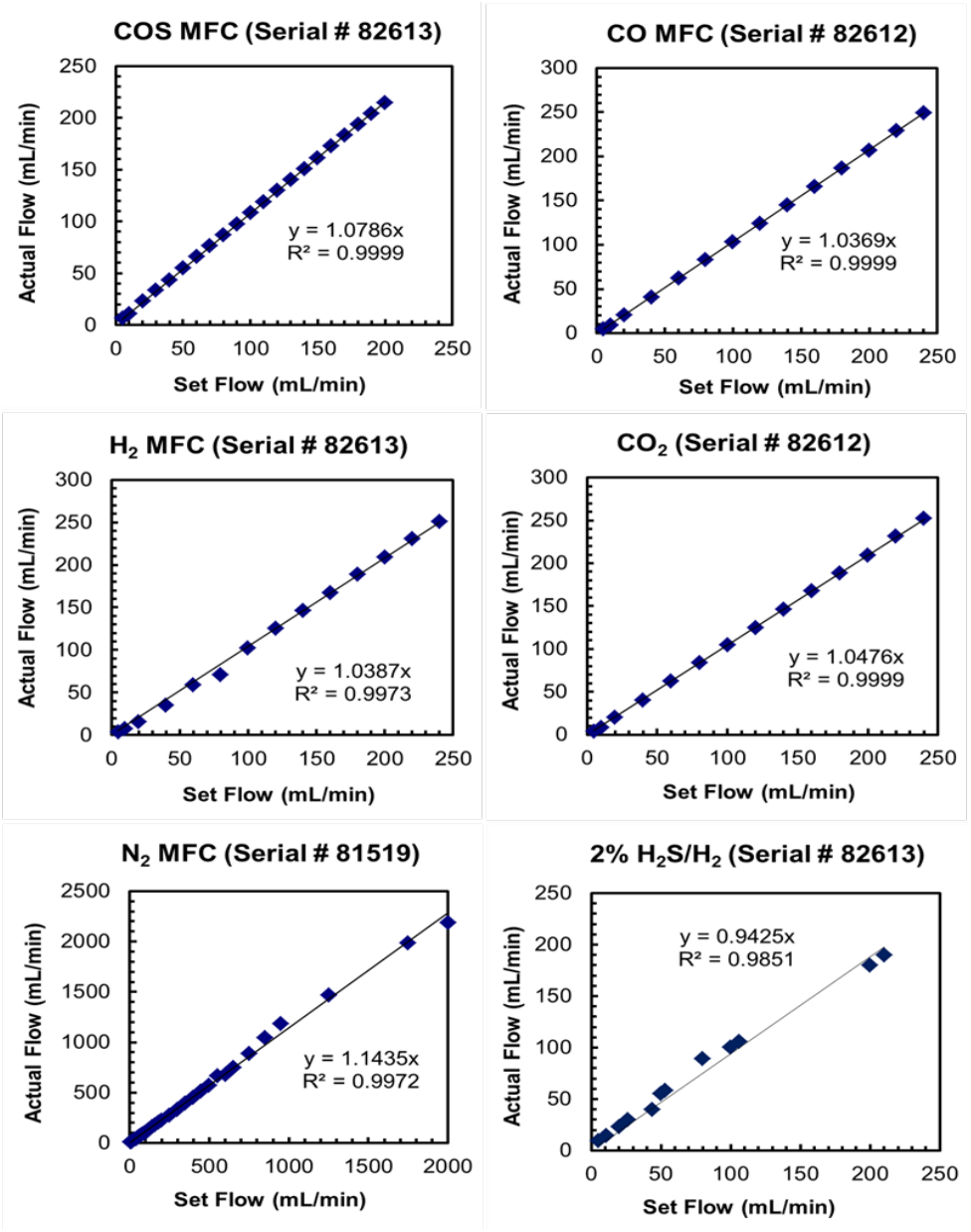

Figure VI Calibration plots for mass flow controllers used to regulate gas flow

II.3. Desulfurization experiments

II.3.1. Calculation of adsorption saturation capacity using numerical integration

The nature of the breakthrough curve decides the method that can be used to calculate saturation capacity of the sorbent. In this work, since some breakthrough curves did not show sharpness and the perfect sigmoidal shape (S-shape), $t_{1/2}$ method cannot be used here to calculate the saturation capacity. The current method involves calculation the approximate area under the breakthrough curve using numerical integration. To begin with, a typical breakthrough curve is shown in Figure II.11. Area under the BT curve from the time of BT ($t_{breakthrough}$) till the saturation time (t_{sat}) is the cumulative amount of challenge gas coming out of the adsorbent bed. So this area indicated the quantity of challenge gas that has not been adsorbed by the adsorbent.

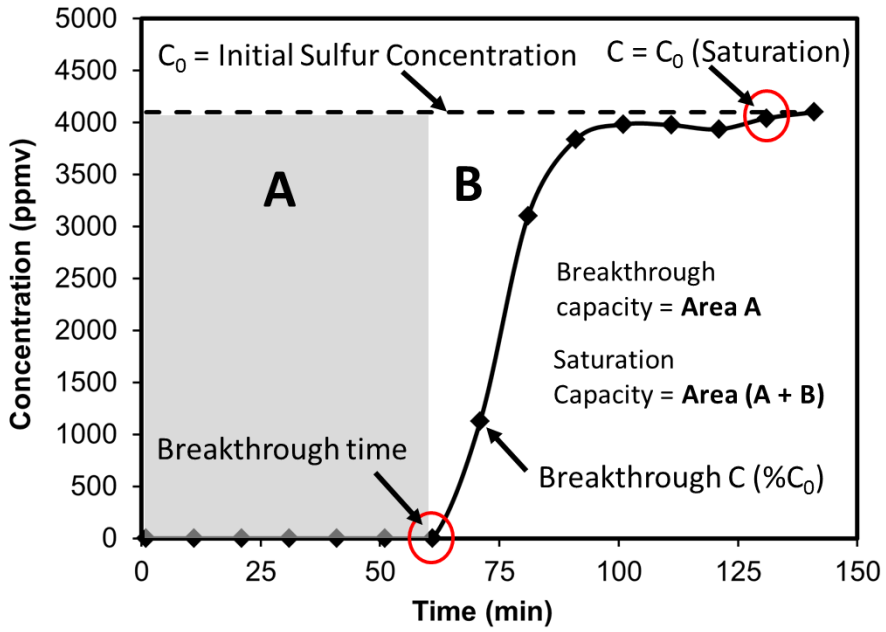

Figure II.4. Graphical representation of breakthrough curve and area under curve

This area is shown as the shaded area on the BT curve. Region confined on the plot between C/C_0 from 0 to 1 on y-axis, time (t) from 0 to $t_{saturation}$ on x-axis and the portion lying above the

BT curve gives the part of challenge gas that has been adsorbed on the sorbent. This area needs to be calculated to find the value of saturation capacity. First area under the BT curve between $t_{breakthrough}$ and $t_{saturation}$ is calculated approximately by using trapezoidal rule. Trapezoidal rule is a technique for approximating a definite integral. The trapezoidal rule works by approximating the region under the graph of the function f(x) as a trapezoid and calculating its area. Therefore, area under the curve between points a and b is given as,

$$\int_a^b f(x)dx = \frac{(b-a)(f(a)-f(b))}{2} \quad \text{..... (1)}$$

For a domain of 'n' equally spaced points and spacing h = (b-a)/n, the area under the curve can be given by

$$\text{Area under Curve} = \left(\frac{b-a}{2n}\right)[f(x_1) + 2\{f(x_2) + f(x_3) + \cdots\} + f(x_n)] \quad \text{..... (2)}$$

In the present study, outlet concentration of challenge gas measured by the GC or manually by an operator is recorded at a fixed predefined data logging interval; above approximation to the definite integration can be used. In this case, $b=t_{saturation}$, a=0 and N is the time interval. Each of f(x) point represents the outlet concentration of challenge gas. In this case, C/C_0 = 0.95 was chosen as the upper limit for the outlet concentration by assuming that the sorbent is practically saturated at this point. Equation (2) can be used to calculate area under the BT curve approximately. Unit of this calculated area is ppm-min. This area was then subtracted from the cumulative amount of challenge gas that has been introduced into the sorbent bed till the saturation point. This subtraction gave the amount of challenge gas adsorbed till the saturation point in 'ppm-min'. Thus at saturation, Total gas adsorbed (ppm-min) = Total gas introduced in bed (ppm-min) – Total gas coming at bed outlet (ppm-min) = (C_0 x $t_{saturation}$) – Area under the BT curve calculated by trapezoidal rule. Amount of gas adsorbed found from above equation is then used in the final equation to calculate the saturation capacity. The equation can be used in case of

any adsorbate with appropriate constants like Mol. Wt. etc.

$$\text{Sat Cap}\left(\frac{\text{mgS}}{\text{g}_{\text{sorbent}}}\right) = \frac{\text{Adsorbed Gas (min}\cdot\text{ppmv)}\times 10^{-6}\left(\frac{1}{\text{ppmv}}\right)\times \text{Total Flow}\left(\frac{\text{m}^3}{\text{min}}\right)\times\left(\frac{\text{P}}{\text{RT}}\right)\left(\frac{\text{gmol}}{\text{m}^3}\right)\times 32\left(\frac{\text{gS}}{\text{gmol}}\right)\times 10^3\left(\frac{\text{mgS}}{\text{gS}}\right)}{\text{Sorbent weight (g)}}$$

Pressure and temperature values at STP are used (P=100 kPa; T =273.15K) to calculate both the breakthrough capacity and saturation capacity. In the above equations, b: Saturation time (mins), usually taken as C/C_0 to reach 0.95; a: Initial time (~ 0 min); n: number of equally spaced points f(x): Concentration in ppmv; $f(x_1)$: Initial Concentration (~ 0 ppmv); $f(x_n)$: Saturation Concentration (value at which C/C_0 is 0.99). Above 'Area under Curve (AUC)' with units (Time X Concentration) represents the amount of gas 'NOT' adsorbed on the sorbent. Therefore from the figure, mathematically (Adsorbed Gas) = Area of whole rectangle – Area under the Curve

= [Inlet Concentration (ppmv) x Saturation time (mins)] – AUC = (mins x ppmv)

II.3.2. Calculation of adsorption saturation capacity using $t_{1/2}$ method

For breakthrough curves that have a large slope and appear as a perfect sigmoidal shape (S-shape) as shown in Figure II.12. The current method can be used here to calculate the saturation capacity based on the time to reach 50% of initial value (t1/2) and is given as,

$$\text{Sat Cap}\left(\frac{\text{mgS}}{\text{g}_{\text{sorbent}}}\right) = \frac{\text{Volume flow of gaseous sulfur species}\left(\frac{\text{m}^3}{\text{min}}\right)\times\left(\frac{\text{P}}{\text{RT}}\right)\left(\frac{\text{mol}}{\text{m}^3}\right)\times t_{\frac{1}{2}}\,(\text{mins})\times 32\left(\frac{\text{gmS}}{\text{mol}}\right)\times 10^3\left(\frac{\text{mgS}}{\text{gmS}}\right)}{\text{Sorbent weight (gm)}}$$

This is usually encountered in gas solid reaction between metal oxides and H_2S at elevated temperatures.

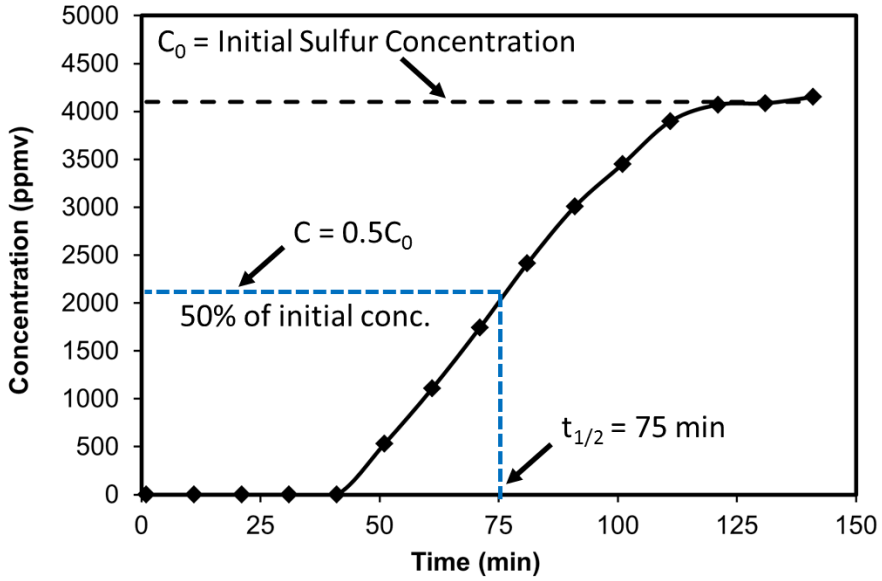

Figure VII Graphical representation of $t_{1/2}$ method in breakthrough curves

II.3.3. ZnO Particle Utilization at Saturation

The ZnO reaction with H_2S is a typically gas solid reaction and can be written as follows,

$$ZnO + H_2S \rightarrow ZnS + H_2O$$

Based on this reaction, for 100% conversion of ZnO to ZnS, the theoretical capacity is 395 mgS/gZnO. However, for supported systems in which the weight loading of ZnO on supports such as SiO_2, TiO_2 etc. the Percentage of ZnO utilization can be calculated knowing the saturation capacity using $t_{1/2}$ method and the weight percent loading of ZnO. Thus,

$$\text{ZnO Utilization (\%)} = \frac{\text{Volumetric flow of } H_2S \left(\frac{m^3}{min}\right) \times \left(\frac{P}{RT}\right)\left(\frac{mol}{m^3}\right) \times t_{\frac{1}{2}}\,(mins) \times 32\ \left(\frac{gmS}{mol}\right) \times 10^3 \left(\frac{mgS}{gmS}\right)}{\text{Sorbent weight (gm)} \times \text{ZnO Loading (\%)}}$$

II.3.4. Sorbent Bed Utilization at Breakthrough

For adsorbent systems with a favorable isotherm, the concentration wave front in the mass transfer zone acquires a characteristic shape and width that do not change as the zone progresses down the bed. Therefore, experiments with different bed lengths give breakthrough curves of same shape; but with longer beds, the mass-transfer zone is a smaller fraction of the bed length, and a greater fraction of the bed is utilized. Thus, at a time of breakthrough, the sorbent particle between the inlet of the bed and the start of the mass transfer zone is completely saturated or in other words in equilibrium with the feed. The scale-up principle is that the amount of unused solid or length of unused bed does not change with the total bed length [102, 103].

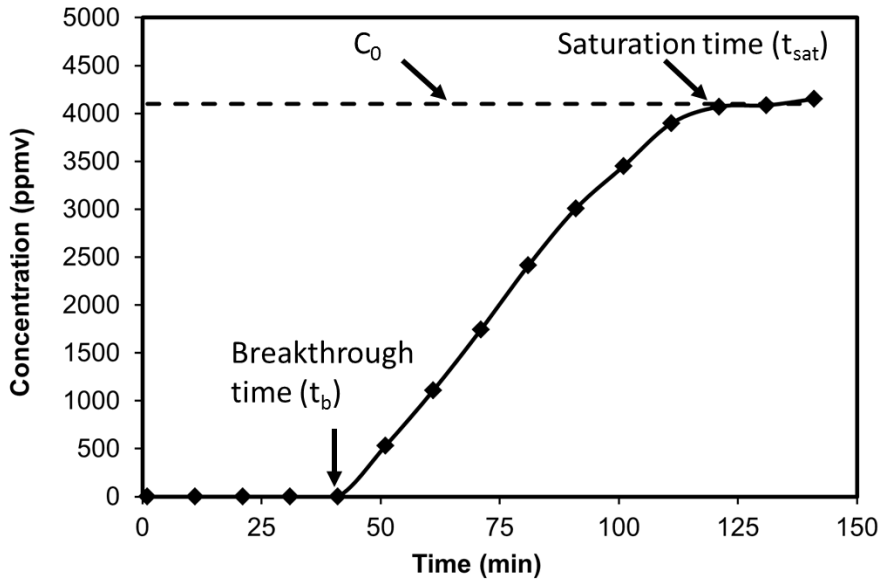

Figure VIII Breakthrough time and saturation time on a breakthrough curve

According to McCabe [102], the fraction of bed capacity unutilized at breakthrough can be rearranged and expressed as a function of breakthrough time and saturation time as follows,

Bed capacity unutilized from breakthrough curves, $\frac{\mathrm{LUB}}{\mathrm{L}}[\%] = \left(1 - \frac{t_{BT}}{t_{1/2}}\right) \times 100$

Where, LUB is an equivalent length of unused bed, which is held constant and L is total length of adsorbent bed. Let the bed capacity unutilized from breakthrough curves be denoted as U_{tBT}. This is shown in Figure II.13.

II.4. Analysis of gas

II.4.1. GC-TCD

The TCD detects changes in the thermal conductivity of the column effluent (usually in gaseous state) and compares it to a reference flow of carrier gas. Typically, most compounds have a thermal conductivity much lower than Helium or Hydrogen which are the most common types of reference and carrier gases. Carrier gas and reference gas must be the same and so when an analyte elutes from the column the effluent thermal conductivity is reduced, and a detectable signal is produced. TCD mounted on Varian CP 3800 GC was used for H_2S and COS concentration that exceeds 500 ppmv. Calibration plot of COS or H_2S concentration was generated from a known concentration of COS or H_2S in the cylinder. For example, COS used in this work is supplied from a 1% COS in N_2 cylinder. High purity N_2 was used as the diluting gas to generate various concentrations by varying the volumetric flowrates of the gases using mass flow controllers. Similarly, for H_2S calibration plot was generated by mixing a 2% H_2S in H_2 with high purity H_2 gas in varying volumetric flowrates to achieve the desired concentration. The concentration of COS or H_2S is directly proportional to the TCD peak areas. The detection limit of TCD was 200±50 ppmv Sulfur. Calibration plots for H_2S and COS concentration versus TCD peak area are shown in Figure II.14. The operating parameters for the TCD are shown in Table II.1 below.

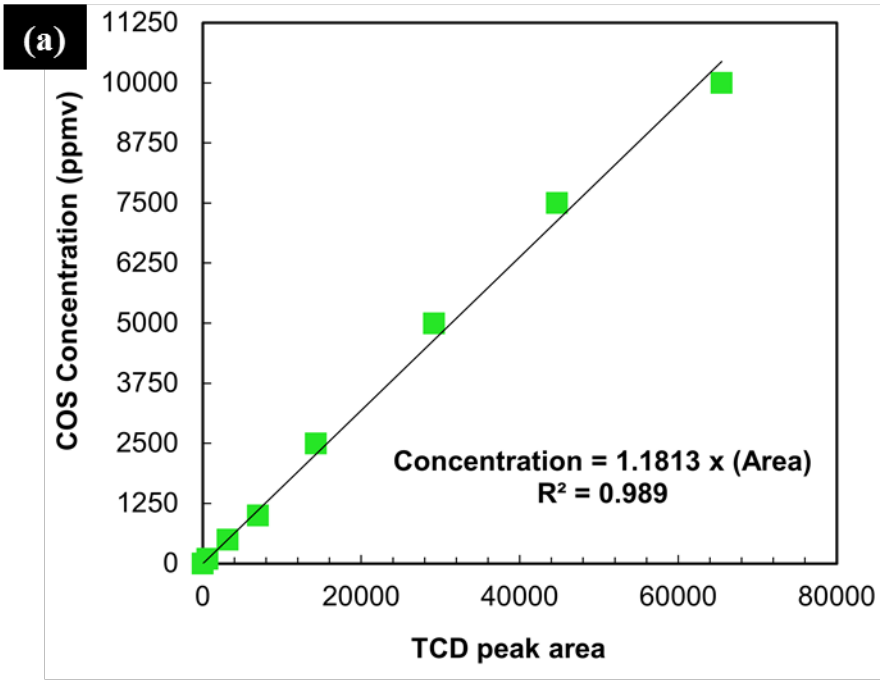

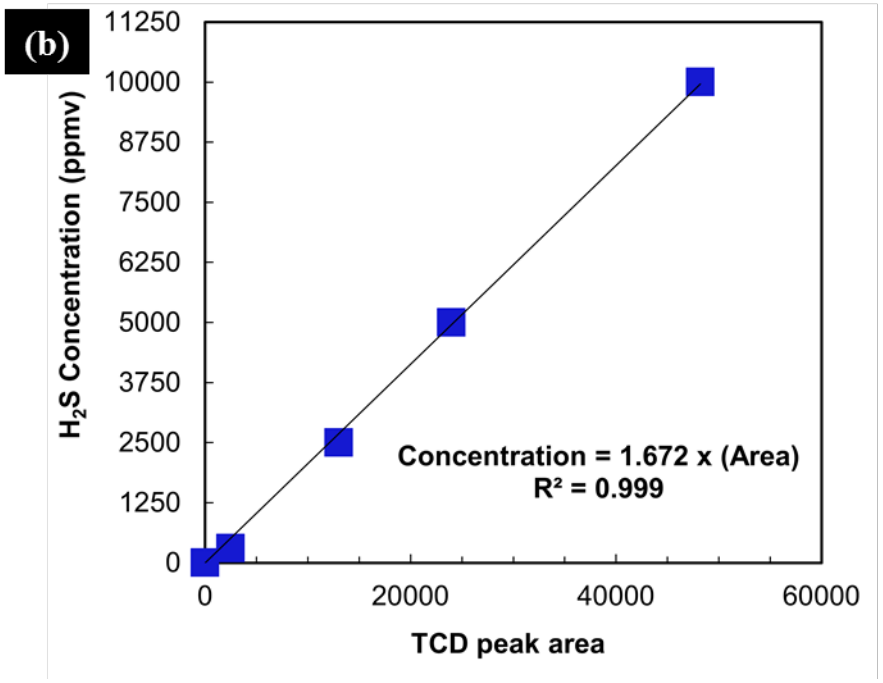

Figure II.7. TCD calibration for (a)COS and (b) H_2S

Table II.1 TCD operating parameters for sulfur analysis on Varian CP 3800

Parameter	**Value**
Column	HayeSep Q, 80/100, 8’ x 1/8” SS (W.R. Grace & Co.)
Oven Temperature (°C)	70
Injector Temperature (°C)	120
Detector Temperature (°C)	175
Filament Temperature (°C)	340
Reference gas	Hydrogen
Reference gas flow (mL/min)	30
Carrier gas	Hydrogen
Carrier gas flow (mL/min)	30
Sampling valve	6 port gas sampling valve with 250 μL injection volume
Sampling interval	Every 10 min

II.4.2. GC-PFPD

The Pulsed Flame Photometric Detector (or PFPD) provides significant improvement over the conventional Flame Photometric Detectors (FPD) in terms of enhanced sensitivity and selectivity for sulfur and phosphorus. In this study, the PFPD mounted on Varian CP 3800 GC was used for H_2S and COS concentration below 500 ppmv. High purity Helium was used as the carrier gas. In the case of PFPD, manual injections were made using a 50 microliter gas tight syringe (Hamilton Co.). The same procedure that was followed for generating calibration plot on TCD was used to generate concentration versus PFPD area. The detection limit of PFPD was 5 ± 2.0 ppmv Sulfur. Unlike the TCD, the PFPD is inert to presence of CO, CO_2, H_2 or N_2. Furthermore, the sulfur concentration in a PFPD varies as the square root of the PFPD peak area. Calibration plots for H_2S and COS concentration versus PFPD peak area are shown in Figure II.15. The operating

parameters for the PFPD are shown in Table II.2 below.

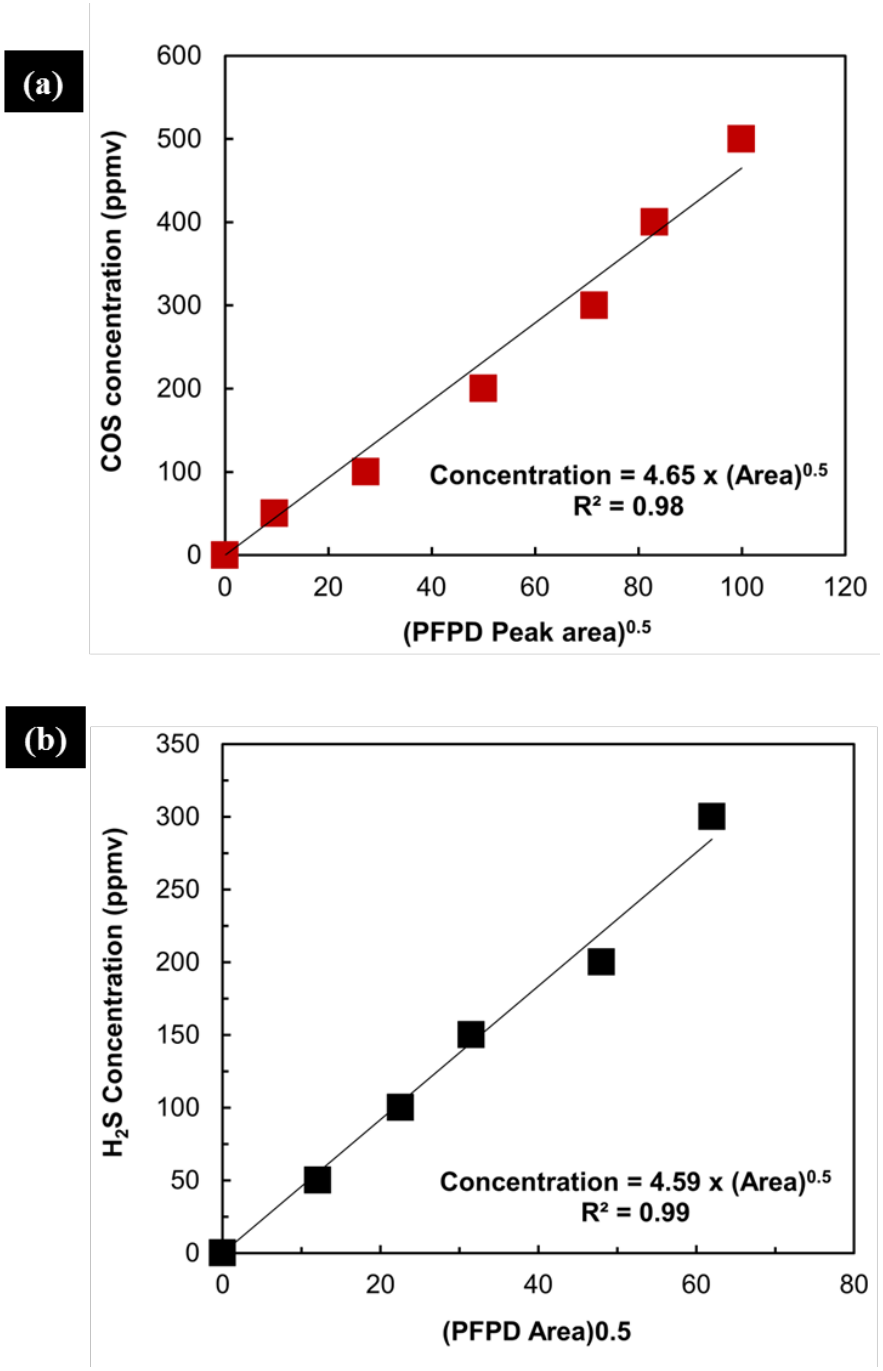

Figure IX PFPD calibration for (a) COS and (b) H_2S

Table II.2. PFPD operating parameters for sulfur analysis on Varian CP3800

Parameter	**Value**
Column	Low Sulfur PLOT Column (Agilent Technologies Inc.)
Oven Temperature (°C)	110
Detector Temperature (°C)	200
Injector Temperature (°C)	120
Carrier gas	Helium
Carrier gas flow (mL/min)	2
Air 1 flow (mL/min)	17
H_2 flow (mL/min)	13
Air 2 flow (mL/min)	10
Split ratio	1:100
Tube Voltage (V)	510
Trigger Level (mA)	200
Sample Delay (ms)	4
Sample Width (ms)	10
Gain Factor	2
Syringe size	50 μL

II.5. Characterization of adsorbents

II.5.1. Nitrogen Physisorption

Nitrogen adsorption-desorption isotherms of adsorbents are generated at 77 K (-196 °C) on Autosorb-1C (Quantachrome Instruments). The samples are outgassed at 150 °C for 6h in vacuum (3×10^{-10} mm Hg) prior to analyses. BET surface area of samples is calculated using the Brunauer-Emmett-Teller (BET) equation. The average pore size and pore-size distribution is

obtained the adsorption curve of N_2 isotherm and calculated using Barrett-Joyner-Halenda (BJH) method.

II.5.2 X-ray diffraction (XRD)

A Bruker D-8 x-ray diffractometer equipped with CuKα source was used at 40KV/40mA. For each sample, the XRD scan range was 10–90° and scan speed was 0.1 second/step (~5.85°/min).

II.5.3 Scanning Electron Microscopy (SEM)

The surface morphology of adsorbent samples was studied using a JOEL 7000-F Scanning Electron Microscope (SEM). The voltage of the equipment was 40 KV during imaging. The samples were analyzed without using any metal sputtering.

II.5.4 UV-Vis Diffuse Reflectance Spectroscopy (UV-Vis DRS)

Diffuse reflectance spectroscopy of adsorbents was carried out on an Avaspec-2048 spectrometer (Avantes Inc.) based on a symmetrical Czerny-Turner design with an optical bench and a focal length of 75 mm suitable for analysis in 245-800 nm wavelength range. The spectrometer is equipped with a standard SMA (Sub Miniature version A) connector for incorporating the fiber optic cable. Diffusely reflected light from adsorbent particles in packed beds was received by the CCD detector array with a sensitivity of 5000 counts μW^{-1} per millisecond of integration time. A 12V DC USB powered interface between the spectrometer and spectrum analyzer (or computer) enabled data transfer speeds in the range of 14-31 milliseconds $scan^{-1}$ with an onboard sample averaging speed of 17 milliseconds $scan^{-1}$. The dimensions of the spectrometer used in this study were 175 mm (length) × 110 mm (height) × 44 mm (width) and weighed approximately 716 g. A

stainless steel fiber optic reflectance probe (FCR-7UV200-2-1.5x100) with dimensions 1.5 mm (diameter) × 100 mm (length) specifically designed for powders was used. The fiber bundle consisted of six illumination or emitter fibers and one read fiber. The material for light guiding effect was Fluorine-doped SiO_2 with a numerical aperture of 0.22. UV-vis light (245-800 nm) from a xenon pulsed light source (Avalight-Xe) was conveyed through emitter fibers directly onto the packed bed of particles. The fibers are protected by a Kevlar reinforced PTFE (Polytetrafluoroethylene) jacket with 3.8 mm outer diameter PVC (Polyvinyl chloride) sleeves. The maximum operating temperature was 65°C. For experiments involving ZnO extrudate particles, a larger fiber optic probe (FCR-7UV200-2-45x140) of dimensions 6 mm (diameter) × 140 mm (length) containing the six emitter fibers and one read fiber was used. The minimum bend radius ranges from 20mm - 60mm depending on how long these fibers are subjected to bending. The maximum operating temperature in this case was 500 °C.

II.5.5 Electron Paramagnetic Resonance Spectroscopy (EPR)

EPR spectroscopy is similar to any other technique that depends on the absorption of electromagnetic radiation. A molecule or atom has discrete (or separate) states, each with a corresponding energy. Spectroscopy is the measurement and interpretation of the energy differences between the atomic or molecular states. With the knowledge of these energy differences, it is possible to gain an insight into the identity, structure, and dynamics of the sample under study. EPR characterization of performed on a Bruker EMX-6/1 EPR spectrometer that consists of an EMX 1/3 console, an ER 041 X6 bridge with a built-in ER-0410-116 microwave frequency counter, an ER-070 magnet and an ER-4102st standard universal rectangular cavity. EPR spectra of samples were recorded at a field modulation of 100 kHz,

modulation frequency of 9.31 GHz. BioEPR software was used for the computer simulation of the EPR signals. In-situ EPR of $Cu_XZn_{100-X}O/SiO_2$ was performed at room temperature by passing the challenge gas (20000 ppmv H_2S in H_2) through the quartz tubular reactor (4 mm: outside diameter, 3 mm inside diameter) that was placed in the cavity filled with the calcined adsorbents.

II.5.6 Fourier Transform Infrared Spectroscopy (FTIR)

A Thermo Scientific Nicolet IR 100 spectroscope was used for this purpose. The analysis range was between 1000–4000 cm^{-1} and the spectral resolution was 4 cm^{-1}. For IR analysis, adsorbent samples were dried over night at 100°C and placed in air tight vials before testing. 100 mg of KBr was physically mixed with approximately 1-2 mg of sample using a mortar and pestle. This mixture was then placed in a bolt holder to obtain an almost transparent thin film held between the grooves of the bolt holder. This procedure is essential for obtaining a well-defined transmission spectrum. During analysis, the IR chamber was continuously purged with high purity N_2 gas to maintain an inert and dry atmosphere.

II.5.7 X-ray Photoelectron Spectroscopy (XPS)

A Kratos Analytical Ltd. AXIS Ultra DLD (delay lines detector) X-ray photoelectron spectrometer (XPS) with a monochromatic Al Ka X-ray source (1486.6 eV) was used for the XPS measurement. The end station consists of a fast entry load lock, sample treatment chamber (STC) and a sample analysis chamber (SAC). The X-ray spot size was about 500 x 700 μm^2, and the angle between the sample holder and X-ray source is 35 degrees. A pass energy of 20 eV was used to measure high resolution spectrum of Zn 2p, O 1s, Si 2p, Cu 3d, La 3d and C 1s narrow

scans. The binding energy shifts due to surface charging were corrected by constraining C 1s peak at 284.8 eV. No surface cleaning treatment was used to remove surface adsorbates during this experiment. The relative atomic density of each species was obtained by deconvolutions of the peaks using XPSPEAKS 4.1 software. Core level peaks were deconvoluted by using Gaussian-Lorenzian (20%) method.

III. XPS, UV-Vis DRS, and EPR Investigation of $Cu_XZn_{100-X}O/SiO_2$ Sorbents for H_2S Adsorption at Ambient Conditions

Abstract

Cu^{2+} promoted ZnO sorbents supported on SiO_2 are studied by in-situ UV-Vis diffuse reflectance spectroscopy (UV-Vis DRS), Electron paramagnetic resonance (EPR) spectroscopy and ex-situ by X-ray photoelectron spectroscopy (XPS) during H_2S adsorption at 22°C. At low CuO loadings (≤ 2 weight %), Cu^{2+} ions exist in an octahedral coordination environment with tetragonal distortions in the Cu-ZnO lattice. The band gap (E_g) of ZnO in ZnO/SiO_2 and $Cu\text{-}ZnO/SiO_2$ shows a linear variation with temperature between 323-473K. E_g value at 22°C is estimated to be 3.61±0.02 eV for ZnO/SiO_2 and 3.29±0.02 eV for 20 atomic% Cu promoted ZnO/SiO_2. The change in band gap with temperature increased from 0.31±0.01 meV K^{-1} for ZnO/SiO_2 to 1.82±0.01 meV K^{-1} for $Cu\text{-}ZnO/SiO_2$ which indicates a red shift in ZnO band position caused by defects in the oxide lattice due to incorporation of Cu^{2+} ion. The XPS intensity ratio of Zn to Si in $Cu_XZn_{100-X}O/SiO_2$ samples increases up to 20 atomic % Cu suggesting a greater number of Zn atoms to be exposed to the surface. Above 20 atomic% Cu, the Zn:Si intensity ratio reduces and correlates with the H_2S adsorption capacity. In-situ EPR profiles reveals partial reducibility of EPR active Cu^{2+} ions to Cu^{1+} rather than complete reducibility to EPR silent Cu0. The presence of Zn in $Cu_XZn_{100-X}O$ matrix facilitates greater degree of reduction of isolated Cu^{2+} ions in calcined sorbents as compared to reduction of clustered Cu^{2+} in CuO/SiO_2 specimen. In situ UV-Vis DRS profiles suggests greater reducibility of Cu^{2+} to Cu^{1+} as the Cu:Zn atomic ratio increases.

III.1. Introduction

ZnO dispersed on porous SiO_2 support via wetness impregnation showed enhanced H_2S adsorption capacity with minimal mass transfer resistance at 400°C compared to commercial ZnO [45]. ZnO/SiO_2 adsorbents were modified for room temperature desulfurization operation by transition metal promoters [9]. Amongst others, $Cu\text{-}ZnO/SiO_2$ with a Cu:Zn molar ratio of 20:80 exhibited effective performance over multiple sulfidation-regeneration cycles [29]. A number of characterization techniques including Electron Paramagnetic Resonance (EPR) [29], X-ray Diffraction (XRD) [104], X-ray Photoelectron Spectroscopy (XPS) [104], Density Functional Theory (DFT) [105] have been employed to understand the surface characteristics and mechanism responsible for enhanced H_2S reactivity of this adsorbent at room temperature. The techniques noted above, however, provide only a narrow depth of knowledge that is ultimately governed by the sensitivity and sampling protocols inherent to each technique. For example, in a previous report on $Cu\text{-}ZnO/SiO_2$ adsorbents, authors reported an artificial XPS-induced reduction of Cu^{2+} species to Cu^{1+} while examining calcined specimen as a result of X-rays, heat and secondary electrons [29]. Klabunde et al. [16] suggest that 40% of nano-dispersed ZnO available for surface reaction with H_2S exist as 4 nm crystallites. However, at 21 weight % optimal ZnO loading in $Cu\text{-}ZnO/SiO_2$ adsorbents, no XRD lines belonging to ZnO or CuO were observed indicating both oxides in highly dispersed phases on SiO_2. Zn^{2+} is diamagnetic with an electronic configuration of [Ar] $4s^0 3d^{10}$, thus, application of EPR spectroscopy will be limited to study of $Cu\text{-}ZnO/SiO_2$ adsorbents. Thus, a complementary non-destructive technique must be employed to study the Cu^{2+} as well as Zn^{2+} ions in Cu-ZnO adsorbents. Moreover, the technique must possess high sensitivity to the concentration of bulk as well as surface species and facilitate characterization in-situ during dynamic adsorption conditions. The highly dispersed ZnO phase

on SiO_2, the presence of defects in the dispersed ZnO lattice and the oxidation environment of the Cu^{2+} promoter ion are all major factors that influence the capacity and stability of this adsorbent during thermal regeneration cycles. Rodriguez et al. [106] have reported a direct correlation between H_2S reactivity of an oxide and size of the oxide band gap. The study suggests that an increase in the oxide band gap stabilizes its valence band and destabilizes the conduction band consequently reducing the ability of the oxide to respond to H_2S via the frontier molecular orbitals. On the other hand, an oxide with a smaller band gap exhibits better reactivity towards H_2S since the rate of decomposition of H_2S will be faster for oxides with a less stable valence band. Thus, it is essential to adopt a technique that provides a direct insight into this phenomenon. UV-Vis Diffuse Reflectance Spectroscopy is considered as an effective technique for probing coordination and oxidation state of metal oxides in bulk [40] and supported forms [107-111]. UV-Vis DRS can also be used to calculate the band gap of metal oxide semiconductors. This is of particular interest since, nano-dispersed ZnO exhibits distinct size dependent light absorption behavior in which the variation of the band gap is a direct consequence. Remote sensing via fiber optics facilitates the study of Zn^{2+} and Cu^{2+} species under real time H_2S adsorption conditions.

In this study, a surface characterization of $Cu_XZn_{100-X}O/SiO_2$ adsorbents has been carried out using UV-Vis diffuse reflectance spectroscopy, X-ray photoelectron spectroscopy and Electron paramagnetic resonance spectroscopy. This article is aimed at (i) elucidating the structure of Cu^{2+} promoter ions, (ii) determining the ZnO band gap in SiO_2 supported Cu-ZnO adsorbents as a function of Cu^{2+} content and temperature (iii) Investigating the UV-Vis spectroscopic behavior of $Cu_XZn_{100-X}O/SiO_2$ adsorbents in-situ during H_2S removal at room temperature and (iv)

Probing the simultaneous reduction of Cu^{2+} ions in presence of H_2S using in-situ EPR spectroscopy.

III.2. Experimental

III.2.1. Preparation of Cu-ZnO/SiO_2 adsorbents

Cu promoted ZnO adsorbents with the nominal formula $Cu_XZn_{100-X}O/SiO_2$ (X: mole% Cu) were prepared by co-impregnating Zinc and Copper nitrate solutions on silica support (Grace Division Inc. pore volume 1 $cm^3\ g^{-1}$; BET surface area 460 $m^2\ g^{-1}$) according to a procedure described in detail elsewhere [29]. The impregnated samples were subsequently dried at 110°C overnight and calcined at 400°C for 3 h in static air. At this temperature, the metal nitrate salts (Cu^{2+} and Zn^{2+}) impregnated on the silica support were decomposed into their oxides (ZnO and CuO).

III.2.2. UV-Vis diffuse reflectance spectroscopy (UV-Vis DRS)

UV-Vis diffuse reflectance spectroscopy of the doped sorbents was performed on an Avaspec-2048-USB-2 spectrometer (Avantes Inc) equipped with an FCR-7UV200-2-1.5X100 fiber optic reflection probe specifically suited for powders. The high temperature rated (500°C) probe was simply dipped into the powders for measurements. For conducting in-situ UV-Vis DRS measurements during H_2S adsorption on 100-200 micron size particles, a reflectance probe of dimensions: 1.5 mm (dia) x 100 mm (length) was used.

III.2.3. X-ray Photoelectron Spectroscopy (XPS)

XPS data were collected by the AXIS Ultra Delay Lines Detector (DLD) X-ray photoelectron spectrometer (XPS) from Kratos Analytical Ltd. ZnO/SiO_2 and $Cu_XZn_{100-X}O/SiO_2$ samples were

evacuated in a load lock chamber under 108 Torr vacuum, prior to admission into the analysis chamber. A monochromatic Al Kα X-ray source with $h\nu$ = 1486.6 eV was used as the photon source. High resolution spectra were obtained for C 1s, and Zn 2p, Si 2p, O1s and Cu 2p using a passing energy of 20 eV. The binding energy shifts due to surface charging were corrected using the reference C 1s level at 284.6 eV. Spectra were fitted by the XPSPEAK program.

III.2.4. Electron Paramagnetic Resonance (EPR) Spectroscopy

In-situ EPR of Cu-ZnO/SiO_2 adsorbents during H_2S adsorption was performed on a Bruker EMX-6/1 EPR spectrometer that consists of an EMX 1/3 console, an ER 041 X6 bridge with a built-in ER-0410-116 microwave frequency counter, an ER-070 magnet and an ER-4102st standard universal rectangular cavity. EPR spectra of samples were recorded at a field modulation of 100 kHz, modulation frequency of 9.31 GHz. BioEPR software was used for the computer simulation of the EPR signals. In-situ EPR was performed at room temperature by passing the challenge gas (20000 ppmv H_2S in H_2) through the quartz tubular reactor (4 mm: outside diameter, 3 mm inside diameter) that was placed in the cavity filled with the calcined adsorbents.

III.2.5. H_2S saturation tests and analyses

H_2S with desired concentration at inlet (C_0) was fed using mass flow controllers (Alicat Inc.).The outlet H_2S concentration from adsorption experiments was collected every 2 min using an automated six-port sampling valve (Valco Intruments) with a 250 μL loop) and analyzed on a Gas Chromatograph (Varian CP3800) with a Thermal Conductivity Detector (TCD) with a lower detection limit of ±200 ppmv.

III.3. Results and Discussion

III.3.1. Structural characterization using XRD

XRD analysis proves samples get more crystalline with increase in Cu content. Upto 20 atomic % Cu concentration, the ZnO and CuO phase appear to be highly dispersed with crystallite sizes below 4 nm (or detection limit of XRD). At 30 atomic % Cu, a distinct crystalline phase of CuO begins to appear on the surface. The 3D cystal structure of CuO phase on $Cu_XZn_{100-X}O/SiO_2$ is as monoclinic when compared to neat Copper (II) Oxide as shown in Figure III.1.

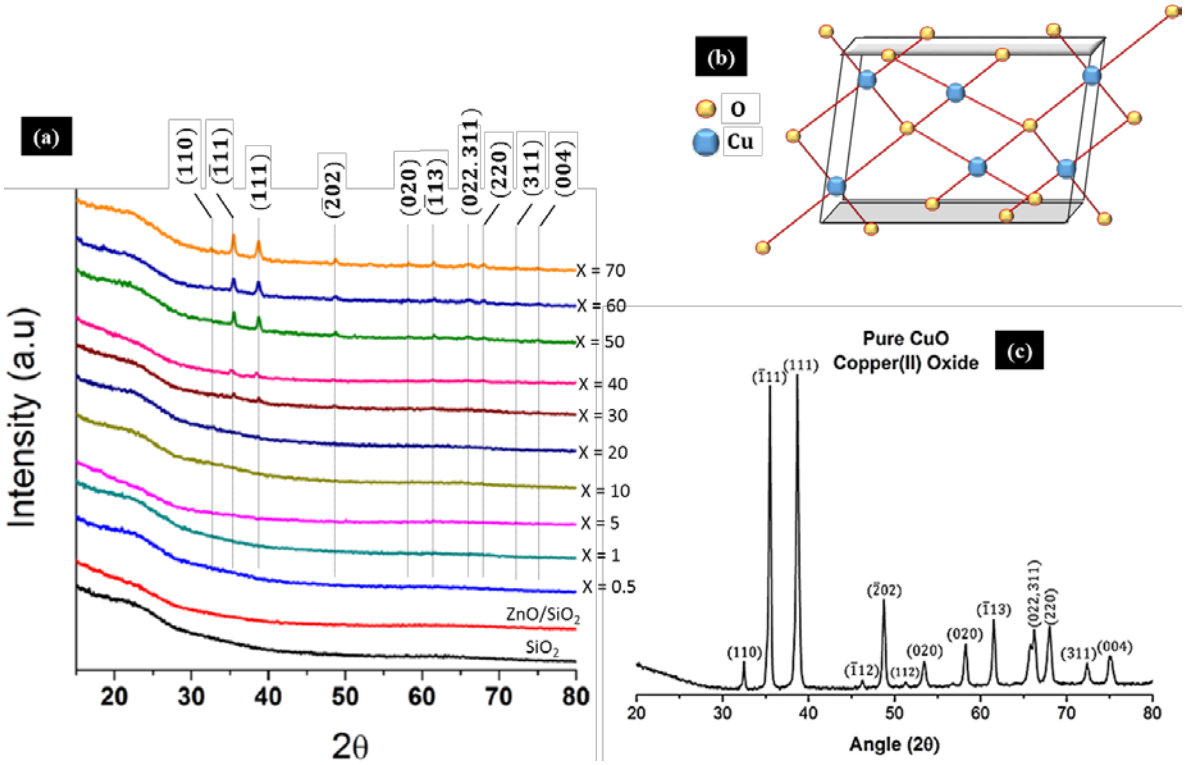

Figure X XRD patterns for (a) $Cu_XZn_{100-X}O/SiO_2$ as a function of Cu:Zn atomic ratio; (b) 3D crystal structure of monoclinic CuO; (c) XRD of neat CuO

III.3.2. XPS Characterization

Theoretical intensity ratio of Zn to Si was determined via quantitative XPS analysis [8] taking into consideration the inelastic mean free path, photoelectron cross section and number of atoms

per cm^2 of support for Zinc and Silicon respectively.

III.3.2a. Self-consistency check for Zn atom balance on SiO_2 surface

Assuming the no discrete arrangement of Zn atoms on the SiO_2 surface, the number of Zn atomic density on SiO_2 surface can be calculated. This can be visualized as shown in Figure III.2.

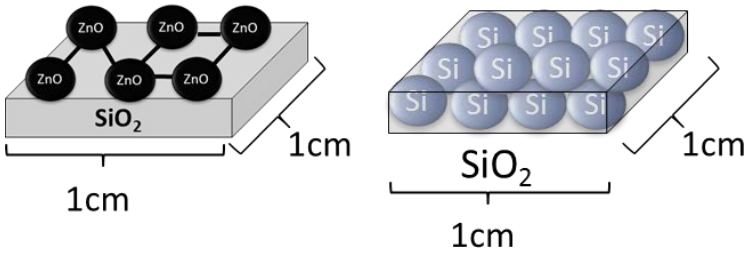

Figure XI Schematic representation of SiO_2 surface loaded with ZnO (left) and Si atoms in the lattice of SiO_2 (right)

For this purpose, the Zn atoms per cm^2 SiO_2 is calculated along with the number of Si atoms per cm^2 SiO_2 as follows,

1. $$Zn \text{ atoms per cm}^2\ SiO_2 \text{surface } (N_{Zn}) = \frac{N_A(\frac{\text{atoms}}{\text{mol}}).\frac{W_{Zn}(g)}{65\frac{g}{\text{mol}}}}{SiO_2 \text{ surface area } (cm^2)}$$

2. $$\text{Si atoms per cm}^3\ SiO_2\text{surface } = \frac{N_A(\frac{\text{atoms}}{\text{mol}}).\frac{W_{Si}\,(g)}{28\frac{g}{\text{mol}}}}{\frac{W_{SiO2}(g)}{\rho_{SiO2}\left(\frac{g}{cm^3}\right)}}$$

3. $$\text{Si atoms per cm}^2\ SiO_2\text{surface } = \left(\text{Si}\frac{\text{atoms}}{\text{cm}^3 SiO_2 \text{ surface}}\right)^{\frac{2}{3}}$$

Table III.1. Atomic density of Zn on SiO_2 surface in ZnO/SiO_2 sorbents

ZnO (wt%)	Zn (wt%)	Si (wt%)	SiO_2 (cm^2)	Zn density (atoms/cm^2)	Si density (atoms/cm^2)
1	0.8	46.2	455×10^4	0.016×10^{15}	0.89×10^{15}
5	4.0	44.3	437×10^4	0.085×10^{15}	0.89×10^{15}
10	8.0	42.0	414×10^4	0.180×10^{15}	0.89×10^{15}
21	16.9	36.9	363×10^4	0.430×10^{15}	0.89×10^{15}
30	24.1	32.7	322×10^4	0.690×10^{15}	0.89×10^{15}
44	35.3	26.1	258×10^4	1.268×10^{15}	0.89×10^{15}

BET Surface area of SiO_2 support: 460 m^2/g; Bulk density of SiO_2: 2.65 g/cm^3

III.3.2b. ZnO continuum calculation

The continuum calculation illustrated below is used to understand dependence of thickness of Zn atomic layer with the amount of ZnO loaded on SiO_2 support and assumes behaviour of materials is modelled as a continuous mass rather than discrete particles. This implies that Zn atoms completely fill the space which they occupy. The following theoretical calculation can be used to determine the thickness of Zn atom layer on SiO_2.

$$\text{Thickness of Zn atomic layer (nm)} = \frac{W_{ZnO}(g)}{\text{Bulk density of ZnO } \left(\frac{g}{nm^3}\right)} \Big/ \text{SiO}_2 \text{ area } (nm^2)$$

Figure III.3 below shows that at 44wt% ZnO loading on SiO_2 surface, the thickness of atomic layer approaches 1 monolayer (ML) or 0.35 nm which is atomic diameter of 1 Zn atom. Thus, at 21% ZnO loading it can be said that the analysis is carried out at 0.103 nm which is 35% of a monolayer (ML).

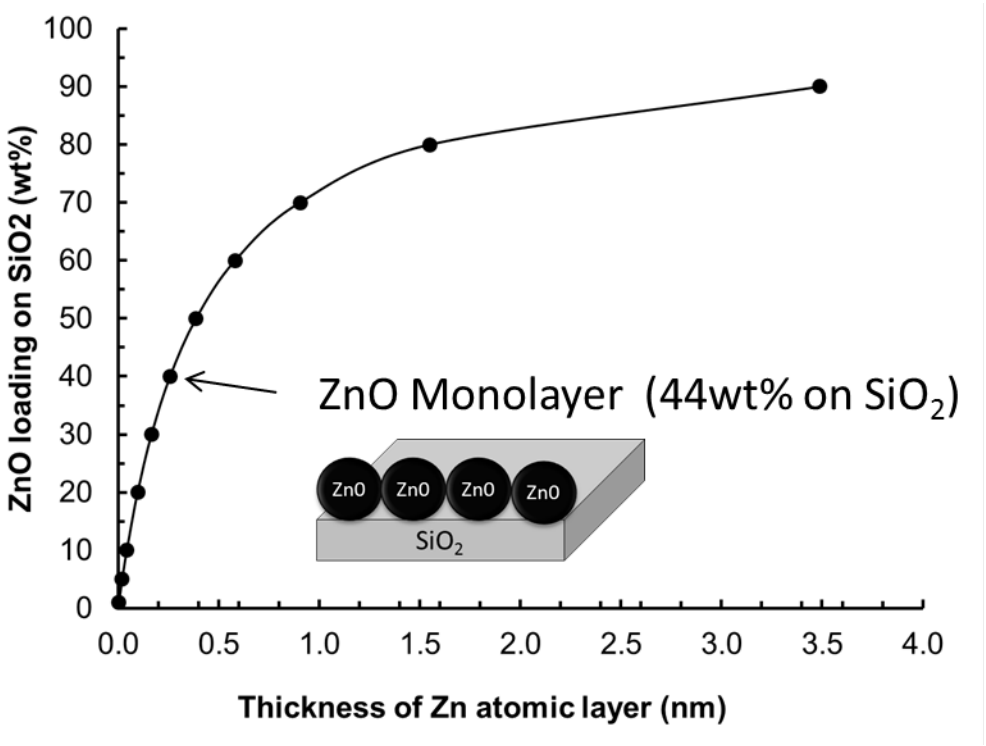

Figure XII ZnO weight loading versus thickness of Zn atomic layer

III.3.2c. XPS intensity ratio in ZnO/SiO_2 sorbents

XPS survey spectra revealed the following elements: Cu, Zn, Si, O, C. Nitrogen from the Zn nitrate precursor was not detected in the samples. A blend of the Shirley and linear backgrounds was used to satisfy the ratios of the T 2p and Ag d doublets. The Gaussian–Lorentzian curve ratio, the relative intensity of the 3ddoublet area ratio, and the peak separation were all held constant. Figure III.4 shows Zn 2p spectra. Zn exists in +2 oxidation state in ZnO/SiO_2 and $Cu_XZn_{100-X}O/SiO_2$ sorbents. The area under the Zn 2p peaks increase with increase in Zn loading. Beyond 21% as shown in Figure III.7 the Zn to Si intensity ratio deviates from theoretical trend and levels off. This indicates the growth or aggregation of the Zn particles on SiO_2. The intensity of the Si 2p peak does change significantly as seen in Figure III.5.

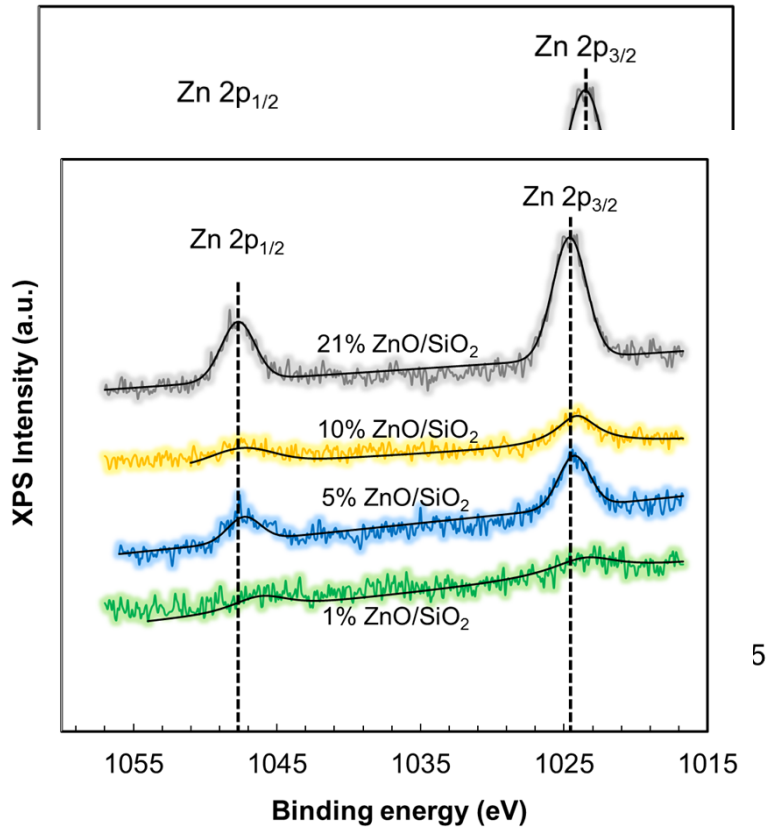

5

Figure XIII Zinc 2p spectrum in ZnO/SiO_2 sorbents

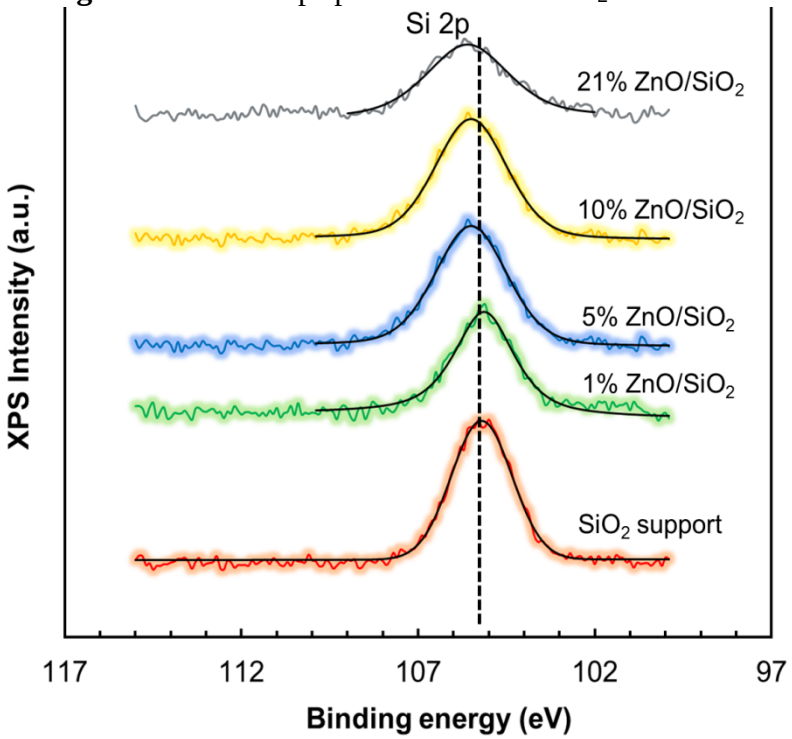

Figure XIV Si 2p spectrum in ZnO/SiO_2 sorbents

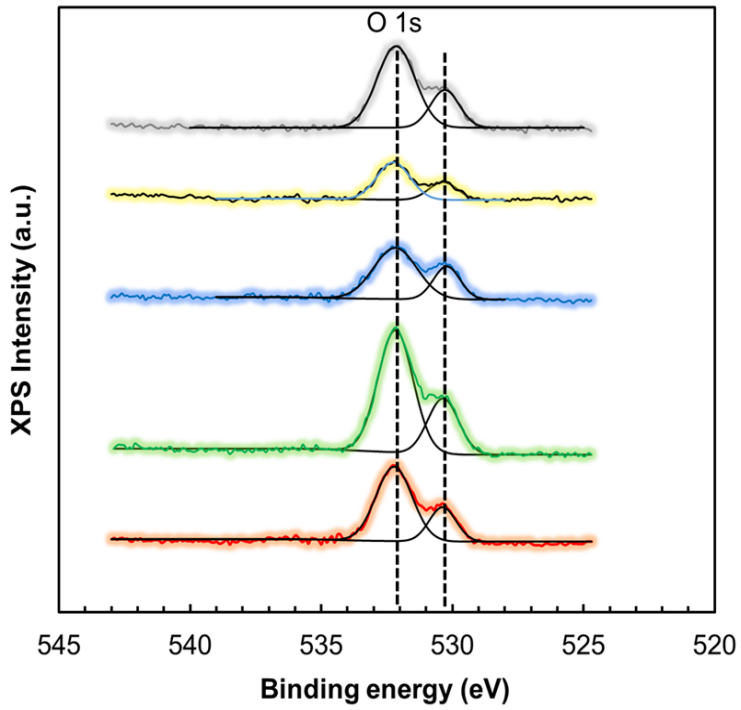

Figure XV O 1s 2p spectrum in ZnO/SiO_2 sorbents

Table III.2 shows atomic ratios of elements in the ZnO/SiO_2 sorbents as a function of ZnO loadings prepared by incipient wetness impregnation at 22°C. Figure III.6 shows the O 1s peak with a weak shoulder around 531 eV belonging to Zn-O bond. The theoretical Zn to Si intensity ratio can be calculated by having knowledge of atomic concentration of Zn per cm^2 of support surface (illustrated in Table III.1), the photoelectron cross section (σ) expressed by the 'p' peak, the inelastic mean free path of a Zn photoelectron (λ) expressed by 'p' peak, and the fraction of all photoelectrons emitted from the sample surface D(KE) which is assumed to be constant. The use of physical constants and constraints reduced ambiguity, elucidated underlying peaks, and eliminated the biases that would affect the assessment of peak areas. Atoms on the surface and buried sub-surfaces will be seen regardless of oxidation state.

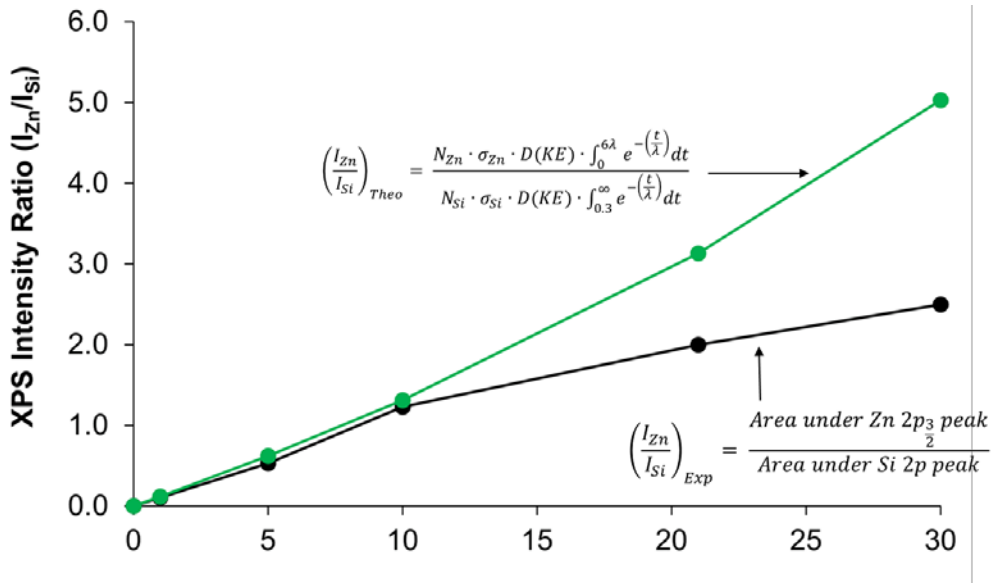

Figure XVI Theoretical and experimental XPS intensity ratio of Zinc to Silicon in ZnO/SiO_2 sorbents

Figure III.8 shows that at 0.103 nm which is 0.34 ML and less than 1λ, more than 37% of the photoelectrons are emitted from the sample surface. At this point, the Zn atoms are still highly dispersed on the surface and thus, show progressively higher H_2S saturation capacities at 22°C

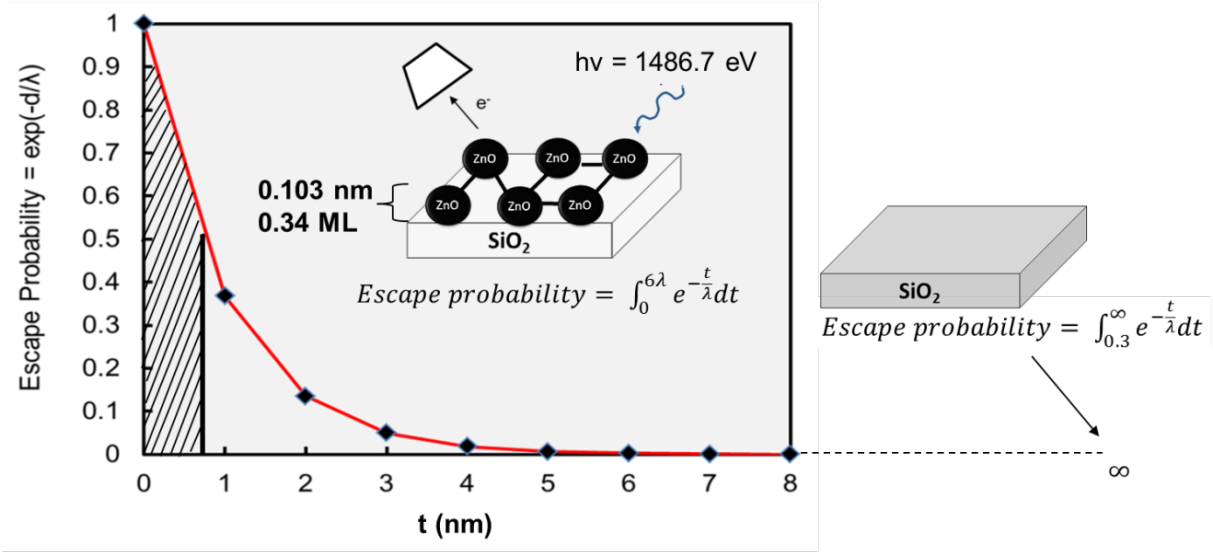

Figure XVII Escape probability of a photoelectron from Zn atom on surface of ZnO/SiO_2

Table III.2. Atomic ratios of elements on ZnO/SiO_2 adsorbent as a function of ZnO loading

Element	SiO_2	**ZnO loading**				
		1% ZnO	5% ZnO	10% ZnO	21% ZnO	30% ZnO
C-1s	0.48	0.53	0.54	0.82	0.51	0.39
O-1s	0.34	0.27	0.17	0.081	0.25	0.502
Zn-2p	-	0.0057	0.0065	0.0061	0.017	0.072
Si-2p	0.17	0.19	0.28	0.092	0.22	0.36
Total	1.00	1.000	1.000	1.000	1.000	1.000

III.3.2d. XPS intensity ratio in $Cu_XZn_{100-X}O/SiO_2$ sorbents

Table III.3 shows the atomic density of Zn atoms on the surface of $Cu_XZn_{100-X}PO/SiO_2$ sorbents and suggests that the number of Zn atoms reduce upon increasing Cu content.

Table III.3. Atomic density of Zn on surface of $Cu_XZn_{100-X}O/SiO_2$ and CuO/SiO_2 sorbents

Sample	CuO (wt%)	ZnO (wt%)	Zn (wt%)	SiO_2 area (cm^2)	Zn atoms/cm^2 SiO_2
$Cu_0Zn_{100}O/SiO_2$	0	21	16.9	363×10^4	0.430×10^{15}
$Cu_5Zn_{95}O/SiO_2$	1	20	16	363×10^4	0.408×10^{15}
$Cu_{10}Zn_{90}O/SiO_2$	2	19	15.2	363×10^4	0.388×10^{15}
$Cu_{20}Zn_{80}O/SiO_2$	4	17	14	363×10^4	0.357×10^{15}
$Cu_{30}Zn_{70}O/SiO_2$	6.2	15	12	363×10^4	0.306×10^{15}
$Cu_{40}Zn_{60}O/SiO_2$	8.2	12.6	10.1	363×10^4	0.258×10^{15}
$Cu_{50}Zn_{50}O/SiO_2$	10.5	10.5	8.51	363×10^4	0.217×10^{15}
$Cu_{70}Zn_{30}O/SiO_2$	14.4	6.7	5.09	363×10^4	0.130×10^{15}
$Cu_{100}Zn_0O/SiO_2$	21	0	0	363×10^4	0

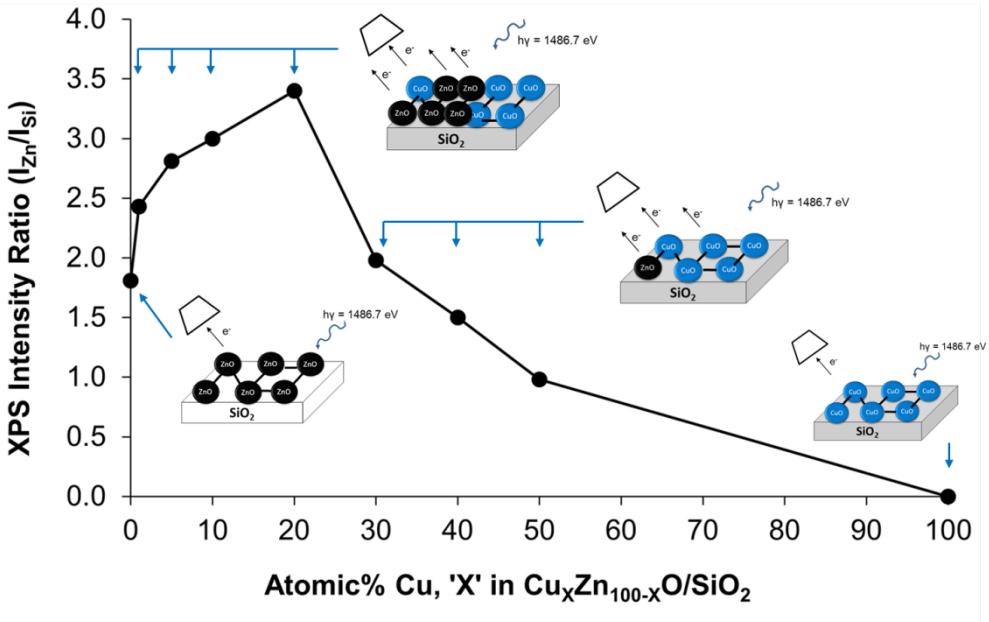

Figure XVIII Experimental XPS intensity ratio of Zinc to Silicon in $Cu_XZn_{100-X}O/SiO_2$ sorbents

Figure III.9 shows that Zn intensity increases up to 20% atomic Cu and thereafter begins to drop. Figure III.10 shows an increase in ZnO dispersion due to neighbouring Cu atoms which implies increase in Zn photoelectrons. In other words, the number of photoelectrons varies between 37% and 100%. Atomic ratios of Si are fairly constant for all weight loadings as shown in Table III.4.

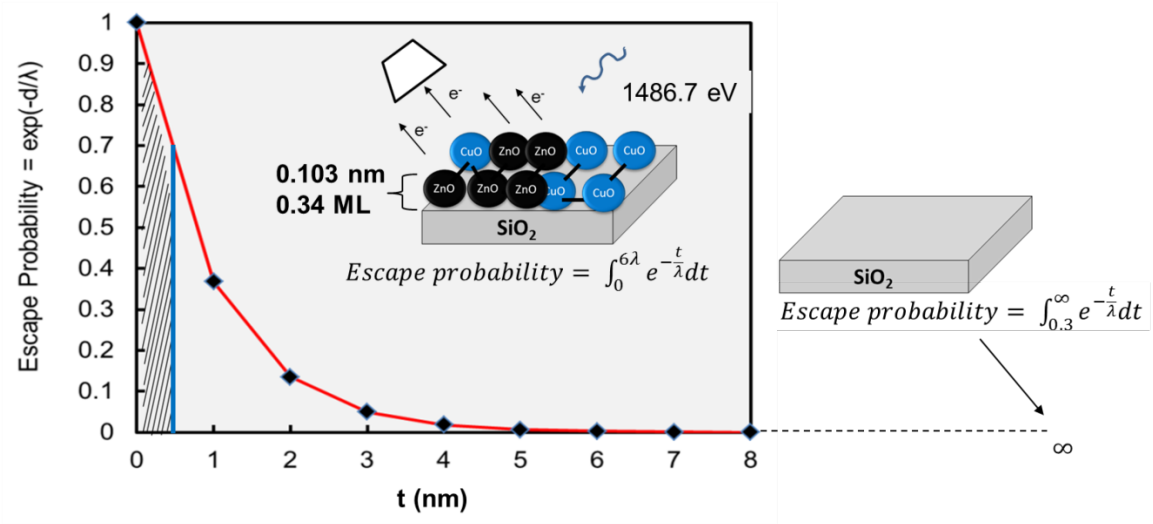

Figure XIX Escape probability of a photoelectron from Zn atom on surface of $Cu_XZn_{100-X}O/SiO_2$

Table III.4. Atomic concentration of elements on $Cu_XZn_{100-X}O/SiO_2$ and CuO/SiO_2 adsorbents

Element	**$Cu_xZn_{1-x}O/SiO_2$**						(21% CuO/SiO_2)	1% CuO/SiO_2
	x = 0.001	x = 0.01	x = 0.05	x = 0.1	x = 0.2	x = 0.5		
C-1s	0.42	0.46	0.55	0.49	0.56	0.45	0.51	0.85
O-1s	0.26	0.20	0.28	0.26	0.20	0.31	0.23	0.062
Zn-2p	0.072	0.035	0.018	0.026	0.036	0.0095	-	-
Cu-3d	UD	UD	UD	UD	UD	UD	0.015	0.0054
Si-2p	0.25	0.33	0.15	0.23	0.25	0.23	0.24	0.085
Total	1.000	1.000	1.000	1.000	1.000	1.000	1.000	1.000

UD – Undetectable

III.3.3. UV-Vis DR analysis

The Schuster – Kubelka - Munk theory states that the absorption properties of solids can be studied as a function of diffuse reflectance occurring on the surface of these solids [1, 112, 113].

$$F(R_\infty) = \frac{(1-R_\infty)^2}{2R_\infty} \quad \text{..... (1)}$$

$F(R_\infty)$ is the Kubelka-Munk function and reveals the apparent absorbance of the sample.

$$R_\infty = \frac{R_{sample}}{R_{reference}} \quad \text{..... (2)}$$

R_∞ is diffuse reflectance the ratio of percent reflectance of the powdered solid (R_{sample}) to the percent reflectance of a white reference ($R_{reference}$) or background spectrum [113]. In these experiments, SiO_2 support was selected as the reference material and subtracted as background spectrum. The UV-Vis DRS spectra of Cu-ZnO/SiO_2 adsorbents with varying Cu^{2+} molar concentration is shown in Figure III.11. The sensitivity of the Kubelka-Munk function towards Cu^{2+} molar concentration as shown in Figure III.1 (inset) indicates a linear variation with Cu^{2+} content as low as 1 mol% Cu. This linearity suggests that the symmetry of the Cu^{2+} ion is the same for all the Cu loaded samples as observed similarly for Cu^{2+} exchanged ZSM-5 sample [114]. The UV absorption edge at ca. 370-380 nm belongs to ZnO dispersed on SiO_2 [115-117], indicative of a charge transfer (CT) between the 4s orbital of Zn^{2+} and the 2s orbital of O^{2-} [118]. A broad absorption band in the visible region of the spectrum between 550-800 nm is indicative of a d-d electronic transition of Copper in a 2+ oxidation state in an octahedral co-ordination geometry [119, 120].

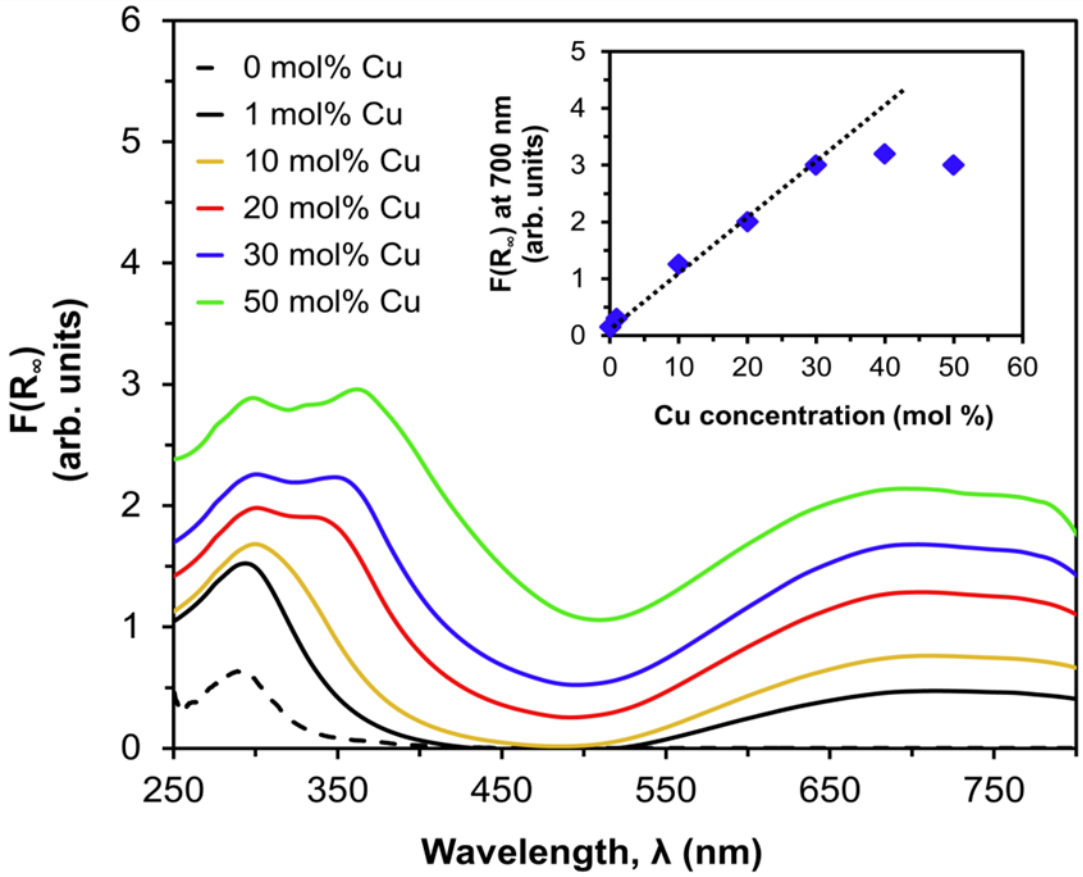

Figure XX UV-Vis DRS spectra of $Cu_XZn_{100-X}O/SiO_2$ sorbents

An additional shoulder at 350 nm is seen at Cu:Zn molar ratios of ≥ 20:80 on SiO_2 support which is attributed to ligand to metal charge transfer (LMCT) between lattice oxygen and the Cu^{2+} ions [120]. The process of Cu^{2+} promotion on ZnO involves creation of electron acceptor levels in the lattice of ZnO. These acceptor levels cause a reduction in the band gap of ZnO and can be studied as a function of the Kubelka Munk absorption [121] as follows,

$$[h\vartheta \cdot F(R_\infty)]^{\frac{1}{n}} = A(h\vartheta - E_g) \quad \text{..... (3)}$$

Where h is Planck's constant, $F(R_\infty)$ is the Kubelka-Munk function, ν is the frequency of the incident UV/Vis light and the value of exponent 'n' is 0.5 which accounts for the direct allowed transition in ZnO [121]. A plot of $[h\nu \cdot F(R_\infty)]^2$ vs photon energy (hν) from Eq.(3) represents a

Tauc as shown in Figure III.12. Band gap (E_g) values of ZnO are obtained when the linear region of the spectrum was extrapolated to intersect the x-axis where $F(R_\infty) = 0$. $Cu_XZn_{100-X}O/SiO_2$ with x = 5 was chosen as a basis for preparation, characterization and comparison of H_2S saturation capacities [9]. Figure III.12 illustrates a reduction in the band gap of ZnO due to the introduction of Cu^{2+} ions in Cu-ZnO/SiO_2 adsorbents in the following order: ZnO/SiO_2 (3.58 eV) < $Cu_5Zn_{95}O/SiO_2$ (3.55 eV) < $Cu_{10}Zn_{90}O/SiO_2$ (3.35 eV) < $Cu_{20}Zn_{80}O/SiO_2$ (3.01 eV) indicating a uniform substitution of Zn^{2+} ion with Cu^{2+} ions in the lattice structure [122, 123]. This phenomenon is known as a red-shift in the band gap of Cu doped ZnO particles arising out of the p-d spin exchange interaction between the p orbital of oxygen and d orbital of the transition metal ion substituting the cation [124].

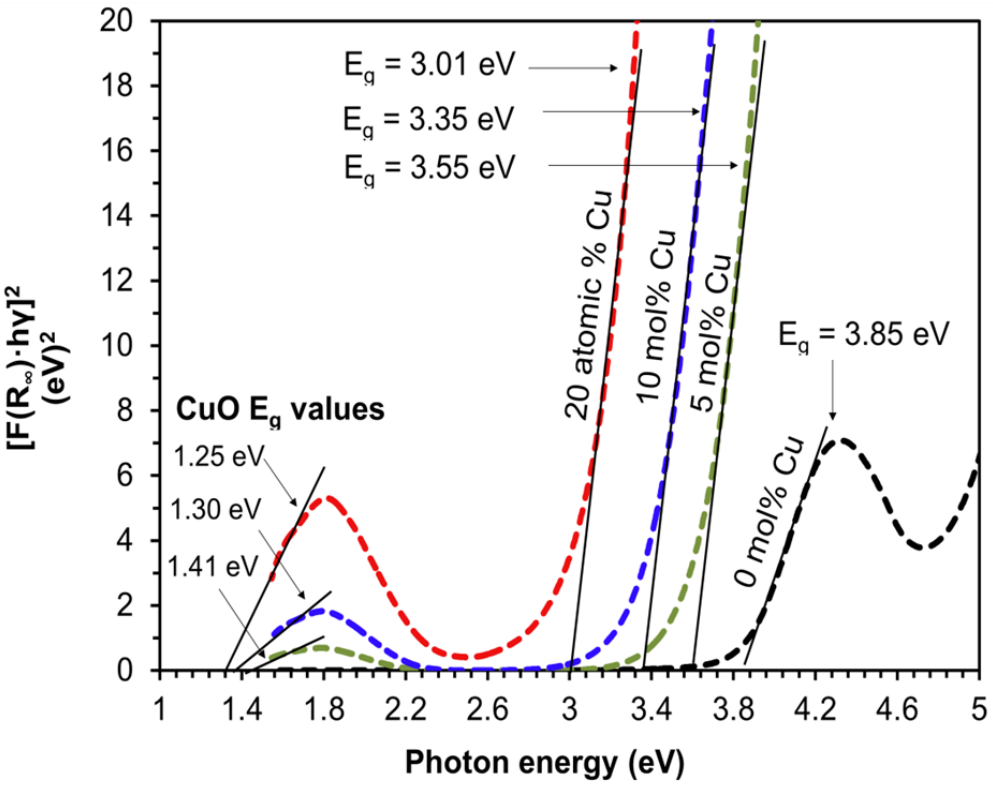

Figure XXI Tauc plot from UV-Vis DRS spectra of $Cu_XZn_{100-X}O/SiO_2$ sorbents

Above a Cu:Zn molar ratio of > 20:80, the sample appear darker in color and, an increase in noise was observed in the UV-Vis region. Temperature dependence of the ZnO optical band gap in adsorbent sample reveals information about the lattics expansion and contraction phenomenon of metal oxides. For these experiments, the fiber optic probe used for UV-Vis DRS measurement is simply immersed in a packed bed of adsorbent contained in a quartz tube. High purity helium at the rate of 50 mL min^{-1} is passed through the adsorbent bed to create an inert atmosphere and the temperature is raised at a rate of 10°C min^{-1} while collecting the UV-Vis diffuse reflectance spectra (R_∞) *in-situ*. There is an expansion of the ZnO crystal lattice along with a weakening of interatomic bonds with increase in temperature. In other words, less energy is needed to excite an electron from the valence band to the conduction band [125]. However, at T<100°C, the shift in the ZnO absorption edge is smaller in comparison with that observed at high temperatures. Moreover, the shift in the blank SiO_2 absorption edge is negligible. This is likely due to the electronic behaviour of SiO_2 as an insulator that has a relatively large and stable band gap (E_g = 6 eV) [105] as compared to bulk ZnO (E_g = 3.3-3.4 eV) or bulk CuO (E_g = 1.2 eV) species. The same protocol for spectral acquisition and band gap calculations as given by Eq. (1-3) is followed for $Cu_XZn_{100-X}O/SiO_2$. It is evident that the rate of change of the ZnO absorption edge is relatively higher in $Cu_XZn_{100-X}O/SiO_2$ adsorbents. At the same time, there is no shift in the CuO absorption edge ~1.5 - 2.0 eV when the temperature is increased from 323 K to 473 K. This shows that the structure and symmetry of Cu^{2+} ion remains unaffected at least up to 473 K (200°C) which is the higher operating temperature range of these adsorbents during desulfurization for low temperature fuel cell applications. Indeed the structure of Cu^{2+} absorption band position in a Cu-ZnO based catalyst was reportedly stable up to 550°C [126]. The relationship between ZnO band gap and temperature is given by the following equation [127] ,

$$E_g(T) = E_{g0} - \beta T \quad \text{..... (4)}$$

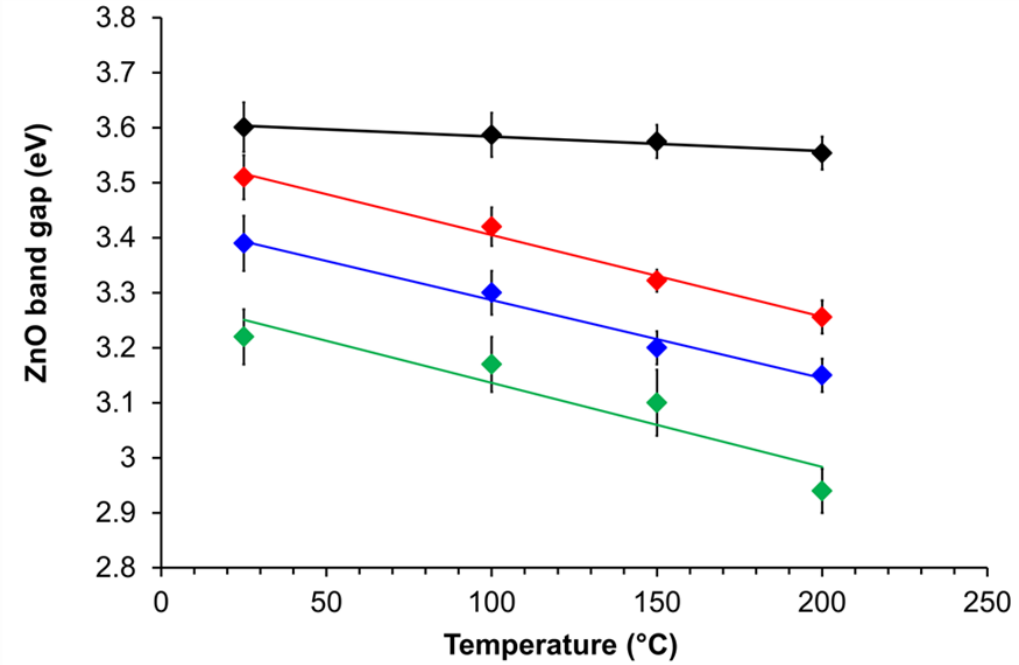

Figure XXII Variation of ZnO band gap as a function of temperature in $Cu_XZn_{100-X}O/SiO_2$ sorbents

Where E_{g0} is the absolute zero value of band gap and $\beta = dE_g/dT$, or the rate of change of band gap with dry temperature. The β and E_{g0} values are determined from the slope and intercept as shown in Figure III.13. A linear dependence of the ZnO band gap values in ZnO/SiO_2 and Cu-ZnO/SiO_2 adsorbents is observed in the temperature range investigated. However, the slope of E_g vs T increases upon introduction of Cu^{2+} ions. As per equation (4) the absolute zero value of the optical band gap $(E_{g0})_{273.15K}$ for ZnO obeys the followed order: 3.62 ± 0.02 eV (ZnO/SiO_2) > 3.59 ± 0.02 eV ($Cu_5Zn_{95}O/SiO_2$) > 3.46 ± 0.02 eV ($Cu_{10}Zn_{90}O/SiO_2$) > 3.33 ± 0.02 eV ($Cu_{20}Zn_{80}O/SiO_2$). On the other hand, β calculated from the slope of E_g versus T as illustrated in Table III.5 increased from 0.31 meV K^{-1} for ZnO/SiO_2 to 1.82 meV K^{-1} for 20 mole% Cu promoted ZnO/SiO_2 adsorbent. In other words, the rate of change of optical gap (β) increases

with an increase in molar Cu^{2+} concentration in Cu-ZnO/SiO_2 adsorbents. This indicates that Cu^{2+} creates an increase in acceptor levels in the ZnO lattice structure which ultimately leads to a red shift in the absorption edge position as confirmed by Fig. III.11.A red shift is caused by a sp-d spin exchange interactions between the band electrons and the localized d electrons of the Cu^{2+} metal ion substituting the Zn^{2+} ion [117, 122].

Table III.5. Temperature correlation of ZnO E_g in sorbents

Adsorbent sample	Temperature correlation
ZnO/SiO_2	$3.61 - (0.26\times10^{-3})T$
$Cu5Zn_{95}O/SiO_2$	$3.55 - (1.40\times10^{-3})T$
$Cu_{10}Zn_{90}O/SiO_2$	$3.43 - (1.48\times10^{-3})T$
$Cu_{20}Zn_{80}O/SiO_2$	$3.29 - (1.53\times10^{-3})T$

III.4. In-situ studies

III.4.1. In-situ UV-Vis DRS

In-situ spectroscopy of catalysts and adsorbents facilitates a fundamental insight into the active sites, intermediates and reaction pathways under real time working conditions [128, 129]. It is envisioned that the fundamental working insight of catalysts or adsorbent will guide in the development of systems with better performance. In-situ UV-Vis spectroscopy is a widely reported technique in the study of heterogeneous catalytic processes involving exchanged zeolites [130-132] and supported transition metal oxides of Chromium [108, 133], Vanadium [110] and Rhodium [107]. In this section, the electronic effects occurring on the surface of ZnO and Cu-ZnO adsorbents during H_2S sorption are probed in-situ using a fiber optic reflectance probe. To obtain a desired signal-to-noise ratio of 200:1 essential for probing the spectral

changes occurring on the adsorbent surface, the scan rate was set to 5s scan^{-1} with an integration time of 10 ms scan^{-1}. The time between the start of spectral data acquisition and GC injection was found to be less than three seconds during experiments. In-situ diffuse reflectance behavior of Cu-ZnO/SiO_2 adsorbents as a function of the Cu:Zn molar ratio is shown in Figure III.14(a-c). The sulfidation of Cu-ZnO/SiO_2 adsorbents proceeds via a charge transfer mechanism in which the Cu^{2+} ion in fresh adsorbent is reduced to Cu^{1+} ($3d^{10}$) in spent adsorbent and the S^{2-} ion ($3p^6$) is oxidized to S^{1-} ($3p^5$) in spent adsorbent.

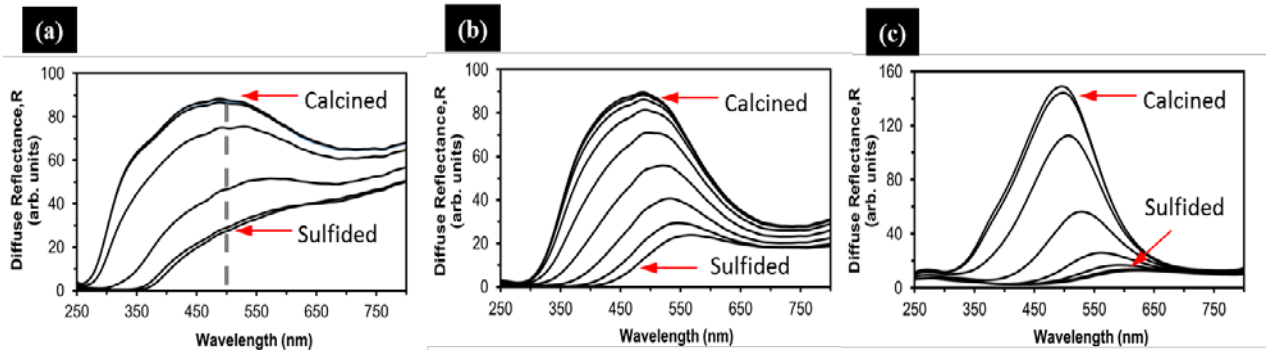

Figure XXIII In-situ UV-Vis DRS of (a) $Cu_1Zn_{99}O/SiO_2$; (b) $Cu_{10}Zn_{90}O/SiO_2$; (c) $Cu_{20}Zn_{80}O/SiO_2$ tested under 100 mL/min of 0.5% H_2S at 22°C

Figure III.14 shows a weak ZnO absorption edge around 325 nm in the spectrum of $Cu_5Zn_{95}O/SiO_2$. The Cu content affects the rate of reduction and the shape of the diffuse reflectance spectrum. For example, a broadening of the UV-Vis spectrum is observed at lower Cu^{2+} concentrations. This is attributed to the partial replacement of Cu^{2+} ions in Cu^{2+}-O-Cu^{2+} structures by Zn^{2+} ions resulting instead in the formation of Zn^{2+}-O-Cu^{2+} structures [134]. The presence of Zinc in the Cu-ZnO matrix influences the reduction behavior of the Cu^{2+} ion. For example, ZnO caused slow reduction of the CuO/Al_2O_3 catalyst for low temperature methanol synthesis [135]. In other words, the reduction of Cu^{2+} ion occurred more easily at a higher Cu:Zn

molar ratio. A higher number of surface Cu^{2+} ions are available for direct interaction with H_2S in bulk phase in accordance to our previous investigation based on EPR spectroscopy of Cu-ZnO/SiO_2 adsorbents [29]. Also, the synergistic effect of the presence of a greater number of Cu^{2+} ions on the surface can arise from the fact that sulfidation of CuO is more thermodynamically favored (ΔG_R = -126 kJ mol^{-1}) than the sulfidation of ZnO (ΔG_R = -76 kJ mol^{-1}) [21].

III.4.2. In-situ EPR spectroscopy of Cu^{2+} ion

In-situ EPR spectroscopy is gaining attention in the study of paramagnetic spin states in heterogeneous catalysts composed of transition metals such as Copper [136, 137], Iron [138], Chromium [109] Vanadium [110] under real time working conditions with particular interest in the study of Cu^{2+} ion in Cu-ZnO mixed oxide systems [122, 126, 139]. In a previous study, it was shown that EPR signal of paramagnetic Cu^{2+} ion was not influenced by CO/CO_2 or H_2 components in the feed during H_2S removal at room temperature [29]. The overall shape of the EPR signal of Cu^{2+} in the "calcined" $Cu_XZn_{100-X}O/SiO_2$ sorbents is in accordance to that of a polycrystalline sample containing isolated Cu^{2+} ions in a site with an axial symmetry. The EPR spectral pattern of Cu^{2+} is influenced by the hyperfine splitting and presence of two major stable isotopes, ^{63}Cu (mole fraction 0.6915, nuclear spin 3/2) and ^{65}Cu (mole fraction 0.3085, nuclear spin 3/2), both have a nuclear spin of 3/2 so that the Zeeman line will be split into four lines (m=3/2, ½, -1/2, -3/2). Since the magnetic moments of these two isotopes are very similar, the hyperfine couplings are nearly coincident. Figure III.16 shows the in-situ EPR spectra of Cu^{2+} in Cu-ZnO/SiO_2 adsorbents at a Cu:Zn molar ratio of 20:80 during H_2S sulfidation at 22°C.

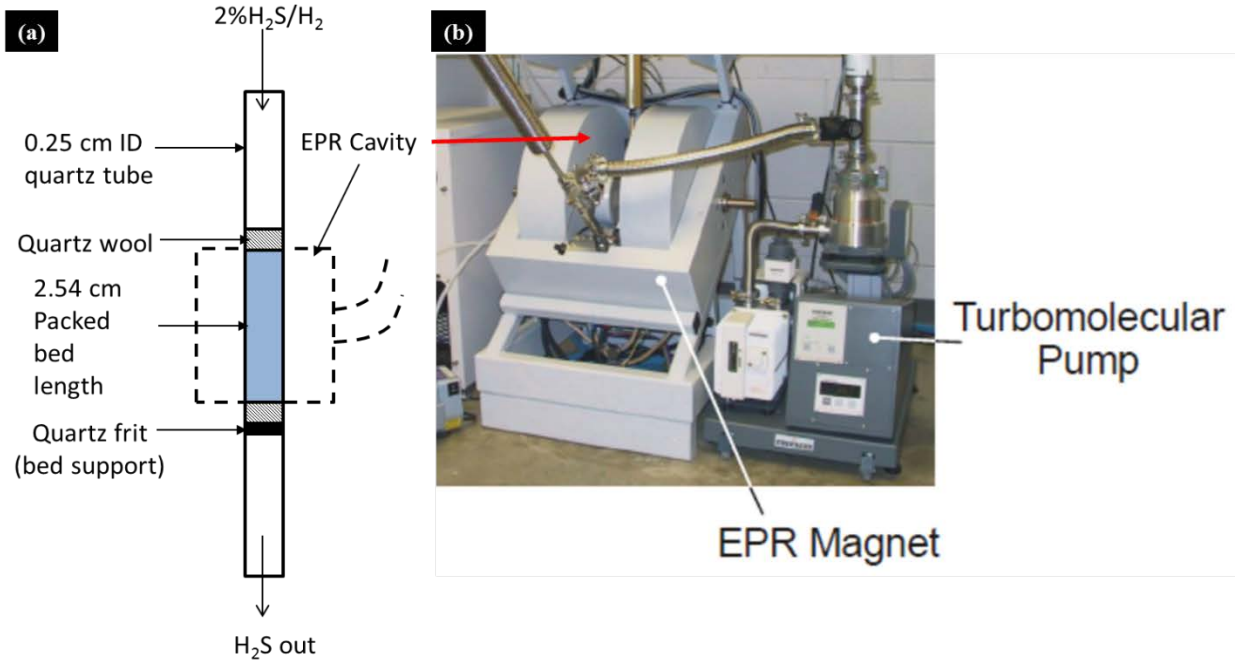

Figure XXIV Experimental setup for in-situ EPR experiments

Upon reaction with H_2S, the EPR signal of Cu^{2+} ion reduces in intensity. As a control experiment, in-situ EPR was conducted on CuO/SiO_2 containing identical CuO loading (~2 wt%) to $Cu_XZn_{100-X}O/SiO_2$ (Cu:Zn = 20:80) to examine the reducibility of Cu^{2+} in absence of Zn^{2+}. A schematic of the reactor setup for in-situ EPR is shown in Figure III.15. The EPR signal for CuO/SiO_2, however, reduces in presence of H_2S, however to a lesser extent when compared to reduction in $Cu\text{-}ZnO/SiO_2$ samples indicating the influence of the Zn^{2+} ions in the paramagnetic signal of the reduced specimen. For example, if some of the Cu^{2+} is dissolved in the ZnO matrix then after primary reduction of Cu^{2+} to Cu^{1+} takes place, the further reduction of Cu^{1+} to Cu^0, if any, will be influenced by neighbouring Zn^{2+} ions because Cu^{1+} is iso-electronic with Zn^{2+} that exists in fresh as well as spent adsorbents. To gain a better understand, in-situ EPR was also conducted when the Cu^{2+} molar concentration was reduced to a Cu:Zn molar ratio of 1:99. Increased Zn^{2+} ions in this sample affects the nature of the spectra as seen by the broad EPR

signal around 3125 gauss.

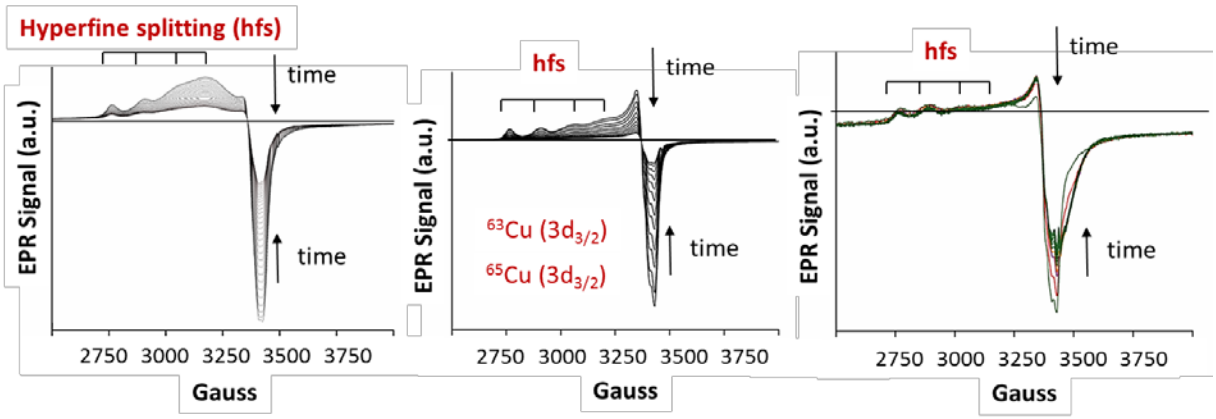

Figure XXV In-situ EPR spectra of (a) $Cu_5Zn_{95}O/SiO_2$; (b) $Cu_{20}Zn_{80}O/SiO_2$; (c) CuO/SiO_2 when tested with 10 mL/min of 2% H_2S at 22°C.

Also, the EPR signal of Cu^{2+} ion in the spent adsorbent is reduced to a lesser extent under same operating conditions. This is further confirmed in EPR measurements of fresh and spent adsorbents performed ex-situ [29]. In this study, EPR measurements indicate that the surface/pores of Cu-ZnO/SiO_2 adsorbents become enriched with Cu^{2+} ions in clustered form when the Cu:Zn molar concentration is increased. The reduction of clustered species is more favourable compared to reduction of isolated species in accordance to a Cu^{2+} supported system examined in an earlier study [140]. Under experimental conditions in this study, the reduction of Cu^{2+} ions did not take place upon introduction with H_2 however, the presence of H_2S led to the steady reduction of the EPR signal of Cu^{2+} ions. Further studies are being conducted to understand the final oxidation state of copper that remains in the spent adsorbent. Considering the poor reduction of isolated Cu^{2+} ions and absence of any paramagnetic signal due to isolated Cu^0 species in the ZnO lattice, the spent adsorbent probably contains a stabilized form of Cu^{1+} ions. To maintain consistency in flow conditions and bed dimensions during H_2S adsorption at 22°C, in-situ UV-Vis and on line GC analyses was performed using the same EPR quartz tube as

described in the experimental section. In this case, a 1.5 mm fiber optic probe was embedded vertically at the bottom of the packed bed and outlet H_2S concentration was analyzed with the help of on line GC TCD. The EPR signal and UV-Vis DRS signal collected in-situ shown in Figure III.17(a) is normalized for comparison with the H_2S breakthrough curves of $Cu_XZn_{100-X}O/SiO_2$ adsorbents.

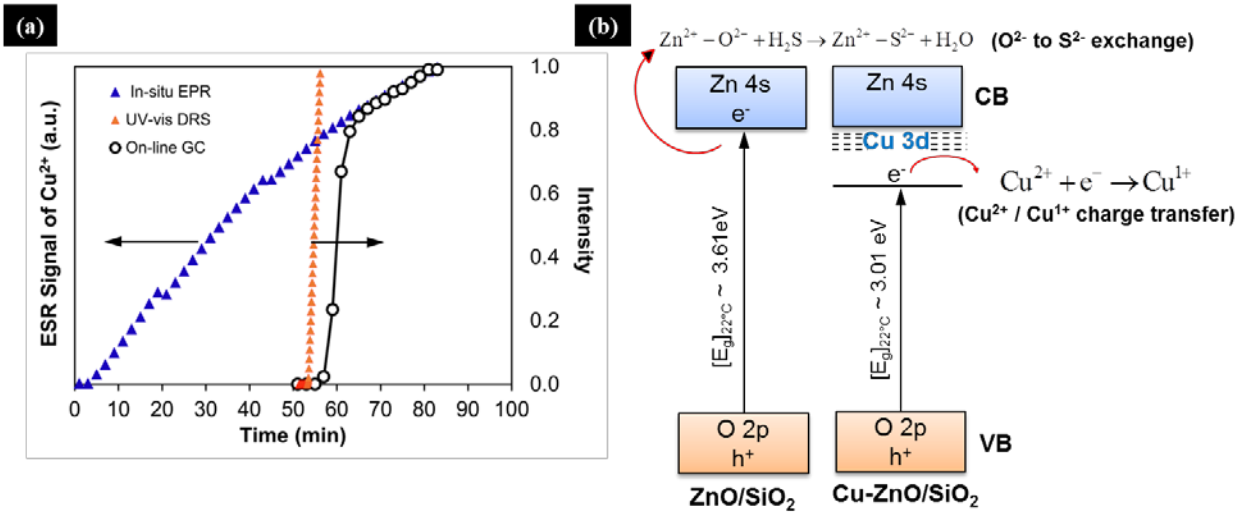

Figure XXVI (a) Combined EPR, UV-Vis and Online GC analysis during H_2S adsorption; (b) Schematic of electronic effects during H_2S adsorption

The length of the EPR cavity surrounding the quartz tube is approximately 1 inch. It is evident that the change in EPR signal of Cu^{2+} occurs appears almost immediately upon admission of H_2S through the packed bed. The EPR signal from the adsorbent is independent of the physicochemical properties of the adsorbent such as pore volume, surface area etc. The time length of the experiment is approximately 90 mins. The time delay between collecting EPR spectrum is 30 seconds for a good signal-noise ratio. The UV-Vis signal recorded simultaneously shows a change in the signal only until the sulfidation wave front has reached the bottom part of the bed which is illuminated by the fiber optic probe. The breakthrough curves reflect the

interaction between metal oxides (ZnO and CuO) and H_2S. Around 55 min, H_2S is detected at the outlet and a change in the UV-Vis signal occurs almost simultaneously. The results from combined EPR/UV-Vis and on line GC analyses indicate that Cu^{2+} and Zn^{2+} react at approximately the same rate with H_2S under given conditions.

III.5. H_2S saturation tests

Sulfur adsorption capacity of fresh and multiply regenerated ZnO, ZnO/SiO_2 and $Cu\text{-}ZnO/SiO_2$ (Cu:Zn = 20:80) at 21 % ZnO loading is reported in Table III.6. The sulfur capacity of commercial ZnO is found to be 52 ± 2 $mgS \cdot gsorbent^{-1}$. The addition of Cu^{2+} promoter resulted in an approximately 50% increase in sulfur saturation capacity from 54 ± 2 $mgS \cdot gsorbent^{-1}$ for ZnO/SiO_2 ion to 81± 2 $mgS \cdot gsorbent^{-1}$ for $Cu\text{-}ZnO/SiO_2$ (Cu:Zn = 20:80). The promotional effect of Cu addition is also evident upon multiple sulfidation-regeneration cycles as illustrated in Table III.6. These findings suggest that that there is formation of highly stable Zn-Si-O or Cu-Si-O bond in multiple regenerated samples. Additional techniques are being employed to gain a better understanding of the states of Cu^{2+} and Zn^{2+} ions in regenerated samples. With this knowledge, it is envisioned that adsorbent systems can be designed with enhanced adsorption capacity, stable performance over multiple cycles and lower regeneration temperatures. Based on the structural and electronic characterization of adsorbents, a band structure of ZnO/SiO_2 and $Cu_XZn_{100-X}O/SiO_2$ adsorbents can be conceptualized as shown in Figure III.17(b). O 2p orbitals constitute the valence band (VB) while Zn 4s constitute the conduction band (CB). Sulfidation of ZnO proceeds via sulfur to oxygen exchange reaction with no charge transfer involved. On the other hand, in the case of $Cu_{20}Zn_{80}O/SiO_2$ samples, the Cu 3d orbitals mixed with Zn 4s contribute to the formation of a hybrid Zn 4s + Cu 3d orbitals since Cu^{2+} creates acceptor levels

in the ZnO band structure and shift in the CB. The electrons in the CB are separated into highly reductive sites of Cu^{2+} ions that cause oxidation of S^{2-} ions via a charge transfer mechanism. Indeed, the sulfur transport is accelerated through Cu containing ZnS layers due to the presence of sulfur vacancies after iso-electronic charge compensation of Cu^{1+} substituting Zn^{2+} ions [26].

Table III.6. Sulfur (as H_2S) capacity of adsorbents tested with 2% H_2S at 22°C

Adsorbent	**Saturation capacity (mg of S/g of sorbent)**	
	Fresh	**After 5th regeneration step**
Commercial ZnO	52.0 ± 2.0	11 ± 2.0
ZnO/SiO_2	54 ± 2.0	25 ± 2.0
Cu-ZnO/SiO_2 [Cu:Zn = 20:80]	81 ± 2.0	32 ± 2.0

Based on the results from UV-Vis DRS, EPR, XRD, and XPS analyses, specific conclusions can be made about the structure and electronic properties of ZnO/SiO_2 and $Cu_XZn_{100-X}O/SiO_2$ sorbents. The various 'unlikely' and 'possible' characteristics of sorbents are summarized in a schematic shown by Figure III.18 and Figure III.19 respectively.

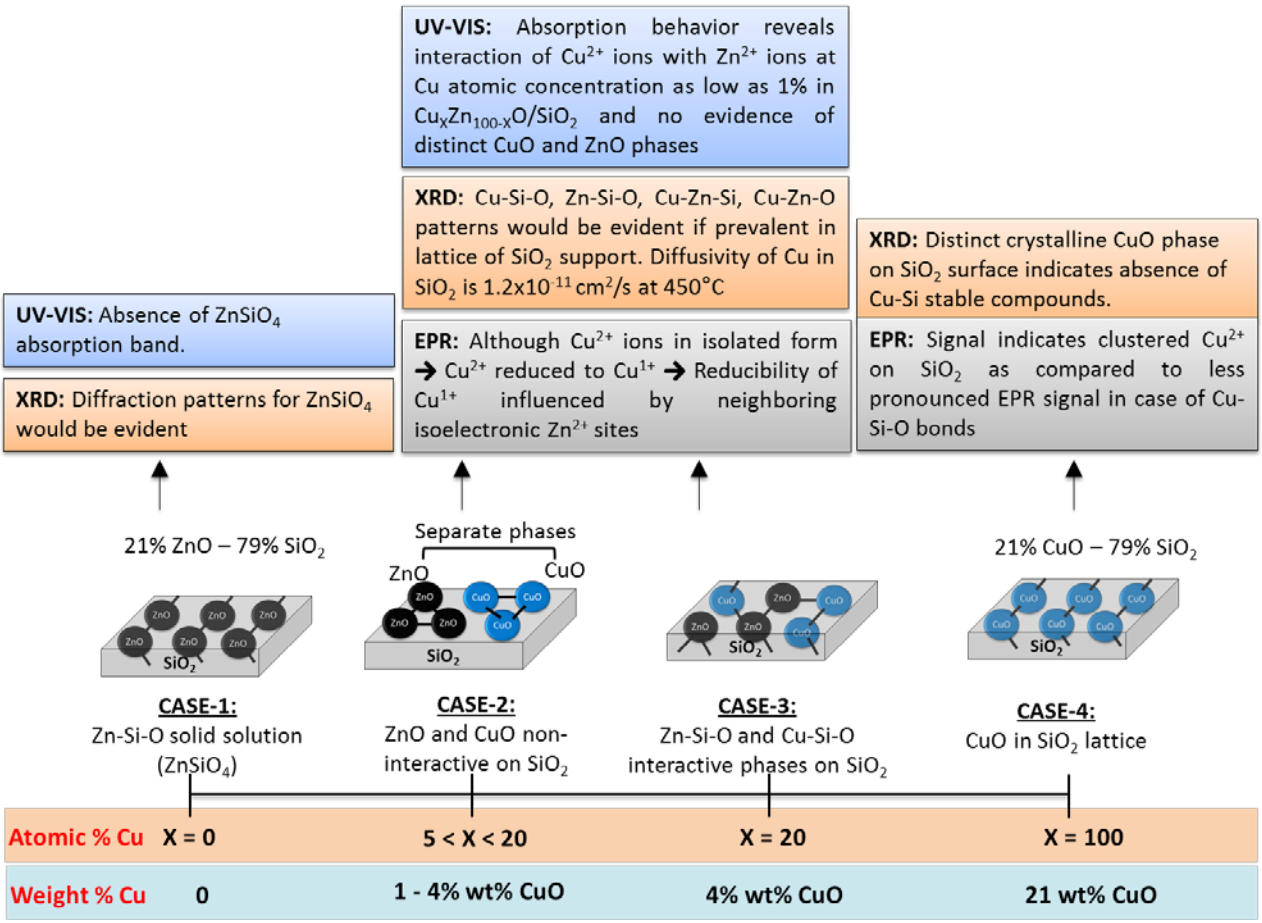

Figure XXVII Schematic representation of un-likely characteristics of ZnO/SiO_2 and

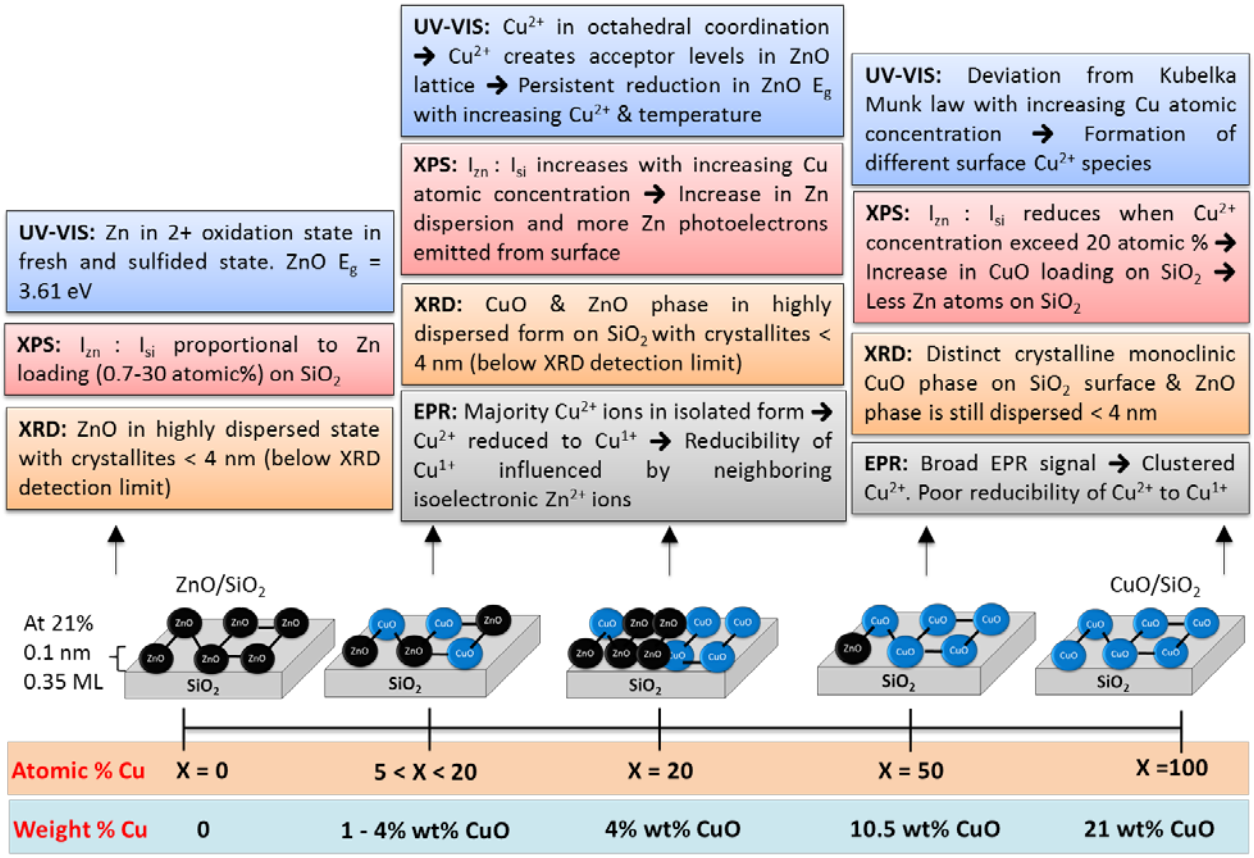

Figure XXVIII Schematic representation of possible characteristics of ZnO/SiO_2 and $Cu_XZn_{100-X}O/SiO_2$ sorbents

III.6. Conclusions

The effect of copper (II) oxide promotion on the optical properties of silica supported zinc oxide adsorbents active for H_2S adsorption at room temperature has been investigated by UV-Vis DRS, XPS and EPR spectroscopy. UV-vis DRS and EPR studies on calcined $Cu_XZn_{100-X}O/SiO_2$ adsorbents suggest that copper is present as Cu^{2+} in an octahedral coordination geometry with tetragonal distortions. A functional relationship exists between the CuO and ZnO highly dispersed phases and the Kubelka Munk absorbance intensity up to 20 mole% CuO loading. 20 % molar concentration of CuO is the critical loading after which $Cu_XZn_{100-X}O/SiO_2$ become increasing crystalline with the development of monoclinic CuO phase on the surface. This corresponds to the possibility that the Cu^{2+} ions populate defects in the dispersed ZnO phase supported on silica support up to this specific molar concentration. Enhanced H_2S adsorption capacity under mild conditions is a combination of the interaction of the CuO, number of defects or vacancies in the ZnO lattice, and the size of the CuO and ZnO crystallites. The H_2S adsorption capacity reduces as the samples become increasingly crystalline as seen from XRD patterns. The effective mass model for the ZnO crystallites in ZnO/SiO_2 and $Cu_XZn_{100-X}O/SiO_2$ adsorbents at 21% loading estimates that the ZnO size is much greater than the Bohr radius of ZnO (2.34 nm), thus indicating absence of any quantum size effects. In-situ EPR was performed for the first time to elucidate the reduction of Cu^{2+} ions to Cu^{+} ions during reactive adsorption of H_2S at room temperature.

IV. A fiber optics system for monitoring utilization of ZnO adsorbent beds during desulfurization for logistic fuel cell applications

Abstract

An in-situ fiber optic based technique for direct measurement of capacity utilization of ZnO adsorbent beds by monitoring bed color changes during desulfurization for fuel cell systems is presented. Adsorbents composed of bulk metal oxides (ZnO) and supported metal oxides (ZnO/SiO_2 and $Cu\text{-}ZnO/SiO_2$) for H_2S removal at 22 °C are examined. Adsorbent bed utilization at breakthrough is determined by the optical sensor as the maximum derivative of area under UV-Vis spectrum from 250-800 nm observed as a function of service time. Since the response time of the sensor due to bed color change is close to bed breakthrough time, a series of probes along the bed predicts utilization of the portion of bed prior to H_2S breakthrough. The efficacy of the optical sensor is evaluated as a function of inlet H_2S concentration, H_2S flow rate and desulfurization in presence of CO, CO_2 and moisture in feed. A 6mm optical probe is employed to measure utilization of a 3/16 inch ZnO extrudate bed for H_2S removal. It is envisioned that with the application of the optical sensor, desulfurization can be carried out at high adsorbent utilization and low operational costs during on-board miniaturized fuel processing for logistic fuel cell power systems.

IV.1. Introduction

Adsorptive desulfurization is a relatively low cost alternative compared to conventional hydro-desulfurization which demands stable catalyst performance, high H_2 partial pressures and elevated temperature. In a compact fuel cell system, depending on the sulfur tolerance of

reforming catalysts, partial oxidation catalysts and the anode side catalyst of fuel cells, desulfurization must be carried out either prior to the reformation step or after reformation (post-reformate desulfurization) and in some cases both locations. Prior to reformation, however, desulfurization is carried out to remove high molecular weight sulfur compounds such as Tetra-hydro Thiophene (THT), T-butyl Mercaptans (TBM) and Dimethyl Sulfide (DMS) etc. that are added as odorants to hydrocarbon fuels for leak detection purposes. However, when these fuels are reformed or gasified, the product (synthesis gas containing mixture of CO and H_2) often contains low molecular weight gaseous sulfur compounds such as H_2S and trace quantities of COS. For this purpose, a polishing bed is usually placed downstream of the reformer to remove any residual H_2S [6]. For this purpose, metal oxides adsorbents composed of ZnO, CuO, TiO_2, Al_2O_3 etc. are placed downstream of the reformer to serve as polishing beds and removal any residual H_2S. COS is commonly converted to H_2S via hydrolysis on pure oxides such as γ-Al_2O_3, TiO_2 [85] or mixed oxide catalysts like CeO_2-Al_2O_3 [141], TiO_2-ZrO_2 [78], Al_2O_3-ZrO_2 [81] etc. then removed by aforementioned adsorbents. Thus, post reformate desulfurization is commonly carried out to protect high value membrane electrode assemblies in fuel cells, especially in a PEM (Polymer Electrolyte Membrane) fuel cell power system.

In fuel cell systems, the desulfurizer unit experiences temperature variations ranging from ambient temperature to several hundred Celsius during cold startup or transient operations [9]. To overcome the limitation of gas phase mass transport and solid state diffusion resistance during H_2S removal at lower temperatures, ZnO may be deposited on porous supports [142-144]. Recent work in our laboratory involving ZnO dispersed on inert SiO_2 support prepared by incipient wetness impregnation showed enhanced H_2S adsorption capacity at 400 °C with regenerable performance of up to 10 cycles compared to bulk ZnO [45]. ZnO/SiO_2 can be

promoted by various transition metals during room temperature desulfurization. At a Zinc to transition metal molar ratio of 19:1, the promoted ZnO/SiO_2 demonstrated a sulfur saturation capacity of 0.213 $g_{sulfur} \cdot g_{ZnO}^{-1}$ (54% of theoretical value) at room temperature [9].

In-situ fiber optic spectroscopy provides a solution to this challenge. It is gaining attention in the field of heterogeneous catalysis [33, 108, 113, 128, 130, 145-148], continuous process analyses [149-153], batch process analyses [154, 155] and clinical applications [156, 157]. For example, a fiber optic based UV-Vis CCD spectrometer was employed for the determination of nickel breakthrough in an ion-exchange column [149]. The non-invasive and inert properties of the optical fibers make them attractive choices for studying chemical processes in-situ without disturbing the integrity of the process. The flexibility of fibers and stainless steel construction of the probe enables high temperature measurements in presence of corrosive gases (H_2S and COS) and moisture. The tip of the probe can be configured in a manner compatible with the plug flow conditions in packed beds. The desulfurization of various sulfur containing gas streams at high temperature is also carried out using metal oxide and zeolite based adsorbents. These adsorbents contain one or more metal oxide components that are optically active in the UV-Vis wavelength region and are known to undergo an apparent color change upon adsorption of sulfur compounds at high temperature. For example, during H_2S removal on $ZnFe_2O_4$ (Zinc Ferrite) adsorbent pellets in the temperature range of 300-500°C, a color change from orange, in fresh state to gray or black was observed [158]. Another study involving metal oxides supported on mesoporous silica, MeOx/SBA-15 (Me=Zn, Fe) during H_2S removal at 300°C exhibited a pale brass-yellow color appearance in the sulfided specimen enriched with FeS [159]. To our knowledge, in-situ reflectance spectroscopy via fiber optics has never been implemented to probe the electronic

effects occurring on the metal oxides during adsorptive desulfurization for logistic fuel cell applications.

In the current study, a fiber optic based UV-Vis diffuse reflectance spectroscopic system was implemented as an embedded sensor in the desulfurizer assembly to measure the utilization of adsorbent beds during H_2S removal at 22 °C for logistic fuel cell applications. The efficacy of the embedded fiber optic sensor is evaluated as a function of (i) H_2S concentration (ii) H_2S contact time (iii) Presence of CO, CO_2 and moisture in feed stream and (iv) H_2S adsorption on 3/16 inch extrudates using a 6mm optical probe.

IV.2. Experimental

IV.2.1 Preparation and characterization of Adsorbents

ZnO/SiO_2 and Cu-promoted ZnO/SiO_2 adsorbents are prepared via incipient wetness impregnation followed by drying and calcination in static air as described elsewhere [15, 46]. In short, metal nitrate (Zinc and Copper) solutions of desired molarity are prepared by dissolving metal salt in de-ionized water. The metal nitrate solutions are then impregnated on 100 μm SiO_2 support (Grace Division Inc., pore volume 1 cm^3g^{-1}, BET surface area 460 m^2g^{-1}) at room temperature. The impregnated samples are then dried overnight for 12h at 110 °C followed by calcination in air for 3h at 400 °C. Commercial ZnO is obtained from BASF (SG-901) in the form of 3/16 inch extrudates. These are used as extrudates as well as crushed and sieved into 100-200 μm. Nitrogen adsorption-desorption isotherms of adsorbents and SiO_2 support are generated at 77 K (-196 °C) on Autosorb-1C (Quantachrome Instruments). The samples are outgassed at 150 °C for 6h in vacuum (3×10^{-10} mm Hg) prior to analyses. BET surface area of samples is calculated using the Brunauer-Emmett-Teller (BET) equation. The average pore size

and pore-size distribution is obtained the adsorption curve of N_2 isotherm and calculated using Barrett-Joyner-Halenda (BJH) method.

IV.2.2. Desulfurization experiments

IV.2.2a. Fiber optic system

Adsorption experiments were conducted on a Cu-ZnO/SiO_2 adsorbent bed with the fiber optic probe in direct contact with adsorbent particles and simultaneous on-line GC analysis downstream of the bed. Utilization of adsorbent beds was determined by observing the sensor response and H_2S breakthrough curve. A schematic of the probe configuration for plug flow conditions is shown in Figure IV(a-b) depicts the comparison between a 1.5 mm probe and a 6 mm probe embedded at the bottom of packed beds. The 6mm probe was not suitable for monitoring the utilization of beds containing micron size adsorbent particles since it disturbs the integrity and uniformity of the bed as shown. Thus, the 1.5 mm probe embedded horizontally at the bottom of 0.1-2 mL packed beds containing <200 μ adsorbent particles was chosen for the remaining experiments in this study. If not mentioned otherwise, the dimensions of the packed bed (4 mm diameter × 25.4 mm length), reflectance probe (1.5 mm dia.) and adsorbent particle size (100-200 μm) were chosen to avoid gas flow channeling through the bed. An experiment was carried at same operating conditions using the 1.5 mm probe embedded in a bed of dimension (12 mm dia. × 25.4 mm length) used in earlier studies [6]. In-situ diffuse reflectance spectroscopy of adsorbents was carried out on an Avaspec-2048 spectrometer (Avantes Inc.) based on a symmetrical Czerny-Turner design with an optical bench and a focal length of 75 mm suitable for analysis in 245-800 nm wavelength range.

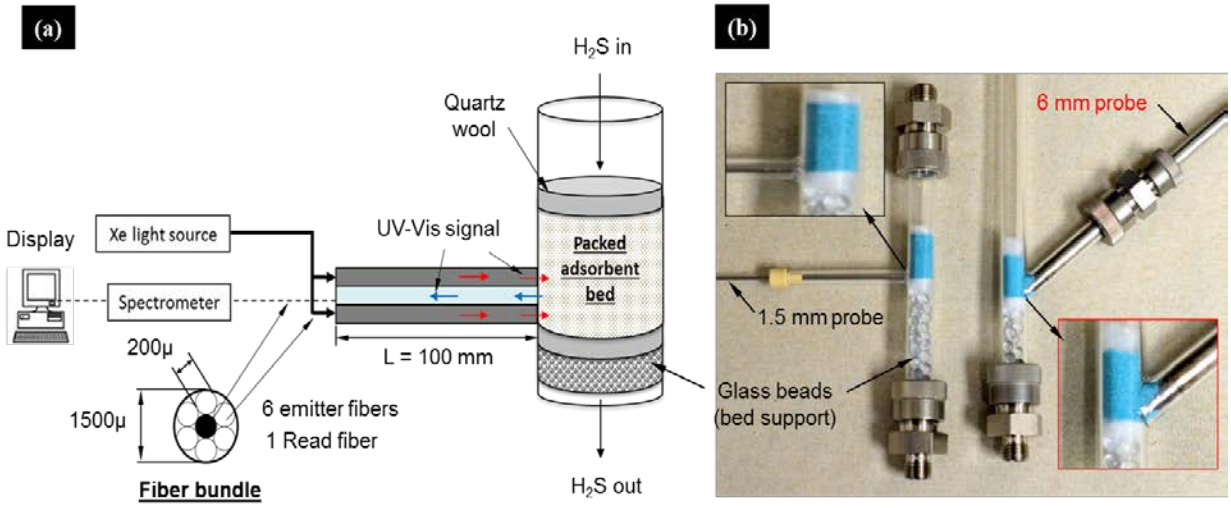

Figure XXIX (a) Schematic diagram of 1.5 mm optical probe, fiber bundle and direction of UV-vis light signal in H_2S breakthrough experiments using packed beds; (b) Comparative representation of packed adsorbent beds embedded with probes used in this study.

The spectrometer is equipped with a standard SMA (Sub Miniature version A) connector for incorporating the fiber optic cable. Diffusely reflected light from adsorbent particles in packed beds was received by the CCD detector array with a sensitivity of 5000 counts μW^{-1} per millisecond of integration time. A 12V DC USB powered interface between the spectrometer and spectrum analyzer (or computer) enabled data transfer speeds in the range of 14-31 milliseconds $scan^{-1}$ with an onboard sample averaging speed of 17 milliseconds $scan^{-1}$. The dimensions of the spectrometer used in this study were 175 mm (length) × 110 mm (height) × 44 mm (width) and weighed approximately 716 g. A stainless steel fiber optic reflectance probe (FCR-7UV200-2-1.5x100) with dimensions 1.5 mm (diameter) × 100 mm (length) specifically designed for powders was used. The fiber bundle consisted of six illumination or emitter fibers and one read fiber. The material for light guiding effect was Fluorine-doped SiO_2 with a numerical aperture of 0.22. UV-Vis light (245-800 nm) from a xenon pulsed light source (Avalight-Xe) was conveyed through emitter fibers directly onto the packed bed of particles. The

fibers are protected by a Kevlar reinforced PTFE (Polytetrafluoroethylene) jacket with 3.8 mm outer diameter PVC (Polyvinyl chloride) sleeves. The maximum operating temperature was 65°C. For experiments involving ZnO extrudate particles, a larger fiber optic probe (FCR-7UV200-2-45x140) of dimensions 6 mm (diameter) × 140 mm (length) containing the six emitter fibers and one read fiber was used. The minimum bend radius ranges from 20mm - 60mm depending on how long these fibers are subjected to bending. The maximum operating temperature in this case was 500 °C. In this case, the fibers are protected by Silicon inner tubes and a 5 mm outer diameter flexible chrome plated brass outer tubing for stress relief.

In this study, data was acquired in the reflectance mode because the percentage of diffusely reflected light is independent of the color of sample. H_2S adsorption experiments were also carried out when the spectrometer was operated in scope mode and absorbance mode. However, since these modes of operation are highly sensitive to degree of color change, they exhibit only a minor change signal response during H_2S adsorption on ZnO and ZnO/SiO_2 materials. The percentage of diffusely reflected light is given as,

$$\text{Diffusely reflected UV} - \text{Vis ligh}, \mathrm{R}(\%) = \frac{\text{sample}-\text{dark}}{\text{reference}-\text{dark}} \quad \dots\dots\dots\dots\dots\dots\dots\dots\dots\dots\dots\dots \text{(1)}$$

In Eq. (1), the term ‘sample’ indicates percent diffusely reflected light from adsorbent particles, ‘dark’ indicates percent reflectance with light source turned off and ‘reference’ indicates the reflectance of a white standard [160], in our case $BaSO_4$ (Puratronic, 99.9% Alfa Aesar) of 150 μm particle size. To obtain a desired signal-to-noise ratio of 200:1 essential for probing the spectral changes occurring on the adsorbent surface, the scan rate was set to 5s scan^{-1} with an integration time of 10 ms scan^{-1}. The time between the start of spectral data acquisition and GC injection was recorded to be less than three seconds during adsorption experiments. This time was considered to be time zero during analyses. It is important to mention, in experiments

throughout the study, UV-Vis light through the fiber optic probe did not cause any photo-induced effects on H_2S gas when passed through an empty quartz tube. Furthermore, the region of the bed probed by the optical sensor did not cause any change in the H_2S adsorption capacity due to UV-Vis light illumination. Spectral data was processed using Origin 2016 software.

IV.2.2b. H_2S breakthrough curves using on-line GC measurements

H_2S gas with desired concentration at inlet (C_0) was fed using mass flow controllers (Alicat Inc.). H_2S at outlet from adsorption experiments was collected every 2 minutes using an automated six-port gas sampling valve (Valco Instruments) of 250 μL sampling volume and injected onto a thermal conductivity detector (TCD) equipped with a packed column (Hayesep Q100) using H_2 carrier gas on a gas chromatograph (Varian CP 3800). The detection limit of the TCD is 200 ± 50 ppmv. Experiments throughout the study were designed to demonstrate a proof of concept rather than determine the detection limit of the sensor with regard to sulfur breakthrough. Depending on the application, detection of lower sulfur levels may be important, however, in this study, we show concentration in the exit at breakthrough only when H_2S is detected at outlet by the TCD. The experimental error in the breakthrough time (t_{BT}) and time to reach 50% saturation ($t_{1/2}$) was ±1 min and ±0.5 min respectively.

IV.3. Results and discussion

H_2S saturation capacities of bulk ZnO, 21% ZnO/SiO_2 and 21% Cu-ZnO/SiO_2 (Cu:Zn molar ratio = 20:80) adsorbents at room temperature (22 °C) are 19 $mgS \cdot g_{adsorbent}^{-1}$, 53 $mgS \cdot g_{adsorbent}^{-1}$ and 78 $mgS \cdot g_{adsorbent}^{-1}$ respectively [29].

IV.3.1. UV-Vis diffuse reflectance (R) spectroscopy of adsorbents

The electronic effects occurring on the surface of ZnO and Cu-ZnO adsorbents during H_2S adsorption can be probed using UV-Vis diffuse reflectance spectroscopy [23]. H_2S adsorption on ZnO and Cu-ZnO adsorbents can be treated as a chemical reaction between H_2S in gas phase and metal oxides (CuO and/or ZnO) in solid phase to form corresponding metal sulfides and moisture. The UV-Vis diffuse reflectance spectra of fresh and spent adsorbents after sulfidation with 20000 ppmv H_2S in H_2 at 22 °C are shown in Figure IV.2 (a-c).

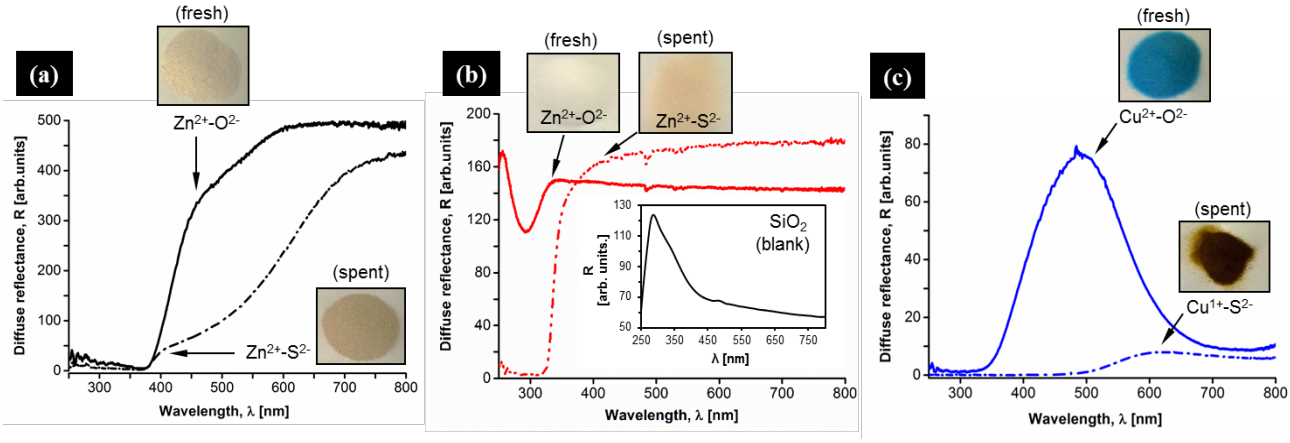

Figure XXX UV-vis diffuse reflectance spectrum of fresh and spent adsorbents after sulfidation with 20000 ppmv H_2S; (a) ZnO; (b) ZnO/SiO_2; (c) Cu-ZnO/SiO_2

At first, we examine the electronic effects during H_2S adsorption on ZnO and ZnO/SiO_2 adsorbents as follows,

$$Zn^{2+} - O^{2-} + H_2S \rightarrow Zn^{2+} - S^{2-} + H_2O \quad \text{..... (2)}$$

Eq. (2) is an oxygen to sulfur exchange reaction with no charge transfer since oxidation state of Zn is 2+ in ZnO as well as ZnS. ZnO in its pure crystalline form is excited around 380 nm by UV radiation [121]. The commercial ZnO used in this study is composed of 90% ZnO by weight and 10% by binders or stabilizers that are added to maintain structural integrity during high temperature (>300 °C) operation. These binders also impart a characteristic color to commercial

ZnO as shown in Figure IV (a). The spectrum of spent adsorbent indicates a slight change in the UV-region of spectrum since ZnS is excited in the same wavelength (380-400 nm) as ZnO [161]. This reduction in area under UV-Vis reflectance spectrum of bulk ZnO is accompanied by a color change from light brown to dark brown as shown in Figure IV (a). The UV-Vis spectrum of ZnO/SiO_2 shown in Figure IV (b) can be distinguished from that of bulk ZnO in terms of electronic structure dependent size effects such as quantum confinement effects [162], nano-dispersion [105] etc. The absorbance of ZnO/SiO_2 starting at 300 nm is heavily influenced by SiO_2 absorbance since SiO_2 is still present in majority (80 percent by weight) compared to ZnO that exists at 20 percent loading by weight on SiO_2 support at. This can be further understood by observing the full spectrum of SiO_2 blank as shown in Figure IV (b) – inset. The sharp peak around 250 nm is indicative of SiO_2 support [163]. The intensity of this peak reduces at higher ZnO loadings and suggests that ZnO may be dispersed not only in pores but also on the surface of SiO_2 support. The spectrum of spent adsorbent in Figure IV (b) shows the reduction of SiO_2 peak at 250 nm. However, at 22 °C, SiO_2 support offers practically negligible capacity. The disappearance of the peak can be due to a change in the composition of chemical species that exist on the surface as well as in the pores of SiO_2 support. In this case, the majority of surface and nanometer size pores of SiO_2 will be covered with sulfur that exist majorly as ZnS but also as H_2S dissolved in stoichiometric H_2O retained in the pores from the ZnO sulfidation reaction according to Equation (2). In the spectrum of spent adsorbent, the shift in the ZnO peak at 325 nm to higher wavelength (~340 nm) is due to ZnS/SiO_2 formation [164]. The resultant color change is from white (fresh state) to beige (spent state) along with an apparent increase in reflectance as shown in Figure IV (b). Similar behavior is observed at higher ZnO loadings and

suggests that color change is independent of ZnO content on ZnO/SiO_2, thus enabling the technique to analyze samples with ZnO loadings as low as 1% by weight (data not shown).

The spectrum of Cu-ZnO/SiO_2 is shown in Figure IV (c). The reflectance maxima observed around 500-550 nm is assigned to the Cu-O-Cu bridged structures [134, 165]. However, the ZnO reflectance edge is attenuated in the spectrum of Cu-ZnO/SiO_2 at a Cu:Zn molar ratio of 20:80. This phenomenon was observed in Cu-Zn mixed oxides [126] prepared by thermal decomposition of co-precipitated Cu and Zn nitrate solutions and was assigned to the presence of electron traps in the ZnO band gap as a result of Cu^{+2} ion dissolved in the ZnO matrix. The reflectance spectrum with maximum intensity around 500 nm is reduced to a flat plateau upon H_2S adsorption. The resultant color change is from bluish green to pale green. XPS and ESR characterization experiments reported earlier [29] suggest that a reduction of Cu^{2+} to Cu^{1+} ion took place during H_2S adsorption on Cu-ZnO/SiO_2 at room temperature. Cu-ZnO/SiO_2 sorbents contain Cu^{2+} and Zn^{2+} ions, thus although Zn exists in an oxidation state of 2+ in sulfided adsorbents, sulfidation of Cu-ZnO/SiO_2 adsorbents involves a chemical reaction with charge transfer. This can be conceptualized based on previous findings [23, 105, 166],

$$2Cu^{2+} + S^{2-} \rightarrow 2Cu^{1+} + S^{2-} \quad \text{..... (3)}$$

The total percentage of diffusely reflected light from surface of adsorbents depends on the degree of darkness of samples. For example, white substances are perfect reflectors of light (UV and visible) when compared to black substances. ZnO/SiO_2 adsorbents containing dispersed ZnO show only a minor color change upon H_2S adsorption when compared to blank SiO_2 support. The introduction of Cu promoter ion induces a blue color to Cu-ZnO/SiO_2 adsorbents. The diffuse reflectance in Cu-ZnO/SiO_2 adsorbents decreases with increasing mole percent Copper as seen in section III. The percent reflectance in the plot is taken as the value at which maximum peak

intensity is observed which corresponds to a wavelength of 380 nm in case of ZnO/SiO_2 and 500 nm for $Cu\text{-}ZnO/SiO_2$ samples. The CuO concentration on the surface will be higher than ZnO with increasing mole percent Cu as seen from the SEM-EDX analysis of these adsorbents [40]. Furthermore, there is no apparent difference in color between fresh and spent adsorbents when X > 40 in $Cu_X\text{-}Zn_{100-X}O/SiO_2$.

IV.3.2. Optical technique for monitoring capacity utilization of adsorbent beds

Contaminant breakthrough curves are used to obtain the important parameters such as breakthrough time, saturation time or time to reach 50% breakthrough. Upon reaching the breakthrough time, the flow of contaminant may be stopped or diverted to a fresh bed. This timely operation is important for fuel cells that allow low sulfur threshold concentrations (0.1 ppmv and less) downstream of the desulfurizer. It is impractical to switch flows after sulfur breakthrough has occurred and thus most of the adsorbent must be utilized at breakthrough point. The utilization of adsorbents at breakthrough can be understood by observing the sharpness of breakthrough curve. In this study, we have defined bed utilization at breakthrough using the $t_{1/2}$ concept (or time at which $C/C_0 = 0.5$) as shown in Figure IV.3 (a). According to McCabe [102], the fraction of bed capacity unutilized at breakthrough can be rearranged and expressed as a function of breakthrough time and saturation time as follows,

$$\frac{LUB}{L}[\%] = \left(1 - \frac{t_{BT}}{t_{1/2}}\right) \times 100 \quad \text{..... (4)}$$

Where, LUB is an equivalent length of unused bed, which is held constant and L is total length of adsorbent bed. Let the bed capacity unutilized from breakthrough curves be denoted as U_{tBT}.

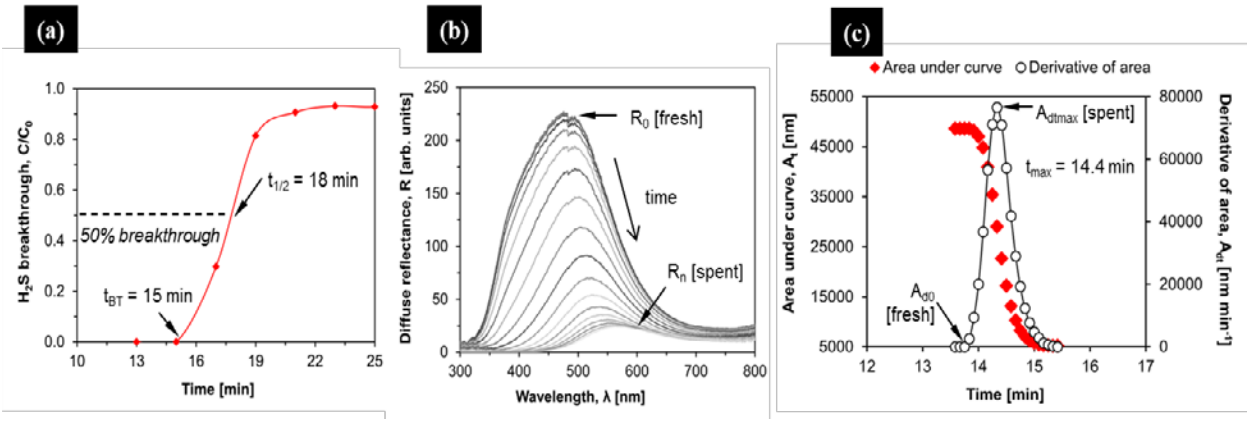

Figure XXXI (a) H_2S breakthrough curve from on-line GC analysis when adsorbent tested with 100 mLmin^{-1} of 5000 ppmv H_2S at 22°C; (b) in-situ UV-vis diffuse reflectance spectra of Cu-ZnO/SiO_2 collected at a scan rate of 12 scansmin^{-1}; (c) integrated area under each spectrum and corresponding first order time derivative of area.

Adsorption capacity is usually calculated by numerical integration of the area under breakthrough curve starting from breakthrough time to saturation time. For a fixed bed containing Cu-ZnO/SiO_2 adsorbent, it is known from section 3.1 that the intensity of the diffuse reflectance spectrum reduces to a constant plateau upon H_2S saturation. The combined in-situ spectroscopic response of ZnO and CuO is recorded and the area under each spectrum (Figure IV.3 (b)) every 0.083 minutes (or 5 seconds) by numerical integration between 250-800 nm of wavelength range is calculated. In Figure IV.3 (b), R_0 and R_n denote percent UV-Vis diffuse reflectance of fresh and spent adsorbent respectively. Thus, the area under each spectrum is given as

$$A_t\left[\mathrm{nm}\right] = \int_{250\,\mathrm{nm}}^{800\,\mathrm{nm}} R_t \; d\lambda \; \ldots\ldots\ldots\ldots\ldots\ldots\ldots\ldots\ldots\ldots\ldots\ldots\ldots\ldots\ldots\ldots\ldots\ldots\ldots\ldots\ldots\ldots\ldots\ldots.. \;(5)$$

Where, subscript t denotes time on stream (or service time). A plot of Eq. (5) versus time is highlighted by data points in red shown in Figure IV.3 (c). The reduction in area (A_t) is due to

the reduction in percentage of UV-Vis light reflected from the surface of adsorbent and is similar to the conversion profile of a solid reactant in a gas-solid reaction, such as H_2S adsorption involving a metal oxide.

In order to determine the precise time at which the portion of the adsorbent bed probed by the optical sensor is utilized at breakthrough, mathematical treatment of in-situ spectral data is necessary. It is important to note that the UV-Vis light conveyed via fiber optic from a pulsed Xenon light source is similar in phenomenon to experiments involving pulsed Xe injections into a process. For example, the output profile of pulsed Xe injections into a carbon molecular sieve column was described by an exponential Gaussian distribution profile [167]. A Gaussian or Lorentzian distribution profile versus time shows a point of maximum intensity. This point can be treated as the time at which there is a sudden change in the behavior of the probed specimen in a process. In the current study, the rate of change of integrated area under the reflectance spectrum (A_t) can be observed for elucidating the time at which sudden change in probed surface of the adsorbent. Thus, the absolute time derivative of numerical values of integrated area (A_{dt}) is calculated as follows,

$$A_{dt}\,[\mathrm{nm\ min^{-1}}] = \left|\frac{d}{dt}\left(A_t\right)\right| \quad \text{..... (6)}$$

Where, subscripts t and d denote time and first order derivative respectively. A_{d0} indicates first order time derivative area under spectrum at t=0 min or fresh adsorbent. As sulfidation proceeds, A_t values decrease with time. The corresponding A_{dt} values increase up to maximum point which coincides with the midpoint of the A_t versus time curve. As in the case of $t_{1/2}$ that occurs at $C/C_0 = 0.5$ on breakthrough curve, the t_{max} occurs at point at which $A_t/A_0 = 0.5$. The plot of A_{dt} in Eq. (6) versus time as shown in Figure IV.3 (c) indicates a maximum value A_{dtmax} corresponding to

the time t_{max}. This point indicates the portion of the bed probed by the optical sensor is spent. Beyond time, t_{max}, the A_{dtmax} values decrease until a constant value indicating completely saturated adsorbent surface. Depending on the probe location, the t_{max} value can then be compared to the breakthrough time and $t_{1/2}$ values which are obtained from breakthrough curve. Since t_{max} also represents the breakthrough of portion of the bed between the top of the bed and the location of the probe t_{BT} in Eq. (4) can be replaced with t_{max} when probe is placed at the bottom of the bed. Thus, at H_2S breakthrough point the bed capacity un-utilized from the optical sensor is given as,

$$U_{t\,max}[\%] = 100 \times \left(1 - \frac{t_{max}}{t_{1/2}}\right) \quad \text{..... (7)}$$

Eq. (7) describes an optical technique for determining the degree of adsorbent bed utilized at breakthrough. In a similar way, the technique may be extended to measuring utilization of ZnO and ZnO/SiO_2 adsorbent beds during H_2S removal by processing in-situ diffuse reflectance data of these materials respectively.

IV.3.3. Effect of H_2S concentration at inlet

In this section, the effect of inlet H_2S concentration is investigated at 22 °C. Adsorption experiments are conducted on a bed containing 0.22 g of Cu-ZnO/SiO_2 using inlet H_2S concentrations of 2500 ppmv, 5000 ppmv, 10000 ppmv and 15000 ppmv at a constant bed length of 2.54 cm and an inlet flowrate of 100 mL min^{-1}. The experimental results are shown in Figure IV.4 (a-d). With increasing H_2S concentration, the treated moles of H_2S per unit time per unit bed length will be higher. According to the mass transfer theory of adsorption, the adsorption wave front will be narrow as compared to the bed length and as a result, the time to reach saturation will be shorter at higher inlet concentration. The $t_{1/2}$ and breakthrough time values

from breakthrough curves decrease with an increase in H_2S concentration. A similar trend is observed with t_{max} values. However, since the fiber optic probe is located at least a few microns above the final layer of randomly distributed adsorbent particles t_{max} values are obtained before bed breakthrough time.

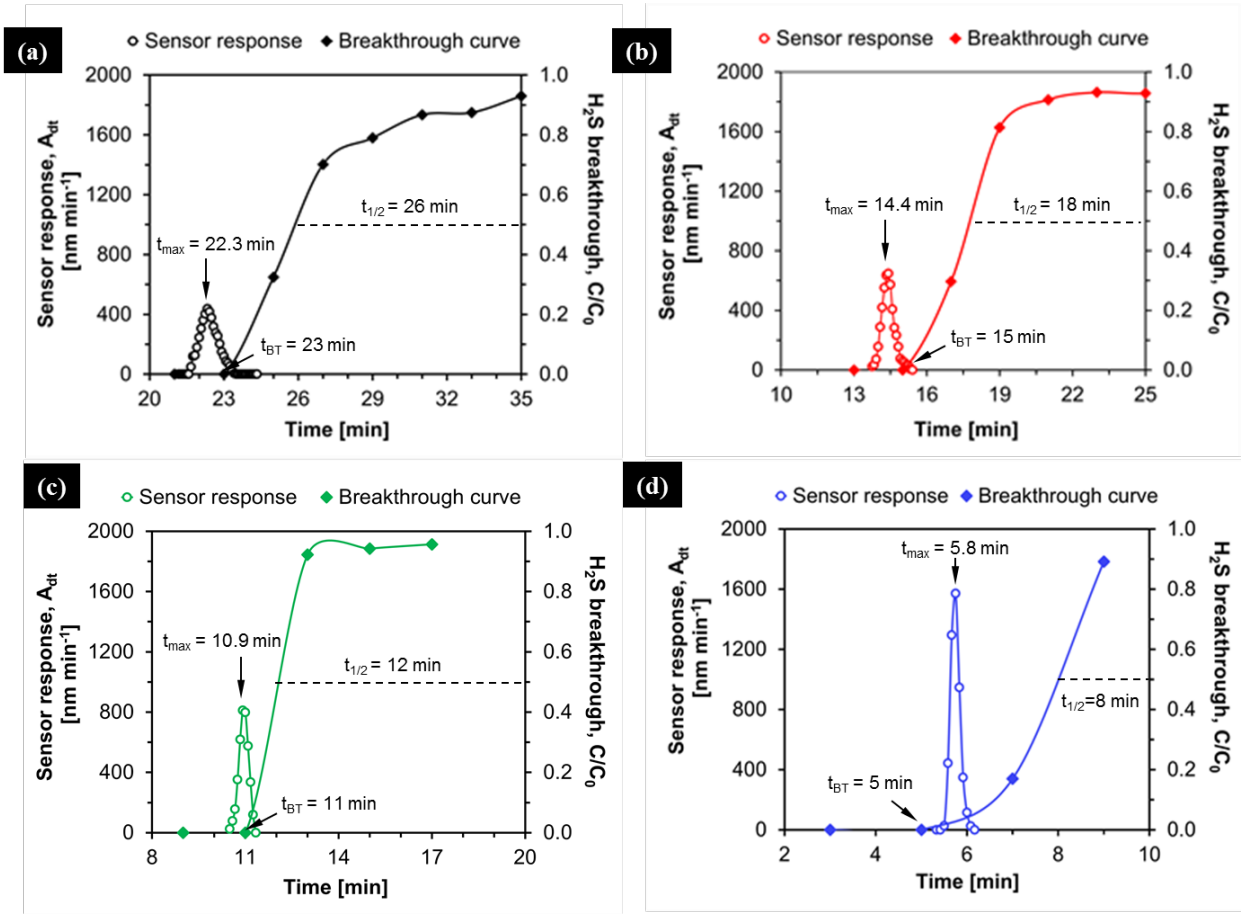

Figure XXXII Optical sensor response and H_2S breakthrough curves of Cu-ZnO/SiO_2 adsorbent when tested as a function of H_2S concentration at constant inlet flow of 100 mLmin^{-1}; (a) 2500 ppmv H_2S; (b) 5000 ppmv H_2S; (c) 10000 ppmv H_2S; (d) 15000 ppmv H_2S.

Indeed, the purpose of the optical sensor is to detect the saturation of adsorbent beds before breakthrough occurs and serve to protect downstream processes from exposure to sulfur contaminants. Although, no apparent difference in color of the adsorbent is observed at different

H_2S concentrations, the intensity of the UV-Vis signal varied proportionately with the H_2S concentration in the following order 2500 ppmv < 5000 ppmv < 10000 ppmv < 15000 ppmv H_2S. Although the sensitivity of the optical technique depends on the rate of change of surface chemical reactions on the ZnO based adsorbents, the global adsorption kinetics that is influenced by bulk properties of the adsorbents such as porosity, surface area etc. is expected to be slow at lower H_2S concentration [168]. Thus, at a fixed scan rate of 12 scans per min, the first order time derivative of area plot as shown by Figure IV.4 appeared sharper at higher H_2S concentrations and most of the adsorbent is utilized at breakthrough.

IV.3.4. Effect of H_2S flowrate at inlet

At high operating feed flowrates, the adsorbent is charged with higher H_2S molar rate per unit bed cross section per unit time and as a result breakthrough occurs earlier. At low flowrates, H_2S adsorption can become external mass controlled [168] leading to breakthrough curves with a high slope and slow saturation of contaminant. In this section, the performance of the embedded sensor is examined as a function of H_2S flowrate (residence time) through the Cu-ZnO/SiO_2 adsorbent bed at 22 °C. The flowrate is varied from10 mL min^{-1} to 100 mL min^{-1} at constant bed length of 2.54 cm and inlet concentration of 20000 H_2S. Figure IV.5 (b-d) shows that most of the adsorbent is utilized at breakthrough when H_2S flowrate is varied from 25 mL min^{-1} to 100 mL min^{-1}. The intensity of the first order time derivative of area plot did not vary proportionately with H_2S flowrate. At a fixed scan rate, the values of t_{max} are closer to $t_{1/2}$ values at higher flowrate because the portion of the adsorbent bed where the probe is located has less capacity at high H_2S flux. In the next set of experiments the residence time in the bed is varied by reducing the length of a 2.54 cm bed by 50 percent of its value to 1.3 cm and lastly by doubling the bed

length to 5.1 cm while keeping total inlet flowrate and H_2S concentration constant. For example for a bed length of 5.1 cm, the t_{max}, breakthrough time and $t_{1/2}$ values obtained are 11.3 min, 12 min and 11 min respectively. For the test with bed length of 1.3 cm, which is above the critical bed length (or the minimum bed length to avoid instantaneous breakthrough) a sharp breakthrough curve is obtained (data not shown) and the t_{max}, bed breakthrough time and $t_{1/2}$ values are 2.8 min, 4 min and 3 min respectively.

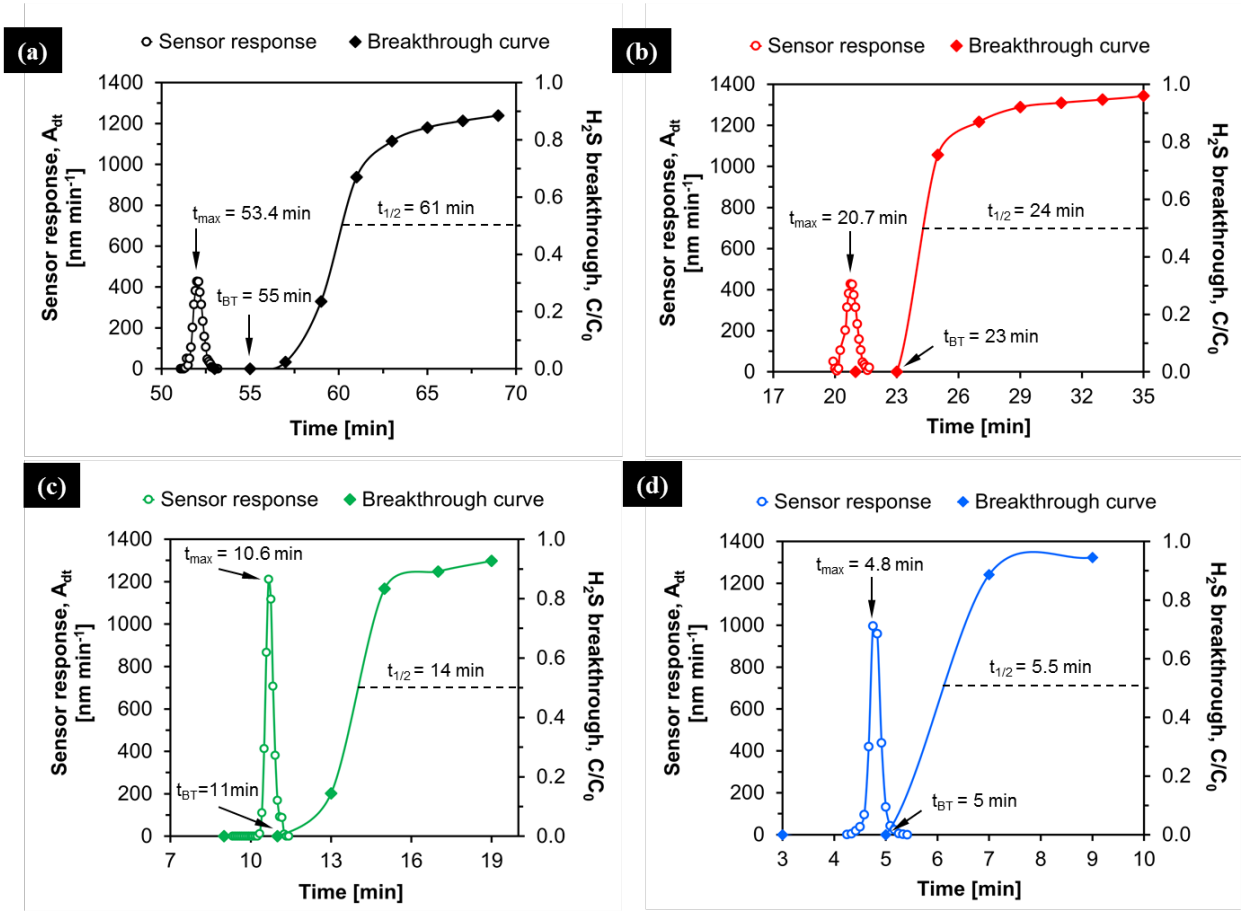

Figure XXXIII Optical sensor response and H_2S breakthrough curves of Cu-ZnO/SiO_2 adsorbent when tested with 20000 ppmv H_2S as a function of inlet flowrate; (a) 10 mLmin^{-1}; (b) 25 mLmin^{-1}; (c) 50 mLmin^{-1}; (d) 100 mLmin^{-1}.

The embedded fiber optic sensor can thus be used for measuring utilization of thin catalyst (or

adsorbent) beds, for example during high throughput testing in micro-reactors [169]. The optical response from the sensor when breakthrough occurs depends on the probe position since the probe measures sites on illuminated layers of the adsorbent bed that are becoming saturated with H_2S. In a theoretical situation, if the probe is placed at the bottom most layer of packed bed, a change in optical response will be observed only after H_2S has started to exit the bed. To avoid this undesirable situation, it is important to place the optical probe by a measure of at least one bed length above the critical bed length (a bed length thin enough to cause instantaneous H_2S breakthrough upon start of any experiment).

IV.3.5. Bed capacity unutilized as a function of probe position

In practical systems, prior testing of variables such as length of adsorbent bed, contaminant concentration at inlet and flowrate at inlet are usually carried out to optimize (minimize) the unutilized portion of an adsorbent bed. However, during the desulfurization of feed stocks with variable H_2S concentrations or flowrates that are commonly unknown to the end user in practical systems, the optical sensor can be used for continuous in-situ monitoring of adsorbent beds. This is because adsorption proceeds via color change due to electronic interactions between s-containing compounds and metal oxides regardless of the operating variables in a desulfurization unit. Under dynamic adsorption process conditions, these interactions correlate to capacity depletion of beds composed of metal oxides. The sensor, however, does not directly measure the amount of bed capacity remaining instead it detects the saturation of the illuminated portion of the bed in terms of a local t_{max} value. This t_{max} value can then be translated into amount of capacity remaining or unutilized depending on its position along the bed length. The application of the optical sensor will significantly reduce the cost and need for prior testing of any operating

variables that is typically conducted to minimize unutilized portion of the bed. In section 3.2.1 and 3.2.2, a linear variation of t_{max}, breakthrough time and $t_{1/2}$ values with H_2S concentrations and contact time through the bed is observed. The physical properties of Cu-ZnO/SiO_2 and ZnO/SiO_2 adsorbents such as pore volume and pore size as well as the physicochemical properties such as bed voidage and bed density are close in values as enlisted in Table IV.1.

Table IV.1. Physical characterization of adsorbents and adsorbent bed properties.

Physical property	Bulk oxides			Supported oxide	Supported binary oxides
	SiO_2	ZnO		ZnO/SiO_2	$Cu\text{-}ZnO/SiO_2$
		Particles	Extrudates		
BET surface area [m^2g^{-1}]	460.0	35.4	35.4	261.0	257.0
Average pore size [nm]	3.80	-	-	4.23	4.00
Average pore volume [cm^3g^{-1}]	0.90	0.04	0.04	0.55	0.51
Weight % loading [L]	-	90.0	90.0	21.0	21.0 (CuO+ZnO)
Bulk density [g mL^{-1}]	2.65	5.61	5.61	-	-
Packed bed density [g mL^{-1}]	0.50	1.15	1.05	0.68	0.67
Packed bed voidage [-][§]	0.31	0.70	0.77	0.41	0.45
H_2S saturation capacity [mgS $g_{adsorbent}^{-1}$][‡]	-	19	19	53	78

§ Calculated as per formulae shown in supplementary information

‡ Data reproduced from Tatarchuk et al [37]

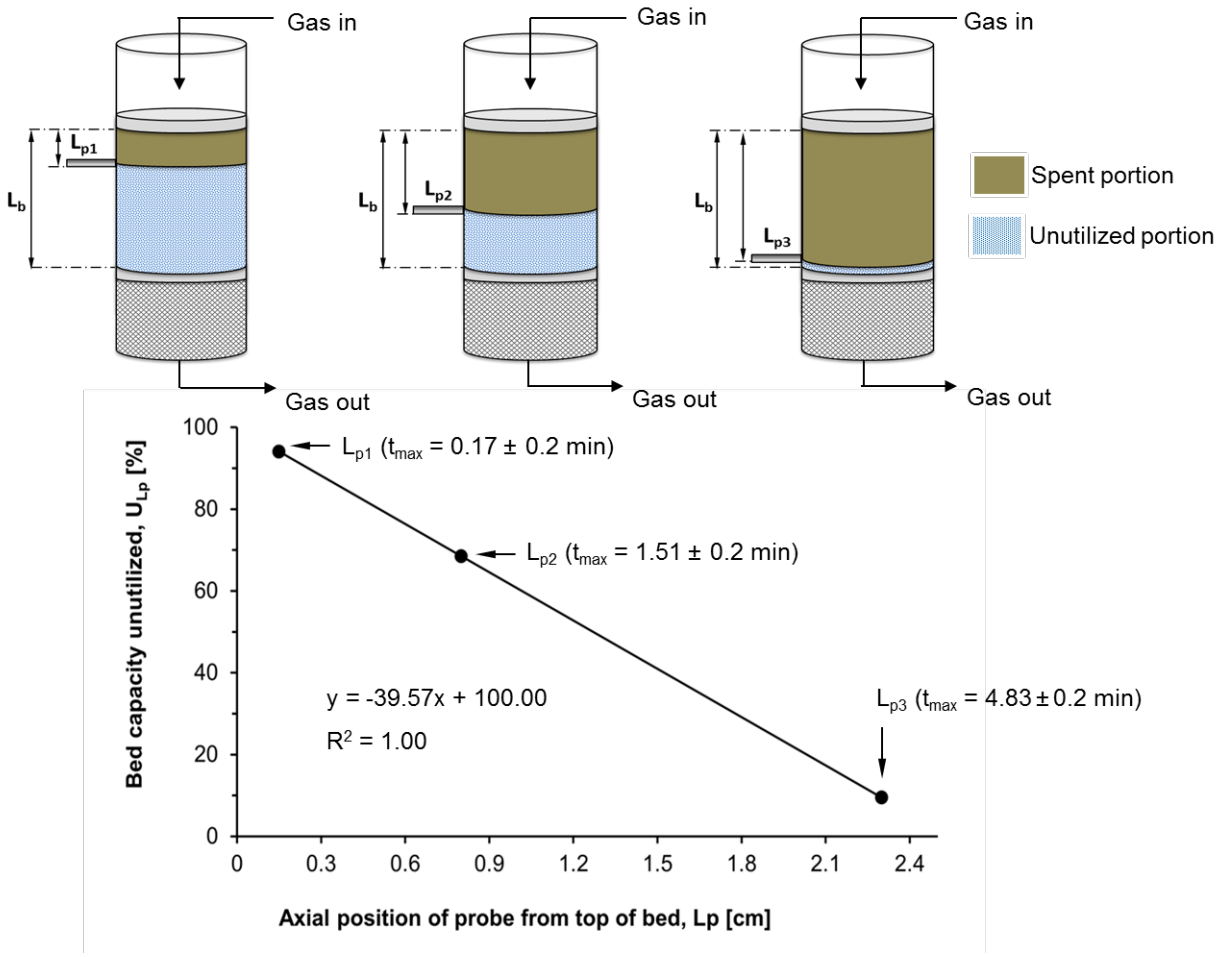

Figure XXXIV (a) Probe positions along axial length of adsorbent bed; (b) unutilized bed capacity predicted by the optical sensor.

However, these properties differ from those of bulk ZnO adsorbent of same particle size. Nevertheless, H_2S adsorption is known to occur on the surface as well as in the pores of bulk ZnO, ZnO/SiO_2 and $Cu\text{-}ZnO/SiO_2$ adsorbents. Since the diameter of the fiber optic probe is 1.5 cm which is almost 100 order of magnitude higher than the average diameter of a single porous adsorbent particle of 0.015 cm diameter (assuming spherical particles) and pore size (4.1 ± 0.1 nm), the optical response from samples will be composed of reflected light from the surface as well as the pores of these adsorbent particles. Thus, assuming (i) absence of any channeling or dispersion effects through the bed (ii) uniform composition of adsorbent bed and (iii) compact

plug flow conditions in the bed, the propagation of the color wave front with time can provide a visual indication of the impending sulfur breakthrough through the bed. However, in absence of any visible color change, the optical sensor can be used to monitor the extent of bed capacity unused. In the next set of experiments, the percent bed capacity unutilized or bed life is determined by placing the fiber optic probe at various points (L_p) along the axial length of a 2.54 cm bed tested with 90 $mLmin^{-1}$ of 20000 ppmv H_2S as shown in Figure IV.6 (a). Figure IV.6 (b) shows a linear dependence of t_{max} values with distance of probe measured from top most layer of the packed bed. For each experiment, a $t_{1/2}$ value of 5.5 (± 0.01) min is obtained from the H_2S breakthrough curve. For example, when the probe is located at probe position L_{p1} (or 0.2 cm) from top, the optical sensor provides a t_{max} value of 0.17 min since it captures the color wave front that propagates through the initial part of the Cu-ZnO/SiO_2 adsorbent bed. The bed utilization measured at this point is approximately 3% using Eq. (7) since only 0.2 cm of bed is saturated with H_2S. Similarly, t_{max} values are obtained by embedding the probe at axial locations of probe L_{p2} (0.8 cm) and L_{p3} (2.3 cm) respectively. A plot of the percent bed capacity unutilized versus t_{max} values results in a linear correlation with slope and intercept values of 39.55 and 103.39 respectively. If t_{max} is substituted with probe distance from top and $t_{1/2}$ values substituted with total bed length (L_b), the plot of bed capacity unutilized (UL_{tmax}) yields a slope and intercept value of 39.37 and 100 respectively as shown in Figure IV.6. These values are almost equal to values calculated using t_{max} and $t_{1/2}$ and Eq. (7) can be rewritten as follows,

$$UL_{tmax}\,[\%] = 100 \times \left(1 - \frac{L_p}{L_b}\right) \quad \text{..... (8)}$$

For example, when the 1.5 mm fiber optic probe is positioned at approximately 0.3cm below the top most layer of the packed bed containing 100-200 μ particles, the bed capacity unused or fresh

will be approximately 88% of total capacity according to Eq. (8). Thus, operating in a regime under which the above mentioned assumptions are valid, the percent bed capacity unutilized can be determined by the optical sensor regardless of variations in H_2S concentration and contact time. In this way, it is possible to incorporate one or more probes along the length of the packed bed to simultaneously measure bed utilization at breakthrough and initiate adsorbent replacement or regeneration operation in a timely manner.

IV.3.6. Presence of moisture, CO and CO_2 in feed

The stainless steel construction of the probe and inert nature of the optical fibers enables the study of H_2S adsorption in presence of feed containing mixture of CO, CO_2 and H_2O at 22 °C. Presence of carbon monoxide, carbon dioxide and moisture can have strong influence on the desulfurization performance of adsorbents due to carbonyl sulfide (COS) formation, water gas shift reaction and reduction in H_2S capacity as result of competitive adsorption in presence of moisture etc. For example, COS formation is observed at temperature of 200 °C or higher on Cu-ZnO/SiO_2 [170] and ZnO/SiO_2 adsorbents [47] while desulfurization of H_2S stream containing CO and CO_2. However at 22 °C, no COS is detected at the outlet and a CO mole balance across the bed indicates absence of water gas shift reaction. The effects of CO, CO_2 and H_2O is studied individually by adding 30 vol% CO, 30 vol% CO_2 and 0.5 vol% H_2O in a feed stream containing 0.5% H_2S. Table IV.2 shows that the adsorbent utilization is on average 84 ± 4% determined by the optical sensor and H_2S breakthrough curves. However, the adsorbent utilization reduced to 79% when 5000 ppmv H_2O is added in the feed containing H_2S, CO and CO_2. Thus, in order to investigate the effect of moisture content, a series of H_2S adsorption experiments are conducted separately in absence of CO or CO_2 in feed.

Table IV.2. Adsorbent utilization determined by optical sensor and from H_2S breakthrough curves for different feed compositions.

Feed composition	$t_{1/2}$ [min]	t_{BT} [min]	t_{max} [min]	Utilization at H_2S breakthrough† [%]	Utilization at bed color change‡ [%]
0.5% H_2S	30.0 ± 0.5	25.0 ± 1.0	23.88 ± 0.2	83.3 ± 2.0	80.1 ± 1.3
0.5% + 30% CO	32.0 ± 0.5	27.0 ± 1.0	26.48 ± 0.2	84.3 ± 2.0	82.8 ± 1.3
0.5%+ 30% CO_2	26.0 ± 0.5	23.0 ± 1.0	22.97 ± 0.2	88.5 ± 2.0	88.5 ± 1.3
0.5%+ 30% CO + 30% CO_2	29.0 ± 0.5	25.0 ± 1.0	23.94 ± 0.2	86.2 ± 2.0	82.7 ± 1.3
0.5%+ 30% CO + 30% CO_2 + 0.5% H_2O	49.0 ± 0.5	39.0 ± 1.0	38.89 ± 0.2	79.6 ± 2.0	79.4 ± 1.3

† Bed utilization from breakthrough curves, $1\text{-}U_{tBT}$ [%] = 100 × [$t_{BT}/t_{1/2}$]

‡ Bed utilization determined by optical sensor, $1\text{-}U_{tmax}$ [%] = 100 × [$t_{max}/t_{1/2}$]

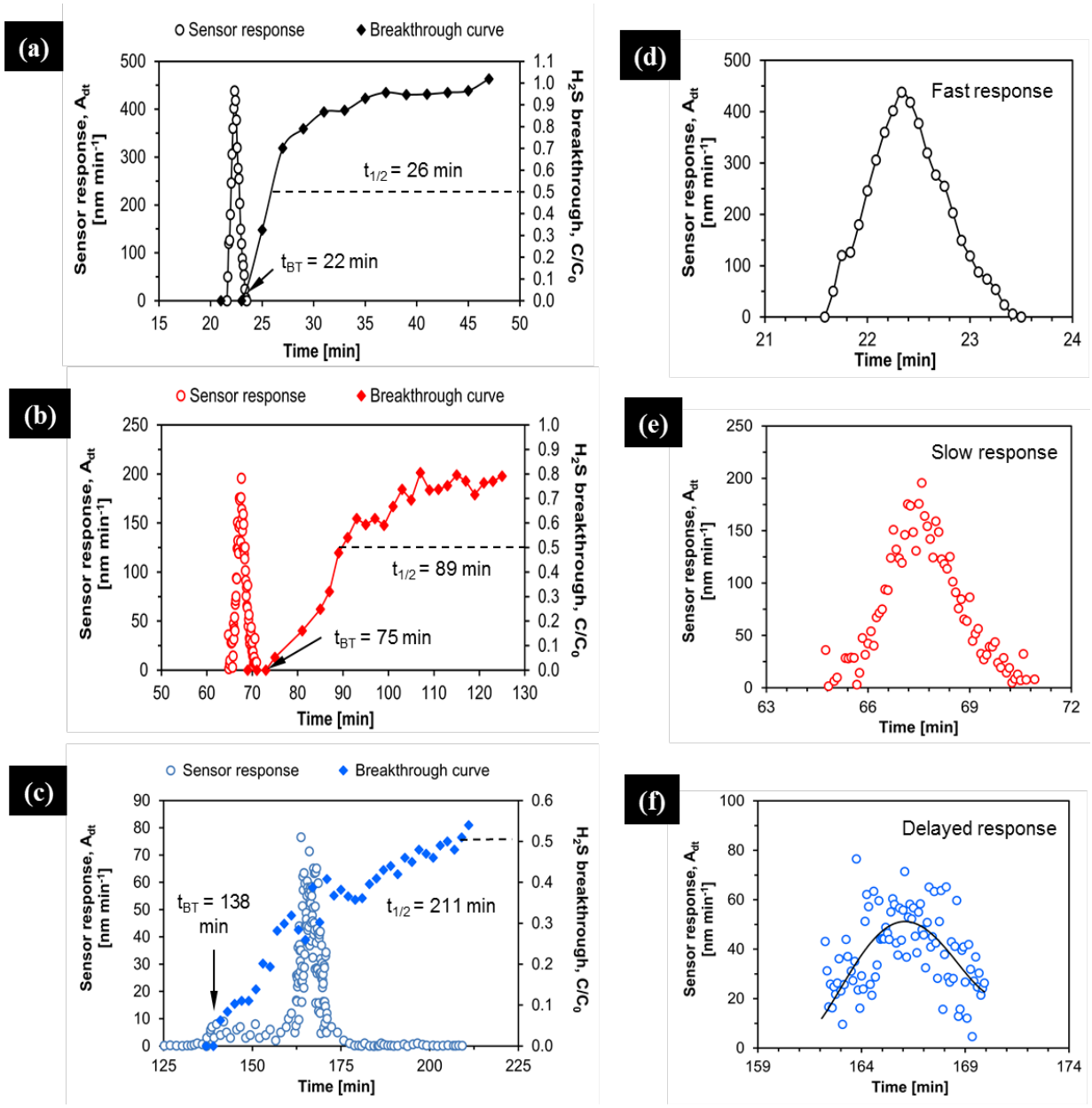

Figure XXXV Optical sensor response (right) and H_2S breakthrough curves (left) of Cu-ZnO/SiO_2 adsorbent when tested as a function of moisture content; 0 ppmv H_2O [Fig. (a) and Fig. (d)]; 5000 ppmv H_2O [Fig. (b) and Fig. (e)]; 10000 ppmv H_2O [Fig. (c) and Fig. (f)].

Based on the vapor pressure of H_2O at 22 °C, the moisture content at the inlet is varied by adjusting the flowrate of high purity H_2 through a saturator containing de-ionized water. H_2S breakthrough curves of Cu-ZnO/SiO_2 adsorbent when tested at different moisture contents are

shown in Figure IV.7. The steps involved during H_2S adsorption in presence of moisture can be known to proceed as follows: (i) H_2S and H_2O from bulk feed are adsorbed on surface of adsorbent (ii) The adsorbed H_2O forms a liquid film inside the 4 nm pores of adsorbent due to capillary condensation (iii) H_2S is readily soluble in water [4 g H_2S L_{H2O}^{-1}] at 25 °C [171] (iv) The dissolved H_2S then dissociates into HS^- and H^+ ions followed by reaction of HS^- species with Cu-ZnO/SiO_2 to form corresponding metal sulfides. A similar observation is reported earlier [172] while studying the effect of moisture, CO_2 and O_2 on H_2S breakthrough behavior of activated carbon adsorbent at 30 °C. When the surface and pores of the adsorbent are saturated with the adsorbed H_2S and H_2S dissolved in H_2O, additional H_2S flow through bed will result in breakthrough. Under dry feed conditions, the breakthrough curves reflect the mass transfer governed reaction between H_2S and metal oxides. However, broader breakthrough curves shown in Figure IV.7 (b-c) obtained during adsorption in presence of moisture means H_2O decelerates the reaction between H_2S and metal oxides. In real applications, maintaining high utilization of adsorbent beds is as important as implementing an optical sensor to monitor bed utilization. Presence of moisture resulted in low adsorbent utilization as seen from the broad breakthrough curves with a prolonged period to reach H_2S saturation point. During these tests, however, the in-situ reflectance spectrum remained unaffected since additional peaks due to formation of intermediates or side reactions is not observed. The optical response obtained from signal processing of in-situ reflectance data, however, appears degraded when examined separately as shown in Figure IV.7 (e-f). When the time scale on the optical response plot shown by Figure IV.7 (d-f) is matched to the time scale of the breakthrough curve, a peak maximum can still be identified in case of 0.5% and 1% moisture content. Although, a delayed response is obtained in case of 1% moisture content, it is evident that the onset of response begins to occur at

approximately the same time as the bed breakthrough time as shown in Figure IV.7 (c). It is a matter of perspective of how problematic the presence of moisture truly is because behaviour of the sensor as seen from optical response is similar in behaviour to the adsorbent breakthrough curves in presence of moisture. In these experiments, it assumed however that UV-Vis irradiation between 250-800 nm via the fiber optic probe did not cause any photo-dissociation of water on the surface of adsorbent, even though photo-dissociation of liquid water is reported at a wavelength of less than 200 nm [173].

IV.3.7. Monitoring utilization of ZnO extrudate beds

During high throughput operation, the size of the packed bed and adsorbent particles are typically higher to minimize pressure drop. In this section, the efficacy of the embedded sensor to measure utilization of large size adsorbent particles during H_2S removal is examined by using ZnO extrudates, SG-901 (BASF). The average dimensions of these adsorbent particles are 1 cm (length) by 0.41 cm (diameter). Properties of extrudates are enlisted in Table IV.1. For this test, however, the 1.5 mm diameter probe cannot accurately determine bed utilization upon H_2S breakthrough due to its relatively small sampling volume compared to the extrudates. For this purpose, a 6 mm diameter stainless steel fiber optic probe suited for millimeter size particles is used. Figure IV.8 (a) shows a stainless steel tubular reactor construction of nominal dimensions 22 mm dia. × 550 mm length with a welded 1 inch hollow stainless side arm equipped with an ultra torr fitting with a gas tight O-ring seal to secure the probe. This type of fitting enabled optimal sensor orientation along the radial geometry of the reactor. The probe is positioned at the bottom of the bed of ZnO extrudates (weight = 15 g, bed volume = 14.3 mL).

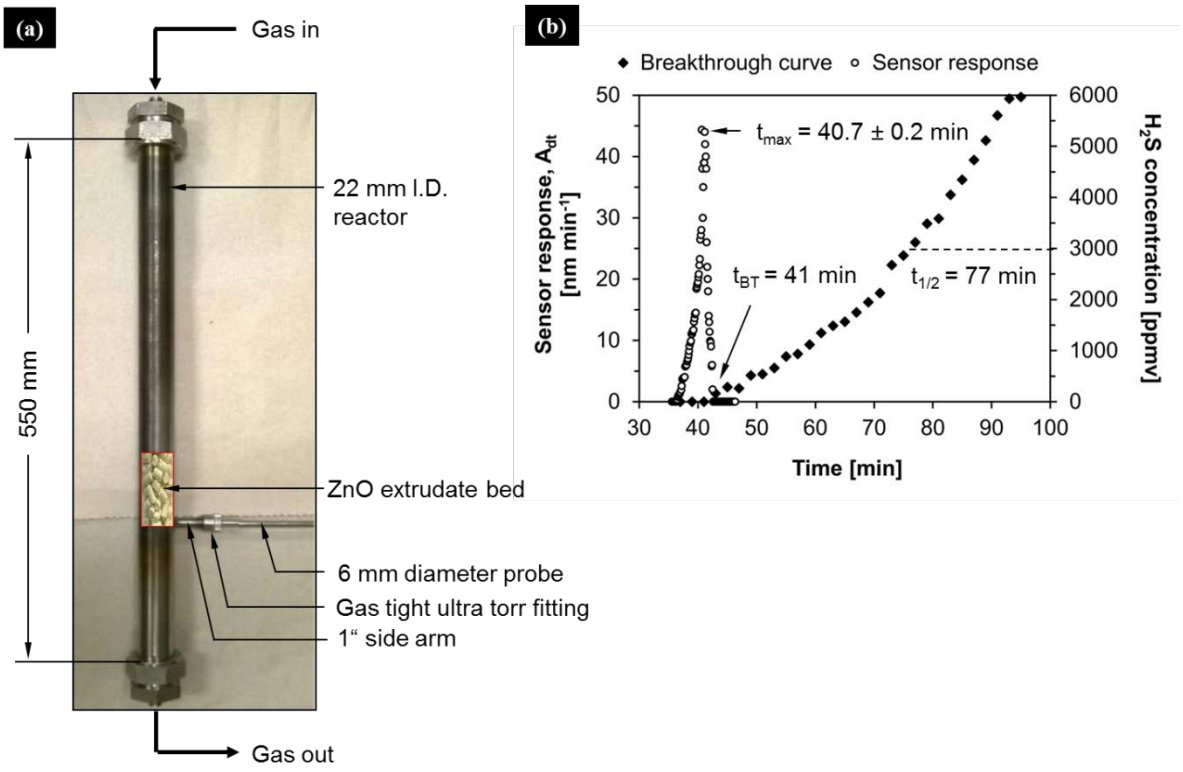

Figure XXXVI (a) Configuration of a 6 mm diameter fiber optic probe in a 22 mm diameter stainless steel reactor containing ZnO extrudates; (b) Optical sensor response and H_2S breakthrough curve.

A feed stream containing 6000 ppmv H_2S is passed over adsorbent bed at 22 °C at 250 mLmin^{-1}. The same signal processing method is followed as discussed in section 3.2 and the outlet H_2S concentration is measured using an on-line GC TCD. Figure IV.8 (b) shows the optical sensor response and H_2S breakthrough curve of extrudates. The in-situ UV-Vis diffuse reflectance spectrum of ZnO extrudates obtained from spectral measurements using the 6 mm probe is the same as the spectrum for 100-200 μ bulk ZnO particles measured by the 1.5 mm probe. In this case, the H_2S breakthrough time is 41 min and a t_{max} value is 40.7 ± 0.3 min obtained. However, the $t_{1/2}$ value is 77 min suggesting an adsorbent utilization of only 53%. The low utilization of extrudate beds as seen from broad H_2S breakthrough curves is attributed to the severe diffusion

resistance of H_2S through the ZnO lattice [46]. This effect will potentially be worse at lower temperatures.

IV.4 Conclusions

A fast sensing technique using fiber optic based UV-Vis diffuse reflectance spectroscopy was developed to accurately measure utilization of packed beds containing metal oxide adsorbents during H_2S removal at room temperature. The area under UV-Vis diffuse reflectance spectrum either decreased or increased upon interaction with H_2S depending upon the light reflecting behavior of fresh and spent adsorbents. During H_2S adsorption, a sharp response with maxima, t_{max} was obtained when the first order derivative of integrated area under in-situ reflectance spectra from 250-800 nm was plotted as a function of service time and compared to the time to reach 50% saturation or breakthrough time of adsorbents. The accuracy of the technique was examined at varying H_2S concentrations and H_2S residence time across the adsorbent bed. The experimental uncertainty in terms of standard error in t_{max} measurements was ± 0.2 min. In the current study, presence of 30 vol% CO or CO_2 in the feed did not impact the efficacy of the technique to measure the adsorbent utilization during H_2S adsorption. However, presence of 0.5-1 vol% moisture in the feed resulted in slow saturation of H_2S with a broad breakthrough curve and corresponding slow and delayed optical response. The capacity depletion of a 15 mL packed bed 3/16 inch ZnO extrudates during H_2S adsorption was monitored using a 6 mm fiber optic probe. Adsorbent bed utilization determined from in-situ optical measurements over wide range of operating parameters is expected to provide significant savings in cost of adsorbent materials and avoid the need for over design of adsorption units during compact and small volume desulfurization operation.

V. Desulfurization Behaviour of ZnO/SiO_2 and Cu Promoted ZnO/SiO_2 Sorbents during H_2S Removal from Model Reformates

Abstract

Carbonyl Sulfide (COS) formation during post-reformer desulfurization is an undesired side reaction between residual H_2S and CO/CO_2 from outlets of Steam Methane Reformer, Oxidative Methane Reforming and Water Gas Shift reactors. COS is known to poison downstream fuel processor catalysts and equipment. The goal of this work is to assess the promotional effect of Cu dopant in Cu-ZnO/SiO_2 sorbents in terms of a COS formation characteristics as a function Cu:Zn molar ratio, moisture and temperature at constant H_2S partial pressure in a simulated reformate. In the current investigation, COS formation was examined in the temperature range of ambient (22°C) to 400°C on ZnO/SiO_2 (21% ZnO loading) and Cu-ZnO/SiO_2 (Cu:Zn Molar Ratio = 20:80 and total oxide loading CuO + ZnO = 21% by weight) sorbents during desulfurization of the simulated stream containing 30%CO, 30% CO_2, 0.6% H_2S and Balance H_2. Homogeneous gas phase reaction occurred between H_2S and CO/CO_2 in the gaseous feed stream operated at 400°C and higher. However, no COS was detected at the outlet when the feed was operating at <100°C. At temperature of 200°C and higher COS formation and subsequent breakthrough occurred on both sorbents. COS concentration formed at saturation was lower in case of Cu-ZnO/SiO_2 sorbent as compared to ZnO/SiO_2. Considering significant H_2 concentration in the feed stream, the lower COS concentration obtained in case of Cu-ZnO/SiO_2 is due to the catalytic hydrogenation of COS (>200°C) on Cu_2S, formed by reduction with H_2S on spent Cu-ZnO/SiO_2. Experiments were carried out with 5000 ppm moisture (H_2S:H_2O ratio ~

1) in feed. Results indicate much lower values of COS concentration at saturation observed on both sorbents. Moisture had a COS inhibition effect most likely due to hydrolysis of COS since ZnS is known to be a catalyst.

V.1. Introduction

ZnO/SiO_2 sorbent is highly selective for H_2S removal for wide temperature desulfurization operation [9, 29, 47] compared to commercial bulk ZnO. Furthermore, Cu- promoted ZnO/SiO_2 (21% ZnO loading and Cu:Zn molar ratio = 5:95) shows 45% increase in H_2S selective adsorption as compared to un-promoted ZnO/SiO_2 with nearly 90% ZnO utilization and regenerability over multiple cycles. For broader applications, ZnO based sorbents need to maintain capacity in presence of other species such as $COS/CO/CO_2/H_2O$. Carbonyl Sulfide formation occurred in one or multiple ways depending on the temperature, equilibrium conditions, moisture content and extent of sorbent utilization (ZnS formation) at breakthrough and at saturation. Carbonyl Sulfide (COS) formation during post-reformer desulfurization is an undesired side reaction between residual H_2S and CO/CO_2 from outlets of Steam Methane Reformers ($CH_4 + H_2O = CO + 3H_2$), Oxidative Methane Reformers ($CH_4 + 1/2O_2 = CO + 2H_2$) and Water Gas Shift ($CO + H_2O = CO_2 + H_2$) reactors. COS is known to poison downstream fuel processor catalysts and equipment. In our previous investigation [47], we have observed COS formation characteristics during desulfurization of a reformate stream at 400°C on ZnO/SiO_2 (17% ZnO loading). The goal of this work is to assess the promotional effect of Cu dopant in Cu-ZnO/SiO_2 sorbents in terms of COS formation characteristics as a function Cu:Zn molar ratio, moisture and temperature at constant H_2S partial pressure in a simulated reformate. In the current investigation, COS formation was examined in the temperature range of 22°C (ambient) to

400°C on ZnO/SiO_2 (21% ZnO loading) and Cu-ZnO/SiO_2 (Cu:Zn Molar Ratio = 5:95 and total oxide loading CuO + ZnO = 21% by weight) sorbents during desulfurization of a stream containing 30%CO, 30% CO_2, 0.6% H_2S and Balance H_2. Homogeneous gas phase reaction occurred between H_2S and CO/CO_2 in the feed stream operated at 400°C and higher. However, no COS was detected at the outlet when the feed was <100°C. At temperature of 200°C and higher COS formation and subsequent breakthrough occurred on both sorbents. Regardless of temperature, COS formation levels were lower in case of Cu-ZnO/SiO_2 sorbent as compared to ZnO/SiO_2. The lower COS concentration detected in the case of Cu-ZnO/SiO_2 was attributed to the catalytic hydrogenation of COS (at 200°C and higher) on Cu_2S (formed by reduction with H_2S on spent Cu-ZnO/SiO_2). When experiments were carried out with 5000 ppm moisture present (H_2S:H_2O ratio ~ 1) in the feed, results indicate much lower values of COS concentration at saturation observed on both sorbents. Moisture had a COS inhibition effect most likely due to hydrolysis of COS (in this case, ZnS is known to be a catalyst)

V.2. Experimental

V.2.1 Sorbent Preparation

ZnO/SiO_2 with 21% ZnO loading was prepared by incipient wetness impregnation method (Dry impregnation) using Zinc nitrate salt solution of appropriate concentration on SiO_2 support (100-200 microns, pore volume of 1 cc/g, BET surface area of 300 m^2/g supplied by Grace Davison). In a similar fashion, Cu-ZnO/SiO_2 was prepared using Copper nitrate solution and co-impregnated on SiO_2 support along with the Zinc nitrate solution. The ZnO loading in the Cu-ZnO/SiO_2 was maintained at 21 weight percent. The molar ratio of Cu:Zn was 5:95. A detailed description of sorbent synthesis is available in previous investigations [9, 29]. The impregnated

support was dried overnight (12 hr) at ambient temperature and calcined in static air at 380 °C for 3 h in a box muffle furnace (Thermo Scientific Inc.)

V.2.2. Sulfur Detection and Breakthrough Analysis

Sulfur concentration was monitored on a Varian CP 3800 Gas Chromatograph (GC) equipped with a Thermal Conductivity Detector (TCD). The chromatographic column employed for the purpose was an Alltech (Part# 16197) on board packed column of length 8 feet, inner diameter of 0.125 inches and thickness of 0.085 inches (Grace Co) and packing of Hayesep Q 80/100. The maximum operating temperature of the column was 275 ^{0}C. The outlet gases from the packed column were injected into the GC at equal time intervals of 3 minutes with the help of an automatic 6-port-sampling-valve of sampling loop volume of 250 µL. The entire sampling system was connected by 1/8" tubing and the pressure drop across the system was negligible at the experimental conditions.

V.2.3. Lab-scale Desulfurization Operation

Adsorption experiments were carried out in a lab-scale reactor setup consisting of a quartz tube reactor followed by a moisture trap consisting of P_2O_5, tubular furnace (Applied Test System Inc.), temperature controller and an on-line GC equipped with a TCD. Weight of the sorbent was kept constant at 0.5 g corresponding to a reactor volume of 1 cm^3. A simulated reformate feed stream consisting of 30% CO, 30% CO_2, 0.6% H_2S/H_2 and Balance H_2 was generated by mixing Ultra High Purity $CO/CO_2/H_2$ respectively using Mass Flow Controllers. Unless otherwise mentioned, 0.6% H_2S/H_2 was generated from a 2% H_2S/H_2 mixture from gas cylinder. All gases cylinders were supplied by Airgas South Inc. The total flow rate of reformate feed stream was

100 cm^3/min STP corresponding to a face velocity of 2 cm/sec and a gas hourly space velocity of 3800 h^{-1}. For tests in presence of moisture, 0.4% H_2O was fed to the reactor by flowing UHP H_2 through a bubbler maintained at 22°C. The percentage of moisture corresponds to the vapour pressure of water at 22 °C.

V.3. Results and Discussion

V.3.1 Reformate desulfurization at 22°C

In this system, reformate feed stream is admitted to sorbent ZnO/SiO_2 and $Cu\text{-}ZnO/SiO_2$ maintained 22°C (Ambient) reactor temperature. In $Cu\text{-}ZnO/SiO_2$ sorbent, samples with various Cu:Zn molar ratios were examined for their H_2S and COS breakthrough characteristics. Cu addition to ZnO/SiO_2 sorbents results in faster kinetics.

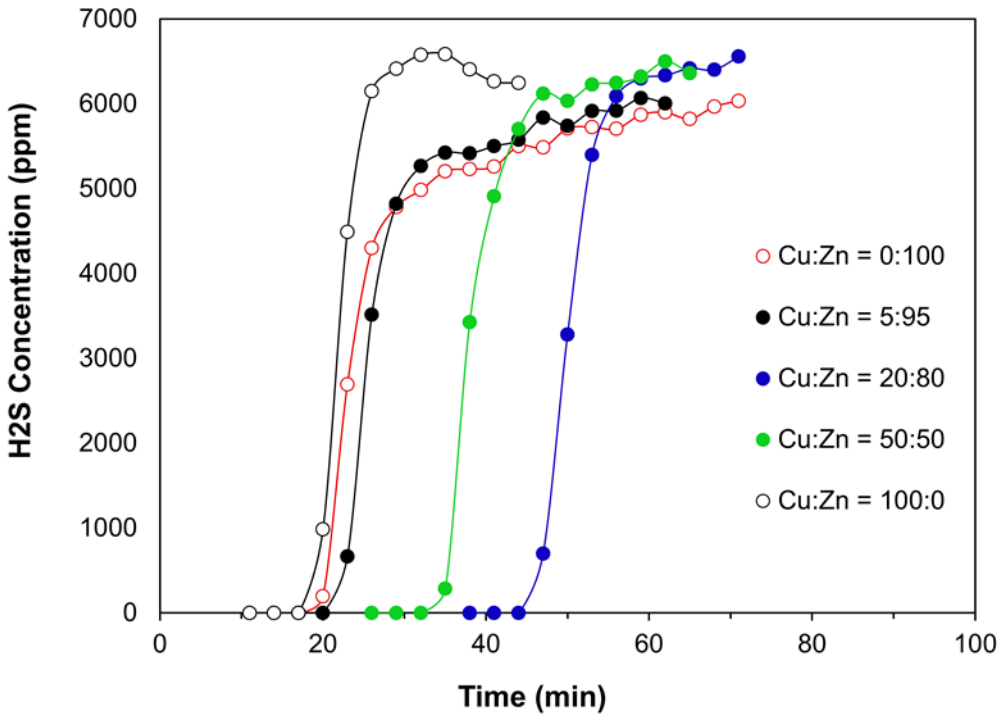

Figure XXXVII H_2S Breakthrough Characteristics on ZnO/SiO_2 and $Cu\text{-}ZnO/SiO_2$ sorbents at 22°C

This is evident since H_2S saturation time is reached faster in all Cu-containing sorbents. It takes longer time for the sorbent to reach saturation in case of ZnO/SiO_2. Another interesting observation is that the saturation time becomes shorter with increasing Cu content. This is also shown in Figure V.1**.** The optimal Cu:Zn ratio in the Cu-ZnO/SiO_2 sorbent is 20:80. A Cu concentration beyond this molar concentration results in a reduction in the H_2S breakthrough and saturation capacity. In the case of pure CuO dispersed on SiO_2 (Cu:Zn = 100:0), the capacity is lowest compared to the Cu-ZnO binary oxide sorbents regardless of the Cu:Zn molar ratio. COS formation was not observed on the sorbents when desulfurization was carried at ambient temperature in presence of $H_2/CO/CO_2$ and the sorbents showed similar H_2S breakthrough characteristics in absence of $H_2/CO/CO_2$.

V.3.2. Reformate desulfurization on ZnO/SiO_2 as a function of temperature

In this part, the desulfurization characteristics of ZnO/SiO_2 (21 weight % ZnO loading) sorbent will be examined as a function of desulfurization temperature in absence of any moisture in the feed stream. From Figure V.2 (a), it can be seen that H_2S breakthrough capacity increases with increasing temperature since temperature has a strong influence on the H_2S (gas) solid (ZnO/SiO_2) mass transfer rate as evidenced in previous investigation[45]. However, the temperature has an effect on the homogeneous and heterogeneous formation of COS. Temperature has a greater influence on the COS formation than H_2S breakthrough on the sorbents. Although the H_2S breakthrough time follows the order: 100°C << 200°C << 400°C, COS breakthrough time for ZnO/SiO_2 is in the following order: 200°C << 100°C << 400°C.

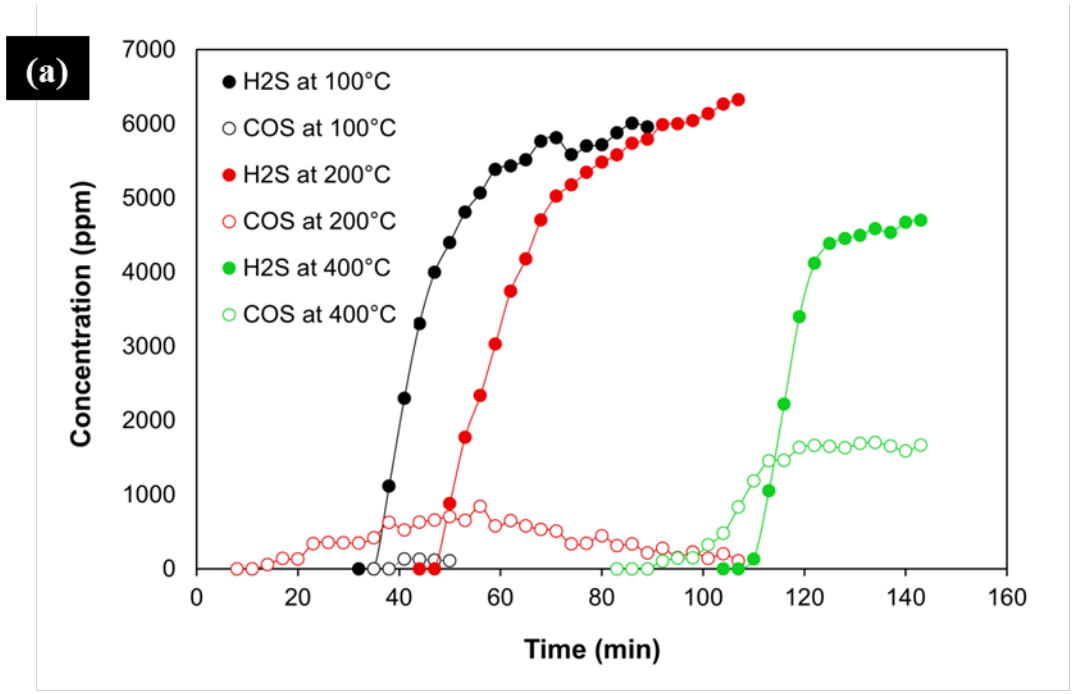

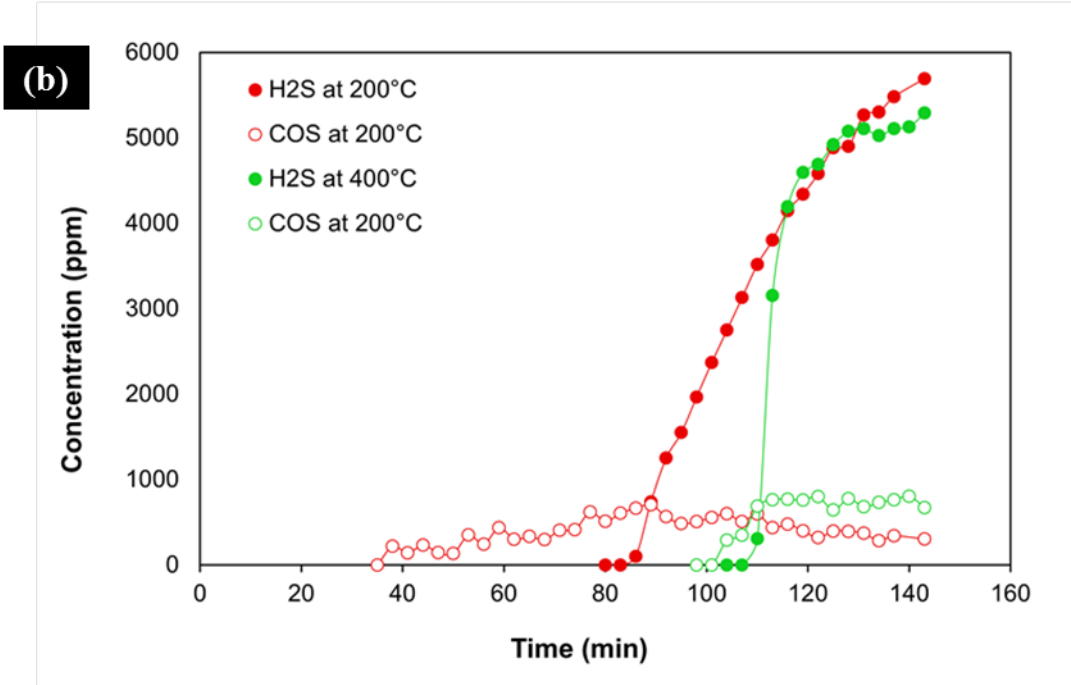

Figure XXXVIII H_2S and COS breakthrough characteristics on ZnO/SiO_2 as a function of temperature (a) No moisture (b) 4000 ppmv moisture in feed

At 400°C, the COS formation level stabilizes at approximately 1700 ppmv and H_2S concentration at saturation at 4900 ppmv which is lower than the inlet H_2S concentration (6000 ppmv). This shows that H_2S is consumed in reaction involving COS formation. In this part Figure V.2 (b), H_2O was added to the feed stream to observe the effect on the COS and H_2S breakthrough characteristics of ZnO/SiO_2 sorbent. Clearly, the COS formation levels were lower as compared to the levels formed in absence of moisture. At 200°C, an increase in the H_2S breakthrough time is caused in presence of moisture. Moisture or steam acts as an oxidizing agent. For this reason, it is also used as a calcination agent similar to oxygen since it helps to maintain the metal oxidation state. In our case, ZnO or CuO acts as active components for H_2S adsorption and they are present in an oxidation state of +2 on SiO_2 support after calcination and decomposition from their nitrate precursors. On the one hand, presence of moisture can be beneficial in the overall desulfurization process by maintaining oxidation state of oxide, higher moisture levels can degrade the kinetics of interaction of ZnO and H_2S and cause a reduction in the breakthrough capacity[47]. Moisture also caused a reduction in the COS formation levels at 200°C and 400°C.

V.3.3. Reformate desulfurization on Cu-ZnO/SiO_2 as a function of temperature

The COS formation levels are much lower in case of Cu-ZnO/SiO_2 (Cu:Zn = 20:80) regardless of the desulfurization temperature as shown in Figure V.3 (a-b). In a hydrogen rich stream, such as in our case consisting of approximately 40% H_2, H_2S tend to reduce CuO according to the following reaction which is thermodynamically highly favourable at ambient conditions.

$2CuO + H_2S + H_2 \rightarrow Cu_2S + 2H_2O$ ……. $\Delta G_{298K} = -253.8$ kJ/mol

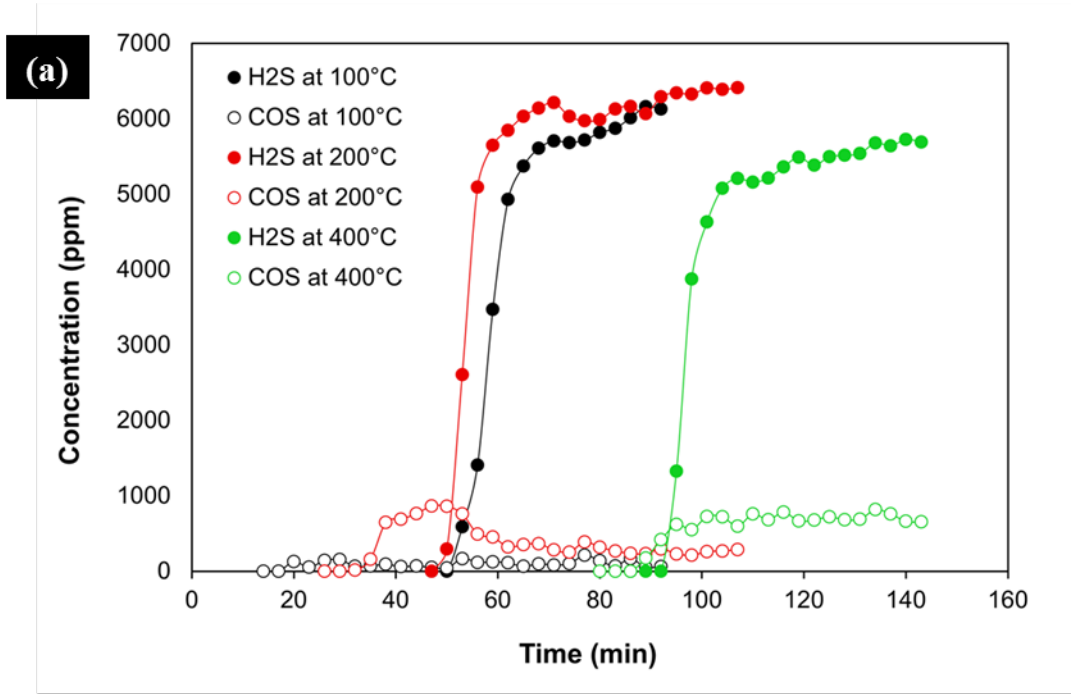

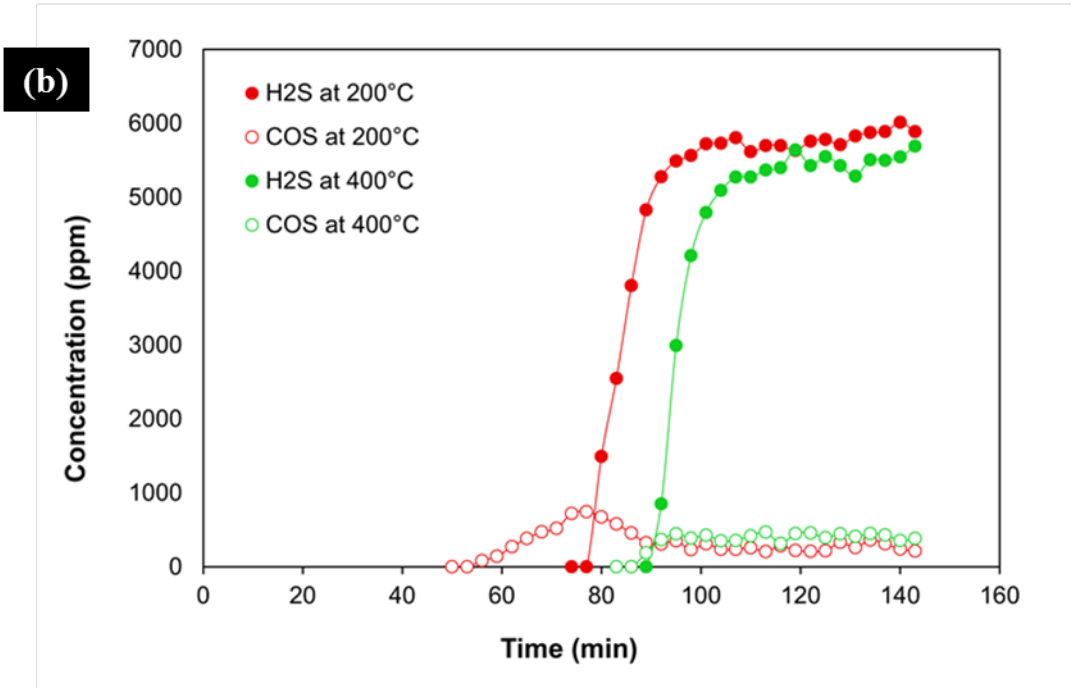

Figure XXXIX H_2S and COS breakthrough characteristics on Cu-ZnO/SiO_2 [Cu:Zn = 20:80] as a function of temperature (a) No moisture (b) 4000 ppmv moisture in feed

The formation of Cu_2S during reformate desulfurization at ambient condition on the Cu-

ZnO/SiO_2 sorbents was confirmed in a previous investigations using Electron Spin Resonance (ESR) technique [29]. Cu_2S formed is known to act as catalyst for the catalytic hydrogenation of COS to H_2S at temperatures higher than 200°C as per the following reaction:

$$COS + Cu_2S \rightarrow CO + 2CuS$$

$$2CuS + H_2 \rightarrow Cu_2S + H_2S$$

A similar study [174] has shown Carbonyl Sulfide hydrogenation occurred on cuprous sulfide in presence of a water gas containing 20% H_2 and operating at 200-250 °C and 1 atm pressure. Moisture had a similar effect on Cu-ZnO/SiO_2. However, the steady state COS concentration was still lower in case of Cu-ZnO/SiO_2 as compared to ZnO/SiO_2 sorbents. This is seen from the breakthrough curves from Figure V.3 (b**)** as indicated by the red curve and green curve.

V.3.4. Reformate desulfurization on CuO/SiO_2 as a function of temperature

The optimal loading for ZnO/SiO_2 sorbents is 21 percent by weight of ZnO[105]. Thus, in order to make a fair comparison between ZnO/SiO_2 and CuO/SiO_2 sorbents, the total oxide loading was also maintained at 21 percent by weight of CuO in CuO/SiO_2 sorbents. The H_2S breakthrough curves for CuO/SiO_2 sorbents revealed in Figure V.4. (a-b) indicate that the COS and H_2S breakthrough occurs simultaneously on CuO/SiO_2 sorbents. This phenomenon is independent of temperature. Regardless of temperature, H_2S breakthrough capacity for CuO/SiO_2 is lower than ZnO/SiO_2 and Cu-ZnO/SiO_2. Bulk CuO appears to show sharper kinetics for H_2S adsorption as compared to ZnO/SiO_2 and Cu-ZnO/SiO_2 sorbents. This can be studied with the help of a Lumped parameter (K) determined from the shape of the breakthrough curves [168].

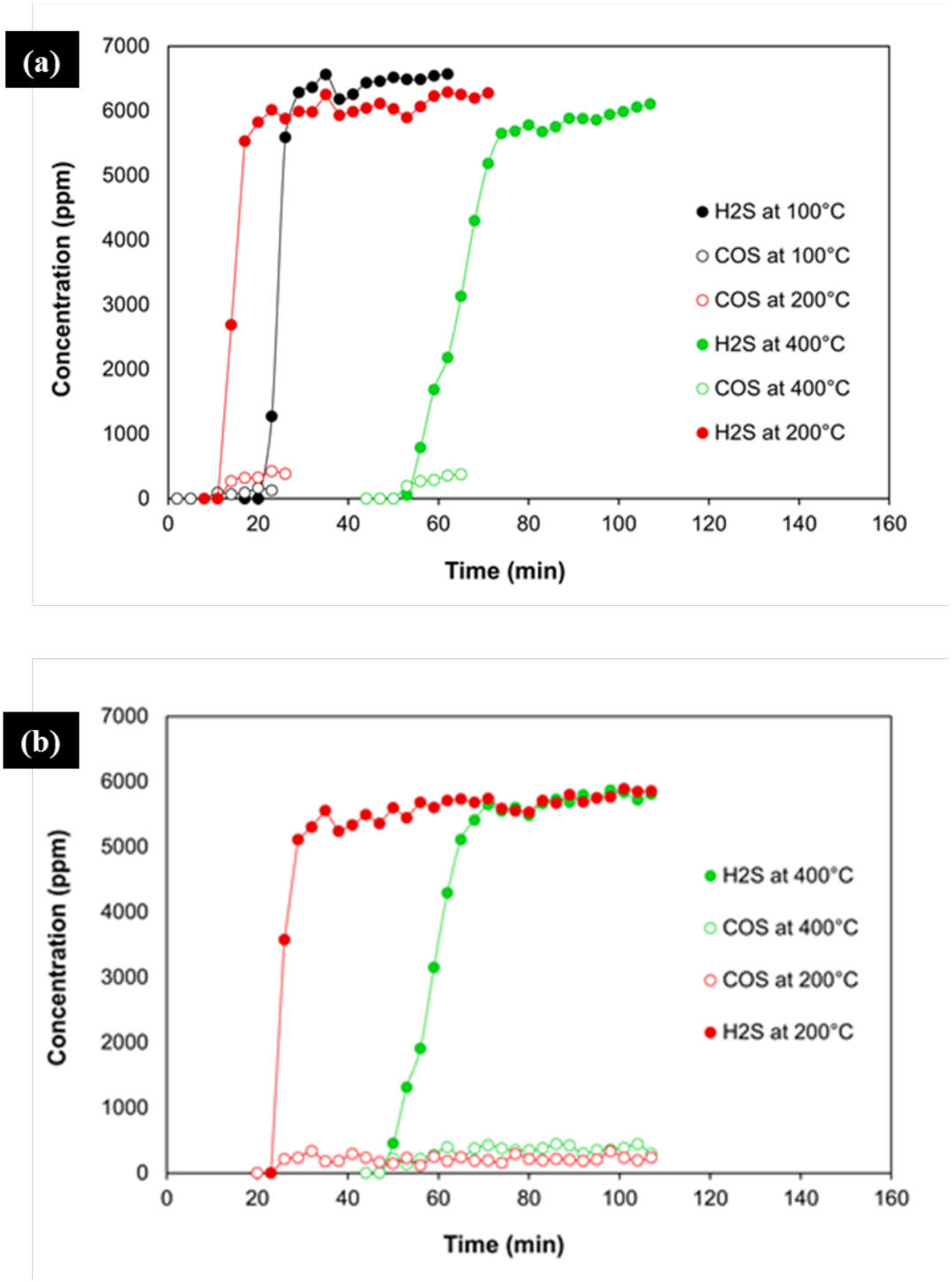

Figure XL H_2S and COS breakthrough characteristics on CuO/SiO_2 as a function of temperature (a) No moisture (b) 4000 ppmv moisture in feed

V.3.5. COS Formation on sulfided sorbents at 400°C

Two experiments were conducted to examine the heterogeneous pathways for COS formation. In each experiment, the first step consisted of pre-sulfidation of a packed bed of ZnO/SiO_2 and Cu-ZnO/SiO_2 sorbent (0.5 g) by 2%H_2S-H_2 challenge concentration at a face velocity of 2 cm/s at 400°C for 35 min. This step resulted in the formation of corresponding reduced metal sulfides. For instance, ZnS in the case of sulfided ZnO/SiO_2 and Cu_2S-ZnS in case of Cu-ZnO/SiO_2 sorbents. At saturation shown in Figure V.5 inset. the H_2S-H_2 flow was stopped and UHP He gas was passed for 15-20 min in order to remove physisorbed H_2S that might possibly react with CO_2/CO gas to form COS. COS formed via reaction between H_2S and CO_2/CO can be misleading if one is interested in probing the COS formation via the reaction between CO_2/CO and reduced metal sulfides (ZnS and Cu_2S). Second step consisted of switching He flow to UHP CO_2 at a flowrate of 100 ml/min STP in the same reactor. This step is conducted to investigate the following reaction on the two sorbents:

$ZnS + CO_2 \rightarrow COS + ZnO$

$ZnS + CO \rightarrow COS + Zn$

It is evident that a high initial concentration of COS is obtained at the outlet in case of both sorbents when UHP CO_2 is passed over sulfided sorbent specimen. Around 13 min the COS concentration stabilizes at 200 ppm on sulfided ZnO/SiO_2 sorbent. The COS formation was monitored on sulfided Cu-ZnO/SiO_2 sorbent and the steady state COS concentration was much lower at 45 ppm measured after 2 h. However, further research efforts are needed to explain the lower COS concentration observed in case of sulfided Cu-ZnO/SiO_2 sorbents versus sulfided ZnO/SiO_2. The phenomenon was attributed to the catalytic hydrogenation of COS to H_2S in H_2 rich stream on sulfided Cu-ZnO/SiO_2 sorbent in which case, Cu_2S behaves as a catalyst.

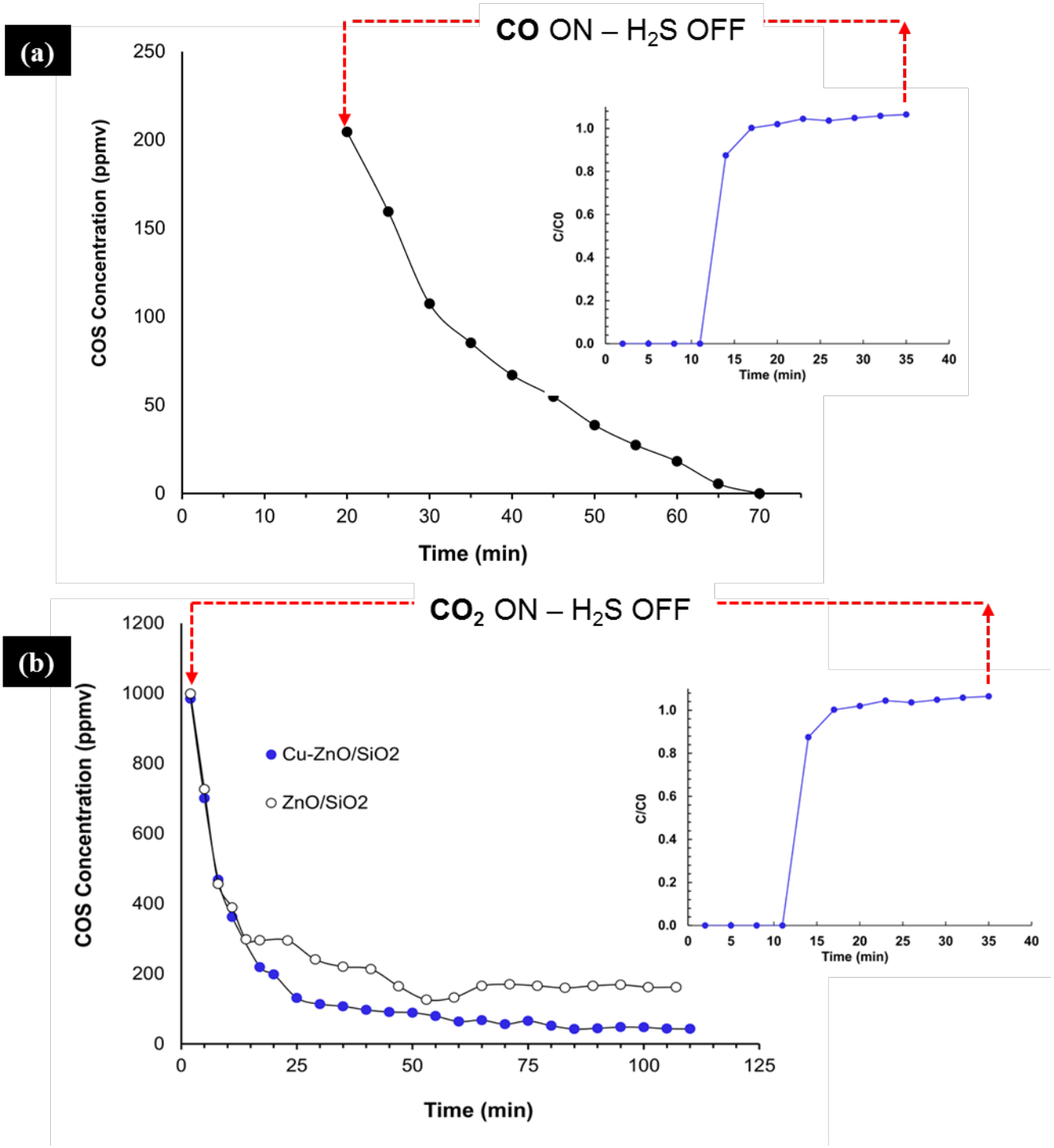

Figure XLI COS formation on sulfided sorbents at 400°C (a) Effect of CO (one plot for both sorbents); (b) Effect of CO_2

V.4. Conclusions

At 200°C, COS formation reaches a maximum value at which H_2S breakthrough occurs. However, this COS levels eventually stabilize at lower values. This is a common observation on all three sorbent samples. At 400°C, COS formation levels are lower in case of pure CuO/SiO_2 and Cu-promoted ZnO/SiO_2 sorbent samples as compared to ZnO/SiO_2 sorbents. This phenomenon was attributed to the catalytic hydrogenation of COS in a H_2 rich stream as commonly encountered in reformate/syngas streams in which case Cu_2S acts a catalyst. Desulfurization carried out at 400°C and presence of 0.4% moisture did not provide any significant improvement in the H_2S breakthrough capacity of the sorbents. The early COS breakthrough at 200 °C as compared to 400 °C makes it even more detrimental to operate the desulfurizer at lower temperatures. Lowering the operating temperature further may be beneficial to avoid to COS formation. For example, COS was not detected when experiments were carried out at mild temperature ranges (Ambient to 100°C). COS must be hydrolysed to H_2S to avoid COS slip and maintain sulfur capacity of H_2S sorbent. In a reformate feed stream, there is presence of multiple species such as $CO/CO_2/H_2S/H_2$ etc. that can severely affect the performance of H_2S sorbent due to capacity loss (competitive adsorption between H_2S and H_2O if present upto 20 mol%), COS formation due heterogeneous and homogeneous pathways. Thus it is necessary to address the possibility of simultaneous removal of COS and H_2S from reformate streams.

VI. La_2O_3 - ZnO sorbents for simultaneous removal of H_2S and COS during high temperature syngas desulfurization

Abstract

Pure ZnO and rare earth metal oxides (La^{3+}, Y^{3+} and Ce^{3+}) promoted ZnO were synthesized using a co-precipitation method and examined for the simultaneous removal of H_2S and COS from syngas at 400°C. The dual functional La_2O_3-ZnO bed showed a four-fold increase in sulfur saturation capacity per unit sorbent weight (176 mg/g) and three-fold increase in sulfur saturation capacity in terms of unit bed volume (56 mg/cm^3) compared to a mixed bed or layered bed consisting of a COS hydrolysis catalyst and H_2S adsorbent. At a 25% La_2O_3 weight loading the sorbent exhibited optimal performance in terms of breakthrough capacity with majority of La^{3+} ions dispersed in the ZnO lattice. The effect of feed composition, choice of precipitating basic solution, and desulfurization temperature was investigated. Results from regeneration tests at 500°C revealed that the sorbent was regenerable up to five cycles in a partially oxidizing atmosphere of 3% H_2O in N_2. The textural, structural, and electronic properties of the sorbents were studied using N_2 physi-sorption, X-ray Diffraction, and X-ray Photoelectron Spectroscopy.

VI.1. Introduction

Carbonyl Sulfide (COS) formation occurs as an undesired side reaction depending on the equilibrium between H_2S and CO, CO_2 in the desulfurizer feed and sorbent behaviour in fresh or spent state [170]. In a way, this phenomenon contradicts the aim of adsorptive desulfurization since the product consists of two sulfur species versus single species (H_2S) in the feed. Even worse, the early COS breakthrough compared to H_2S is detrimental to downstream processes and

demands additional separation or conversion efforts to ensure proper desulfurization operation. Catalytic hydrolysis of COS is an effective technique compared to COS adsorption or hydrogenation due to low temperature thermodynamics and high conversion efficiency. Hydrolysis of COS to H_2S followed by subsequent H_2S adsorption is an attractive means to control the sulfur content of reformed/gasified fuel over wide temperature range. The desulfurization efficiency of this dual step process ultimately depends on the sorption capacity of the H_2S adsorbent materials used downstream of a hydrolysis catalyst bed.

The simultaneous removal of H_2S and COS is gaining increasing attention and R&D efforts are directed to synthesize materials that possess the catalytic activity to hydrolyze COS as well as adsorb H_2S. The immediate advantage of using such bifunctional materials is the elimination of a dual step process to achieve higher sulfur capacity per unit packed bed volume. Among the various rare earth metals studied, lanthanum has shown to maximum sorption capacity of supported and bulk metal oxide systems during desulfurization greater than 300°C [175-178]. However, these studies primarily deal with the adsorption of H_2S from syngas which comprises of CO, H_2, CO_2, and balance N_2. Moreover, the regeneration temperature is 700°C which is approximately 150°C above typical calcination temperatures. The studies on the simultaneous removal of H_2S and COS is limited and among the ones reports are rare earth metals doped tin oxide [175], activated carbon [101], iron oxides, [72], and modified ZnO [50]. In this study, the desulfurization behavior of La_2O_3-ZnO sorbents is studied as a function of (i) feed composition, (ii) choice of base precipitant, and (iii) desulfurization temperature. Finally, the total sulfur capacity of a La_2O_3-ZnO bed is compared with a layered bed and mixed bed consisting of γ-Al_2O_3 hydrolysis catalyst and a Cu-ZnO/SiO_2 H_2S adsorbent. The textural, structural, and electronic properties of La_2O_3-ZnO sorbents was studied via N_2 physisorption, X-ray diffraction,

and X-ray photoelectron spectroscopy respectively.

VI.2. Preparation of adsorbents

The rare earth metal-oxide promoted ZnO sorbents were prepared using a co-precipitation method at room temperature. 55 – 66g of Zinc nitrate and a rare earth metal nitrate with an M/Zn atomic ratio of 1:9 (M = Y, La or Ce) were dissolved in 200 mL of deionized water. A 2 mol/L K_2CO_3 solution was added into the solution with vigorous stirring to adjust the pH to 10. The resulting slurry was maintained for 6h at 80°C prior to filtering the mixture via vacuum filtration and washing with deionized water until the pH reached 7. Finally, the precipitate was dried in air at 110°C overnight and calcined at 400°C for 3 h. Neat ZnO sorbent was prepared using the same precipitation method without rare earth metal nitration. All of the prepared sorbents were crushed and sieved through 100-250 microns.

VI.3. Characterization of adsorbents

Nitrogen adsorption-desorption isotherms of adsorbents and SiO_2 support are generated at 77 K (-196 °C) on Micromeritics Tristar II surface area analyzer. The samples are outgassed at 150 °C for 6h in vacuum (3×10^{-10} mm Hg) prior to analyses. BET surface area of samples is calculated using the Brunauer-Emmett-Teller (BET) equation. The average pore size and pore-size distribution is obtained the adsorption curve of N_2 isotherm and calculated using Barrett-Joyner-Halenda (BJH) method. A Bruker D-8 x-ray diffractometer equipped with Cu$K\alpha$ source was used at 40KV/40mA. For each sample, the XRD scan range was 10–90° and scan speed was 0.1 second/step (~5.85°/min). XPS data were collected by the AXIS Ultra Delay Lines Detector (DLD) X-ray photoelectron spectrometer (XPS) from Kratos Analytical Ltd. La_2O_3-ZnO samples

at various La_2O_3 to ZnO weight ratios were evacuated in a load lock chamber under 108 Torr vacuum, prior to admission into the analysis chamber. 5 mg of adsorbent sample was placed on 2 mm x 2mm pure indium foil of 0.5mm thickness (Alfa Aesar) to dissipate the charging effects from the X-rays. A monochromatic Al Kα X-ray source with hv = 1486.6 eV was used as the photon source. High resolution spectra were obtained for C 1s, and Zn 2p, La 3d, N1s, O1s and K 2p using a passing energy of 20 eV. The binding energy shifts due to surface charging were corrected using the reference C 1s level at 284.6 eV. Spectra were fitted by the XPSPEAK program.

VI.4. Desulfurization experiments

A schematic of the reactor setup used is shown in Figure VI.1. Gases from cylinders were connected to MFC (Alicat Inc.) using 1/8' stainless steel tubing. Desired flowrate of gases was achieved based on the calibrated settings on each controller as discussed in section II.2. Depending on the on the vapor pressure of H_2O at 22 °C, the moisture content at the inlet was varied by adjusting the flowrate of high purity H_2 through a saturator containing de-ionized water. A carbonyl trap composed of PbO/Al_2O_3 (BASF) was placed in front of the CO MFC to minimize the formation of nickel carbonyl at high temperature. The stream of gases was then admitted to a quartz chamber for generating uniform mixture before entering the quartz reactor containing adsorbent packed bed. The chamber was equipped with an RH probe to measure the humidity and as a result the moisture content of the feed stream. Adsorptive desulfurization was carried out in a quartz tube (1.1cm I.D. x 30 cm Length) which can withstand temperature up to 1200°C. The tube was co-axially mounted in a tubular furnace. The temperature of the tubular furnace was controlled by placing a K-type thermocouple directly in contact with the packed

adsorbent bed during experiments. A moisture trap containing 6g of pure P2O5 powder was placed downstream of the desulfurizer tube to trap any moisture from entering the GC. Gas sampling from adsorption experiments was performed every 10 minutes using an automated six-port gas sampling valve (Valco Instruments) of 250 μL sampling volume and injected onto a thermal conductivity detector (TCD) equipped with a packed column (Hayesep Q100) using H_2 carrier gas on a gas chromatograph (Varian CP 3800). The detection limit of the TCD is 200 ± 50 ppmv. Depending on the application, detection of lower sulfur levels may be important, however, in this study, we show concentration in the exit at breakthrough only when H_2S and COS are detected at outlet by the TCD. If not otherwise mentioned, 0.2 – 1g of 100-200 microns size adsorbent samples were used depending on the packed bed density and the desired gas residence time in the bed (52000 h-1). This corresponds to a bed volume of $1cm^3$. Inlet gas feed rate was 200 mL/min STP and reactor temperature of 400°C was maintained. Prior to each experiment, the adsorbent sample was heated at 250°C for 30 mins in high purity He flow at 100 mL/min to remove moisture, presence of impurities, and create an inert atmosphere. This operation did not have any impact on the performance of these sorbents in the temperature range studied. Regeneration of sulfided (or spent) adsorbents was carried out at 500°C for 3 hours under various environments, to study the effect of reducing, oxidizing or inert gases on the regenerable performance. The various gaseous environments constitute Air (21% O_2 – 79% N_2), 5%O_2 in N_2, 5%O_2 – 3% H_2O balance N_2, high purity N_2, and 3% H_2O in N_2. The total flowrate was maintained at 150 mL/min using a rotameter (VWR). Upon completion of regeneration, the regeneration gas was switched with high purity He at 100 mL/min until the desired desulfurization temperature was attained. Once the desulfurization temperature was reached, He was replaced with the sulfur feed stream at 200 mL/min and GC analysis immediately.

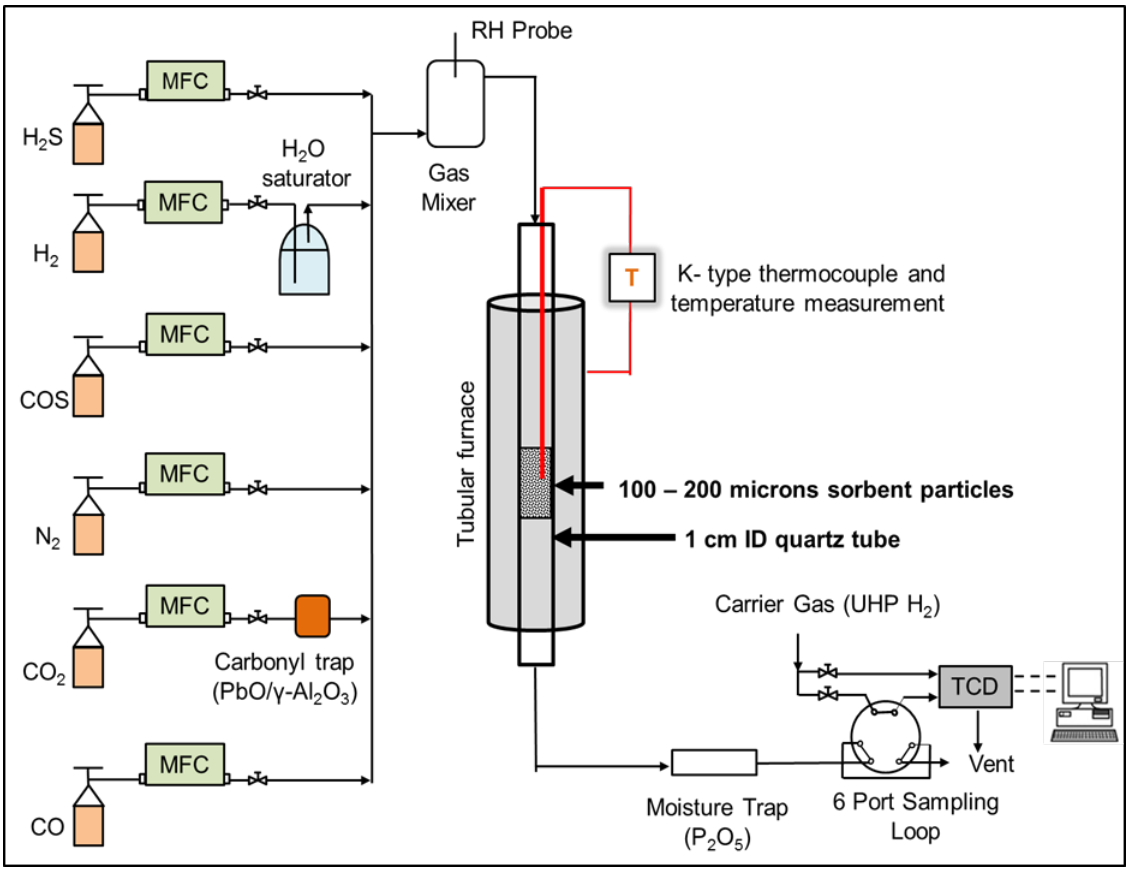

Figure XLII Experimental setup for syngas desulfurization

VI.5. Results and discussion

VI.5.1. Comparison between La_2O_3-ZnO and catalyst sorbent mixed beds or layered beds

H_2S and COS is usually removed in two steps consisting of a catalytic hydrolysis process followed by a H_2S adsorption process. In this study, γ-Al_2O_3 (hydrolysis catalyst) and $Cu_{20}Zn_{80}O/SiO_2$ (H_2S adsorbent) is used in the form of a mixed bed or a layered bed configuration for removal of H_2S and COS from a gas stream containing COS and H_2O at 400°C. The experiment was carried out at 400°C with a feed consisting of 0.45% COS – 1.5% H_2O and balance N_2 at a flowrate of 200 mL/min corresponding to a space velocity of 52000 h^{-1} in a 2 cm^3 bed. The properties of materials are shown in Table VI.1. The total bed weight of Cu-ZnO/SiO_2 and Al_2O_3 bed was held constant at 0.5g (0.25g Cu-ZnO/SiO_2 and 0.25g γ-Al_2O_3). From Figure

b, no COS was observed at the outlet of each bed configuration. However, an H_2S breakthrough time of 10 min was observed for the mixed bed and layered beds. This indicates that Al_2O_3 converted all the incoming COS to H_2S in presence of H_2O. The H_2S formed as a result of this reaction, is then adsorbed by the Cu-ZnO/SiO_2 placed downstream of the γ-Al_2O_3 bed.

Table VI.1. Textural properties of adsorbent and adsorbent bed properties

Material	**Packed bed density (g/cm^3)**	**BET surface area (m^2/g)**	**Average pore volume (cm^3/g)**
γ-Al_2O_3	0.40	250	1.14
$Cu_{20}Zn_{80}O/SiO_2$	0.67	257	0.51
25% La_2O_3–ZnO	0.32	36	0.2

Results were compared to a 25% La_2O_3-ZnO bed of equal volume. A schematic of the bed configuration is shown in Figure VI (a). γ-Al_2O_3 is a highly active COS hydrolysis catalyst at elevated temperatures [91] and is capable of hydrolyzing high COS concentrations even at short residence times. The total sulfur removal in both these configurations depends ultimately on the capacity of the sorbent bed, since the catalyst does not typically saturate at steady state. The sulfur capacity in terms of unit bed weight and unit bed volume is illustrated in Table VI.2.

Table VI.2. Saturation capacity of various bed configurations

Bed configuration	**Saturation capacity (mgS/g)**	**Saturation capacity (mgS/cm^3 bed)**
Mixed bed	45.0	24.3
Layered bed (2 beds in series)	35.0	18.9
25% La_2O_3–ZnO bed	176.0	56.3

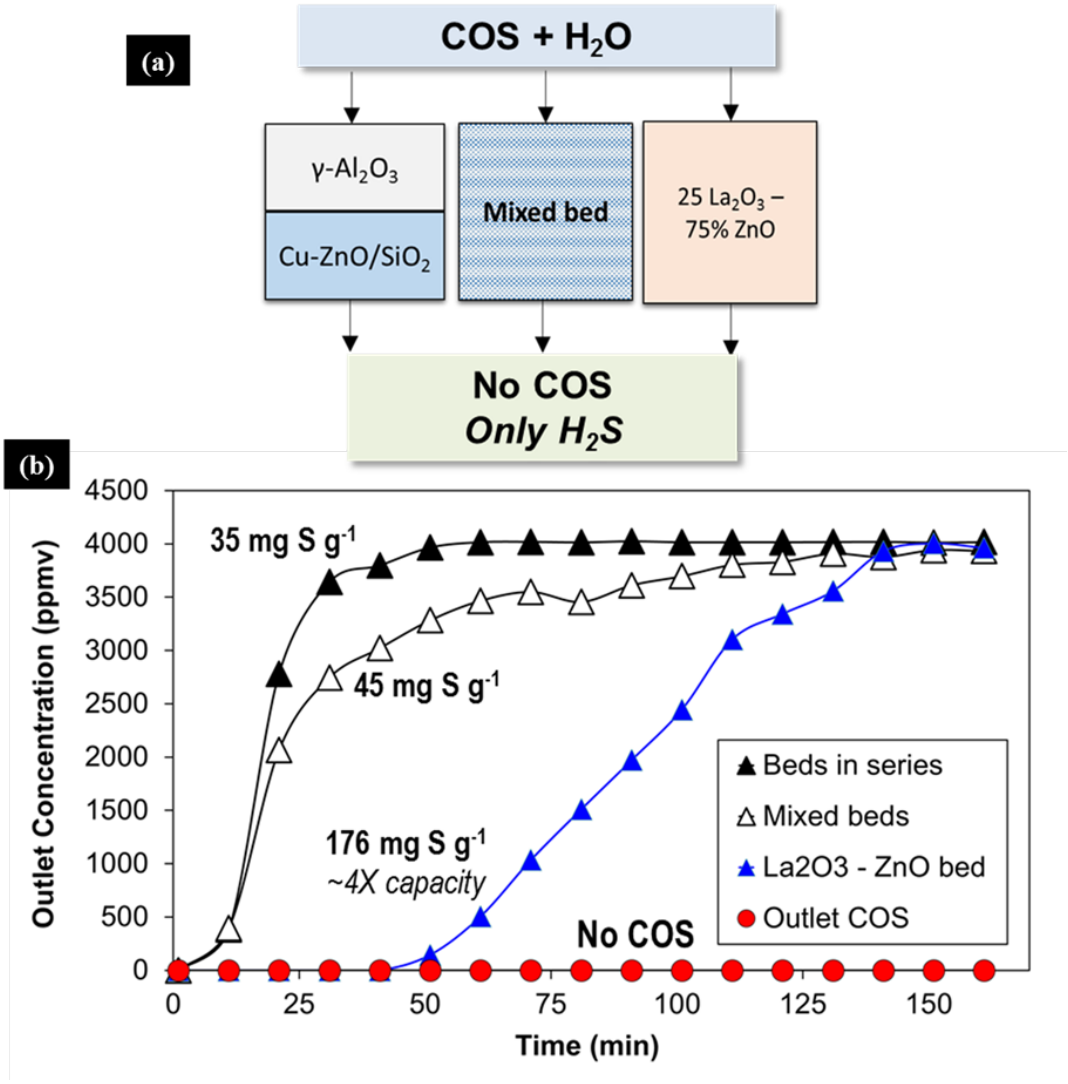

Figure XLIII (a) Schematic of bed configurations; (b) Breakthrough curves

Table VI.2**.** shows that 25% La_2O_3-ZnO bed provided a saturation capacity which is nearly 4 times the capacity of mixed bed or layered beds in terms of unit weight of adsorbent or catalyst material and a 3 times improvement in terms of unit bed volume. To match the performance of the La_2O_3-ZnO bed, the larger sorbent bed and so greater amount of sorbent would be needed while operating in the layered bed or mixed bed configuration. This automatically leads to an increase in the overall cost of the process. The absence of any COS at the outlet of 25%La_2O_3-ZnO indicates the dual functional nature of the process while using a 25% La_2O_3-ZnO sorbents.

In other words, COS is converted to H_2S via hydrolysis on La_2O_3 and H_2S is then adsorbed by ZnO on the same material.

VI.5.2. Effect of promoter

Rare earth metal are known to improve their COS hydrolysis activity and enhance the H_2S adsorption capacity of bulk and supported metal oxides [175, 177, 178]. In this study, rare earth metal oxides (Y^{3+}, Ce^{3+}, and La^{3+}) were chosen for doping ZnO as shown in Figure VI.3.

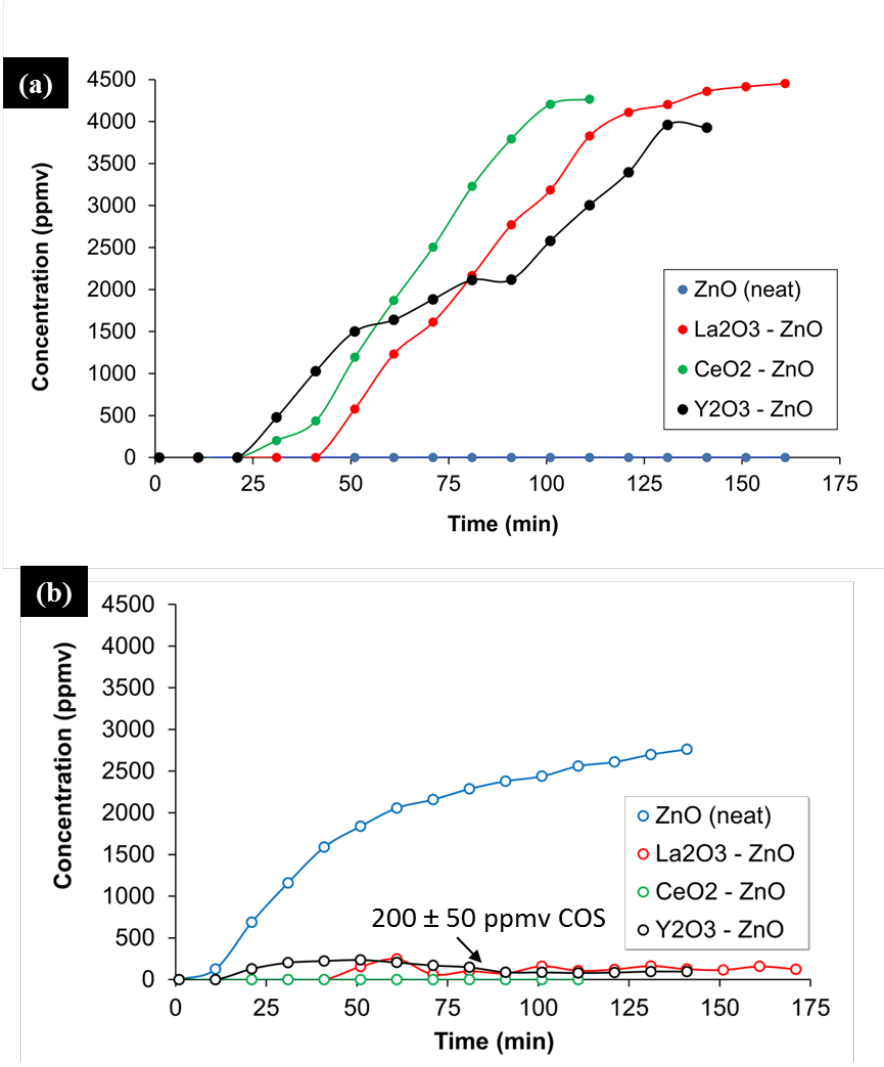

Figure XLIV Effect of promoter (a) H_2S breakthrough curves; (b) COS breakthrough curves

200 ± 50 ppmv COS was seen at the outlet at times 40 min and 13 min for 10% La_2O_3-ZnO and 10% Y_2O_3-ZnO respectively as shown in Figure VI (b). The COS breakthrough concentration for 10% CeO_2-ZnO was less than 50 ppmv as detected by the TCD. With regard to neat ZnO (prepared by coprecipitation), the COS breakthrough occurred at 10 min which suggests that neat ZnO did not exhibit any activity for conversion of COS to H_2S at 400°C. The H_2S breakthrough times for Neat ZnO, 10%Y_2O_3, 10% CeO_2, and 10% La_2O_3 was 0 min, 22 min, 22 min, and 40 min respectively. Thus, 10% La_2O_3-ZnO showed the highest breakthrough capacity for removal of H_2S when desulfurizing a feed containing 0.4% COS and 1% H_2O. When COS was converted into H_2S, the product (i.e., H_2S) can be captured by the ZnO. ZnS has a positive effect on COS hydrolysis [49].

VI.5.3. Effect of La_2O_3 loading

The effect of La_2O_3 loading is investigated in this section. 10% La_2O_3 and 25% La_2O_3 doped ZnO showed an improvement in COS and H_2S removal. An increase in the COS conversion to H_2S was observed up to 25 weight % La_2O_3 loading. However, the H_2S breakthrough capacity reduced above 25% La_2O_3 as shown in Figure a. With 100% conversion of COS, the COS conversion is no longer the restrictive procedure in the simultaneous removal of COS and H_2S. Reports show that the surface La content increased linearly with the La content when concentration exceeded 10% [179]. The XRD results as shown in Figure VI.9 indicate that with the increase of La content, the diffraction peaks of ZnO became weaker in spite of the absence of a secondary phase. Therefore, the La dopant was still well dispersed on the surface of the sorbent and included in the lattice structure of ZnO. In addition, with the La content increase, the pore size became larger and the total pore volume increased as shown in Table VI.3.

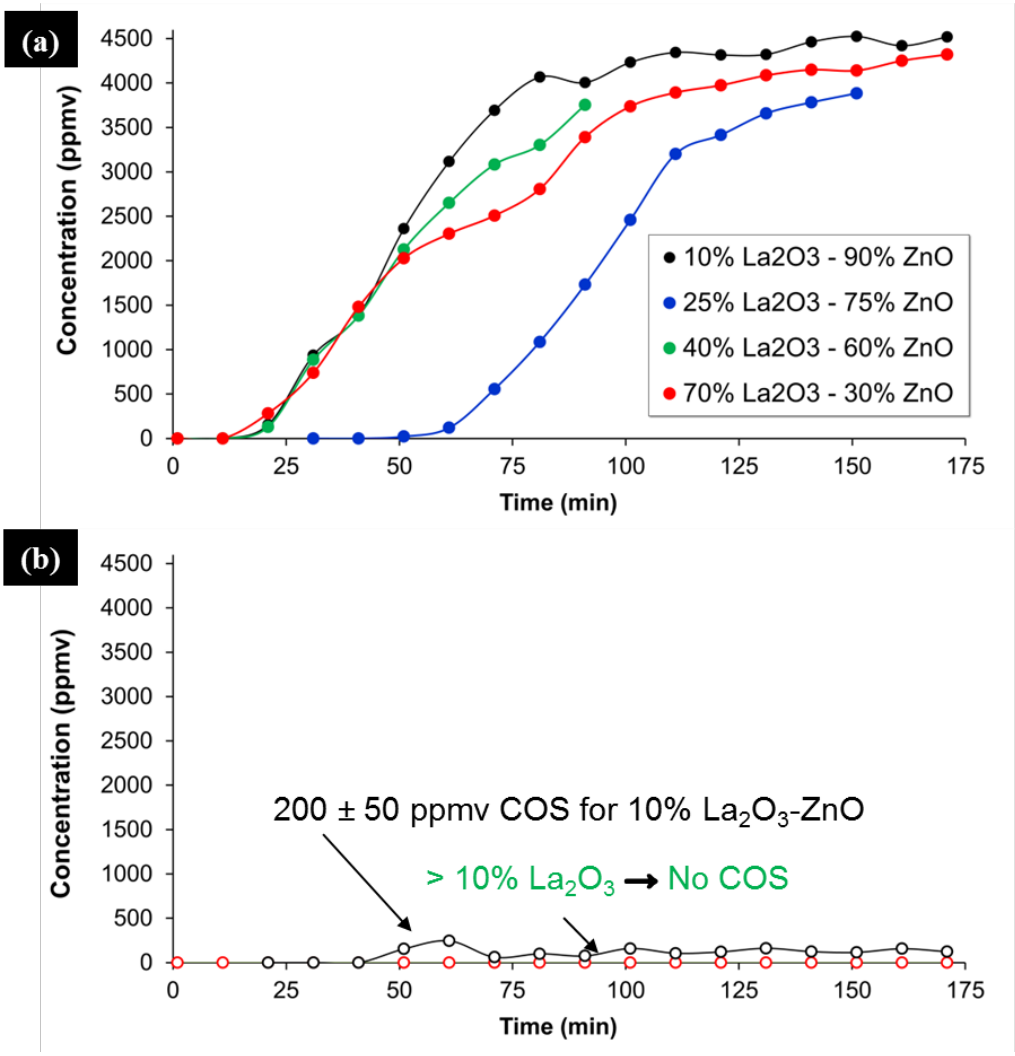

Figure VI.4. Effect of La_2O_3 loading (a) H_2S breakthrough curves; (b) COS breakthrough curves

The shape of the H_2S breakthrough curves was similar for all La_2O_3 loadings which suggest that La dopant does not alter the adsorption kinetics of the sorbent. Earlier reports suggest that presence of La^{3+} acts as an electronic promoter rather than a structural promoter in which it was claimed that La^{3+} increased the outer layer electron density of Zn atom, and an enhanced oxygen transfer ability making it more receptive to H_2S [180]. The 70% La_2O_3-ZnO showed highest BET surface area, largest pore volume and pore size. Thus, it is expected to perform better than La_2O_3-ZnO with lower La_2O_3 loadings, however, there was no correlation in terms of H_2S and

COS removal capacity. 25% La_2O_3 promoted ZnO was then used as the sorbent for the remainder part of this study.

VI.5.4. Effect of base precipitants

In this section, the effect of various basic solutions on the performance of 25% La_2O_3-ZnO sorbent is investigated for simultaneous removal of H_2S and COS from reformate stream (0.4% H_2S, 30% CO, 30% CO_2 balance H_2) at 400°C.

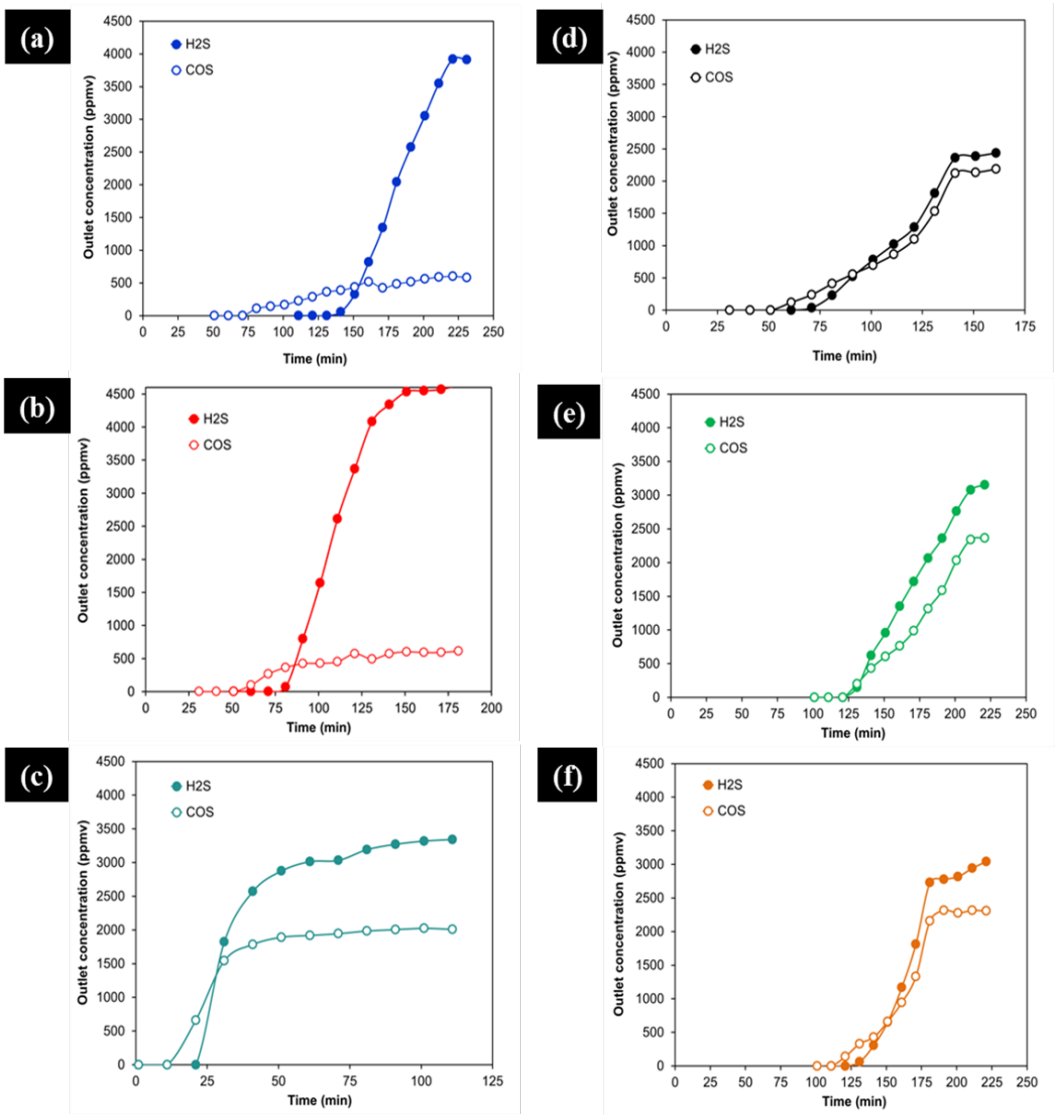

Figure XLV Effect of various basic solutions used during synthesis of 25% La_2O_3-ZnO

The basic solutions used for precipitating the metal nitrate solutions (La^{3+} and Zn^{2+}) comprised of metal hydroxides, KOH, NaOH, and NH_4OH and metal carbonates, K_2CO_3, Na_2CO_3, and NH_4CO_3 due to their common use as basic solutions used to prepare sorbents for combined H_2S and COS removal [50, 175, 181]. In Figure VI.4 (a-c), the steady state outlet COS concentration was 520±10 ppmv, 520±10 ppmv, and 2000 ppmv for 25% La_2O_3-ZnO prepared using 2M NaOH, 2M KOH, and 2M NH_4OH respectively. The H_2S breakthrough time followed the trend: KOH route (130 min) > NaOH route (75 min) > NH_4OH (12 min). Whereas, the COS breakthrough time followed the trend: KOH route (70 min) > NaOH route (50 min) > NH_4OH (13 min). Ammonium hydroxide (or aqueous ammonia) is a weak base as compared to KOH and NaOH at the equal solution concentration [182]. Thus, NH_4OH will only ionize to a limited extent in water to form hydroxyl groups ($NH_4OH \rightarrow NH_3 + OH^- + H^+$). NaOH and KOH, however, are strong bases and will ionize completely in water and produce a significant amount of hydroxyl ions ($NaOH/KOH \rightarrow Na^{2+}/K^{2+} + OH^-$). Furthermore, breakthrough time for both contaminants in KOH synthesized sorbents is higher as compared to NaOH synthesized sorbents due to higher reactivity of more electronegative potassium compared to sodium toward acidic molecules like H_2S and COS. At saturation, the sorbent in each case appeared yellow which suggests the formation of elemental sulfur in spent sorbents.

VI.5.5. Effect of desulfurization temperature

Figure VI.5 shows the effect of desulfurization temperature on the simultaneous removal of H_2S and COS on 25% La_2O_3-ZnO. In this case, the feed was 0.4%COS-1% H_2O balance N_2. The following reactions are expected to occur,

$$La_2O_3 + 3COS \rightarrow La_2S_3 + 3CO_2 \quad \text{……...…. (1)}$$

$ZnO + COS \rightarrow ZnS + CO_2$ ……...… (2)

At 200°C, the equilibrium constant for reaction 1 is 2.32 x 10^{19}, whereas the equilibrium constant for reaction 2 is 1.8 x 10^{11}. COS is more likely to react with La_2O_3 component of the sorbent. Once 50% of breakthrough is reached then, H_2S breakthrough begins to occur at 28 min.

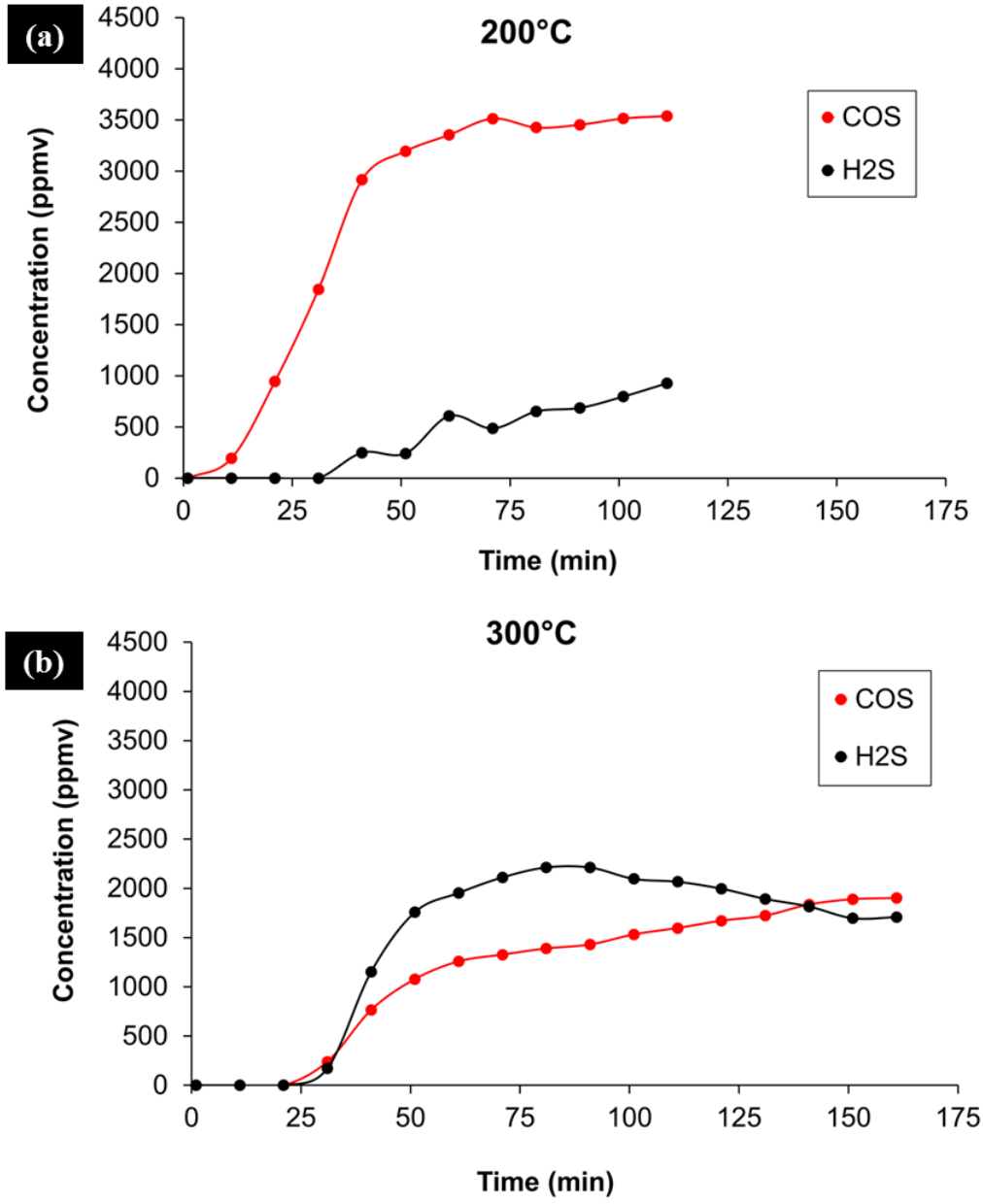

Figure XLVI Effect of desulfurization temperature (a) 200°C; (b) 300°C

At 300°C, the equilibrium constant for reaction 1 is 3.3 x 10^{13}, whereas the equilibrium constant for reaction 2 is 9.8 x 10^{7}. At 300°C, however, the H_2S concentration reached approximately 2500 ppmv. At 130 min, the H_2S concentration reduced to 1700 ppmv and COS concentration increased to 2000 ppmv at steady state. The simultaneous breakthrough of both contaminants was observed at 300°C and higher suggesting that the forward reaction rate in reactions 1-4 is favored at high temperature.

VI.5.6. Effect of feed composition on desulfurization performance

In this section, the effect of various feed composition on the simultaneous removal of H_2S and COS on 25% La_2O_3-ZnO was investigated at 400°C. For this purpose, three experiments were performed depending on the composition of feed stream as follows (i) 0.4% COS, 1% H_2S balance N_2 and H_2, (ii) 0.4% COS, 1% H_2O balance N_2 (or hydrolysis feed) (iii) 0.4% H_2S, 30% CO, 30% CO_2 balance H_2 (or reformate feed). In case (i), the COS to H_2S molar ratio was approximately 1:2. **Figure** shows that H_2S and COS breakthrough occurred simultaneously around 10 min. H_2S at the outlet saturates at 12000 ppmv which is ~ 200 ppmv higher than the inlet concentration. This may be conversion of some of the inlet COS to H_2S as a result of COS hydrogenation reaction with H_2 in the feed. This phenomenon is also supported by the fact that the outlet COS saturates at 0.38 % approximately 200 ppmv less than inlet COS concentration. The product composition did not reveal the presence of any other sulfur species such as CS_2. However, the sorbent appeared yellow in color suggesting formation of elemental sulfur. Sulfidation of metal oxides can also occur due to H_2S based on reaction 3 and 4.

$$La_2O_3 + 3H_2S \rightarrow La_2S_3 + 3H_2O \quad \text{..... (3)}$$

$$ZnO + H_2S \rightarrow ZnS + H_2O \quad \text{..... (4)}$$

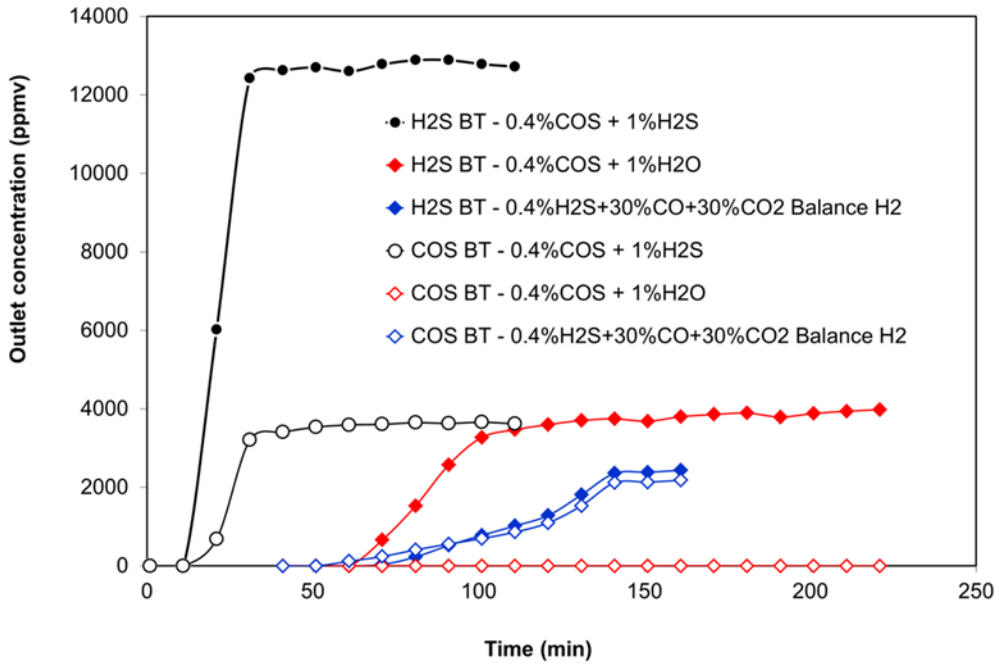

Figure XLVII Effect of feed composition on desulfurization performance of 25%La_2O_3-ZnO

In case (ii), H_2S was replaced with H_2O due to which the composition represents the feed for the COS hydrolysis reaction. This is represented by the red solid diamonds and red open diamonds in Figure VI.6. 100% conversion of COS to H_2S at 400°C on 25% La_2O_3-ZnO occurs. Clearly, no COS was seen at the outlet from the start of the experiment, which implies H_2S breakthrough occurred at 60 mins and the concentration stabilized to 4000 ppmv at 100 min. Finally, in case (iii) a reformate stream consisting of only H_2S as the sulfur species in the feed was introduced in the reactor. The breakthrough data is shown by the blue line in Figure VI.6. In this case, the simultaneous adsorption of H_2S and COS was observed and occurred at 50 min. However, in this case, the COS and H_2S concentration stabilized at approximately 2000 ppmv. The higher COS concentration at the outlet can be attributed to the absence of H_2O in the feed which if present will catalyze the COS conversion to H_2S via hydrolysis. The homogeneous COS formation due to CO_2 and CO in the feed is expected to occur as per reactions described in section I.5.

VI.5.7. Regeneration of sorbents

In this section the regeneration characteristics of 25% La_2O_3 – ZnO is investigated as a function of number of cycles and also regeneration atmosphere. In a separate experiment, the optimal regeneration temperature was determined at an arbitrary regeneration gas atmosphere, for example air (21% O_2 balance N_2) at 400°C, 450°C, 500°C and 550°C. The result of this experiment revealed that regeneration at 500°C provided maximum capacity recovery over a 3 cycle test. Figure VI.7 (a) shows the effect of regeneration gas atmosphere used to regenerate spent sorbent at 500°C. The La_2O_3 and ZnO components in 25% La_2O_3-ZnO sorbent is expected to be in sulfided states, La_2S_3 and ZnS upon interaction with H_2S or COS. This can be conceptualized based on the reactions 1-4. Figure shows that by using 3% H_2O in N_2 at 500°C, it is possible to recover almost 90 percent capacity of fresh sorbent (176 mgS/g). The following reactions may be thought to occur while using rich oxidizing conditions,

$$La_2S_3 + 6O_2 \rightarrow La_2(SO_4)_3 \quad \text{..... (5)}$$

$La_2(SO_4)_3$ or Lanthanum Sulfate is a relatively stable compound as compared to La_2S_3 and may be responsible for permanent deactivation of sorbent which results in loss of capacity over regeneration. Re-oxidation to Lanthanum Oxide (La_2O_3) can still be achieved by using slight lower O_2 concentration based on the following reaction –

$$La_2S_3 + \frac{9}{2}O_2 \rightarrow La_2O_3 + 3SO_2 \quad \text{........ (6)}$$

However, in both cases, a constant supply of O_2 is required during regeneration and this can be an expensive operation. On the other hand, using 3% H_2O (steam) can be easily achieved by passing N_2 gas through a water saturator maintained at 22°C to regenerate the spent sorbent as follows –

$$La_2S_3 + 3H_2O \rightarrow La_2O_3 + 3H_2S \quad \text{..... (7)}$$

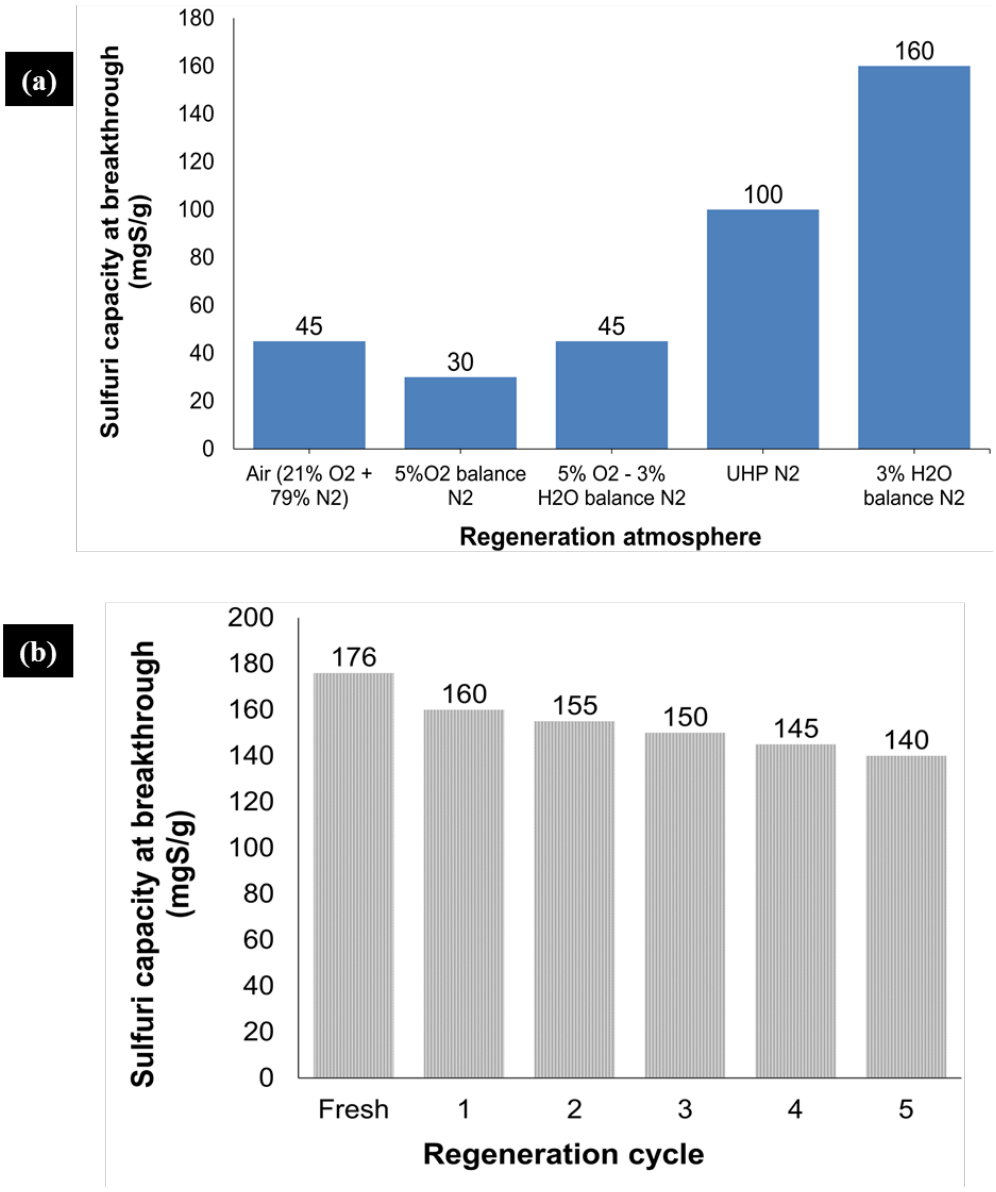

Figure VI.8. Breakthrough capacity of 25% La_2O_3-ZnO as function of (a) Regeneration gas atmosphere; (b) Regeneration cycles

Figure VI.7 (b), shows that 25% La_2O_3-ZnO can be regenerated up to 5 cycles in 3% H_2O in N_2 without significant loss in capacity over multiple cycles. The capacity after 5 cycles was stable at 140 mgS/g or 80% of the capacity of the fresh sorbent.

VI.6. Characterization

VI.6.1. N_2 Physisoprtion

Understanding the adsorption isotherm is essential while choosing an appropriate adsorbent for the contaminant removal process and can be useful while design the adsorption process unit [102]. Figure VI.8 shows the adsorption isotherms and the BJH pore size distribution of La_2O_3-ZnO as a function of La_2O_3 loading. It is evident that most adsorbent exhibit the Type II isotherms. The intermediate flat region of P/P_0 value between 0.1 and 0.9 corresponds to a monolayer formation. The BJH pore size distribution (Figure inset) indicates that majority of the pores are in the size range of 1 – 10 nm indicating the presence of micro-pores (2-50 nm).

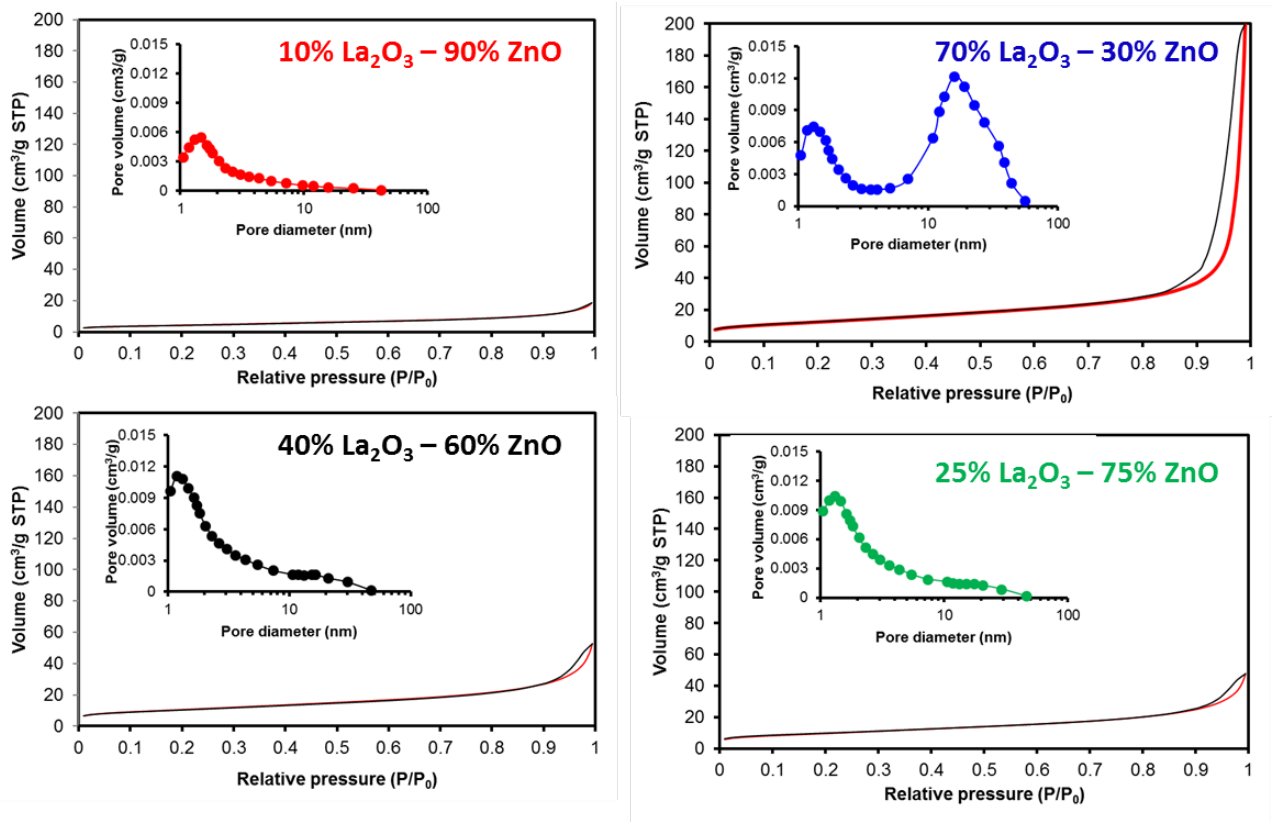

Figure XLVIII N_2 adsorption isotherms and BJH pore size distribution (inset) of La_2O_3-ZnO sorbents

However, in case of 70% La_2O_3-ZnO, presence of macro-pores (pore size > 50 nm) was observed and this may explain the reason for higher pore volume at 70% La_2O_3 loading. This observation consistent with a previous observation in which SnO_2 sorbent doped with La in the concentration range between 11.1% to 40% weight showed an increase in the total pore volume and pore size [175]. BET surface areas of La_2O_3-ZnO are shown in Table VI.3.

Table VI.3. Textural properties of La_2O_3-ZnO as a function of La_2O_3 loading

Sample	**BET (m^2/g)**	**Average pore volume (cm^3/g)**	**Average Pore diameter (nm)**
10% La_2O_3 - ZnO	15.45	0.07	4.5
25% La_2O_3 - ZnO	36.26	0.2	5.28
40% La_2O_3 - ZnO	33.55	0.1	5.07
70% La_2O_3 - ZnO	43.29	0.3	27.95

Table VI.3 indicates that 70% La_2O_3-ZnO showed the highest BET surface area, pore volume and pore size, however the textural properties did not reveal a direct dependence on the performance for simultaneous removal of H_2S and COS.

VI.6.2. XRD analysis

The red curve in Figure VI.9 indicates the XRD data for 10% La_2O_3-ZnO and shows strong diffraction peaks between 2θ = 30–40° that belong to crystalline ZnO in the wurtzite phase indicated by the black circles. However, no distinct phase of La_2O_3 was seen at 10% loading indicating the formation of a solid solution. At 25% loading however, peak at 2θ = 29° begins to

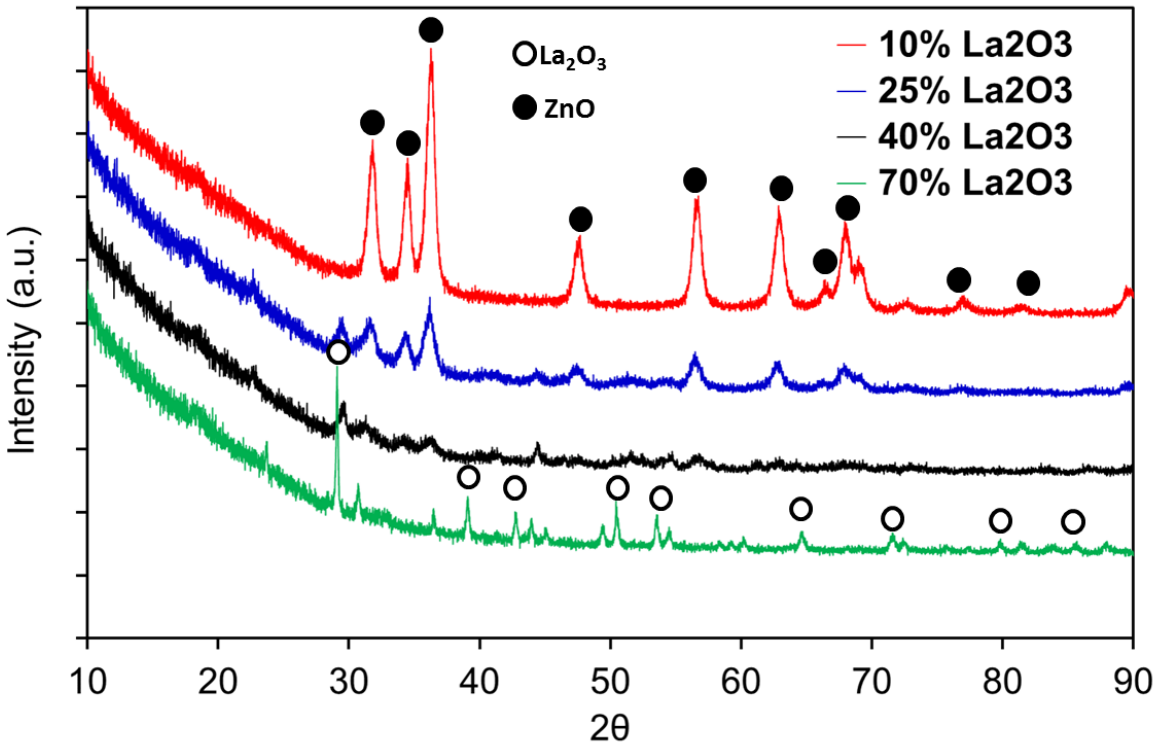

appear that belongs to La_2O_3 [183], however the position of the ZnO diffraction peak did not change, which indicates that the crystal phase of the sorbent was still ZnO. With an increase in

Figure XLIX XRD patterns of La_2O_3-ZnO sorbents as a function of La_2O_3 loading

La_2O_3 loading, the ZnO diffraction peak clearly becomes less pronounced and diffraction peaks belonging to La_2O_3 begin to appear. At 70% loading, the diffraction peaks belonging to ZnO is almost absent. The intensity of the diffraction peaks (100), (101) and (002) decreased and the full width half maximum (fwhm) increased for samples doped with La_2O_3. Such changes in the crystallinity were attributed to the changes in the atomic level environment in ZnO lattice in doped samples [184] . The existence of La^{3+} in the wurtzite lattice of ZnO was confirmed by calculating the lattice parameters according to Bragg's Law. For the (100) orientation at $2\theta = 31.7°$, the lattice constant a is calculated by,

$$a = \frac{\lambda}{\sqrt{3}\sin\theta}$$

And for the (002) orientation at 2θ = 34.34°, the lattice constant c is calculated by,

$$c = \frac{\lambda}{\sin\theta}$$

Where, λ is the X-ray wavelength, and equal to 1.5418Å for Cu Kα radiation; θ is Bragg angle.

Table VI.4 shows the lattice constants a and c for pure ZnO and promoted ZnO adsorbents.

Table VI.4. Lattice constant a and c for pure ZnO and doped samples

Sample	**a (Å)**	**Angle (°)**	**c (Å)**	**Angle (°)**	**c/a**
Neat ZnO	3.260	31.70	5.222	34.34	1.602
10% La_2O_3 – ZnO	3.259	31.69	5.201	34.49	1.595
25% La_2O_3 - ZnO	3.273	31.56	5.226	34.32	1.597
40% La_2O_3 – ZnO	3.418	30.28	5.270	34.02	1.542
70% La_2O_3 - ZnO	-	UD	-	UD	-

UD: Diffraction peak (100) and (002) belonging to ZnO is too weak for analysis

The 'c/a' values give insight into the structure of metal oxide ZnO. For example, a c/a value of 1.60 is value for ideal hexagonal closed packed structure. Change in the lattice parameter a and c can occur due to presence of defects, oxygen vacancies, and the mismatch in the ionic radii between La^{3+} (0.122 nm) and Zn^{2+} (0.074 nm) in the lattice of ZnO [183].

VI.6.3. XPS analysis

XPS spectra of fresh sorbents are shown in Figure VI.10 (a-c). In Figure VI.10 (a), the peaks at binding energy of 1045 eV and 1022 eV belongs to $Zn2p_{1/2}$ and $Zn2p_{3/2}$ respectively which suggests that Zn exists mainly in the form of Zn^{2+} on the sorbent surface [185-187]. A shift in

these two peaks at 70% La_2O_3 suggests (i) charge redistribution in process of chemical interaction with La3+ and (ii) final state effects of the photoemission process.

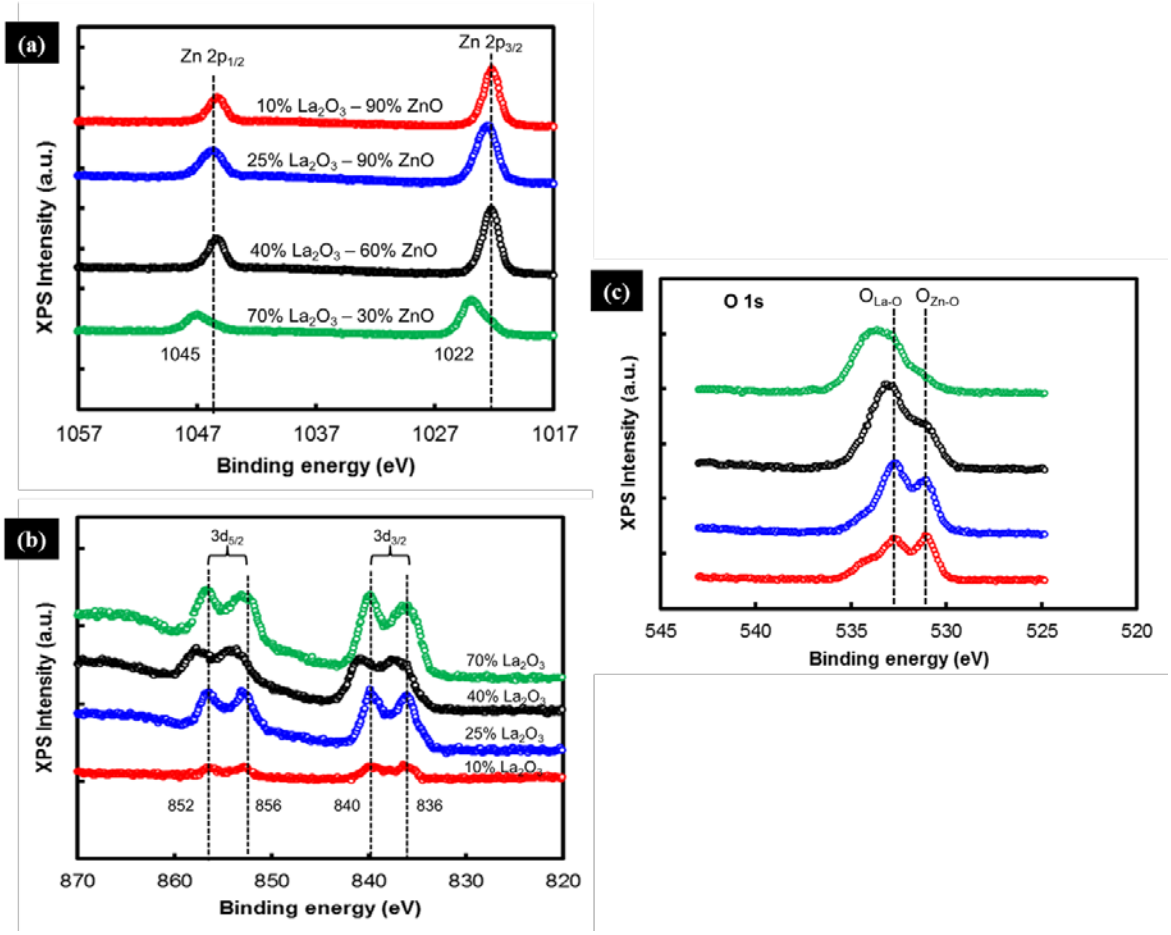

Figure L XPS spectra of fresh La_2O_3-ZnO sorbents (a) Zn 2p; (b) La 3d; (c) O 1s

In this study, the final effect of the photo-emission process is explained in terms of relaxation energy involved in the process. In other words, the photoemission process involves the creation of holes that undergo relaxation by recombining with electrons. The kinetic energy of the photo-emitted electron is influenced by the screening effect of the hole. In presence of large number of Zn atoms such as those encountered in higher weight loadings of ZnO in adsorbent samples, the relaxation effect is minimal. In contrast, at lower ZnO (or Zn) loadings or in the case of ZnO nanocrystals, the relaxation effect is prominent with less number of electrons participating in the

screening of the holes. The La 3d profile in Figure VI.10 (b), exhibits four peaks with binding energy of 836 eV, 840 eV belonging to La $3d_{3/2}$ and 852 eV and 856 eV belonging to La $3d_{5/2}$ [185-187]. The La 3d peaks reveal that La exists in +3 valence state in sorbents. The La 3d peaks become sharper and more prominent with increasing La loading suggesting an increase in La concentration on the surface as corroborated by XRD measurements. The separation distance from between La $3d_{5/2}$ and La $3d_{3/2}$ and their respective satellite peaks is nearly 4 eV which implies the existence of $La(OH)_3$ on the ZnO surface [186]. The presence of this hydroxyl group is favorable for base catalyzed reactions such as the COS hydrolysis reaction. This may be the reason why no COS is seen at the outlet while using La_2O_3-ZnO class of sorbents. Figure VI.10 (c), shows O 1s spectra in various La_2O_3 loaded ZnO sorbents. An asymmetrical O 1s peak is observed for 10, 25, and 40% La_2O_3 loading which indicates contribution from oxygen in different chemical states. For example, O_{Zn-O} means lattice oxygen belonging to ZnO and O_{La-O} indicates lattice oxygen from La_2O_3. The presence of hydroxyl groups can be detected at 531.28 eV [186]. However, peaks at this binding energy are overlaid by the O_{Zn-O} peak [185]. However, it is safe to assume that a reduction of hydroxyl groups take place at 70% La_2O_3 loading.

VI.7. Conclusion

A novel rare earth metal oxide promoted ZnO sorbent was synthesized by co-precipitation for syngas desulfurization at 400°C. The absence of any COS at the outlet of 25%La_2O_3-ZnO demonstrates the dual functional nature in which COS is converted to H_2S via hydrolysis on La_2O_3 and H_2S is then adsorbed by ZnO on the same material. 25% La_2O_3-ZnO bed provided a saturation capacity which is nearly 4 times the capacity of mixed bed or layered beds in terms of unit weight of adsorbent or catalyst material and a 3 times improvement in terms of unit bed

volume. Although high COS concentrations were observed in case of basic carbonate precursors used for synthesis of La_2O_3-ZnO, the COS and H_2S breakthrough times were much closer when compared to sorbents synthesized using basic hydroxide precursors. As long as the desulfurization operation is carried out until breakthrough, the carbonate route can guarantee simultaneous removal of H_2S and COS. COS hydrolysis and H_2S adsorption are reactions favored at elevated temperatures which translates into increase in adsorption capacity at high temperatures. 25% La_2O_3-ZnO was effective in desulfurizing H_2S and COS from a variety of streams including reformate stream, hydrolysis stream and stream containing H_2S and COS. The capacity after 5 cycles was stable at 140 mgS/g or 80% of the capacity of the fresh sorbent. Change in the lattice parameters of ZnO indicates that La^{3+} is progressively occupying sites in the ZnO lattice until 10% La_2O_3 loading as indicated by XRD patterns. XPS characterization reveals that Zn and La exist in +2 and +3 oxidation states in La_2O_3-ZnO sorbents.

VII. Conclusions and recommendations for future work

VII.1. Conclusions from research

The summary of findings can be found at the end of each chapter. This work has led to the synthesis of novel materials for simultaneous removal of H_2S and COS from a variety of sulfur laden gas streams. Initial work deals with understanding important physical and chemical characteristics of bulk and supported adsorbent systems and contributes to the knowledge of such materials. This knowledge can then be used to develop improved catalysts or adsorbents for contaminant removal. The development of the fiber optic monitoring system serves as a unique process control alternative. An optical method was developed for rapid and accurate monitoring of sorbent bed utilization at breakthrough. An overview of all research efforts conducted will be mentioned in this section as follows:

1. A combination of characterization including N_2 physisorption, XRD, FTIR, XPS, and UV-Vis DRS were employed to study the physical and chemical properties of the species in the sorbent.
2. Oxidation number of Zn in ZnO/SiO_2 is 2+ in calcined (ZnO) and sulfided (ZnS) state and the ZnO band gap from Tauc plot was determined to be 3.61 eV.
3. The intensity ratio of Zn to Si is linear until 21% ZnO on SiO_2 (0.103 nm or 0.35 fraction of monolayer) when compared to theoretical intensity ratio suggesting a high level of dispersion of Zn atoms on surface of SiO_2. Beyond 21% ZnO, the intensity ratio begins to level off suggesting particle growth or nucleation. This translates into reduction in H_2S adsorption capacity beyond 21% ZnO loading.
4. The dispersed ZnO exists in the wurtzite crystalline phase. However, XRD and UV-Vis

absorption bands confirm the absence of $ZnSiO_4$ solid solution and that ZnO particles are likely to exist as crystallites less than 4 nm.

5. Cu^{2+} in $Cu_XZn_{100-X}O/SiO_2$ exists in octahedral coordination and lead to a persistent reduction in the ZnO band gap over wide temperature range.
6. Presence of Cu increases dispersion of Zn atoms on surface as seen from an increase in the Zn to Si intensity ratio in $Cu_XZn_{100-X}O/SiO_2$ sorbents.
7. In-situ UV-Vis DRS and in-situ EPR spectra suggest that majority of Cu^{2+} is in isolated form and that Cu^{2+} is reduced to Cu^{1+} upon interaction with H_2S.
8. A fiber optic based UV-vis diffuse reflectance spectroscopic system was implemented as an embedded sensor in the desulfurizer assembly to measure the utilization of adsorbent beds during H_2S removal at 22 °C
9. During H_2S adsorption, a sharp response with maxima, t_{max} was obtained when the first order derivative of integrated area under in-situ reflectance spectra from 250-800 nm was plotted as a function of service time and compared to the time to reach 50% saturation or breakthrough time of adsorbents.
10. The accuracy of the technique was examined at varying H_2S concentrations and H_2S residence time across the adsorbent bed.
11. Presence of 0.5-1 vol% moisture in the feed resulted in slow saturation of H_2S with a broad breakthrough curve and corresponding slow and delayed optical response.
12. The capacity depletion of a 15 mL packed bed 3/16 inch ZnO extrudates during H_2S adsorption was monitored using a 6 mm fiber optic probe.
13. La_2O_3-ZnO sorbents were synthesized using co-precipitation method for the simultaneous removal of H_2S and COS at 400°C from syngas

14. La_2O_3-ZnO sorbents were optimized in terms of loadings effects, type of base precipitants and choice between supported and unsupported formulation.
15. The synthesized sorbents were effective in desulfurizing a variety of gas streams containing H_2S and COS and ultimately reducing the sulfur concentration to less than 10 ppmv Sulfur.
16. The sorbents were regenerable up to 5 cycles in a partial oxidizing environment consisting of 3% H_2O and balance N_2 (inert).

The optical technique monitors adsorbent utilization with accuracy. Simultaneous removal of H_2S and COS eliminates the need for two step process, hydrolysis catalysts. The synergistic effect of catalyst-sorbent approach can be realized when material was subjected to sulfur containing feed streams. The low packed bed density ensures higher saturation capacity per unit bed volume as compared to mixed beds containing H_2S adsorbent and COS hydrolysis catalyst. Light-weight and compact structure of desulfurizer is essential during desulfurization for logistic fuel cell applications.

VII.2. Recommendations for future work

VII.2.1. Optimization of process for simultaneous removal of H_2S and COS at low temperature

PEM fuel cells usually operate at low temperature (80°C), the COS hydrolysis and H_2S adsorption capacity of 25% La_2O_3-ZnO diminishes at T<100°C which is common in bulk metal oxide systems. In contrast, metal oxides dispersed on/in the supports are expected to be far more effective for H_2S adsorption because of less solid state diffusion resistance at low temperature. The hypothesis is that La_2O_3-ZnO can be supported on supports such as γ-Al_2O_3, TiO_2 and ZrO_2

which are active for COS hydrolysis [80, 81, 85]. The supported sorbent can be further promoted with alkali metals like Cs_2O, K_2O, Na_2O to increase basicity which is an essential criterion for improved hydrolysis activity at low temperature [89, 141]. The final formulation which can be represented by Cs_2O/La_2O_3-ZnO/support can be tested with a hydrolysis feed (COS-H_2O) and reformate feed (H_2S-CO-CO_2-H_2) and examined for the simultaneous removal of H_2S and COS.

VII.2.2. Optical, structural and morphological characterization of La_2O_3-ZnO sorbents using Raman spectroscopy, FTIR and Electron microscopy.

As seen earlier, enhanced reactivity of ZnO with sulfur can be due to surface defects, oxygen vacancies etc. Presence of La can induce surface defects that activate the Raman modes of ZnO such as E_{2H}-E_{2L} (332 cm^{-1}), A_{1T} (378 cm^{-1}) and E_{2H} (437 cm^{-1}) [188]. At 10% La_2O_3 loading, the La^{3+} ions are dissolved in the ZnO lattice but due to the large ionic radii of La^{3+} (0.112nm) compared to Zn^{2+} (0.074 nm), at higher loadings, the La^{3+} may form distinct phases on the surface and this phenomenon can be observed by additional peaks in the Raman spectra. The incorporation of La^{3+} into the ZnO lattice can be further examined via FTIR spectroscopy by observing the stretching vibrations of the La-Zn-O or Zn-O or La-O bonds [189]. For bulk systems, rare-earth metals could prevent an increase in growth of SnO_2 particles due to formation of a segregation layer of rare earth cations on the particle surface [175]. The same phenomenon can be examined for La_2O_3-ZnO using SEM-EDS for morphological changes and surface composition analysis.

VII.2.3. Characterization of reaction between CO, CO_2, H_2, COS, H_2S, H_2O and calcined (La_2O_3-ZnO) or sulfided sorbent (La_2S_3-ZnS)

Reformate streams contain varying amounts of CO, CO_2, COS, H_2S, H_2 and H_2O among other molecules. For example, it is possible that sulfided specimen act as catalysts for COS hydrolysis based on the following sequential reactions taking place after formation of sulfided specimen.

If H_2S is prevalent in the stream, reaction 1: $ZnO + H_2S \rightarrow ZnS + H_2O$ takes places and then reaction 2: $ZnS + H_2O \rightarrow ZnO + H_2S$ followed by reaction 3: $ZnO + COS \rightarrow ZnS + CO_2$ In this case, ZnS acts as a hydrolysis catalyst. The same can be true for La_2O_3 as follows, reaction 1: $La_2O_3 + 3H_2S \rightarrow La_2S_3 + 3H_2O$ takes places and then reaction 2: $La_2S_3 + 3H_2O \rightarrow La_2O_3 + 3H_2S$ followed be reaction 3: $La_2O_3 + 3COS \rightarrow La_2S_3 + 3CO_2$ In this case, La_2S_3 can as a hydrolysis catalyst. In this way, the COS or H_2S formation/adsorption on surface of sorbents can be studied by dynamic interruption experiments with CO, CO_2, H_2O, and H_2 in the feed. This will also inform about the nature of active sites for example, whether La metal formed in reduced atmosphere (CO or H_2) may be involved. Such experiments are particularly important while sorbents are employed in real applications involving intermittent operations, frequent shutdown of desulfurization equipment or recycle operations.

VII.2.4. Effect of reactor pressure

Increasing reactor pressure has a positive effect on the COS hydrolysis rate of catalysts [190]. An change in pressure influences the diffusivity of the gas molecules. For this purpose, it is necessary to use metal tubes as opposed to quartz tubes. A back pressure regulator downstream of the reactor must be installed and a manual needle valve to adjust the reactor pressure. It is necessary to exercise caution during this operating. For example, the metal tube reactor must be capable of withstanding the pressure range values; the inlet pressure to the mass flow controller must always be higher than the reactor pressure; finally a back flow preventer can be installed in

case of flammable gases. In case of high temperature measurements, adjust the desired pressure at 22°C then begin to increase temperature. With an increase in pressure, the system weight and volume can be reduced while simultaneously optimizing costs.

VII.2.5. Capacity to remove other sulfur species

Promoted ZnO sorbents can be a versatile choice for desulfurizing different feed stocks such as biogas, landfill gas, associated gas, boiler exhaust gas etc. which contain carbon disulphide (CS_2), Sulfur dioxide (SO_2) etc. Further experiments and equipment can be developed to address this issue.

References

[1] D. Stirling, The Sulphur Problem: Cleaning Up Industrial Feedstocks, Royal Society of Chemistry, UK, 2000.

[2] P.R. Westmoreland, J.B. Gibson, D.P. Harrison, COMPARATIVE KINETICS OF HIGH-TEMPERATURE REACTION BETWEEN H_2S AND SELECTED METAL-OXIDES, Environmental Science & Technology, 11 (1977) 488-491.

[3] R.V. Siriwardane, J.A. Poston, INTERACTION OF H2S WITH ZINC TITANATE IN THE PRESENCE OF H-2 AND CO, Applied Surface Science, 45 (1990) 131-139.

[4] M. Yumura, E. Furimsky, COMPARISON OF CAO, ZNO, AND FE2O3 AS H2S ADSORBENTS AT HIGH-TEMPERATURES, Industrial & Engineering Chemistry Process Design and Development, 24 (1985) 1165-1168.

[5] C.S. Song, X.L. Ma, Ultra-deep desulfurization of liquid hydrocarbon fuels: Chemistry and process, International Journal of Green Energy, 1 (2004) 167-191.

[6] D.B. Dushyant Shekhawat, James J. Spivey, Fuel Cells: Technologies for Fuel Processing, Elsevier B.V., UK, 2011.

[7] S. Satokawa, Y. Kobayashi, H. Fujiki, Adsorptive removal of dimethylsulfide and t-butylmercaptan from pipeline natural gas fuel on Ag zeolites under ambient conditions, Applied Catalysis B-Environmental, 56 (2005) 51-56.

[8] G. Kolb, Fuel Processing for Fuel Cells, Wiley-VCH Verlag GmbH & Co.2008.

[9] H.Y. Yang, B. Tatarchuk, Novel-Doped Zinc Oxide Sorbents for Low Temperature Regenerable Desulfurization Applications, Aiche Journal, 56 (2010) 2898-2904.

[10] I. Rosso, C. Galletti, M. Bizzi, G. Saracco, V. Specchia, Zinc oxide sorbents for the removal of hydrogen sulfide from Syngas, Industrial & Engineering Chemistry Research, 42 (2003) 1688-1697.

[11] P.D.N. Svoronos, T.J. Bruno, Carbonyl sulfide: A review of its chemistry and properties, Industrial & Engineering Chemistry Research, 41 (2002) 5321-5336.

[12] S.V. Sotirchos, H.C. Yu, OVERLAPPING GRAIN MODELS FOR GAS SOLID REACTIONS WITH SOLID PRODUCT, Industrial & Engineering Chemistry Research, 27 (1988) 836-845.

[13] J. Skrzypski, I. Bezverkhyy, O. Heintz, J.P. Bellat, Low Temperature H_2S Removal with Metal-Doped Nanostructure ZnO Sorbents: Study of the Origin of Enhanced Reactivity in Cu-Containing Materials, Industrial & Engineering Chemistry Research, 50 (2011) 5714-5722.

[14] P.J.H. Carnell, Feedstock Purification, Catalyst Handbook, Wolfe Publishing Ltd., London, 1989.

[15] B. Tatarchuk, H. Yang, P. Dhage, Doped Zinc Oxide Sorbents for Desulfurization Applications., USA, 2008.

[16] C.L. Carnes, K.J. Klabunde, Unique chemical reactivities of nanocrystalline metal oxides toward hydrogen sulfide, Chemistry of Materials, 14 (2002) 1806-1811.

[17] A. Samokhvalov, B.J. Tatarchuk, Characterization of active sites, determination of mechanisms of H_2S, COS and CS_2 sorption and regeneration of ZnO low-temperature sorbents: past, current and perspectives, Physical Chemistry Chemical Physics, 13 (2011) 3197-3209.

[18] J. Sun, S. Modi, K. Liu, R. Lesieur, J. Buglass, Kinetics of zinc oxide sulfidation for packed-bed desulfurizer modeling, Energy & Fuels, 21 (2007) 1863-1871.

[19] H. Zhou, A. Hofstaetter, D.M. Hofmann, B.K. Meyer, Magnetic resonance studies on ZnO nanocrystals, Microelectronic Engineering, 66 (2003) 59-64.

[20] R.B. Slimane, J. Abbasian, Regenerable mixed metal oxide sorbents for coal gas desulfurization at moderate temperatures, Advances in Environmental Research, 4 (2000) 147-162.

[21] D.H. Jiang, L.H. Su, L. Ma, N. Yao, X.L. Xu, H.D. Tang, X.N. Li, Cu-Zn-Al mixed metal oxides derived from hydroxycarbonate precursors for H_2S removal at low temperature, Applied Surface Science, 256 (2010) 3216-3223.

[22] M. Xue, R. Chitrakar, K. Sakane, K. Ooi, Screening of adsorbents for removal of H_2S at room temperature, Green Chemistry, 5 (2003) 529-534.

[23] T. Baird, P.J. Denny, R. Hoyle, F. McMonagle, D. Stirling, J. Tweedy, MODIFIED ZINC-OXIDE ABSORBENTS FOR LOW-TEMPERATURE GAS DESULFURIZATION, Journal of the Chemical Society-Faraday Transactions, 88 (1992) 3375-3382.

[24] K. Polychronopoulou, J.L.G. Fierro, A.M. Efstathiou, Novel Zn-Ti-based mixed metal oxides for low-temperature adsorption of H_2S from industrial gas streams, Applied Catalysis B-Environmental, 57 (2005) 125-137.

[25] D. Montes, E. Tocuyo, E. Gonzalez, D. Rodriguez, R. Solano, R. Atencio, M.A. Ramos, A. Moronta, Reactive H_2S chemisorption on mesoporous silica molecular sieve-supported CuO or ZnO, Microporous and Mesoporous Materials, 168 (2013) 111-120.

[26] I. Bezverkhyy, J. Skrzypski, O. Safonova, J.-P. Bellat, Sulfidation Mechanism of Pure and Cu-Doped ZnO Nanoparticles at Moderate Temperature: TEM and In Situ XRD Studies, Journal of Physical Chemistry C, 116 (2012) 14423-14430.

[27] Z.P. Fu, B.F. Yang, L. Li, W.W. Dong, C. Jia, W. Wu, An intense ultraviolet photoluminescence in sol-gel ZnO-SiO_2 nanocomposites, Journal of Physics-Condensed Matter, 15 (2003) 2867-2873.

[28] J.W.L. Wong, W.D. Sun, Z.H. Ma, I.K. Sou, XPS studies of Auger parameter shift of $ZnS_{1-x}Te_x$ alloys, Journal of Electron Spectroscopy and Related Phenomena, 113 (2001) 215-220.

[29] P. Dhage, A. Samokhvalov, D. Repala, E.C. Duin, M. Bowman, B.J. Tatarchuk, Copper-Promoted ZnO/SiO_2 Regenerable Sorbents for the Room Temperature Removal of H_2S from Reformate Gas Streams, Industrial & Engineering Chemistry Research, 49 (2010) 8388-8396.

[30] D. Brion, STUDY BY PHOTOELECTRON-SPECTROSCOPY OF SURFACE DEGRADATION OF FES2, CUFES2 ZNS AND PBS EXPOSED TO AIR AND WATER, Applications of Surface Science, 5 (1980) 133-152.

[31] A. Martinez-Arias, R. Cataluna, J.C. Conesa, J. Soria, Effect of copper-ceria interactions on copper reduction in a Cu/CeO_2/Al_2O_3 catalyst subjected to thermal treatments in CO, Journal of Physical Chemistry B, 102 (1998) 809-817.

[32] A. Gurlo, R. Riedel, In situ and operando spectroscopy for assessing mechanisms of gas sensing, Angewandte Chemie-International Edition, 46 (2007) 3826-3848.

[33] B.M. Weckhuysen, Determining the active site in a catalytic process: Operando spectroscopy is more than a buzzword, Physical Chemistry Chemical Physics, 5 (2003) 4351-4360.

[34] L.G.A. van de Water, G.L. Bezerner, J.A. Bergwerff, M. Versluijs-Helder, B.M. Weckhuysen, K.P. de Jong, Spatially resolved UV-vis micro spectroscopy on the preparation of alumina-supported Co Fischer-Tropsch catalysts: Linking activity to Co distribution and speciation, Journal of Catalysis, 242 (2006) 287-298.

[35] L.G. van de Water, J.A. Bergwerff, T.A. Nijhuis, K.P. de Jong, B.M. Weckhuysen, UV-Vis microspectroscopy: Probing the initial stages of supported metal oxide catalyst preparation, Journal of the American Chemical Society, 127 (2005) 5024-5025.

[36] P. Dhage, A. Samokhvalov, M. Mckee, E. Duin, B. Tatarchuk, Reactive adsorption of hydrogen sulfide by promoted sorbents CuZnO/SiO_2: active sites by experiment and simulation., Surface and Interface Analysis, 2012.

[37] T.P. GmbH.

[38] S. Katikaneni, J. Daly, On-line Monitoring Assembly for Detection of Sulfur Breakthrough in a Desulfurization Assembly and Sulfur Breakthrough Detection Method, USA, 2007.

[39] J. Daly, Sulfur Breakthrough Detection Assembly for use in a Fuel Utilization System and Sulfur Breakthrough Detection Method, Fuel Cell Energy Inc., USA, 2012.

[40] A. Sujan, B. Tatarchuk, An Embedded Sensor Approach for Monitoring the Desulfurization Process of Industrial Reformates on Doped Supported Zinc Oxide Adsorbents Using Fiber Optic Based Diffuse Reflectance Spectroscopy, PITTCON 2013Philadelphia, PA, 2013.

[41] B. Tatarchuk, H. Yang, P. Dimick, Direct In-situ Monitoring of Adsorbent and Catalyst Beds, Intramicron Inc., USA, 2013.

[42] G.W. Roberts, D.M. Brown, T.H. Hsiung, J.J. Lewnard, DEACTIVATION OF METHANOL SYNTHESIS CATALYSTS, Industrial & Engineering Chemistry Research, 32 (1993) 1610-1621.

[43] Z.T. Liu, J.L. Zhou, B.J. Zhang, POISONING OF IRON CATALYST BY COS IN SYNGAS FOR FISCHER-TROPSCH SYNTHESIS, Journal of Molecular Catalysis, 94 (1994) 255-261.

[44] L. Wang, S.D. Wang, Q.A. Yuan, Removal of carbonyl sulfide at low temperature: Experiment and modeling, Fuel Processing Technology, 91 (2010) 777-782.

[45] H. Yang, Gas Phase Desulfurization Using Regenerable Microfibrous Entrapped Metal Oxide based Sorbents for Logistic PEM Fuel Cell Applications., Auburn University, 2007.

[46] H. Yang, Y. Lu, B.J. Tatarchuk, Glass fiber entrapped sorbent for reformates desulfurization for logistic PEM fuel cell power systems, Journal of Power Sources, 174 (2007) 302-311.

[47] H.Y. Yang, R. Sothen, D.R. Cahela, B.J. Tatarchuk, Breakthrough Characteristics of Reformate Desulfurization Using ZnO Sorbents for Logistic Fuel Cell Power Systems, Industrial & Engineering Chemistry Research, 47 (2008) 10064-10070.

[48] S. Watson, R. Kimmitt, R.B. Rhinesmith, Study compares COS-removal processes, Oil & Gas Journal, 2003, pp. 1-7.

[49] E. Sasaoka, K. Taniguchi, S. Hirano, M.A. Uddin, S. Kasaoka, Y. Sakata, CATALYTIC ACTIVITY OF ZNS FORMED FROM DESULFURIZATION SORBENT ZNO FOR CONVERSION OF COS TO H_2S, Industrial & Engineering Chemistry Research, 34 (1995) 1102-1106.

[50] S. Ju, Y. Zhao, H. Fan, L. Liang, F. Shen, M. Miao, Desulfurization behavior of zinc oxide based sorbent modified by the combination of Al_2O_3 and K_2CO_3, Fuel, 108 (2013) 80-84.

[51] E.C. Rupp, E.J. Granite, D.C. Stanko, Catalytic formation of carbonyl sulfide during warm gas clean-up of simulated coal-derived fuel gas with Pd/gamma-Al_2O_3 sorbents, Fuel, 92 (2012) 211-215.

[52] A. Ryzhikov, V. Hulea, D. Tichit, C. Leroi, D. Anglerot, B. Coq, P. Trens, Methyl mercaptan and carbonyl sulfide traces removal through adsorption and catalysis on zeolites and

layered double hydroxides, Applied Catalysis a-General, 397 (2011) 218-224.

[53] D.E. Sparks, T. Morgan, P.M. Patterson, S.A. Tackett, E. Morris, M. Crocker, New sulfur adsorbents derived from layered double hydroxides I: synthesis and COS adsorption, Applied Catalysis B-Environmental, 82 (2008) 190-198.

[54] M.L. Sattler, R.S. Rosenberk, Removal of carbonyl sulfide using activated carbon adsorption, Journal of the Air & Waste Management Association, 56 (2006) 219-224.

[55] H. Zhao, D.X. Zhang, F.F. Wang, T.T. Wu, J.S. Gao, Modification of Fe-Mn mixed oxide COS removal sorbent by rare-earth oxides addition, Process Safety and Environmental Protection, 87 (2009) 274-280.

[56] K. Sakanishi, A. Matsumura, I. Saito, T. Hanaoka, T. Minowa, Removal of Hydrogen Sulfide and Carbonyl Sulfide for Purification of Biomass Gasified Synthetic Gas using Active Carbons, ACS National MeetingPhiladelphia, PA, 2004, pp. 580.

[57] E. Sasaoka, K. Taniguchi, A. Uddin, S. Hirano, S. Kasaoka, Y. Sakata, Characterization of reaction between ZnO and COS, Industrial & Engineering Chemistry Research, 35 (1996) 2389-2394.

[58] Y. Wu, Y. Yu, J.Z. Zhou, J. Liu, Y. Chi, Z.P. Xu, G. Qian, Effective removal of pyrophosphate by Ca-Fe-LDH and its mechanism, Chemical Engineering Journal, 179 (2012) 72-79.

[59] F. Li, J.J. Liu, D.G. Evans, X. Duan, Stoichiometric synthesis of pure MFe2O4 (M = Mg, Co, and Ni) spinel ferrites from tailored layered double hydroxide (hydrotalcite-like) precursors, Chemistry of Materials, 16 (2004) 1597-1602.

[60] Y. Ohishi, T. Kawabata, T. Shishido, K. Takaki, Q.H. Zhang, Y. Wang, K. Nomura, K. Takehira, Mg-Fe-Al mixed oxides with mesoporous properties prepared from hydrotalcite as precursors: Catalytic behavior in ethylbenzene dehydrogenation, Applied Catalysis a-General, 288 (2005) 220-231.

[61] F. Basile, P. Benito, G. Fornasari, A. Vaccari, Hydrotalcite-type precursors of active catalysts for hydrogen production, Applied Clay Science, 48 (2010) 250-259.

[62] F. Cavani, F. Trifiro, A. Vaccari, HYDROTALCITE-TYPE ANIONIC CLAYS: PREPARATION, PROPERTIES AND APPLICATIONS, Catalysis Today, 11 (1991) 173-301.

[63] A.E. Palomares, J.M. Lopez-Nieto, F.J. Lazaro, A. Lopez, A. Corma, Reactivity in the removal of SO2 and NOx on Co/Mg/Al mixed oxides derived from hydrotalcites, Applied Catalysis B-Environmental, 20 (1999) 257-266.

[64] G. Centi, G. Fornasari, C. Gobbi, M. Livi, F. Trifiro, A. Vaccari, NOx storage-reduction catalysts based on hydrotalcite - Effect of Cu in promoting resistance to deactivation, Catalysis

Today, 73 (2002) 287-296.

[65] A. Corma, A.E. Palomares, F. Rey, F. Marquez, Simultaneous catalytic removal of SOx and NOx with hydrotalcite-derived mixed oxides containing copper, and their possibilities to be used in FCC units, Journal of Catalysis, 170 (1997) 140-149.

[66] M. Tsuji, G. Mao, T. Yoshida, Y. Tamaura, HYDROTALCITES WITH AN EXTENDED AL3+-SUBSTITUTION - SYNTHESIS, SIMULTANEOUS TG-DTA-MS STUDY, AND THEIR CO_2 ADSORPTION BEHAVIORS, Journal of Materials Research, 8 (1993) 1137-1142.

[67] L.T. Nemeth, e. al., Removal of sulfur compounds from liquid organic feedstreams, USA, 1994.

[68] T.J. Toops, M. Crocker, New sulfur adsorbents derived from layered II. DRIFTS study of COS and H_2S double hydroxides adsorption, Applied Catalysis B-Environmental, 82 (2008) 199-207.

[69] P. Ning, L. Yu, H. Yi, X. Tang, H. Li, H. Wang, L. Yang, Effect of Fe/Cu/Ce loading on the coal-based activated carbons for hydrolysis of carbonyl sulfide, Journal of Rare Earths, 28 (2010) 205-210.

[70] X. Wang, Y. Ma, P. Ning, J. Qiu, X. Ren, Z. Li, W. Chen, W. Liu, Adsorption of carbonyl sulfide on modified activated carbon under low-oxygen content conditions, Adsorption-Journal of the International Adsorption Society, 20 (2014) 623-630.

[71] J.P. Wakker, A.W. Gerritsen, J.A. Moulijn, HIGH-TEMPERATURE H_2S AND COS REMOVAL WITH MNO AND FEO ON GAMMA-Al_2O_3 ACCEPTORS, Industrial & Engineering Chemistry Research, 32 (1993) 139-149.

[72] K. Miura, K. Mae, T. Inoue, T. Yoshimi, H. Nakagawa, K. Hashimoto, SIMULTANEOUS REMOVAL OF COS AND H_2S FROM COKE-OVEN GAS AT LOW-TEMPERATURE BY USE OF AN IRON-OXIDE, Industrial & Engineering Chemistry Research, 31 (1992) 415-419.

[73] M.P. Cal, B.W. Strickler, A.A. Lizzio, High temperature hydrogen sulfide adsorption on activated carbon I. Effects of gas composition and metal addition, Carbon, 38 (2000) 1757-1765.

[74] T.J. Bandosz, Effect of pore structure and surface chemistry of virgin activated carbons on removal of hydrogen sulfide, Carbon, 37 (1999) 483-491.

[75] B.P. Williams, N.C. Young, J. West, C. Rhodes, G.J. Hutchings, Carbonyl sulphide hydrolysis using alumina catalysts, Catalysis Today, 49 (1999) 99-104.

[76] R. Fiedorow, R. Leaute, I.G.D. Lana, A STUDY OF THE KINETICS AND MECHANISM OF COS HYDROLYSIS OVER ALUMINA, Journal of Catalysis, 85 (1984) 339-348.

[77] Y.Q. Zhang, Z.B. Xiao, J.X. Ma, Hydrolysis of carbonyl sulfide over rare earth oxysulfides,

Applied Catalysis B-Environmental, 48 (2004) 57-63.

[78] J. Bachelier, A. Aboulayt, J.C. Lavalley, O. Legendre, F. Luck, ACTIVITY OF DIFFERENT METAL-OXIDES TOWARDS COS HYDROLYSIS - EFFECT OF SO2 AND SULFATION, Catalysis Today, 17 (1993) 55-62.

[79] P.E. Hoggan, A. Aboulayt, A. Pieplu, P. Nortier, J.C. Lavalley, MECHANISM OF COS HYDROLYSIS ON ALUMINA, Journal of Catalysis, 149 (1994) 300-306.

[80] C. Lahousse, K. Aboulayt, F. Mauge, J. Bachelier, J. Lavalley, Preparation, Texture et proprietes acido-basiques des oxydes Binaires ZrO_2 ,Al_2O_3 et ZrO_2 ,TiO_2, J. Soc. Alger. Chim, 35 (1993) 154.

[81] C. Lahousse, A. Aboulayt, F. Mauge, J. Bachelier, J.C. Lavalley, ACIDIC AND BASIC PROPERTIES OF ZIRCONIA-ALUMINA AND ZIRCONIA-TITANIA MIXED OXIDES, Journal of Molecular Catalysis, 84 (1993) 283-297.

[82] A. Aboulayt, P.E. Hoggan, J.C. Lavalley, Combined FTIR, reactivity and quantum chemistry investigation of COS hydrolysis at metal oxide surfaces used to compare hydroxyl group basicity, Catalysis Letters, (1996) 213-218.

[83] H.M.e.a. Huisman, Hydrolysis of COS on Titania Catalysts, ACSWashington D.C., 1994.

[84] C. Lahousse, F. Mauge, J. Bachelier, J.C. Lavalley, ACIDIC AND BASIC PROPERTIES OF TITANIA-ALUMINA MIXED OXIDES - ACTIVE-SITES FOR PROPAN-2-OL DEHYDRATION, Journal of the Chemical Society-Faraday Transactions, 91 (1995) 2907-2912.

[85] S. Tong, I.G.D. Lana, K.T. Chuang, KINETIC MODELING OF THE HYDROLYSIS OF CARBONYL SULFIDE CATALYZED BY EITHER TITANIA OR ALUMINA, Canadian Journal of Chemical Engineering, 71 (1993) 392-400.

[86] H. Wang, H. Yi, P. Ning, X. Tang, L. Yu, D. He, S. Zhao, Calcined hydrotalcite-like compounds as catalysts for hydrolysis carbonyl sulfide at low temperature, Chemical Engineering Journal, 166 (2011) 99-104.

[87] M. Akimoto, I.G. Dallalana, ROLE OF REDUCTION SITES IN VAPOR-PHASE HYDROLYSIS OF CARBONYL SULFIDE OVER ALUMINA CATALYSTS, Journal of Catalysis, 62 (1980) 84-93.

[88] Z.M. George, KINETICS OF COBALT-MOLYBDATE-CATALYZED REACTIONS OF SO2 WITH H_2S AND COS AND HYDROLYSIS OF COS, Journal of Catalysis, 32 (1974) 261-271.

[89] Z.M. George, EFFECT OF CATALYST BASICITY FOR COS-SO_2 AND COS HYDROLYSIS REACTIONS, Journal of Catalysis, 35 (1974) 218-224.

[90] J.X. Ma, M. Fang, N.T. Lau, Activation of La_2O_3 for the catalytic reduction of SO2 by CO, Journal of Catalysis, 163 (1996) 271-278.

[91] H. Huang, N. Young, B.P. Williams, S.H. Taylor, G. Hutchings, High temperature COS hydrolysis catalysed by gamma-Al_2O_3, Catalysis Letters, 110 (2006) 243-246.

[92] J. West, B.P. Williams, N. Young, C. Rhodes, G.J. Hutchings, Low temperature hydrolysis of carbonyl sulfide using gamma-alumina catalysts, Catalysis Letters, 74 (2001) 111-114.

[93] S.S. Tan, C.H. Li, S.Z. Liang, H.X. Guo, COMPENSATION EFFECT IN CATALYTIC HYDROLYSIS OF CARBONYL SULFIDE AT LOWER TEMPERATURE COMPENSATION EFFECT IN COS HYDROLYSIS, Catalysis Letters, 8 (1991) 155-168.

[94] B. Thomas, B.P. Williams, N. Young, C. Rhodes, G.J. Hutchings, Ambient temperature hydrolysis of carbonyl sulfide using gamma-alumina catalysts: effect of calcination temperature and alkali doping, Catalysis Letters, 86 (2003) 201-205.

[95] S. Zhao, Y. Honghong, e. al, Characterization of Zn-Ni-Fe hydrotalcite-derived oxides and their application in the hydrolysis of carbonyl sulfide, Applied Clay Science, 56 (2012) 84-89.

[96] H. Wang, H. Yi, X. Tang, P. Ning, L. Yu, D. He, S. Zhao, K. Li, Catalytic hydrolysis of COS over calcined CoNiAl hydrotalcite-like compounds modified by cerium, Applied Clay Science, 70 (2012) 8-13.

[97] S. Tong, University of Alberta, Canada, 1991, pp. 11.

[98] Ratnasam.P, A.J. Leonard, X-RAY SCATTERING TECHNIQUES IN STUDY OF AMORPHOUS CATALYSTS, Catalysis Reviews, 6 (1972) 293-&.

[99] T. Dupin, R. Voirin, CATALYST ENHANCES CLAUS OPERATIONS, Hydrocarbon Processing, 61 (1982) 189-191.

[100] T.T. Chuang, Dallalan.Ig, C.L. Liu, CO_2 POISONING OF GAMMA ALUMINA-CATALYZED REACTION OF COS WITH SO_2, Journal of the Chemical Society-Faraday Transactions I, 69 (1973) 643-651.

[101] K. Sakanishi, Z.H. Wu, A. Matsumura, I. Saito, T. Hanaoka, T. Minowa, M. Tada, T. Iwasaki, Simultaneous removal of H_2S and COS using activated carbons and their supported catalysts, Catalysis Today, 104 (2005) 94-100.

[102] W.L. McCabe, J.C. Smith, P. Harriott, Unit Operations of Chemical Engineering, 4th ed., McGraw-Hill1985.

[103] J.J. Collins, The LUB/equilibrium section concept for fixed bed adsorption., Chem. Eng. Prog. Symp. Ser., 1967.

[104] P. Dhage, Promoted ZnO Sorbents for Wide Temperature Range H_2S/COS Removal for Applications in Fuel Cells, Chemical Engineering, Auburn University, Auburn, Alabama, USA, 2011.

[105] P. Dhage, A. Samokhvalov, M.L. McKee, E.C. Duin, B.J. Tatarchuk, Reactive adsorption of hydrogen sulfide by promoted sorbents Cu-ZnO/SiO_2: active sites by experiment and simulation, Surface and Interface Analysis, 45 (2013) 865-872.

[106] J.A. Rodriguez, S. Chaturvedi, M. Kuhn, J. Hrbek, Reaction of H_2S and S^{-2} with metal/oxide surfaces: Band-gap size and chemical reactivity, Journal of Physical Chemistry B, 102 (1998) 5511-5519.

[107] Q. Lin, K.-i. Shimizu, A. Satsuma, Kinetic analysis of reduction process of supported Rh/Al_2O_3 catalysts by time resolved in-situ UV-vis spectroscopy, Applied Catalysis a-General, 419 (2012) 142-147.

[108] A. Bensalem, B.M. Weckhuysen, R.A. Schoonheydt, In Situ Diffuse Reflectance Spectroscopy of Supported Chromium Oxide Catalysts: Kinetics of the Reduction Process with Carbon Monoxide, Journal of Physical Chemistry B, 101 (1997) 2824-2829.

[109] A. Bruckner, Simultaneous combination of in situ-EPR/UV-VIS/on line GC: a novel setup for investigating transition metal oxide catalysts under working conditions, Chemical Communications, (2001) 2122-2123.

[110] A. Bruckner, E. Kondratenko, Simultaneous operando EPR/UV-vis/laser-Raman spectroscopy - A powerful tool for monitoring transition metal oxide catalysts during reaction, Catalysis Today, 113 (2006) 16-24.

[111] N. Moussa, A. Ghorbel, UV-vis-DR study of VO_x/SiO_2 catalysts prepared by sol-gel method, Applied Surface Science, 255 (2008) 2270-2275.

[112] R.A. Schoonheydt, UV-VIS-NIR spectroscopy and microscopy of heterogeneous catalysts, Chemical Society Reviews, 39 (2010) 5051-5066.

[113] B.M. Weckhuysen, P.V.D. Voort, G. Catana, Spectroscopy of Transition Metal Ions on Surfaces, Leuven University Press, Netherlands, 2000.

[114] A. Davydov, Study of Cation States by DRES and FTIR Spectroscopies of the Probe Molecules, in: N.T. Sheppard (Ed.) Molecular Spectroscopy of Oxide Catalyst Surfaces, John Wiley and Sons Ltd, UK, 2003, pp. 188.

[115] P. Sathishkumar, R. Sweena, J.J. Wu, S. Anandan, Synthesis of CuO-ZnO nanophotocatalyst for visible light assisted degradation of a textile dye in aqueous solution, Chemical Engineering Journal, 171 (2011) 136-140.

[116] J.B. Bulko, R.G. Herman, K. Klier, G.W. Simmons, OPTICAL-PROPERTIES AND

ELECTRONIC INTERACTIONS OF MICROCRYSTALLINE CU-ZNO CATALYSTS, Journal of Physical Chemistry, 83 (1979) 3118-3122.

[117] R. Elilarassi, G. Chandrasekaran, Structural, optical and magnetic characterization of Cu-doped ZnO nanoparticles synthesized using solid state reaction method, Journal of Materials Science-Materials in Electronics, 21 (2010) 1168-1173.

[118] A. Le Nestour, M. Gaudon, G. Villeneuve, R. Andriessen, A. Demourgues, Steric and electronic effects relating to the Cu2+ Jahn-Teller distortion in Zn1-xCuxAl2O4 spinels, Inorganic Chemistry, 46 (2007) 2645-2658.

[119] L. Martins, R.P.S. Peguin, M. Wallau, E.A. Urquieta-Gonzalez, Selective catalytic reduction of NO to N-2 with copper and cobalt exchanged ZSM-5 zeolites: The effect of calcium addition, Journal of the Brazilian Chemical Society, 16 (2005) 589-596.

[120] Y. Teraoka, C. Tai, H. Ogawa, H. Furukawa, S. Kagawa, Characterization and NO decomposition activity of Cu-MFI zeolite in relation to redox behavior, Applied Catalysis a-General, 200 (2000) 167-176.

[121] P.R. Potti, V.C. Srivastava, Comparative Studies on Structural, Optical, and Textural Properties of Combustion Derived ZnO Prepared Using Various Fuels and Their Photocatalytic Activity, Industrial & Engineering Chemistry Research, 51 (2012) 7948-7956.

[122] A.J. Reddy, M.K. Kokila, H. Nagabhushana, R.P.S. Chakradhar, C. Shivakumara, J.L. Rao, B.M. Nagabhushana, Structural, optical and EPR studies on ZnO:Cu nanopowders prepared via low temperature solution combustion synthesis, Journal of Alloys and Compounds, 509 (2011) 5349-5355.

[123] H.J. Lee, B.S. Kim, C.R. Cho, S.Y. Jeong, A study of magnetic and optical properties of Cu-doped ZnO, Physica Status Solidi B-Basic Research, 241 (2004) 1533-1536.

[124] R.B. Bylsma, W.M. Becker, J. Kossut, U. Debska, D. Yodershort, DEPENDENCE OF ENERGY-GAP ON X AND T IN ZN1-XMNXSE - THE ROLE OF EXCHANGE INTERACTION, Physical Review B, 33 (1986) 8207-8215.

[125] B.L. Kniep, Microstructural Modifications of Copper Zinc Oxide Catalysts as a Function of Precipitate Ageing, Technical University of Berlin, Berlin, Germany, 2005.

[126] G. Sengupta, A. Chakraborty, S. Banerjee, D.P. Das, R.P. Choudhury, R.K. Banerjee, R.M. Sanyal, SOLID SOLID INTERACTION AND ELECTRONIC-PROPERTIES OF COPPER-ZINC OXIDE CATALYSTS, Applied Catalysis, 68 (1991) 1-9.

[127] M. Caglar, Y. Caglar, S. Aksoy, S. Ilican, Temperature dependence of the optical band gap and electrical conductivity of sol-gel derived undoped and Li-doped ZnO films, Applied Surface Science, 256 (2010) 4966-4971.

[128] B.M. Weckhuysen, In-situ Spectroscopy of Catalysts., American Scientific Publishers, USA, 2004.

[129] A. Sujan, H.Y. Yang, P. Dimick, B.J. Tatarchuk, A fiber optics system for monitoring utilization of ZnO adsorbent beds during desulfurization for logistic fuel cell applications, Journal of Power Sources, 315 (2016) 242-253.

[130] M.H. Groothaert, K. Lievens, H. Leeman, B.M. Weckhuysen, R.A. Schoonheydt, An operando optical fiber UV-vis spectroscopic study of the catalytic decomposition of NO and N2O over Cu-ZSM-5, Journal of Catalysis, 220 (2003) 500-512.

[131] F. Giordanino, P.N.R. Vennestrom, L.F. Lundegaard, F.N. Stappen, S. Mossin, P. Beato, S. Bordiga, C. Lamberti, Characterization of Cu-exchanged SSZ-13: a comparative FTIR, UV-Vis, and EPR study with Cu-ZSM-5 and Cu-beta with similar Si/Al and Cu/Al ratios, Dalton Transactions, 42 (2013) 12741-12761.

[132] G. Grubert, M. Wark, N.I. Jaeger, G. Schulz-Ekloff, O.P. Tkachenko, Reduction kinetics of zeolite-hosted mono- and polynuclear titanium oxide species followed by UV/Vis diffuse reflectance spectroscopy: Influence of location and coordination, Journal of Physical Chemistry B, 102 (1998) 1665-1671.

[133] R.L. Puurunen, B.M. Weckhuysen, Spectroscopic study on the irreversible deactivation of chromia/alumina dehydrogenation catalysts, Journal of Catalysis, 210 (2002) 418-430.

[134] M. Amara, L. Gengembre, D. Olivier, PREPARATION OF MONO-VALENT COPPER BY A SINGLE ELECTRON-TRANSFER STEP IN THE PHOTOREDUCTION OF ZINC OXIDE-SUPPORTED COPPER-CATALYSTS, Applied Catalysis, 41 (1988) 147-164.

[135] O. Ruggeri, F. Trifiro, A. Vaccari, CATALYSTS FOR LOW-TEMPERATURE METHANOL SYNTHESIS .1. A STUDY OF THE REDUCTION PROCESS, Journal of Solid State Chemistry, 42 (1982) 120-124.

[136] A.V. Kucherov, J.L. Gerlock, H.W. Jen, M. Shelef, IN-SITU ESR MONITORING OF CUH-ZSM-5 UP TO 500-DEGREES-C IN FLOWING DRY MIXTURES OF NO(NO2), C3H6(C2H5OH), AND EXCESS O-2, Journal of Catalysis, 152 (1995) 63-69.

[137] J. Soria, A. Martinez-Arias, A. Martinez-Chaparro, J.C. Conesa, Z. Schay, Influence of the preparation method, outgassing treatment, and adsorption of NO and/or O-2 on the Cu2+ species in Cu-ZSM-5: An EPR study, Journal of Catalysis, 190 (2000) 352-363.

[138] M.S. Kumar, M. Schwidder, W. Grunert, A. Bruckner, On the nature of different iron sites and their catalytic role in Fe-ZSM-5 DeNO(x) catalysts: new insights by a combined EPR and UV/VIS spectroscopic approach, Journal of Catalysis, 227 (2004) 384-397.

[139] E. Giamello, B. Fubini, P. Lauro, INVESTIGATION ON THE STATE OF COPPER IN COPPER-ZINC OXIDE BIPHASIC CATALYST BY ELECTRON-PARAMAGNETIC-RES

AND ADSORPTION MICROCALORIMETRY, Applied Catalysis, 21 (1986) 133-147.

[140] N. Takezawa, H. Kobayashi, Y. Kamegai, M. Shimokawabe, CHARACTERIZATION OF COPPER SILICA CATALYSTS IN REDUCED STATES, Applied Catalysis, 3 (1982) 381-388.

[141] A. Sujan, B. Tatarchuk, Carbonyl Sulfide Hydrolysis over Alkali Promoted CeO_2-Al_2O_3 Mixed Oxide Catalysts for Wide Temperature Desulfurization Applications, *24th North American Catalysis Society Meeting*Pittsburgh, PA, 2015.

[142] M. Mureddu, I. Ferino, E. Rombi, M.G. Cutrufello, P. Deiana, A. Ardu, A. Musinu, G. Piccaluga, C. Cannas, ZnO/SBA-15 composites for mid-temperature removal of H_2S: Synthesis, performance and regeneration studies, Fuel, 102 (2012) 691-700.

[143] X. Wang, T. Sun, J. Yang, L. Zhao, J. Jia, Low-temperature H(2)S removal from gas streams with SBA-15 supported ZnO nanoparticles, Chemical Engineering Journal, 142 (2008) 48-55.

[144] G. Liu, Z.-H. Huang, F. Kang, Preparation of ZnO/SiO_2 gel composites and their performance of H_2S removal at room temperature, Journal of Hazardous Materials, 215 (2012) 166-172.

[145] D. Mores, E. Stavitski, B.M. Weckhuysen, Space- and Time-Resolved In-situ Spectroscopy on the Coke Formation in Molecular Sieves: Methanol-to-Olefin Conversion over H-ZSM-5 and H-SAPO-34, Chemistry European Journal, 14 (2008) 11320-11327.

[146] R.L. Puurunen, B.G. Beheydt, B.M. Weckhuysen, Monitoring chromia/alumina catalysts in situ during propane dehydrogenation by optical fiber UV-visible diffuse reflectance spectroscopy, Journal of Catalysis, 204 (2001) 253-257.

[147] B.M. Weckhuysen, Snapshots of a working catalyst: possibilities and limitations of in situ spectroscopy in the field of heterogeneous catalysis, Chemical Communications, (2002) 97-110.

[148] F. Benito-Lopez, W. Verboom, M. Kakuta, J.G.E. Gardeniers, R.J.M. Egberink, E.R. Oosterbroek, A. van den Berg, D.N. Reinhoudt, Optical fiber-based on-line UV/Vis spectroscopic monitoring of chemical reaction kinetics under high pressure in a capillary microreactor, Chemical Communications, (2005) 2857-2859.

[149] M.A. Liauw, L.C. Baylor, O'Rourke, UV-visible Spectroscopy for On-line Analysis, Wiley, UK, 2010.

[150] D.J.W. Ng, M. Assirelli, Mixing study in batch stirred vessels using a fibre-optic UV-VIS monitoring technique: A novel method, Chemical Engineering Research & Design, 85 (2007) 1348-1354.

[151] W.H. Shen, X.Q. Chen, Online Monitoring of Kappa Number during Batch Pulping by Visible Spectroscopy, Industrial & Engineering Chemistry Research, 48 (2009) 4872-4876.

[152] S.G. Mueller, J.R. Werber, M.H. Al-Dahhan, M.P. Dudukovic, Using a fiber-optic probe for the measurement of volumetric expansion of liquids, Industrial & Engineering Chemistry Research, 46 (2007) 4330-4334.

[153] P. Ege, A. Grislingas, H.I. deLasa, Modelling turbulent fluidized bed reactors: Tracer and fibre optic probe studies, Chemical Engineering Journal and the Biochemical Engineering Journal, 61 (1996) 179-190.

[154] S.P. Gurden, J.A. Westerhuis, A.K. Smilde, Monitoring of batch processes using spectroscopy, Aiche Journal, 48 (2002) 2283-2297.

[155] J. Gabrielsson, H. Jonsson, J. Trygg, C. Airiau, B. Schmidt, R. Escott, Combining process and spectroscopic data to improve batch modeling, Aiche Journal, 52 (2006) 3164-3172.

[156] J.Q. Brown, K. Vishwanath, G.M. Palmer, N. Ramanujam, Advances in quantitative UV-visible spectroscopy for clinical and pre-clinical application in cancer, Current Opinion in Biotechnology, 20 (2009) 119-131.

[157] M.D. Keller, S.K. Majumder, M.C. Kelley, I.M. Meszoely, F.I. Boulos, G.M. Olivares, A. Mahadevan-Jansen, Autofluorescence and Diffuse Reflectance Spectroscopy and Spectral Imaging for Breast Surgical Margin Analysis, Lasers in Surgery and Medicine, 42 (2010) 15-23.

[158] G.D. Focht, P.V. Ranade, D.P. Harrison, HIGH-TEMPERATURE DESULFURIZATION USING ZINC FERRITE - REDUCTION AND SULFIDATION KINETICS, Chemical Engineering Science, 43 (1988) 3005-3013.

[159] M. Mureddu, I. Ferino, A. Musinu, A. Ardu, E. Rombi, M.G. Cutrufello, P. Deiana, M. Fantauzzi, C. Cannas, MeOx/SBA-15 (Me = Zn, Fe): highly efficient nanosorbents for mid-temperature H_2S removal, Journal of Materials Chemistry A, 2 (2014) 19396-19406.

[160] AvaSpec Operating manual, in: Avantes (Ed.), April 2009, pp. 73.

[161] E.S. Agorku, M.A. Mamo, B.B. Mamba, A.C. Pandey, A.K. Mishra, Cobalt-doped ZnS-reduced graphene oxide nanocomposite as an advanced photocatalytic material, Journal of Porous Materials, 22 (2015) 47-56.

[162] L.E. Brus, ON THE DEVELOPMENT OF BULK OPTICAL-PROPERTIES IN SMALL SEMICONDUCTOR CRYSTALLITES, Journal of Luminescence, 31-2 (1984) 381-384.

[163] H. Yoshida, T. Shimizu, C. Murata, T. Hattori, Highly dispersed zinc oxide species on silica as active sites for photoepoxidation of propene by molecular oxygen, Journal of Catalysis, 220 (2003) 226-232.

[164] M. Tan, W.P. Cai, L.D. Zhang, Optical absorption of ZnS nanocrystals inside pores of silica, Applied Physics Letters, 71 (1997) 3697-3699.

[165] V.F. Anufrienko, T.M. Yurieva, F.S. Hadzhieva, T.P. Minyukova, S.Y. Burylin, SPECTROSCOPIC STUDIES OF THE STATE OF CU-2+ IONS IN CU-ZN-AL OXIDE CATALYSTS, Reaction Kinetics and Catalysis Letters, 27 (1985) 201-205.

[166] C. Corrado, Y. Jiang, F. Oba, M. Kozina, F. Bridges, J.Z. Zhang, Synthesis, Structural, and Optical Properties of Stable ZnS:Cu,Cl Nanocrystals, Journal of Physical Chemistry A, 113 (2009) 3830-3839.

[167] S.-j. Liu, Z.-y. Chen, Y.-z. Chang, S.-l. Wang, Q. Li, Y.-q. Fan, H.-m. Jia, X.-j. Zhang, Y.-g. Zhao, The breakthrough curve combination for xenon sampling dynamics in a carbon molecular sieve column, Analyst, 140 (2015) 428-433.

[168] H. Yang, D.R. Cahela, B.J. Tatarchuk, A study of kinetic effects due to using microfibrous entrapped zinc oxide sorbents for hydrogen sulfide removal, Chemical Engineering Science, 63 (2008) 2707-2716.

[169] S. Senkan, e. al., High throughput testing of heterogeneous catalyst libraries using array micro reactors and mass spectrometry, Angewandte Chemie, 38 (1999) 2794-2799.

[170] A. Sujan, B. Tatarchuk, Carbonyl sulfide formation during wide temperature reformate desulfurization on ZnO/SiO_2 and Cu promoted ZnO/SiO_2 adsorbents, 249th ACS National MeetingDenver, Colorado, 2015.

[171] NIST Chemistry Web book.

[172] R. Sitthikhankaew, D. Chadwick, S. Assabumrungrat, N. Laosiripojana, Effects of humidity, O_2, and CO_2 on H_2S adsorption onto upgraded and KOH impregnated activated carbons, Fuel Processing Technology, 124 (2014) 249-257.

[173] V.e.a. Engel, Photodissociation of water in the first absorption band: a prototype for dissociation on a repulsive potential energy surface, Journal of Physical Chemistry, 96 (1992) 3201-3213.

[174] R.J. Ferm, THE CHEMISTRY OF CARBONYL SULFIDE, Chemical Reviews, 57 (1957) 621-640.

[175] Y. Yang, Y. Shi, N. Cai, Simultaneous removal of COS and H_2S from hot syngas by rare earth metal-doped SnO2 sorbents, Fuel, 181 (2016) 1020-1026.

[176] D. Liu, W. Zhou, J. Wu, La_2CuO_4/ZSM-5 sorbents for high-temperature desulphurization, Fuel, 177 (2016) 251-259.

[177] Z.Y. Wan, B.S. Liu, F.M. Zhang, X.H. Zhao, Characterization and performance of LaxFeyOz/MCM-41 sorbents during hot coal gas desulfurization, Chemical Engineering Journal, 171 (2011) 594-602.

[178] B.S. Liu, Z.Y. Wan, Y.P. Zhan, C.T. Au, Desulfurization of hot coal gas over high-surface-area LaMeOx/MCM-41 sorbents, Fuel, 98 (2012) 95-102.

[179] C. Fu, J. Wang, M. Yang, X. Su, J. Xu, B. Jiang, Effect of La doping on microstructure of SnO2 nanopowders prepared by co-precipitation method, Journal of Non-Crystalline Solids, 357 (2011) 1172-1176.

[180] L. Li, P. Zhou, H. Zhang, X. Meng, J. Li, T. Sun, Mid-temperature Deep Removal of Hydrogen Sulfide on Rare Earth (RE = Ce, La, Sm, Gd) Doped ZnO Supported on KIT-6: Effect of RE Dopants and Interaction between Active Phase and Support Matrix, Applied Surface Science.

[181] P. Ning, K. Li, H. Yi, X. Tang, J. Peng, D. He, H. Wang, S. Zhao, Simultaneous Catalytic Hydrolysis of Carbonyl Sulfide and Carbon Disulfide over Modified Microwave Coal-Based Active Carbon Catalysts at Low Temperature, Journal of Physical Chemistry C, 116 (2012) 17055-17062.

[182] J.A. Dean, Lange's Handbook of Chemistry, 12th ed.1979.

[183] M. Khatamian, A.A. Khandar, B. Divband, M. Haghighi, S. Ebrahimiasl, Heterogeneous photocatalytic degradation of 4-nitrophenol in aqueous suspension by Ln (La3+, Nd3+ or Sm3+) doped ZnO nanoparticles, Journal of Molecular Catalysis A: Chemical, 365 (2012) 120-127.

[184] B. Houng, C.-J. Huang, Structure and properties of Ag embedded aluminum doped ZnO nanocomposite thin films prepared through a sol–gel process, Surface and Coatings Technology, 201 (2006) 3188-3192.

[185] T. Jia, W. Wang, F. Long, Z. Fu, H. Wang, Q. Zhang, Fabrication, characterization and photocatalytic activity of La-doped ZnO nanowires, Journal of Alloys and Compounds, 484 (2009) 410-415.

[186] A.N. Ökte, Characterization and photocatalytic activity of Ln (La, Eu, Gd, Dy and Ho) loaded ZnO nanocatalysts, Applied Catalysis A: General, 475 (2014) 27-39.

[187] C. Li, R. Hu, L. Qin, R. Ding, X. Li, H. Wu, Enhanced photocatalytic activity of ZnO/La_2O_3 composite modified by potassium for phenol degradation, Materials Letters, 113 (2013) 190-194.

[188] S. Tian, Y. Zhang, D. Zeng, H. Wang, N. Li, C. Xie, C. Pan, X. Zhao, Surface doping of La ions into ZnO nanocrystals to lower the optimal working temperature for HCHO sensing properties, Physical Chemistry Chemical Physics, 17 (2015) 27437-27445.

[189] W. Raza, M.M. Haque, M. Muneer, Synthesis of visible light driven ZnO: Characterization and photocatalytic performance, Applied Surface Science, 322 (2014) 215-224.

[190] J. West, B.P. Williams, N.C. Young, C. Rhodes, G.J. Hutchings, New directions for COS hydrolysis: Low temperature alumina catalysts, in: A. Parmaliana, D. Sanfilippo, F. Frusteri, A. Vaccari, F. Arena (Eds.) Natural Gas Conversion V, Elsevier Science Publ B V, Amsterdam, 1998, pp. 373-378.